JUL 1969
RECEIVED
NASA STI FACILITY
INPUT BRANCH

research report

WYLE LABORATORIES
TESTING DIVISION, HUNTSVILLE FACILITY

FACILITY FORM 602

N69-40127	
(ACCESSION NUMBER)	(THRU)
255	1
(PAGES)	(CODE)
NASA-Cr-#102269	12
(NASA CR OR TMX OR AD NUMBER)	(CATEGORY)

WYLE LABORATORIES - RESEARCH STAFF

REPORT WR 69-3

CHARACTERISTICS OF THE STATIC- AND FLUCTUATING-PRESSURE ENVIRONMENTS INDUCED BY THREE-DIMENSIONAL PROTUBERANCES AT TRANSONIC MACH NUMBERS

By

J. E. Robertson

Work Performed Under Contract NAS8-21026

June 1969

WYLE LABORATORIES
RESEARCH DIVISION, HUNTSVILLE FACILITY

COPY NO. 13

FOREWORD

This report was prepared by Wyle Laboratories, Research Division, Huntsville, Alabama for the Unsteady Gasdynamics Branch, Aero-Astrodynamics Laboratory, Marshall Space Flight Center (MSFC), National Aeronautics and Space Administration (NASA), Huntsville, Alabama under Contract NAS8-21026. The work was performed under the direction of Messrs. G. Wilhold - Deputy Chief of the MSFC Unsteady Gasdynamics Branch, and J. Jones - Technical Monitor of the contract.

This report contains the results of a wind tunnel test conducted at the Arnold Engineering Development Center (AEDC) during the period from May 22 through June 7, 1968. The tests were conducted under the direction of Mr. H. C. Dubose of ARO, Inc., contract operator of AEDC, with Mr. T. R. Brice as the project engineer.

The author wishes to express his appreciation and to extend thanks to all persons at NASA-MSFC, AEDC, and Wyle Laboratories who participated in this program of study. Those particularly instrumental in the various phases of planning and conducting the test, reducing the test results, and preparing the data for presentation in this report were: Messrs J. Jones, P. Howard, H. Bush, C. Walker, B. Borcherding and W. Edwards of NASA-MSFC, Messrs. T. Brice and J. Black of ARO, Inc. - AEDC, and Messrs. A. Jolly, D. Wallis, J. Matzkiw and S. Dendrinos of Wyle Laboratories.

ABSTRACT

A wind tunnel investigation was conducted to study the flow field induced by three-dimensional protuberances at transonic Mach numbers. The perturbed flow environments of both the protuberances and the surrounding structure were analyzed utilizing static- and fluctuating-pressure measurements and oil-flow visualization techniques. Test results for the generalized configurations which consisted of 2-, 4-, and 8-inch diameter cylindrical protuberances are discussed herein. The range of test variables consisted of protuberance heights from zero to 2 diameters, free-stream Mach numbers from 0.60 to 1.60, and unit Reynolds numbers from 1.5 to 4.5 million per foot. The static pressure results are presented in coefficient form to show the axial pressure distributions associated with the protuberance induced flow field as well as the distribution of surface pressures over the wall of the protuberances. Fluctuating pressure measurements are presented in the form of overall RMS fluctuating pressure coefficients, power spectra, cross-power spectra, and narrow band convection velocities. From the static- and fluctuating-pressure measurements and the oil-flow patterns, the structure of the perturbed flow field has been defined. One of the most significant findings is that the upstream separated flow field induced by three-dimensional protuberances consists of a complex, multiple vortex system which generates fluctuating pressures an order of magnitude greater than those observed in two-dimensional separated flows. The extreme fluctuating pressures encountered within the three-dimensional separated flow field are attributed to the shear interaction of two major vortices within the separated region.

TABLE OF CONTENTS

TABLE OF CONTENTS (Continued)

LIST OF FIGURES

LIST OF FIGURES (Continued)

LIST OF FIGURES (Continued)

LIST OF FIGURES (Continued)

LIST OF FIGURES (Continued)

LIST OF FIGURES (Continued)

LIST OF FIGURES (Continued)

LIST OF FIGURES (Continued)

LIST OF FIGURES (Continued)

LIST OF FIGURES (Continued)

LIST OF FIGURES (Continued)

LIST OF FIGURES (Continued)

LIST OF SYMBOLS

Symbol	Description
$A(k)$	Finite Fourier transform of discrete function X
$A'(k)$	Smoothed form of A(k)
$B(k)$	Finite Fourier transform of discrete function Y
$B'(k)$	Smoothed form of B(k)
B	Frequency bandwidth of the overall level computation
C_1, C_2	Constants denoting the decay rate of empirical cross-spectra
C_p	Static pressure coefficient (see Appendix A)
$C(\xi, f)$	Co-spectral density (see Appendix B)
$c(\xi, f)$	Normalized co-spectral density (see Appendix B)
$\Delta C_p(RMS)$	Root-mean-square coefficient of the fluctuating pressure about the mean, $\Delta P(RMS)/q_\infty$
D	Protuberance diameter
$E(f)$	Frequency response function for the microphone system electronics
$e[\ ]$	Error term for the parameter within the brackets
f	Frequency
f_ℓ	Lower frequency of 1/3-octave band
f_u	Upper frequency of 1/3-octave band
Δf	Frequency bandwidth
Δf_k	Frequency bandwidth corresponding to k
$\Delta f_{1/3}$	Frequency bandwidth for 1/3-octave band
$G(\xi, f)$	Total cross power spectral density

LIST OF SYMBOLS (Continued)

Symbol	Description
h	Protuberance height
$I(k)$	Periodogram of a discrete function of time
$\bar{I}(k)$	Averaged periodogram
i	$\sqrt{-1}$
j	Index of discrete functions of time such that the time corresponds to $j\ \Delta t$
k	Index of discrete functions of frequency such that the frequency corresponds to $k\ \Delta f$
ℓ_s	Length of the separated region induced upstream of the protuberance with $\ell_s = 0$ at the protuberance center
M_n	Mach number at boundary layer probe n
M_∞	Free-stream Mach number
$M(f)$	Frequency response function for the effect of finite microphone size
m	Number of discrete data used for each Fourier transform when calculating the averaged periodogram from subsections of a function of time
N	Total number of discrete data used in calculating statistical parameters of fluctuating pressure data (total number of digital samples)
n	Number of statistical degrees of freedom of computation
OASPL	Overall sound pressure level in dB
P_ℓ	Local static pressure
P_s	Local static pressure for orifices nearest the forward and aft rakes
P_t	Total pressure
P_∞	Free-stream static pressure
p	Number of subsections of microphone data of length m formed from the total number N

LIST OF SYMBOLS (Continued)

Symbol	Description
$\Delta P(RMS)$	Root-mean-square fluctuating pressure level
$Q(\xi, f)$	Quad-spectral density (see Appendix B)
$q(\xi, f)$	Normalized quad-spectral density (see Appendix B)
q_∞	Free-stream dynamic pressure, $0.7\, P_\infty M_\infty^2$
$R(f)$	Total frequency response function, $E(f)\, M(f)$
Re	Reynolds number per foot (unit Reynolds number)
Re_D	Reynolds number based on protuberance diameter
RMS	Root-mean-square
r	Radial location of test panel instrumentation with $r = 0$ at the protuberance center. For the present report, negative values of r/D denote the region upstream of the protuberances and positive values denote the region downstream of the protuberances
$S(f)$	1/3-octave band sound pressure level, dB
s.d. [ ]	Standard deviation of parameters within the brackets
T	Time
T_t	Free-stream total temperature
Δt	Increment of time
U	Local mean velocity
$U_c(f)$	Narrow-band convection velocity
$\overline{U}_c$	Broad-band convection velocity
U_n	Velocity at boundary layer probe n
U_ℓ	Local mean velocity over the test panel
U_∞	Free-stream velocity

LIST OF SYMBOLS (Continued)

Symbol	Description
u	Local fluctuating velocity
VCO	Voltage controlled oscillator
X(j)	Discrete function of time obtained at j Δt values of time
X(k)	Discrete function of frequency obtained at k Δf values of frequency
x	Coordinate in the direction of flow
Y(j)	Discrete function of time obtained at j Δt values of time
Y(k)	Discrete function of frequency obtained at k Δf values of frequency
y	Vertical position over the wall of the 8-inch diameter protuberance

Greek Symbol	
$\alpha(\xi, f)$	Phase angle between signals measured ξ apart at frequency f
$\gamma^2(\xi, f)$	Coherence function (see Appendix B)
δ	Boundary layer thickness
δ^*	Boundary layer displacement thickness
θ	Boundary layer momentum thickness
θ^+	Polar angle of static pressure orifices measured clockwise when vieweing the test article from above with $\theta^+ = 0$ deg at the upstream longitudinal centerline
θ^-	Polar angle of the microphones measured counterclockwise when viewing the test panel from above with $\theta^- = 0$ deg at the upstream longitudinal centerline
ϵ [ ]	Normalized standard error of the parameter within the brackets. Statistical uncertainty, based on a 68 percent confidence level, is given by $\pm\ \epsilon$
ξ	Longitudinal separation distance between two microphones
τ	Wall shear stress

LIST OF SYMBOLS (Continued)

Greek Symbol	Description
$\boldsymbol{\Phi}(f)$	True power spectral density
$\phi(f)$	Computed power spectral density
$\phi_{\xi}(f)$	Computed power spectral density at a point ξ from the location of a neighboring point for which $\phi(f)$ was computed
$\phi(k)$	Computed power spectral density of discrete functions of frequency obtained at $k\ \Delta f$ values of frequency
ω	Circular frequency

Subscript	
B	Denotes unperturbed boundary layer noise
E	Denotes total extraneous noise
e	Frequency response function due to microphone system electronics
I	Denotes instrumentation noise
m	Denotes microphone location over the wall of the 8-inch diameter protuberance, frequency response function due to microphone size
n	Boundary layer profile conditions at the location of probe n of the boundary profile rake (see Figure 10).
0	Protuberance-free conditions
p	Denotes static pressure orifice location over the wall of the 8-inch diameter protuberance
R	Denotes total frequency response function terms
s	Denotes statistical uncertainty term
T	Denotes tunnel background noise
t	Denotes technique error and uncertainty terms
x	Corresponding to the time function X

LIST OF SYMBOLS (Continued)

Subscript	Description
y	Corresponding to the time function Y
xy	Cross term corresponding to the time functions X and Y

1.0 INTRODUCTION

1.1 Background

Protuberances have an infinite number of possible geometries so that a general discussion of the flow field is difficult. For example, the Saturn V alone has approximately 75 individual protuberances which include reaction control rockets, auxiliary propulsion systems, vents, tunnels, etc. (Reference 1). Each protuberance generates its own flow field which may interact with the external flow field already present and lead to the imposition of large steady and fluctuating loads on both the protuberance and the surrounding structure. It is obviously impractical to investigate the environment of every protuberance which may be attached to the external surface of a launch vehicle, especially if some general features of the flow can be defined from a systematic study involving generalized protuberance geometries. In view of the free interaction hypothesis first advanced by Chapman, Kuehn, and Larson (Reference 2), it appears that the use of generalized protuberance shapes is a reasonable approach in studying protuberance flow fields. Essentially, they suggest that boundary layers undergo separation in a manner which is independent of the original cause. The separation commences well ahead of the protuberance, so that it is reasonable to suppose that the flow near the separation point is unaffected by the detail geometry of the protuberance. This phenomenon has been proven in experiments for two-dimensional supersonic flow and it is expected to apply to the three-dimensional case as well. However, even with this simplification, the flow close to the protuberance must be expected to be a function of the detailed protuberance shape. It follows that a definitive study of protuberance flow would involve measurements on the protuberance as well as on the structure which is in close proximity to the protuberance.

For the past two years, Wyle Laboratories have been engaged in a research program under Contract NAS8-21026 with NASA-MSFC to investigate the steady and unsteady aerodynamic characteristics of the flow around three-dimensional protuberances which extend into, and well beyond, attached turbulent boundary layers. The first task of this study was to conduct an extensive search of available literature for the purpose of accumulating data for a variety of protuberance geometries. Results of the literature survey indicated that considerable data were available for evaluating the mean flow around protuberances at supersonic speeds (see References 3-16, for examples). However, little data were available on the fluctuating air loads which may be experienced in the vicinity of the protuberances. Further, there appeared to be a complete lack of both steady and unsteady aerodynamic data for protuberance flows at transonic speeds, particularly for three-dimensional protuberances. This lack of transonic data poses a serious problem in predicting the steady and fluctuating air loads in the vicinity of protuberances for a launch vehicle, since, in the transonic flow regime, a launch vehicle experiences maximum dynamic pressure and, consequently, maximum aerodynamic loads. However, for the literature survey, some general features of protuberance flows were discovered and the results of this study are summarized in Reference 17.

Following the survey and analysis of the data from published literature, a small scale wind tunnel test program was planned and subsequently conducted in the MSFC 14 by 14 inch Transonic Wind Tunnel. This test was conducted with three primary objectives. The first objective was to investigate general features of protuberance flows at transonic speeds using generalized protuberance geometries. Right circular cylinders of various heights and diameters which project into the flow with the cylinder axis normal to the flow direction were selected for this study. The second objective of the small scale test was to investigate similarities between the flow fields for generalized protuberances and the flow fields for protuberances with specific geometries. For this phase of the study, models of the reaction control system (RCS) and the auxiliary propulsion system (APS) on the Saturn V were tested at the same conditions as for the generalized protuberance study. The third objective was to obtain base data that could be used to plan a large scale investigation of protuberance flows. The test results for the small scale wind tunnel study are presented in Reference 18. At best, the small scale test results revealed only cursory features of the protuberance flow fields due to the limitations imposed by the model size on instrumentation density and measurement accuracy. This is particularly true for fluctuating pressure measurements because of the relatively large size of the microphones.

1.2 Present Test Program

The large scale wind tunnel test program, reported herein, was planned to obtain more detailed static and fluctuating pressure measurements for protuberance flows. For this test, an existing model of the same general design as that tested in the small scale study, but of considerably larger scale was used. The test was conducted in the Propulsion Wind Tunnel, Transonic (16T) at the Arnold Engineering Development Center (AEDC), Arnold Air Force Station, Tennessee, from May 22 through June 7, 1968.

The wind tunnel test reported herein was based to some degree on the free interaction hypothesis discussed in Section 1.1. A basic detailed study was conducted using cylindrical protuberances of various heights and diameters for which some mean flow data were available. A basic reference length in the separated boundary layer generated by a protuberance is the undisturbed boundary layer thickness. Thus, protuberance height and diameter must be scaled with boundary layer thickness, and to accomplish this the test configuration included protuberances lying both within and well beyond the boundary layer. In addition, protuberances having more specific geometries were tested which consisted of scale models of the RCS and APS protuberances on the Saturn V.

The primary objective of the test was to determine the steady and fluctuating pressure characteristics of the protuberance flow field so that the environments of both the protuberances and the surrounding structure could be adequately defined. A comprehensive description of the test program was presented in a pre-test report, Reference 19. The test was performed according to the test plan with only minor modifications. Pertinent excerpts from this reference are included herein for the purpose of clarity and coherence. The protuberances were mounted to a curved panel model which was supported above the floor of the wind tunnel test section in a splitter-plate type installation. The surface panel and certain protuberances were instrumented with static pressure orifices and microphones to obtain the desired steady and fluctuating pressure measurements. Also, pitot pressure rakes were installed in the test panel to obtain descriptive boundary layer profile measurements. A comprehensive discussion of the test apparatus is presented in Section 2.0. The protuberances were tested over a range of Reynolds number and Mach numbers. The detailed description of the test conditions and procedure is presented in Section 3.0. The data reduction procedure, which consisted of both on-line and off-line phases, and an analysis of the precision of measurements are presented in Sections 4.0 and 5.0, respectively. A general discussion of the test results is presented in Section 6.0. It should be noted that over 300,000 static pressure measurements and over 100,000 microphone recordings were obtained during this test. Thus, any reduction and analysis of the test results must be selective. For the present phase of the study, emphasis was placed on the reduction and analysis of data obtained from the longitudinal centerline distribution of instruments which were located in the plane of symmetry of the perturbed flow field. An analysis of these data, which defines the salient characteristics of the static and fluctuating pressures associated with the protuberance flow field, is also presented in Section 6.0. From these data, the basic features of the flow field induced by three-dimensional protuberances and similarities and differences between two- and three-dimensional protuberance flows have been defined. Finally, conclusions resulting from this study and a description of areas to be studied in the future are presented in Section 7.0.

2.0 TEST APPARATUS

2.1 Test Facility

The test was conducted in the Propulsion Wind Tunnel, Transonic (16T) at AEDC. Tunnel 16T is a variable density wind tunnel with a 16 ft square test section. The walls of the test section are composed of perforated plates which allow continuous operation through the Mach number range from 0.55 to 1.60 with minimum wall interference. Details of the test section showing the model location are presented in Figures 1 and 2. A more extensive description of the tunnel is given in the AEDC Test Facilities Handbook and the latest calibration results are presented in References 20 and 21.

2.2 Test Article

The basic test article consisted of a 30-degree segment of a cylindrical shell having a radius of curvature of 130 inches. The curved panel was mounted in a splitter-plate type fixture which was supported above the tunnel floor (see Figure 1). The protuberances and instrumentation were mounted on a secondary panel (hereafter referred to as the test panel) which was 36.00 inches wide and 75.18 inches long and flush fitted into the basic panel structure (Figure 3). The right hand side of the test panel (when viewed looking upstream) was attached to the basic structure through hinges which allowed the test panel to be pivoted open and, thus, provide easy access to the instrumentation and protuberance drive system without having to completely disassemble the test article. Also the instrumentation and drive system were attached to the test panel so that they were exposed when the model was open as shown in Figure 4. This feature of the model design greatly simplified model configuration changes and the replacement of instrumentation. Protuberances for the basic study were right cylinders of 2-, 4- and 8-inch diameter and were telescoped into the flow over the test panel with the axes of the cylinders normal to the flow direction. Geometric details of the protuberances are shown in Figure 5. All the protuberances were raised and lowered with the same drive system. The drive system, shown in Figures 4 and 6, enabled the protuberances to be remotely raised and lowered to any height ranging up to 8 inches. Space limitations inside the splitter-plate limited the maximum travel of the drive system to 8 inches and since it was desirable to test all of the protuberances at heights ranging up to at least two diameters, it was necessary to add an 8-inch extension to the basic 8-inch diameter protuberance for certain runs. In the fully retracted position, the top surface of all but the 8-inch diameter protuberance with the 8-inch extension were flush with the test panel surface.

The drive system (Figure 6) consisted of three jack screws and a lift plate to which the various cylindrical protuberances were mounted. The drive system was supported between the underside of the test panel and a base plate by six support rods and two spacer bars. The jack screws were driven by a common 1/3 horsepower, 30 rpm electric motor through a chain and sprocket drive system. An O-ring seal was inserted in the test panel around the protuberance to seal the splitter-plate cavity from the top of the test panel and thus prevent leakage of air between the protuberance and test panel during the test.

Protuberance configuration changes were accomplished by removing the protuberance cap (see Figure 6) and detaching the base of the protuberance from the lift plate. Hole patterns in the lift plate provided for mounting all of the cylindrical protuberances on a common centerline as well as rotating the 8-inch diameter protuberance from 0 degree to polar angles of 15 and 60 degrees (counter clockwise when viewed from the top). For the 2- and 4-inch diameter protuberances, the gap between the test panel and the protuberance was filled with an instrumented insert panel. The insert panels were attached to the test panel in the place of the removable ring (see Figure 6). O-ring seals similar to that used for the 8-inch diameter protuberance, were inserted between the insert panels and the smaller diameter protuberances to seal the gap.

In addition to the basic study, models of the RCS and APS protuberances on the Saturn V of approximately 20 percent scale were tested. These models were mounted to the same test panel used for the basic study, so that existing instrumentation could be utilized. Details of the RCS and APS protuberances are not presented herein, since test results for these configurations will be forthcoming in a later report.

2.3 Instrumentation for Data Acquisition

Instrumentation in a given configuration of the test article consisted of a maximum of 296 static pressure orifices and 122 piezo-electric microphones which were flush mounted in the test panel and the 8-inch diameter protuberance. The basic 8-inch diameter protuberance and the 8-inch diameter protuberance with the extension are the only protuberances that contained instrumentation. Details of the instrumentation in the test panel, the insert panels and the 8-inch diameter protuberance configurations are shown in Figures 7, 8 and 9, respectively. The test panel contained 216 static pressure orifices that were distributed in a polar array centered at the protuberance center (Model Station = 0), Figure 7a. The polar angles for the static pressure orifices are denoted by θ^+ and are measured in the clockwise direction when viewing the test panel from above. Most of the static pressure orifices were distributed along the centerline of the test panel ($\theta^+ = 0$, and 180 degrees) and to the right side when viewed looking upstream. One ray of static pressure orifices was located at $\theta^+ = 270$ degrees so that symmetry of the flow could be determined. The locations shown in Figure 7a are nominal dimensions and exact locations are presented in Reference 19. Also, the test panel contained 107 microphones that were distributed in a polar array along the panel centerline and to the left side of the test panel when viewed looking upstream (Figure 7b). The polar angles for the microphones are denoted by θ^- and are measured in the counterclockwise direction when viewing the test panel from above. This array of steady and fluctuating pressure instruments provided optimum utilization of the instruments since the protuberance flow fields were symmetrical about the panel centerline.

The insert panels that were used for the 2- and 4-inch diameter protuberances contained static pressure orifices and microphones that were distributed in polar arrays similar to those of the test panel (see Figure 8). Each insert panel contained 39 static pressure orifices and 15 microphones. Since the 2- and 4-inch diameter protuberances do not contain instrumentation, there were a total of 255 active static pressure orifices and 122 active microphones for these two configurations. The total number of microphone channels available with the recorder system was limited to 122. Thus, microphone distributions in the insert panels provided only qualitative information of the unsteady pressure flow field in close proximity to 2- and 4-inch diameter cylindrical protuberances. However, detailed definition of the fluctuating pressure flow field near the cylindrical protuberances was obtained for the 8-inch diameter protuberance which had a relative high density of microphones in close proximity to the protuberance.

Both static and fluctuating pressure instruments were located in the basic 8-inch diameter protuberance and the extension of this protuberance. Details of the instrument locations for the 8-inch diameter protuberance configurations are shown in Figure 9. The basic 8-inch protuberance contained 24 static pressure orifices and 6 microphones distributed at polar angles of 0, 30 and 120 degrees in the wall of the protuberance and 32 static pressure orifices and 9 microphones distributed in a polar array in the protuberance cap. Thus, for this configuration, there were a total of 272 active static pressure orifices and 122 active microphones. For the 8-inch diameter protuberance configuration with the extension there were 48 static pressure orifices and 15 microphones distributed at polar angles of 0, 30 and 120 degrees in the wall of the protuberance. All of the microphones for this configuration were located in the walls of the extension portion of the protuberance with the base of the protuberance and the protuberance cap containing only static pressure instrumentation. The protuberance cap contained 32 static pressure orifices as for the case of the basic 8-inch diameter protuberance configuration. Thus, for the 8-inch diameter protuberance configuration with the extension there were a total of 296 active static pressure orifices and 122 active microphones. Both 8-inch diameter protuberance configurations were rotated about the centerline from 0 degree to polar angles of 15 and 60 degrees such that static and fluctuating pressures were recorded on the wall of the protuberances at polar angles of 0, 15, 30, 45, 60, 90, 120, 165 and 180 degrees. Because of the slight curvature of the protuberance cap, it was necessary to maintain the cap at the 0-degree position. That is, the cap was not rotated with the protuberance.

Other instrumentation on the test panel consisted of two pitot pressure rakes which were extended through the boundary layer for measurement of the boundary layer velocity profiles. Details of the rakes are shown in Figure 10. The forward rake was remotely controlled so that it could be extended and retracted as desired during the test. This rake was designed such that, when in the fully retracted position, the top surface of the test panel remained smooth. Further, this rake contained 15 pitot pressure probes distributed above the centerline of the test panel as denoted in Figure 10. The pressure for the static orifice in the test panel immediately aft of the forward rake was recorded with the rake in the retracted position, and was used together with the pitot pressures in the computation of the boundary layer velocity profiles in the upstream vicinity of the test panel. The aft rake was a fixed device and was present throughout the test. The aft rake contained 25 pitot pressure probes which were distributed above the panel centerline as shown in Figure 10. The pressure for the most aft static orifice in the test panel was used in conjunction with the pitot pressures to compute the boundary layer velocity profiles for the aft region of the test panel.

A pitot-static probe was extended into the secondary flow between the splitter-plate and tunnel floor to monitor the flow in this region. The previous small scale test indicated that the secondary flow may be partially blocked at Mach numbers near 1.0. By monitoring the pitot-static probe beneath the splitter-plate and the boundary layer rakes above the test panel, the effect of any flow spillage over the leading edge of the model could be readily determined. The static and total pressures (forward rake only) were connected to a system of pressure scanning switches (Scani-valves) which were mounted to the underside of the test panel. A total of ten 48-port Scani-valves were available to record the pressures. A typical static pressure installation is shown in Figure 11a. The total pressures for the aft rake were conditioned through the AEDC-PWT Precision Pressure Balance (PPB) system. This system, which was considered to be more accurate than the Scani-valve system, was also used to compute a reference pressure which was compared to its counterpart on each of the Scani-valves. The outputs from the Scani-valve and the PPB systems were reduced and tabulated on-line utilizing the AEDC-PWT digital computer facilities. Also, the static and total pressure parameters were stored together with identification and test condition parameters, on 800 bpi, IBM compatible digital magnetic tape for post-test analyses.

The microphones (or pressure transducers) used for this test were Kistler 601L quartz pressure transducers. These microphones have a resonant frequency of 130 kHz and previous calibrations conducted at NASA-MSFC indicate that frequency and phase were linear up to 20 kHz. The full scale pressure range was 300 psi and the active area of the diaphragm was 5/32-inch diameter. Kistler 553A charge amplifiers were used to convert the quartz charge to a voltage signal. The charge amplifiers limited the low frequency response to approximately 10 Hz. The amplifiers were also housed inside the model. A typical microphone installation is shown in Figure 11b.

The Kistler pressure transducer systems were calibrated in place by the use of a Photocon model PC-125 acoustic calibrator which was modified so as to be hand held over each pressure transducer. The calibration level was 150 dB (referenced to 0.0002 dynes per square centimeter) at 1 kHz.

The data acquisition system for the fluctuating pressure measurements consisted of the NASA-MSFC, 20 kHz constant bandwidth multiplexer and 14 track, 1.5 MHz magnetic tape recorder. A block diagram of the system is shown in Figure 12. The multiplexer provided close phase matching for data groups recorded on a single track and also enabled up to 122 data channels to be stacked on fourteen tracks. The data channels were stacked 7 and 9 to a tape track with each channel having a 10 Hz to 20 kHz frequency response. To provide for cross-spectrum analyses between data recorded on different tape tracks, it was necessary to record a crystal oscillator signal and a wide-band white noise signal on all channels at the beginning of each reel of tape since phase matching across tape tracks was limited by the alignment of the tape recorder heads and type skew. Also, the output from the crystal oscillator could be used in conjunction with a reference modulator to correct for tape speed errors. These signals were recorded continuously with the microphone data during the test. A complete system calibration was conducted immediately prior to the test and spot checked periodically during the test.

The vertical position of the various protuberances was measured by a linear potentiometer which was housed inside the model. The output from the potentiometer was conditioned through the AEDC-PWT force and moment readout system (FAMROS) and subsequently reduced and tabulated on-line. Calibration of this instrument was performed prior to the start of the test and checked periodically during the test.

3.0 TEST DESCRIPTION

3.1 Test Conditions

Basic tests of all protuberance configurations were conducted in the Mach number range from 0.60 to 1.60 and at a constant Reynolds number of 3×10^6 per foot. This unit Reynolds number was near the maximum that could be held constant in Tunnel 16T for the specified Mach number range. The 4-inch diameter protuberance was tested also at a Reynolds number of 1.5×10^6 per foot and the 8-inch diameter protuberance at Reynolds number of 1.5×10^6 and 4.5×10^6 per foot. For the 4.5 million Reynolds number condition, the maximum Mach number attainable was 1.2; however, data were obtained at Mach number 1.4 at a slightly reduced Reynolds number. Variations of unit Reynolds number with Mach number are presented in Figure 13a for the various configurations. Similar variations of dynamic pressure, q_∞, with Mach number are presented in Figure 13b.

Tests were conducted for the 4-inch diameter protuberance at a unit Reynolds number of 3×10^6 per foot with an artificially thickened boundary layer over the test panel. For this study, the boundary layer was tripped near the leading edge of the model so that the effects of boundary layer thickness on the protuberance flow field could be evaluated.

During the latter part of the test, experiments were conducted to develop effective flow visualization techniques in the region affected by the protuberance flow field. These experiments were performed concurrent with other phases of the test by using a 2-inch diameter, fixed protuberance located near the edge of the model, off the test panel. The technique evolved in these experiments was then used to obtain photographs of the flow patterns around the 4-inch diameter protuberance installed on the test panel. For the test, the Mach number ranged from 0.60 to 1.60 with unit Reynolds number held constant at 3×10^6 per foot. For all these studies, oil with paint pigment mixtures of various colors was released forward of, around, and behind the protuberance through small orifices so that the various regions of the perturbed flow field could be made visible. The individual colors of oil were controlled with solenoid valves which were regulated from the control room. The reservoir containers for the oil were pressurized to facilitate the flow of oil over the test panel surface. The resulting flow patterns were recorded on color still and motion pictures using cameras positioned on the top wall of the tunnel test section at a location approximately over the protuberance. The primary oil flow studies, using the 4-inch diameter protuberance, were conducted during the last two days of testing. For these studies, the microphones were removed from the model, and the holes were sealed with epoxy. Further, the test panel was painted with white enamel to improve color identification of the oil flow patterns. This technique proved extremely efficient for flow visualization over the test panel since it eliminated the need to interrupt testing between test conditions as required for conventional flow visualization studies. That is, the oil for the present technique remains sufficiently fluidic that it adjusts to a change in flow pattern rather easily; whereas, conventional oil flow techniques (titanium dioxide solutions for example) require that the oil evaporate leaving a residue of substance in order to identify the flow pattern. A titanium dioxide solution was applied to the test article for the last run of the test to identify the flow pattern over the wall of the 4-inch diameter protuberance at $M_{\infty} = 1.0$, $h/D = 2.0$. For this run, the surfaces of the test panel and protuberance were painted black.

3.2 Test Procedure

Prior to testing on each day, a complete system calibration was performed. This "pre-test" calibration consisted of zeroing the protuberance height potentiometer readout, leak checking of all the pressure orifices and probes, and both acoustically and electrically calibrating the microphone/data acquisition system. The acoustic calibration consisted of exciting each microphone at 150 dB with the Photocon PT-125 calibrator, and adjusting the input electronics to the tape recorder so that equal sensitivity was obtained for each microphone channel. The electrical calibration consisted of inserting a 458 mv (equivalent to 170 dB which was full scale) 1000 Hz sinusoidal oscillator signal into the microphone charge amplifier self-test inputs and recording the resulting signal on the data tape. This calibration was followed by a 45.8 mv (equivalent to 150 dB) 1000 Hz self-test input which was recorded also on the data tape. Further, a broad band random noise signal was recorded on tape through the self-test input. The sinusoidal self-test calibration was repeated at the beginning of each new reel of data tape during each day of testing. Periodically, the entire microphone/data acquisition calibration sequence was repeated following a day of testing for hot "post-test" calibration records.

For air-on testing of the cylindrical protuberances, the protuberance height was varied with Mach number held constant for a given run. In general, data were obtained for monotonic increases in protuberance height because of possible hysteresis effects associated with boundary layer separation. For several configurations and test conditions, data were obtained also for variations in protuberance height which monotonically decreased so that hysteresis effects could be evaluated. There was no noticeable effect on the test results. The procedure of varying protuberance height while holding Mach number constant was adopted because of the lesser time involved in protuberance height variations as compared to variations in Mach number. However, for the RCS and APS protuberances, variations in height were not required, and data were obtained for monotonic variations in Mach number - with both increasing and decreasing trends.

The test procedure for each cylindrical protuberance was as follows:

- Data acquisition with the protuberance and forward rake in the fully retracted, flush, position.

- Data acquisition with the protuberance in the retracted position and the forward rake in the fully extended postion.

- Data acquisition with the rake in the retracted position and the protuberance extended to heights ranging from zero to eight inches in fixed increments of 0.25 diameters.

The data acquisition procedure consisted of, first, acquisition of the static pressure data followed by acquisition of the fluctuating pressure recordings. Previous experience with the present instrumentation systems indicated that noticeable instrumentation noise was generated by the operation of the Scani-valve cyclic drive systems which affected the microphone signals. Thus, static pressure data and microphone data were obtained in sequential order rather than simultaneously. This procedure also allowed for examination of the on-line tabulation of mean flow data prior to proceeding to new test conditions.

For several configurations and tunnel test conditions, data were also obtained for transient variations in protuberance height (with Mach number held constant) and transient variations in Mach number (with protuberance height held constant). For these runs, the protuberance height and Mach number were monitored and static pressure data were obtained at discrete intervals without stopping the transient run for data acquisition. The microphone outputs were recorded continuously for the duration of each transient run.

4.0 DATA REDUCTION PROCEDURE

4.1 Introduction

It was necessary to perform a relatively extensive reduction of the measured data to define the tunnel test environment and the basic mean-flow and unsteady-flow environments induced by three-dimensional protuberances at transonic speeds. It is convenient to discuss the data reduction in terms of 1) tunnel flow parameters, 2) mean-flow parameters for the protuberance flow field, and 3) unsteady-flow parameters for the protuberance flow field. It should be noted that the computation of mean flow parameters was performed on-line during the test; whereas, the computation of the unsteady-flow parameters was performed off-line, subsequent to the test, utilizing the microphone recordings stored on magnetic tape.

4.2 Tunnel Flow Parameters

The computation of tunnel flow parameters was performed on-line during the test using standard data acquisition and computer program routines adopted for this purpose by the engineering personnel at AEDC. It suffices to state that the following flow parameters were computed and tabulated utilizing the facilities at AEDC.

• Free-Stream Mach Number,	M_∞
• Free-Stream Dynamic Pressure,	q_∞
• Free-Stream Static Pressure,	P_∞
• Free-Stream Unit Reynolds Number,	Re/ft
• Stilling Chamber Total Pressure,	P_t
• Stilling Chamber Total Temperature,	T_t

4.3 Mean-Flow Parameters

The computation of mean-flow parameters over the test article for the various configurations consisted, primarily, of reducing the measured static and total pressures to descriptive engineering terms. The static pressure measurements were reduced to ratios of the local to free-stream pressure, P_ℓ/P_∞ and to standard pressure coefficients, C_p. The total pressures from the boundary layer rakes were reduced to ratios of velocity, U_n/U_∞, and to profile Mach number, M_n. The boundary layer displacement thickness, δ^*, and momentum thickness, θ, were computed also from the total pressures at both the forward and aft rake positions. Further, the boundary layer displacement thickness and momentum thickness were computed at model station zero utilizing Bie's empirical relationships (Reference 22). The reduction of all static and total pressure measurements to mean-flow parameters were performed utilizing the digital computer facilities in the AEDC Propulsion Wind

Tunnel Facility. Pertinent equations used in the computation of the mean-flow parameters are presented in Appendix A. A typical printout of the on-line data is presented also in Appendix A.

4.4 Unsteady Flow Parameters

The computation of unsteady flow parameters to define the salient fluctuating pressure characteristics of the perturbed flow field induced by three-dimensional protuberances consisted of reducing the microphone recordings to descriptive statistical parameters. The procedure for this data reduction was very complex and certainly the most time consuming phase of the study. Both analog and digital techniques were employed in the data reduction process as noted in the following sections.

4.4.1 Analog Data Reduction

The analog data reduction instrumentation consisted of the following:

- A 1.5 MHz magnetic tape recorder with a nine channel, demodulator/tuner system for demultiplexing the FM signals recorded on each tape track. The demultiplexed signals were a reconstruction of the originally recorded microphone signals for the frequency range from 0 to 20 kHz.
- A Brüel and Kjaer Type 2112 Audio Frequency Spectrometer. The B&K spectrometer provided for 1/3-octave spectra and overall sound pressure level analyses.
- A Brüel and Kjaer Type 2305 Graphic Level Recorder. The B&K Level Recorder provided plots of the 1/3-octave spectra and overall sound pressure level.

The analog instrumentation was used in the reduction of all fluctuating pressure measurements to overall sound pressure level (OASPL) which were plotted on a dB scale by the graphic level recorder. Approximately 15 seconds of the real-time microphone signals were used in the analysis of each OASPL. Further, the frequency range covered by the analog equipment for the determination of the OASPL was from 2 Hz to 20 kHz.

The procedure adopted for the OASPL data reduction was to, first, adjust the data reduction electronics to give a 170 dB reading on the graphic level recorder for a 458 mv calibration signal recorded on each reel of tape for each data channel to be reduced. The calibration signal was recorded for each channel so that a permanent record could be maintained. Following the calibration set-up, the desired data channels were reduced to OASPL. This procedure was repeated for data on each new reel of tape. The OASPL data were reduced further to root-mean-square coefficients of fluctuating pressure, ΔC_p (RMS), by hand computation, using the following equation to relate the OASPL to the RMS fluctuating pressure:

$$\text{OASPL} = 20 \log_{10} \Delta P(\text{RMS}) + 127.582 \text{ dB} \qquad (4.1)$$

where the OASPL is referenced to 2×10^{-5} Newtons per square meter and ΔP(RMS) is in units of pounds per square foot.

The analog instrumentation facilitated a rapid reduction of the fluctuating pressure measurements to RMS coefficients, thus, enabling the important microphone channels to be selected for digital reduction to more complex statistical parameters. The analog data reduction instrumentation was employed also to obtain 1/3-octave spectra of representative microphone channels for comparison with digital computations.

4.4.2 Digital Data Reduction

Selected data were reduced to descriptive terms using a CDC 3300 digital computer facility. The output from the magnetic tape system was converted to digital form using the CDC 3300 computer equipped with Texas Instruments Model 846 analog-to-digital converters and two model 845E multiplexers. The computer system was capable of acquiring analog data and converting it to digital format over two simultaneous channels at a rate of 41,700, 12-bit samples per second per channel. The converted data was recorded on 7-track digital magnetic tape for subsequent analysis and tabulation. A comprehensive description of the computer programs used for digital analysis of the fluctuating pressure data is presented in References 23 and 24. The computations consisted of the following parameters.

- Root-Mean-Square Fluctuating Pressure Level, ΔP(RMS), psf
- Overall Sound Pressure Level, OASPL, dB
- 1/3-Octave Center Frequency, f, Hz
- 1/3-Octave Reduced Frequency Parameter, $f\xi/U_c$
- 1/3-Octave Sound Pressure Level, S(f), dB
- Power Spectral Density at 1/3-Octave Center Frequencies, $\phi(f)$, $(\text{psf})^2/\text{Hz}$
- Normalized Co-Spectral Density, $c(\xi,f)$
- Normalized Quad-Spectral Density, $q(\xi,f)$
- Total Cross-Spectral Density, $G(\xi,f)$, $(\text{psf})^2/\text{Hz}$
- Phase Angle, $\alpha(\xi,f)$, deg
- Coherence Function, $\gamma^2(\xi,f)$
- Convection Velocity, $U_c(f)$, ft/sec

The analog forms of pertinent data reduction equations for the foregoing unsteady flow parameters are presented in Appendix B.

It was noted in the preceding section that the fluctuating pressures were reduced to RMS levels using analog instrumentation. However, data which were selected for more complex analysis on the computer were also reduced to RMS levels, thus, providing a means of cross-checking the results. A discussion of the comparison between analog and digital results is presented in Section 5.3.3. The digital computation of RMS fluctuating pressure was performed using digital samples taken at N points in time as follows:

$$\Delta P(\mathrm{RMS}) = \left[\frac{1}{N}\sum_{n=1}^{N} P_n^2\right]^{\frac{1}{2}} \qquad (4.2)$$

where P_n is the digital sample of the pressure P(t) with $\overline{P} = 0$.

The method of digital computation of the spectral density parameters was based on a direct, finite, Fourier transform of the pressure time signals which were thence converted to power spectral density. The "Fast Fourier Transform" (FFT) algorithm was used to calculate the finite Fourier transform. The method is briefly summarized in the following paragraphs.

Let X(j) and Y(j) be the microphone pressure signals recorded at times $j\,\Delta t$, that is, the time functions defined at N points in time, Δt apart. The finite Fourier transform of X and Y are:

$$A(k) = \frac{1}{N}\sum_{j=0}^{N-1} X(j)\exp\left(-2\pi i\,\frac{kj}{N}\right) \qquad (4.3)$$

$$B(k) = \frac{1}{N}\sum_{j=0}^{N-1} Y(j)\exp\left(-2\pi i\,\frac{kj}{N}\right) \qquad (4.4)$$

where

$k = 0,1,2,\ldots, N-1$

$i = \sqrt{-1}$

A spectral window is required and may be applied by weighing the X and Y samples; or, for the window used in the present analysis (see Reference 24), may be applied by smoothing the real and imaginary parts of A and B with weights -1/4, 1/2, -1/4. Thus, modified periodograms are used (a periodogram obtained from data to which a window other than the Dirac comb function has been applied is known as a modified periodogram). The modified direct- and cross-periodograms of the signal pairs are:

$$I_x(k) = |A'(k)|^2 \tag{4.5}$$

$$I_y(k) = |B'(k)|^2 \tag{4.6}$$

$$I_{xy}(k) = A'(k)\, B'^*(k) \tag{4.7}$$

where A'(k) and B'(k) are the smoothed forms of A and B and the asterisk means complex conjugate. These periodograms may be converted to power spectral density with each value having 2 degrees of freedom. To increase the statistical accuracy, a series of p periodograms from adjacent sets of data are averaged, thus giving power spectral density results with 2p degrees of freedom. The method is to divide the N values of X(j) and Y(j) into p sections each of length m, sum the I(k) for each k and divide by p, i.e.,

$$\overline{I}_x(k) = \frac{1}{p} \sum_{r=1}^{p} [I_x(k)]_r \tag{4.8}$$

$$\overline{I}_y(k) = \frac{1}{p} \sum_{r=1}^{p} [I_y(k)]_r \tag{4.9}$$

$$\overline{I}_{xy}(k) = \frac{1}{p} \sum_{r=1}^{p} [I_{xy}(k)]_r \tag{4.10}$$

where now k = 0,1,2, ..., m - 1 and the total number of values of each signal which has been used is mp. Power spectral density results are defined for m/2 + 1 positive frequencies from 0 Hz to 1/(2 Δt) Hz, giving a frequency interval of 1/(m Δt) Hz. The direct and cross-power spectral densities are given by

$$\phi_x(k) = 32\, m\, \Delta t\, \overline{I}_x(k) \tag{4.11}$$

$$\phi_y(k) = 32\, m\, \Delta t\, \overline{I}_y(k) \tag{4.12}$$

$$\phi_{xy}(k) = 32\, m\, \Delta t\, \overline{I}_{xy}(k) \tag{4.13}$$

for the spectral window defined for the modified periodogram as discussed in Reference 24.

The power spectral density expressions given above were obtained at the frequency interval of 1/(m Δt) Hz and subsequently converted to values representative of 1/3-octave bands. USASI preferred frequencies were used in the specification of the 1/3-octave frequency intervals and center frequencies. This averaging process was performed utilizing power spectral densities from Equations 4.11 to 4.13 contained within each 1/3-octave band as follows:

$$\phi_x(f) = \frac{1}{\Delta f_{1/3}} \sum_{f_\ell}^{f_u} \phi_x(k)\, \Delta f_k = \phi(f) \qquad (4.14)$$

$$\phi_y(f) = \frac{1}{\Delta f_{1/3}} \sum_{f_\ell}^{f_u} \phi_y(k)\, \Delta f_k = \phi_\xi(f) \qquad (4.15)$$

$$\phi_{xy}(f) = \frac{1}{\Delta f_{1/3}} \sum_{f_\ell}^{f_u} \phi_{xy}(k)\, \Delta f_k = G(\xi, f) \qquad (4.16)$$

where $\Delta f_{1/3}$ represents the 1/3-octave band, Δf_k is the interval over which the power spectral densities values $\phi(k)$ apply, and f_ℓ and f_u are the lower and upper frequencies, respectively, of the 1/3-octave band, $\Delta f_{1/3}$. At the edges of each 1/3-octave band, the value of $\phi(k)$ was obtained by linear interpolation between the appropriate neighboring values of $\phi(f)$. It should be noted that this averaging process results in average energy per Hz within each 1/3-octave band rather than the total energy in the 1/3-octave band. Further, this averaging process increases the number of degrees of freedom of the direct and cross-power spectral density estimates in the same way as averaging the periodograms as indicated in Equations 4.8 to 4.10. See Section 5.3.3 for a discussion of the statistical accuracy of the computation. It will be noted in Section 5.3.3 that, to further increase the statistical accuracy of the computations at the low frequencies (below 200 Hz) and concurrently maintain acceptable computational times, it was necessary to average power spectral density values over full octave bands. Thus, below 200 Hz, data are presented only at the full-octave center frequencies.

The method of calculating direct and cross-power spectral density results in which the frequency range is divided into a series of bands, as described in Reference 24, was used in the data reduction computer programs. This method requires the use of a digital filter to successfully halve the frequency content of the time signal. The largest frequency interval is obtained in the upper frequency band and the interval is successively halved in each lower band. This process accounts for the nonlinear variations of the number of statistical degrees of freedom and normalized standard error with frequency as discussed in Section 5.3. A considerable amount of computer time was saved by the digital filtering process compared with the method of calculating the power spectral density with a constant frequency interval low enough to obtain the one-third octave band centered at 25.1 Hz.

The direct and cross-power spectral densities were used in the calculation of several useful functions which express the properties of the fluctuating pressure. Noting that the cross-power spectral density consists of both real and imaginary components, such that

$$G(\xi,f) = C(\xi,f) - i\,Q(\xi,f) \tag{4.17}$$

the following functions can be defined:

Normalized Co-Spectral Density

$$c(\xi,f) = \frac{C(\xi,f)}{[\phi(f)\,\phi_\xi(f)]^{\frac{1}{2}}} \tag{4.18}$$

where $C(\xi,f)$ is the real component of the cross-power spectral density, $G(\xi,f)$.

Normalized Quad-Spectral Density

$$q(\xi,f) = \frac{Q(\xi,f)}{[\phi(f)\,\phi_\xi(f)]^{\frac{1}{2}}} \tag{4.19}$$

where $Q(\xi,f)$ is the imaginary component of the cross-power spectral density, $G(\xi,f)$.

Coherence Function

$$\gamma^2(\xi,f) = \frac{|G(\xi,f)|^2}{|\phi(f)|\,|\phi_\xi(f)|} \tag{4.20}$$

Phase Angle

$$\alpha(\xi,f) = \tan^{-1}\left[\frac{Q(\xi,f)}{C(\xi,f)}\right] \tag{4.21}$$

Narrow-Band Convection Velocity

$$U_c(f) = \frac{2\pi f \xi}{\alpha(\xi, f)} \tag{4.22}$$

Broad-Band Convection Velocity

$$\overline{U}_c = \frac{\sum_{n=1}^{k} U_c(f)_n \Delta f_n}{\sum_{n=1}^{k} \Delta f_n} \tag{4.23}$$

A typical printout of the digital computations is presented in Appendix B. Also, the analog form of pertinent equations used in the computations are discussed in Appendix B.

5.0 PRECISION OF MEASUREMENTS

5.1 Tunnel Flow Parameters

The uncertainties associated with maintaining tunnel conditions were computed by AEDC personnel (Reference 25). These uncertainties are estimated as follows:

Mach Number, Subsonic	± 0.005
Mach Number, Supersonic	± 0.010
Total Temperature	± 5^{o}F
Total Pressure	± 5 psf

The uncertainties in tunnel flow parameters result from variations in setting and maintaining tunnel conditions. The longitudinal variation of Mach number along the centerline of the test section in the vicinity of the model is not included in the above values and reaches a maximum of ± 0.007 at supersonic Mach numbers.

5.2 Mean-Flow Parameters

The pressure measurements of the model pneumatic system have been evaluated by measuring a common pressure on all pressure scanning switches (Scani-valves) and on the tunnel Precision Pressure Balance (PPB) system. The variations were a function of the test condition total pressure (or Unit Reynolds number) and Mach number. The variations were linear with tunnel total pressure such that, when expressed in terms of pressure coefficient, the variations were constant at a given Mach number. The maximum variations in C_p, based on the worst cases encountered, ranged from ± 0.009 at $M_\infty = 0.60$ to ± 0.026 at $M_\infty = 1.60$. These variations were computed directly from the variations in measured static pressures using the PPB system as a standard and do not take into account the uncertainties associated with either the PPB system or the uncertainties in dynamic pressure.

In addition to the uncertainties presented above, variations in C_p were measured over the test panel for protuberance-free flow conditions (protuberance in fully retracted position). These spatial variations resulted from nonuniform flow over the test panel and are attributed to the aerodynamic characteristics of the model rather than variations in tunnel flow. A discussion of the spatial variations in C_p due to nonuniform aerodynamic effects is presented in Section 6.2.1.

5.3 Unsteady Flow Parameters

Precision in the measurement and reduction of fluctuating pressure data is an important, but often neglected, characteristic of the results. Almost any review of published test results for fluctuating pressure environments will reveal considerable scatter (and often a lack of agreement) between the results from the various experimental studies. One good example is the case of attached turbulent boundary layers. Here, numerous studies have been conducted in both wind tunnel facilities and in free flight; however, considerable scatter has been shown in the results from the various sources. Further, only in rare cases has the precision of measurements been presented with the data. Thus, it must be concluded that the errors and uncertainties contribute significantly to the lack of agreement between experiments. This is particularly true for fluctuating pressure environments of relative low overall level since numerous sources of error can be present in the measured data which are of the same order of magnitude as the fluctuating pressure of the phenomena under study. For the present test results, a comprehensive analysis of the precision of measurements has been made. For the purposes of this analysis, the precision of measurements will be distinguished by 1) errors, and 2) uncertainties. Errors are defined as deviations from the true values which are deterministic in the sense that they can be assessed through proper calibration and analysis. Further, errors may be applied directly to the measured data to minimize the inaccuracies in the final results. Uncertainties, on the other hand, are defined as deviations in the measured data about the true value and are nondeterministic in the sense that they cannot be applied directly to the data to determine the true value. Uncertainties represent the confidence band or confidence limits of the test results. At this point it should be noted that the data presented herein have not been corrected for the estimated errors. However, the errors are presented in a form which is consistent with that of the results, and, thus, may be applied with relative ease to selected results. The extent of the present data reduction and analysis (with the primary aim of determining the salient features of the protuberance flow fields) precluded the correction of all the data for known errors, and thus the data is presented in uncorrected form with the errors specified in this section.

Inaccuracies in the measurement and reduction of fluctuating pressure data result from a number of sources ranging from the inaccuracies associated with the data acquisition electronics to the statistical inaccuracies of the final computations. The purpose of this section is to note the predominant sources of inaccuracies and to assess their order of magnitude. It will be noted that errors presented herein could be interpreted as uncertainties in the data, since no effort has been made to adjust the test results for known error contributions. For example, reasonable estimates of instrumentation noise, tunnel background noise and system response are determinable; however, these contributions are relatively small compared to the level of the fluctuating pressure associated with the protuberance flow field. Thus, the contributions from these extraneous sources could be regarded as uncertainty errors in the precision of the measurements if so desired. On the other hand, the data may be refined in accuracy by applying the appropriate corrections presented herein.

The following tabulation consists of errors and uncertainties which are known to be prevalent in the data presented herein:

- Extraneous Noise Errors
  - Instrumentation System Noise
  - Tunnel Background Noise
- Frequency Response Errors
  - System Frequency Response
  - Finite Microphone Size
- Data Reduction Errors and Uncertainties
  - Statistical
  - Technique

In the following sections, the errors and uncertainties associated with each of the foregoing sources are discussed and assessed. For the purposes of this analysis, it is assumed that the various extraneous noise sources are uncorrelated between microphone channels such that noise correlation errors are not present in the cross-spectral density computations. A thorough examination of the noise correlation problem is in progress; however, these results are not available at this time for inclusion in the present report. It is anticipated that a separate report will be prepared in the near future defining in more detail the uncertainties in the cross-spectra due to the possible correlation of extraneous noise. The present precision of measurement analysis has considered the overall fluctuating pressure level and the power spectra. This analysis is summarized in Section 5.3.4.

5.3.1 Extraneous Noise Errors

The presence of extraneous noise in recorded data may have a significant effect on the accuracy of the various statistical parameters used to describe the characteristics of random phenomena under study. For the present wind tunnel investigation, the recorded fluctuating pressure data contained extraneous signals superimposed on the true pressure-time histories. The notable extraneous noise sources are the instrumentation system noise associated with the data acquisition equipment, and aerodynamic noise associated with the test facility air stream. Since the frequency domain of interest for the true fluctuating pressure data may coincide with that of the extraneous noise, removal of the noise cannot be accomplished by a simple filtering of the measured signals. Thus, one must resort to statistical means of extracting the true fluctuating pressure data from the measured data. One other alternative is to evaluate the statistical characteristics of the extraneous noise and include these data as errors in the precision of measurements. This latter approach is certainly feasible when the fluctuating pressures associated with the unsteady flow phenomena under study are much larger than the effective level of the extraneous noise. For the present test, the levels of extraneous noise are relatively small compared to the fluctuating pressure levels associated with the protuberance flow field and, consequently, the extraneous noise may be considered as uncertainties in the precision of measurements. A brief assessment of the two predominant extraneous noise sources - instrumentation system noise and tunnel background noise - are presented herein.

Instrumentation Noise

The instrumentation system noise was analyzed from the wind-off data records. The overall system noise levels expressed as equivalent RMS fluctuating pressure and representing the mean of the track-to-track deviations are presented as variations with VCO carrier frequency in Figure 14a. The presentation of results representing the mean of the 14 tape tracks is felt to be appropriate here, since track-to-track deviations about the mean are effectively errors in the error and, thus, have a second order effect on the precision of the measurements. The system noise increased with increasing carrier frequency. This increase is explained by: 1) the noise of the tape recorder increases at higher frequencies corresponding to the higher carrier frequencies, 2) the high frequency channels are more susceptible to tape flutter due to their small percentage deviation, and 3) the harmonics of the lower frequency channels are present in the higher channel pass bands. Previous calibrations conducted by NASA-MSFC indicated that worse case signal-to-noise ratios run from 26 dB to 38 dB relative to the full scale deviation of all channels. These data are consistent with the present test results which show mean signal-to-noise ratios ranging from 27.7 dB for VCO channel No. 9 to 37.3 dB for VCO channel No. 1.

The power spectra of the instrumentation noise for the various microphone channels examined were all similar in shape. Thus, it suffices to examine only the mean power spectrum obtained by averaging the spectra for the nine VCO channels. The tape tracks from which the nine VCO channels were selected were typical of all 14 tracks. It should be noted that variations in instrumentation noise from channel to channel results in a corresponding variation in measured data. Thus, a comparison of averaged instrumentation noise with averaged measured data introduces little error into the final analyses. Further, deviations about the average due to channel-to-channel and track-to-track variations are errors in the error and thus may be considered as having a second order effect as previously mentioned. The mean spectrum for the instrumentation noise is presented in Figure 14b as the distribution of equivalent mean-square fluctuating pressure with frequency.

Tunnel Background Noise

The most difficult extraneous noise source to evaluate is the wind tunnel background noise. Accurate measurement of the wind tunnel background noise is complicated by the fact that any calibration probe will generate its own aerodynamic flow field which may result in the measurement of erroneous tunnel noise. In the past, little attention has been given to the problem of wind tunnel noise, and the general trend has been to ignore the problem. Fortunately, measurements have been made for the test facility used in the present study; although, these data do not completely define the noise environment. The data, presented in Reference 21, consist of overall RMS fluctuating pressure and power spectra. These data were obtained using a slender, modified cone having a 5-degree half angle. Microphones were flush mounted along one meridian of the cone and spaced so that measurements could be obtained in both the laminar and turbulent regions of the cone boundary layer. Typical overall fluctuating pressure levels, in terms of the ΔC_p(RMS), are presented in Figure 15a for the Mach number range from 0.60 to 1.40. Maximum free-stream fluctuating pressures were present at Mach numbers near 0.70. It will be noted that data for the present study as obtained from the test panel with the protuberance in the fully retracted position are presented also in Figure 15a, and these data compare reasonably well with the calibration results. The data for the test panel at each Mach number represent the mean of approximately 88 microphone readings taken along the centerline of the test panel. As for the instrument noise case, the deviations about the mean have a second order effect and, thus, are neglected. The agreement between the calibration probe results and the test panel results is not too surprising even though a relatively thick turbulent boundary layer was present during the test panel measurements. It will be shown that the fluctuating pressures contributed by the attached turbulent boundary layer range from 10 to 20 percent of the total fluctuating pressure level based on a mean square comparison. Based on this finding, it is concluded that the protuberance-free, test panel results can be used to estimate the extraneous noise by applying an empirical correction to these data for the turbulent boundary layer noise. That is, with the protuberance in the retracted position (denoted by the subscript, 0) consider the measured pressure, $P(t)_0$, as the sum of three stationary random processes - tunnel noise, $P(t)_T$, instrumentation noise, $P(t)_I$, and attached boundary layer noise, $P(t)_B$, where the total extraneous noise, $P(t)_E$, is the sum of $P(t)_T$ and $P(t)_I$, such that

$$P(t)_0 = P(t)_T + P(t)_I + P(t)_B = P(t)_E + P(t)_B \qquad (5.1)$$

It follows that, if the various components of the measured signal, $P(t)_0$, are statistically independent, then the mean square fluctuating pressure is given by

$$[P(RMS)]_0^2 = e[\Delta P(RMS)]_T^2 + e[\Delta P(RMS)]_I^2 + [\Delta P(RMS)]_B^2$$

$$= e[\Delta P(RMS)]_E^2 + [\Delta P(RMS)]_B^2 \qquad (5.2)$$

where the prefix e denotes an error term.

In RMS coefficient form, the mean square fluctuating pressure as given in Equation 5.2 becomes

$$[\Delta C_p(\mathrm{RMS})]_0 = \left\{e\,[\Delta C_p(\mathrm{RMS})]_T^2 + e\,[\Delta C_p(\mathrm{RMS})]_I^2 + [\Delta C_p(\mathrm{RMS})]_B^2\right\}^{\frac{1}{2}}$$

$$= \left\{e\,[\Delta C_p(\mathrm{RMS})]_E^2 + [\Delta C_p(\mathrm{RMS})]_B^2\right\}^{\frac{1}{2}} \qquad (5.3)$$

Thus, the test panel results may be used to obtain an estimate of the total extraneous noise level by direct subtraction of the mean square boundary layer noise from the mean square test panel data. A comprehensive analysis of turbulent boundary layer fluctuating pressures has been made by Lowson (Reference 26). This analysis was based on a broad selection of experimental results from a number of different sources. An empirical formula for the boundary layer fluctuating pressure level which appears to agree with the general trend in the data is given by

$$[\Delta C_p(\mathrm{RMS})]_B = 0.006/(1 + 0.14\,M^2) \qquad (5.4)$$

The variation of the estimated boundary layer noise from Equation 5.4 with Mach number is presented also in Figure 15a.

Utilizing Equations 5.3 and 5.4, the following expressions are derived for the total extraneous noise and the tunnel noise.

$$e\,[\Delta C_p(\mathrm{RMS})]_E = \left\{[\Delta C_p(\mathrm{RMS})]_0^2 - \frac{3.6 \times 10^{-5}}{(1 + 0.14\,M^2)^2}\right\}^{\frac{1}{2}} \qquad (5.5)$$

$$e\,[\Delta C_p(\mathrm{RMS})]_T = \left\{[\Delta C_p(\mathrm{RMS})]_0^2 - e\,[\Delta C_p(\mathrm{RMS})]_I^2 - \frac{3.6 \times 10^{-5}}{(1 + 0.14\,M^2)^2}\right\}^{\frac{1}{2}} \qquad (5.6)$$

where the instrument noise, $e\,[\Delta C_p(\mathrm{RMS})]_I$, may be obtained from Figure 15b.

Variations of the total extraneous noise, instrumentation noise, and tunnel noise with Mach number are presented in Figure 15b showing a comparison with the total measured results. It is evident that, for the protuberance-free case, the tunnel noise dominates the measured signal from the relative magnitude of the contributing processes. It is also evident that little insight into the attached turbulent boundary layer case could be gained from the test panel measurements with the protuberance retracted. Again, it should be emphasized that the primary objective of this study was the examination of the protuberance flow fields and not the undisturbed boundary layer noise. For this reason, the protuberance-free data are presented only as an indication of the extraneous noise levels in the protuberance flow fields in subsequent figures.

The errors in the power spectra resulting from extraneous noise may be analyzed in a manner similar to that used in the overall fluctuating pressure level analysis. Again, it is necessary to rely on an empirical formula for adjusting the measured test panel results for the contribution of attached turbulent boundary layer noise. For the boundary layer, Lowson (Reference 26) derived the following empirical formula for the power spectral density.

$$[\phi(f)]_B = [\Delta C_p(\mathrm{RMS})]_B^2 \; \frac{q_\infty^2}{2\pi f_0 \left(1 + \frac{f^2}{f_0^2}\right)^{3/2}} \tag{5.7}$$

where

$$f_0 = \frac{4}{\pi} \; \frac{U_\infty}{\delta}$$

It will be noted that the power spectral densities for turbulent boundary layers are a function of free-stream dynamic pressure (q_∞), free-stream velocity (U_∞), and boundary layer thickness (δ). There is much uncertainty regarding the appropriate boundary layer parameter to be used in the normalization of the power spectral density. Lowson used the thickness (δ); whereas, others have used displacement thickness (δ^*), momentum thickness (θ), and wall shear stress (τ). For the present report, δ^* has been selected so that the results would be consistent with the two-dimensional protuberance results of Chyu and Hanly (Reference 27). However, it should be noted that protuberance diameter definitely controls the scale of the perturbed flow field in the three-dimensional case, and any generalization of the data should include this parameter.

For the analysis presented herein, comparison between two- and three-dimensional protuberance flows are discussed, and δ^* appeared to be an adequate normalizing parameter. For the undisturbed flow case, it is felt that Equation 5.7 is appropriate for estimation of the boundary layer noise spectra even though δ^* is used as the normalizing parameter.

Using arguments similar to that for the overall fluctuating pressure analysis, the measured power spectral density for the protuberance-free test panel may be expressed as:

$$\begin{aligned}[\phi(f)]_0 &= e\,[\phi(f)]_T + e\,[\phi(f)]_I + [\phi(f)]_B \\ &= e\,[\phi(f)]_E + [\phi(f)]_B \qquad (5.8)\end{aligned}$$

where, as before, the subscripts T, I, B and E represent the tunnel, instrumentation, boundary layer and total extraneous noise contributions to the measured signal (subscript 0). The errors in the measured power spectra are given, for the total extraneous noise and the portion due to tunnel background noise, by:

$$\begin{aligned}e\,[\phi(f)]_E &= [\phi(f)]_0 - [\phi(f)]_B \\ e\,[\phi(f)]_T &= [\phi(f)]_0 - [\phi(f)]_B - e\,[\phi(f)]_I \qquad (5.9)\end{aligned}$$

where $[\phi(f)]_B$ is defined by Equation 5.7 and $e\,[\phi(f)]_I$ is given in Figure 14b. Power spectra, representing the protuberance-free measured data, total extraneous noise, instrumentation noise, tunnel noise and boundary layer noise, are presented in Figures 16a through 16f for free-stream Mach numbers of 0.60 through 1.60, respectively. It is noted in the spectra that the difference between the extraneous noise and the protuberance-free measurements cannot be distinguished since the contribution of the boundary layer noise is negligibly small. Further, the extraneous noise is attributed primarily to the tunnel background noise as was noted in the overall level results.

At this point it should be noted that the tunnel background noise was affected also by the frequency response characteristics of microphone system (see next section). However, it is convenient to leave the tunnel noise error (and total extraneous noise error) in a form which is uncorrected for frequency response errors as discussed in the next section.

5.3.2 Frequency Response Errors

In addition to the extraneous noise errors discussed in the preceding section, another important source of error should be evaluated - the frequency response. The frequency response of the data acquisition system is a function of 1) the electronics of the system, and 2) the attenuation characteristics of the microphone due to the finite size of the microphone sensitive area. In the evaluation of the frequency response errors, it is convenient to discuss, first, the effect of frequency response on the power spectra, and from this evaluation, assess the effect of the response error on the overall fluctuating pressure level. It will be noted that the frequency response errors cannot be expressed as an absolute value as was the case for the extraneous noise, but rather, must be expressed as a function of the measured power spectral density. Thus, each power spectrum presented herein will have an associate frequency response correction spectrum.

System Electronics

The frequency response characteristics of the electronics of the microphone/data acquisition system are illustrated by results obtained from NASA-MSFC in Figure 17. The recording system frequency response was flat for the frequency range from 20 Hz to 20 kHz. Thus, no errors are attributed to the recording system. The frequency response of the microphone electronics was obtained from discrete frequency calibration signals inserted into the charge amplifier self-test inputs, recorded on tape, and subsequently played back for analysis. Typical calibration results are expressed as the ratio of the output-to-input power. The frequency response is shown to be flat within ± 1 dB for the frequency range from 20 Hz to 10 kHz. The frequency range of the present power spectra analyses corresponded to the 1/3 octave bands with center frequencies ranging from 25 Hz to 16,000 Hz, and the response attenuation was less than 3 dB for this frequency range. Before proceeding to the development of the error due to frequency response characteristics of the microphone electronics, it is convenient to assess the frequency response error attributed to the finite size of the microphone.

Microphone Size Effect

The measurement of a random pressure field by a microphone having a finite size sensitive area is subject to error because the microphone senses the spatial average over its face rather than a point value. To assess this error, it is necessary to have a priori knowledge of the true pressure field. Since the true pressure field is unknown, and in fact is precisely the parameter under study, determination of the microphone size effect becomes very difficult to assess. Several investigators have evaluated this problem through various mathematical models of the pressure field for attached boundary layers (References 28 - 33). However, their results are not directly applicable to the separated and wake flow fields as encountered in protuberance flow fields. In particular, the correction factor for the finite microphone size is a function of the cross-spectrum characteristics of the pressure field. For the boundary layer case, sufficient data is available to provide an empirical formula for the cross-spectrum, and thus a priori knowledge sufficient to enable empirical size correction factors to be derived. The problem is considerably more complex for the three-dimensional protuberance flow field. First, previous data is not available with which to compare the present results. Second, if data were available, the nonhomogeneous character of the flow field would preclude the derivation of a general correction factor. Thus, only a crude approximation of the correction factor appears feasible without an extensive, and time consuming study of the problem.

For the present analysis, it will be assumed that the turbulence structure for the protuberance flow field bears some resemblance to that of the boundary layer. In particular, it is assumed that the cross-spectra for the protuberance flow field has the same form as that for the boundary layer, and thus may be defined by the following empirical formula:

$$G(\xi,\omega) = \Phi(\omega) \exp\left[- C_1 \left|\frac{\omega\,\xi_1}{U_c}\right| - i\,\frac{\omega\,\xi_1}{U_c}\right]$$

$$\times \exp\left[- C_2 \left|\frac{\omega\,\xi_2}{U_c}\right|\right] \qquad (5.10)$$

where ξ_1 and ξ_2 are the separation between points in the longitudinal and lateral directions, respectively, and C_1 and C_2 are constants which represent how fast the correlation decays in the longitudinal and lateral directions. For the boundary layer, $C_1 \approx 0.1$ and $C_2 \approx 0.7$. For the protuberance flow field the decay appears to be more rapid in the longitudinal direction due to the dispersive nature of the flow field both upstream and downstream of the protuberance. In the neck region of the wake, the cross-spectra correspond closely to the exponentially decaying cosine with $C_1 \geq 0.2$. In the separated region upstream of the protuberance, the decay is noticeably more rapid with the constant C_1 ranging from approximately 0.4 to 0.8. It was noted in Reference 28 that an increase in the longitudinal decay rate would increase the sensitivity of the microphone, and consequently decrease the response error. Thus, a conservative estimate of the microphone size response error would correspond to the lower C_1 value of 0.2 associated with the wake data. Lateral cross-spectra were not computed for the present data, however, it is reasonable to expect the lateral decay rate to be equivalent to the boundary layer (0.7) or less because of the three-dimensional character of the flow field. Transverse velocity components will have a tendency to decrease the lateral decay rate. Thus, a value of $C_2 = 0.4$ is arbitrarily chosen. For the range of C_1 and C_2 which appears practical for the protuberance flow field, there does not appear to be a very significant change in the microphone correction factor (see Reference 28). Thus, the selection of $C_1 = 0.2$ and $C_2 = 0.4$ appears to be adequate for a prediction of the microphone correction factor. The response function, M(f), which represents the ratio of the measured power spectral density to the true power spectral density in regard to microphone size effects, is presented versus normalized frequency in Figure 18. These data were obtained from Reference 28. Since the convection velocity is a function of frequency, the proper numerical values of U_c may be used in estimating M(f) for a particular frequency. The radius of the microphone effective diameter, r, is 0.078 in.

For a further approximation of the microphone size error, consider the neck region of the protuberance wake as in the preceding discussion. Here, the convection velocity (at high frequencies where microphone size becomes important) is approximately equal to the free-stream velocity. Thus, making this substitution for U_c, the variation of M(f) with frequency may be approximated for each Mach number. These results are discussed in combination with the frequency response characteristics of the system electronics in the next section.

Combined Response Error

At this point, the frequency response functions, E(f) for the system electronics and M(f) for the finite microphone size effect, may be combined to give a total frequency response function, R(f). Noting that:

$$E(f) = \frac{[\text{Output Power}]_e}{[\text{Input Power}]_e} \tag{5.11}$$

$$M(f) = \frac{[\text{Output Power}]_m}{[\text{Input Power}]_m} \tag{5.12}$$

and

$$[\text{Input Power}]_e = [\text{Output Power}]_m \tag{5.13}$$

it follows that:

$$R(f) = E(f)\,M(f) = \frac{[\text{Output Power}]_e}{[\text{Input Power}]_m} \tag{5.14}$$

where $[\text{Output Power}]_e$ is the power associated with the measured signal and $[\text{Input Power}]_m$ is the power associated with the fluctuating pressure field under examination. The total frequency response function, R(f), is presented in Figure 19 and it is these data that should be used in the evaluation of the total frequency response errors.

To utilize the frequency response function to evaluate the error which it contributes to the measured signal, it is necessary to re-examine in some detail the characteristics of the extraneous noise presented in the preceding section. The instrumentation system noise resulted primarily from the data recording electronics. Thus, the instrumentation noise was not affected by the frequency response characteristics of the microphone system. It follows that the instrumentation noise error must be removed from the measured data prior to applying the frequency response correction. On the other hand, the tunnel noise error was affected by the frequency response of the microphone system, and, thus, it may be removed either before or after the frequency response correction. If the tunnel noise error is removed after the frequency response correction, then the tunnel noise correction must also be adjusted for the frequency response error. It is obviously more convenient to adjust the measured data for the tunnel noise error prior to applying the frequency response correction, and for this reason, the tunnel noise (and total extraneous noise) were presented in the preceding section without the frequency response correction.

Since the frequency response function is presented as the ratio of output-to-input power, the results may be applied directly to the power spectra adjusted for extraneous noise errors. That is, the power spectral density, corrected for both frequency response and extraneous noise errors, is given by:

$$\Phi(f) = \frac{\phi(f) - e\,[\phi(f)]_E}{R(f)} \tag{5.15}$$

where $e\,[\phi(t)]_E$ is given in Figure 16 and R(f) is given in Figure 19. Again it should be noted that R(f) as presented in Figure 19 is only an approximation due to the assumptions made regarding the cross-spectra of the fluctuating pressure field in the microphone size analysis.

Equation 5.15 may be used to derive an expression for the total error in the measured power spectra due to the combined effect of the extraneous noise and the frequency response. Noting that

$$e\,[\phi(t)]_{E+R} \doteq \phi(f) - \Phi(f) \tag{5.16}$$

it follows from Equation 5.15 that

$$e\,[\phi(f)]_{E+R} = \phi(f) - \frac{\left\{\phi(f) - e\,[\phi(f)]_E\right\}}{R(f)} \tag{5.17}$$

The error attributed only to the frequency response is given by

$$e\,[\phi(f)]_R = \left\{\phi(f) - e\,[\phi(f)]_E\right\}\left[1 - \frac{1}{R(f)}\right] \tag{5.18}$$

To assess the effect of the response errors on the overall sound pressure level, it is necessary to know the power spectra of the measured fluctuating pressure environment. Generally, the effect of the present response errors on the overall level will be negligibly small since the errors occur primarily at high frequencies where the power spectral density is small. However, noting that the overall fluctuating pressure level is related to the power spectral density by the following equation, the error may be computed for any given case.

$$\Delta P(\mathrm{RMS}) = \left[\int_0^\infty \phi(f)\, df \right]^{\frac{1}{2}} \tag{5.19}$$

For the present analysis, a broad band filter with a band pass from 2 Hz to 20 kHz was used in the reduction of the microphone measurements to overall RMS level.

Thus, the error in the measured RMS fluctuating pressure, expressed in coefficient form, for the frequency range from 2 Hz to 20 kHz is given by

$$e\,[\Delta C_p(\mathrm{RMS})]_R = \left\{ [\Delta C_p(\mathrm{RMS})]^2 - \frac{1}{q_\infty} \int_{2\ \mathrm{Hz}}^{20\ \mathrm{kHz}} \frac{\phi(f) - e\,[\phi(f)]_E}{R(f)}\, df \right\}^{\frac{1}{2}} \tag{5.20}$$

where the subscript, R, denotes that the error is due to the system frequency response.

It will be noted that the error resulting from the system response characteristics will always be negative, such that the measured $\Delta C_p(\mathrm{RMS})$ is less than the true value.

5.3.3 Data Reduction Errors and Uncertainties

The primary errors and uncertainties in the final data result from inaccuracies associated with the data reduction process. Errors and uncertainties associated with the initial setup prior to acquiring the raw data are virtually eliminated since the calibration, as recorded on tape, are used in the data reduction process. Errors and uncertainties associated with the calibrations themselves are considered negligibly small as compared to those of the data reduction process. Thus, only the inaccuracies associated with the data reduction process are considered in the estimation of errors and uncertainties in the final data as presented herein.

Data reduction errors and uncertainties may be classified as 1) statistical, and 2) technique. The statistical inaccuracies result, primarily, from uncertainties associated with the computation of estimated values of the various statistical parameters. In random data analysis, use is made of finite bandwidths and finite sample lengths. Thus, the final computations are not true values, but estimations of the true values (see Reference 34). As bandwidth and/or sample length is increased, the uncertainties associated with the data reduction process are decreased. However, to obtain a certain degree of frequency resolution, finite bandwidths are employed. This, together with the practical necessity to limit the time of the sample, results in a certain degree of statistical uncertainty in the final statistical parameters. Technique errors and uncertainties result from the inaccuracies associated with the equipment employed in the data reduction process and the ability of the person performing the data reduction. For example, the accuracy of setting up the data reduction instrumentation, the accuracy of the various instruments employed, and the ability of the individual in reading the reduced data, say, from a graphic level recorder, will have a direct effect on the error and uncertainty of the final data. Technique inaccuracies are very difficult to assess, since several individuals, instruments, and sequences may be involved in the interim between the raw data as recorded on tape and the final data parameter as presented in the report. It should be noted that technique errors and uncertainties are not limited to microphone measurements; but, rather, are present in all experimental data. However, for the present precision of measurement analysis, only the microphone data will be considered in the assessment of technique errors and uncertainties.

The purpose of this section is to define the inaccuracies associated with the computation of each statistical parameter. In particular, the inaccuracies will be estimated for the RMS fluctuating pressure levels, the power spectral densities, and the cross power spectral densities.

The analysis of the inaccuracies for these parameters are discussed separately in the following paragraphs.

Overall Fluctuating Pressure Level

The most convenient term to use in the specification of the statistical uncertainties in the overall fluctuating pressure level is the normalized standard error (ϵ). The normalized standard error is the ratio of the standard deviation of the estimate to the true value. Physically, the normalized standard error may be interpreted as a fluctuation or scatter superimposed on the true estimate. In terms of confidence level, the probability that the computed (or estimated) value of $\Delta P(RMS)$ will be within $\pm\epsilon$ of the true value is 68 percent, or one has 68 percent confidence that the uncertainty will be within the limits imposed by $\pm\epsilon$. The normalized standard error for the overall RMS fluctuating pressure level is given by (see Reference 34).

$$\epsilon\,[\Delta P(RMS)]_s = \frac{s.d.\ [\Delta P(RMS)]}{[\Delta P(RMS)]_{true}} \approx \frac{1}{2\sqrt{BT}} \tag{5.21}$$

where the prefix ϵ implies the uncertainty normalized standard error of the term with the brackets, s.d. implies standard deviation; B is the bandwidth of the analysis, and T is the sample length of data used. For the present analysis of $\Delta P(RMS)$, using both analog and digital techniques, the BT product was sufficiently large that ϵ was negligibly small. For the analog analysis:

$$B \approx 20{,}000 \text{ Hz}$$

$$T = 15 \text{ sec}$$

$$BT = 300{,}000$$

$$\epsilon\,[\Delta P(\text{RMS})]_s \approx \frac{1}{2\sqrt{BT}} = 0.0009 \qquad (5.22)$$

For the digital computation, the normalized standard error may be expressed directly as a function of the number of independent samples, N. For the present digital computation,

$$N = 65{,}536$$

$$\epsilon\,[\Delta P(\text{RMS})]_s = \sqrt{\frac{1}{2N}} = 0.0026 \qquad (5.23)$$

Thus, for both analog and digital computations, the normalized standard error in the overall RMS fluctuating pressures is less than 1 percent and may be disregarded as a significant uncertainty.

To assess the technique inaccuracies in the overall RMS fluctuating pressure level, it suffices to use a comparative technique whereby the analog computations are compared with the digital computations. The basis for this analysis is that technique errors and uncertainties are primarily associated with the analog instrumentation and the personnel performing the data reduction; whereas, the digital computations are relatively free of technique errors and uncertainties. Noting that both analog and digital computations are free of significant statistical uncertainties, it suffices to evaluate the technique inaccuracies from a comparison of the analog and digital computations. Data, representing 286 calculations for the Mach number range from 0.60 to 1.60, are presented in Figure 20. It is evident from the results presented in Figure 20 that the analog results are, in general, greater than the digitally computed results. Therefore, it appears that the analog results have been biased to the high side, although this error is very slight - on the order of 4 percent or 0.4 dB. This error is well within the accuracy of the analog instrumentation employed in the data reduction process. The scatter about the mean, which is representative of the technique uncertainty in the data, is bounded by ± 8 percent with 95 percent confidence. That is, 95 percent of the data falls within ± 8 percent of the mean. Thus, assuming a Gaussian distribution of the scatter about the mean, the normalized standard error - which is based on a 68 percent confidence level - is one half of the 95 percent confidence interval, or $\epsilon = 0.04$. In summary, the technique error is given by:

$$e\,[\Delta P(\text{RMS})]_t = 0.04\,[\Delta P(\text{RMS})] \qquad (5.24)$$

and the technique uncertainty is given by

$$\pm\ \epsilon\ [\Delta P(RMS)]_t = \pm 0.04\ [\Delta P(RMS)] \tag{5.25}$$

In coefficient form (neglecting the uncertainty in q_∞), Equations 5.24 and 5.25 become

$$e\ [\Delta\ C_p(RMS)]_t = 0.04\ [\Delta\ C_p(RMS)] \tag{5.26}$$

$$\pm\ \epsilon\ [\Delta\ C_p(RMS)]_t = \pm 0.04\ [\Delta C_p(RMS)] \tag{5.27}$$

Power Spectral Density

Uncertainties in the power spectra are dominated by the statistical uncertainties since these data were reduced to descriptive terms by digital computation. It is felt that technique errors and uncertainties are very small for the power spectra since calibrations recorded on tape were used for the specification of the sensitivity for each microphone without any intermediate conversion or interpretation of the data by personnel. Certainly, the technique errors are negligibly small compared to the statistical uncertainties. The normalized standard error for conventional digital computation of the power spectral density is given by

$$\epsilon\ [\phi(f)]_s = \sqrt{m/N} \tag{5.28}$$

where m is the maximum number of correlation lag values of the computation and N is the size of the digital sample. During the present computations, a rather complicated digital filtering technique was employed whereby a series of power spectral density points were calculated with each having 16 degrees of freedom. The method of calculating the power spectral density points involved dividing the frequency range into a series of frequency intervals such that the power spectral density for each interval was computed with 16 degrees of freedom. This technique is discussed further in Section 4.4.2. The power spectral density for each 1/3 octave frequency was then computed by averaging the power spectral density for the number of discrete points (k) within the 1/3 octave band. The resulting number of degrees of freedom for each 1/3 octave band thus becomes 16 k. To increase the statistical accuracy at the lower frequencies, the 1/3 octave data were further averaged to give octave band results for the octave band center frequencies of 31.5 Hz, 63 Hz and 125 Hz. The resulting variation of the statistical number of degrees of freedom, n, with frequency is presented in Figure 21. The normalized standard error for the power spectral density may be determined directly from the number of degrees of freedom as follows:

$$\epsilon\ [\phi(f)]_s = \sqrt{\frac{2}{n}} \tag{5.29}$$

The resulting variation of $\epsilon[\phi(f)]_s$ with frequency is presented also in Figure 21.

5.3.4 Summary of Errors and Uncertainties

The following is a summary of the errors and uncertainties associated with the test results presented herein. The errors and uncertainties are presented in equation form with the required terms referenced to figures presented in the report where necessary.

Overall Level

Error

$$e\ [\Delta C_p(\mathrm{RMS})] = \left\{ e[\Delta C_p(\mathrm{RMS})]_E^2 + e\ [\Delta C_p(\mathrm{RMS})]_R^2 + e\ [\Delta C_p(\mathrm{RMS})]_t^2 \right\}^{\frac{1}{2}}$$

$$= \left\{ e\ [\Delta C_p(\mathrm{RMS})]_{E+R}^2 + e\ [\Delta C_p(\mathrm{RMS})]_t^2 \right\}^{\frac{1}{2}}$$

where

$$e\ [\Delta C_p(\mathrm{RMS})]_{E+R}^2 = [\Delta C_p(\mathrm{RMS})]^2 - \frac{1}{q_\infty} \int_{2\ \mathrm{Hz}}^{20\ \mathrm{kHz}} \frac{\phi(f) - e\ [\phi(f)]_E\ df}{R(f)}$$

$$e\ [\Delta C_p(\mathrm{RMS})]_t^2 = 0.0016\ [\Delta C_p(\mathrm{RMS})]^2$$

$e\ [\phi(f)]_E$ is given in Figure 16, and

$R(f)$ is given in Figure 19.

Uncertainty

$$\pm\ \epsilon\ [\Delta C_p(\mathrm{RMS})] = \pm\ \epsilon\ [\Delta C_p(\mathrm{RMS})]_t$$

$$= \pm\ 0.04\ [\Delta C_p(\mathrm{RMS})]$$

Power Spectral Density

Error

$$e\,[\phi(f)] = e\,[\phi(f)]_E + e\,[\phi(f)]_R$$

$$= e\,[\phi(f)]_{E+R}$$

$$= \phi(f) - \frac{\left\{\phi(f) - e\,[\phi(f)]_E\right\}}{R(f)}$$

Uncertainty

$$\pm\ \epsilon\,[\phi(f)] = \pm\ \epsilon\,[\phi(f)]_s$$

where $\epsilon\,[\phi(f)]_s$ is given in Figure 21.

6.0 DISCUSSION OF TEST RESULTS

6.1 Introduction

Because of the large number of data measurements obtained during the test, it is necessary to be selective in the presentation and discussion of the test results. Noting that the primary objective of the present report is to define the basic features of the flow field induced by three-dimensional protuberances, the measurements obtained along the longitudinal centerline of the model were selected as being primary data. These data represent the plane of symmetry of the flow around the protuberances and, thus, show the basic features of the flow in both the upstream separated region and the downstream wake region. The flow around the protuberances, which is characterized by the transition from separated to wake flow is discussed only briefly. A comprehensive presentation of the data for the flow around the protuberances will be made in a later report.

The test results are discussed under the following section titles:

- Clean Model Flow Characteristics
- Protuberance Induced Flow Characteristics
  - Protuberance Induced Static Pressure Field
  - Protuberance Induced Fluctuating Pressure Field
- Analysis of the Protuberance Induced Flow Field

The clean model flow characteristics were determined from the test panel measurements for the protuberance in the fully retracted position. Results for the clean model indicate the quality of the flow over the test panel and the suitability of the model for the investigation of protuberance flow fields. The static pressure field induced by the protuberances is exhibited by surface pressure measurements taken over the test panel and the wall of the protuberance. Similarly, the fluctuating pressure field induced by the protuberance is exhibited by surface microphone measurements. Finally, the static and fluctuating pressure measurements are combined with the oil-flow visualization results to determine the salient features of the protuberance induced flow field.

6.2 Clean Model Flow Characteristics

6.2.1 Surface Pressure Distributions

Static pressure data as obtained from the distribution of orifices along the longitudinal and transverse centerlines of the test panel are presented in terms of the pressure coefficient, C_p, in Figure 22. The variations of C_p over the surface of the test panel are significantly greater than the uncertainty associated with the measuring instrumentation and, also, these data show some consistent trends. Thus, it is concluded that the variations are indicative of the aerodynamic characteristics of the model, or the model/tunnel combination. The longitudinal variations in C_p, Figure 22a, exhibit the irregularities of the clean model flow field, and when compared with the transverse variations, Figure 22b, it is evident that the flow is less uniform in the longitudinal direction than in the transverse direction. It is interesting to note the agreement between the longitudinal and transverse pressure distributions as indicated by the solid symbols on each figure. The agreement is within the accuracy of the instrumentation employed. This further substantiates the conclusion that static pressure variations result from aerodynamic effects associated with either the model or the model/tunnel combination. Since the variations appear to be greater at $M_\infty \geq 1.0$ than at subsonic Mach numbers, it is felt that extraneous Mach waves in the tunnel contribute significantly to the static pressure variations. Also, the boat tail of the model splitter-plate appears to have affected the longitudinal centerline pressures at $M_\infty = 1.20$. In general, the static pressure variations about the free-stream pressure are within ±0.1 of the free-stream dynamic pressure. Normally, variations should be contained within the uncertainty limits of the instrumentation. Thus, it is felt that the quality of the flow over the test article was not as good as desired; however, the flow is acceptable for the study of protuberance flow fields since the clean model variations in pressure are relatively small compared with the pressure variations induced by the protuberances.

At this point it should be noted that the static pressure results for the protuberance induced environments were adjusted for the clean model results by subtracting the static pressures for the protuberance-free case from the static pressure for the perturbed case. This adjustment contributes to the uncertainty of the final results; however, a significant improvement in the static pressure distributions was obtained for the perturbed flow. Thus, it is felt that this adjustment was justified.

6.2.2 Boundary Layer Characteristics

Further information of the characteristics of the flow over the clean model may be gained from an examination of the boundary layer characteristics. Boundary-layer velocity profiles were determined from pitot pressure measurements obtained with the forward and aft rakes with the protuberance in the fully retracted position. The velocity profiles, at the locations of the forward and aft rake, are presented in Figure 23. Since the rakes were positioned near the leading and trailing edges of the test panel at approximately equidistance from the location of the protuberance, the boundary layer characteristics at the protuberance location may be taken as the mean of the data for the forward and aft rakes.

It is evident from the test results that an extremely thick boundary layer existed over the region of the test panel for $M_\infty = 0.60$ and 0.80. A similar environment was observed in the small scale tests reported in Reference 18. This environment is attributed to a partially blocked secondary flow under the splitter plate which induces local separation at the leading edge of the model. The separation and subsequent reattachment of the flow at the leading edge results in a thickened boundary layer over the test panel. Also, it will be noted that the velocity ratios do not approach 1.0 at the edge of the boundary layer at every Mach number. This anomaly resulted from the deviation of the local velocity from free-stream conditions as indicated by the variations in static pressure presented in the preceding section.

The variations of the boundary layer displacement thickness, δ^*, with free-stream Mach number are presented in Figure 24. The displacement thicknesses for the rake data were determined from numerical integrations of the velocity profiles. For free-stream Mach numbers of 0.90 and above, the displacement thickness varied irregularly with Mach number about an approximately constant value. For $M_\infty = 0.60$ and 0.80, the thick boundary layer resulting from leading edge separation is clearly evident in the large values of δ^*. The displacement thicknesses shown for $M_\infty = 0.60$ and 0.80 were obtained by numerical integrations to the point where U_n is approximately 0.95 U_∞, thus, it is anticipated that δ^* may be slightly greater than the values shown. The experimental results are compared with an empirical prediction using Bies' formula (see Reference 22). The empirical prediction represents the estimated displacement thickness at the location of the protuberance which would correspond to the mean between the forward and aft rake results. The empirical results agree closely with the results presented for the forward rake, indicating that the boundary layer at the protuberance location was somewhat thicker than predicted. Surface excrescences in the boundary layer upstream of the test panel apparently caused a slight artificial thickening of the boundary layer.

The variations of boundary layer momentum thickness, θ, with free-stream Mach number are shown in Figure 25. For the Mach number range of the present test, momentum thickness is essentially invariant with Mach number except for the anomaly due to the separation induced thickening of the boundary layer at $M_\infty = 0.60$ and 0.80. Again, agreement is shown between the experimental measurements for the forward rake and the empirical results.

The effects of free-stream unit Reynolds number on the boundary layer characteristics in the vicinity of the test panel (Figures 24 and 25) were negligibly small. This is as anticipated since, for a turbulent boundary layer on a flat plate, the boundary layer thickness is inversely proportional to the Reynolds number to the one-fifth power.

A summary of important boundary layer and free-stream flow conditions which are characteristic of the undisturbed flow over the model in the vicinity of the protuberance for a unit Reynolds number of 3×10^6 are presented in the following table.

UNDISTURBED FLOW PARAMETERS OVER THE TEST PANEL

$Re/ft = 3 \times 10^6/ft$

M_∞	U_∞ ft/sec	q_∞ psf	δ in.	δ^* in.	θ in.
0.60	676	388	≈ 8	≈ 0.80	≈ 0.50
0.80	880	479	≈ 8	≈ 0.80	≈ 0.50
1.00	1067	559	2.5	0.36	0.21
1.20	1264	611	2.5	0.37	0.19
1.40	1391	644	2.5	0.36	0.19
1.60	1528	662	2.5	0.31	0.20

6.3 Protuberance Induced Flow Characteristics

Before discussing the static and fluctuating pressure measurements, some general comments in regard to the protuberance flow field should be made. A photograph of a typical oil flow pattern around the protuberance is presented in Figure 26. Any protuberance which extends into or through an attached boundary layer will (1) tend to induce separated flow upstream of the protuberance and (2) generate a wake downstream of the protuberance. For a three-dimensional protuberance the upstream separated flow will have a curved separation line or front as clearly shown in Figure 26. The wake will be characterized by a short converging region which is terminated by a narrow neck followed by a diverging region. The converging region will be denoted as the near wake and the diverging region as the far wake with the neck region separating the two. The neck and far wake are clearly shown in Figure 26; however, the near wake is partially obscured by the protuberance due to the slight downstream angle of the camera view. There are several other interesting features of the flow field shown in Figure 26; however, these will be discussed in detail in later sections. At this point, it suffices to recognize only the presence of the upstream separated flow and the downstream wake regions, and that the region of perturbed flow may extend for several diameters around the protuberance.

The length of the upstream separated flow region at the longitudinal centerline was evaluated from oil-flow studies of the 4-inch diameter protuberance for the Mach number range from 0.60 to 1.40 and h/D range from 0 to 2.0. The separation point is identified in Figure 26. The resulting variations of normalized separation length, ℓ_s/D, with h/D for the various Mach numbers of the test are presented in Figure 27. The curve presented for $M_\infty = 1.60$ was determined by extrapolation of the lower Mach number data to $M_\infty = 1.60$. An increase in either protuberance height or Mach number resulted in an increase in separation length. The trend in the data indicates that the separation length will approach asymptotic values for large protuberance heights.

In the wake, it is obvious that the flow will be perturbed for many diameters downstream of the protuberance. The aft rake, which was present throughout the test, revealed noticeable distortion in the velocity profiles due to the wake for the various protuberances. For the 2-inch diameter protuberance, the rake was located at 18.28 diameters aft of the protuberance and the effect of the wake was barely detectable. Thus, it is felt that the test panel surface measurements for the three protuberance configurations adequately cover the region of perturbed flow as discussed in following sections. Generally, the neck region which separates the near- and far-wake regions appeared to occur at approximately one diameter aft of the protuberance ($r/D \approx 1.5$) for $M_\infty \geq 1.20$. For lower Mach numbers, the wake was ill defined by the oil flow pictures; however, the fluctuating pressure measurements indicate that the neck region moved aft with decreasing Mach number.

6.3.1 Protuberance Induced Static Pressure Field

The static pressure field induced by the protuberances is represented by the distribution of the pressure coefficients along the test panel centerline, forward and aft of the protuberance, Figures 28-30. Test results are presented, separately, for the 2-, 4-, and 8-inch diameter protuberances for various heights ranging up to two diameters. The 2-inch diameter protuberance results, Figure 28, show the extent of the perturbed flow field upstream and downstream of the protuberance; however, little detail of the pressure field is given for the region in close proximity to the protuberances. The 4-inch diameter protuberance results, Figure 29, give a cursory definition of the perturbed flow field for the region in close proximity to the protuberance as well as the outer extremities of the protuberance environment. Finally, the 8-inch diameter protuberance results, Figure 30, show, in detail, the perturbed flow field for the region in close proximity to the protuberance.

An examination of the results presented in Figures 28-30 reveals several distinct characteristics of the pressure field which are typical of cylindrical protuberances. The static pressure field associated with the upstream separated flow is characterized by positive pressure coefficients; whereas, the static pressure field associated with the wake is characterized by 1) negative pressure coefficients in the near wake and neck regions, and 2) approximately zero pressure coefficients in the far wake. Clearly, the regions most affected by the protuberance lie in close proximity to the protuberance. It is important to note that the region of perturbed flow upstream of the protuberance is not bounded by the region of separated flow, but may extend beyond this point. A comparison of the separation points (Figure 27) with the static pressure distributions will show this characteristic. At subsonic and slightly supersonic Mach numbers, the perturbed flow field extends significantly beyond the separation point; whereas, at $M_\infty \geq 1.20$, the shock strength is sufficiently large to cause separation near the foot of the shock wave. For the latter Mach number range, the region of upstream perturbed flow (which is bounded by the shock wave) and the region of separated flow occur over approximately the same area with the separated flow region being contained slightly within the perturbed flow region. Consistent with this finding are the trends in the pressure gradients associated with the upstream perturbed flow. At subsonic Mach numbers, a gradual increase in static pressure in the flow direction is observed. The effect of the positive pressure gradient is to retard the boundary layer flow near the wall - eventually causing separation. The critical pressure at separation is discussed below. At supersonic Mach numbers, a rapid increase in static pressure is observed across the shock wave; thus inducing separation immediately aft of the mean location of the shock wave. The variations of the static pressure ratio at separation with Mach number are presented in Figure 31. The results for the different size protuberances were obtained based on the separation lengths as defined from oil flow patterns for the 4-inch diameter protuberance. It should be noted that separation length probably varies with protuberance diameter rather than separation pressure such that all three configurations would have the same separation pressure ratio as given by the 4-inch diameter protuberance data.

Downstream of the separation point, a region of relatively constant, plateau, pressure occurs. The plateau pressure region is particularly noticable for $M_\infty \geq 1.20$. For two-dimensional separation, the plateau pressure extends to near the step face; however, for the three-dimensional case, the plateau region is terminated significantly upstream of the protuberance. For the latter case, the plateau region is terminated by a sudden reduction in static pressure which is followed by a sharp increase in pressure near the protuberance. The low pressure region imbedded within the separated flow field is unique to the three-dimensional protuberance case and provides much insight into the understanding of the structure of the three-dimensional separated flow field. The separated flow field is discussed at length in Section 6.4.

The wake region exhibits noticable variations in static pressure for approximately four diameters aft of the protuberance. It is interesting to note that distortion in the velocity profiles were observed for approximately 18 diameters aft of the protuberances as previously mentioned; however, the retarded flow in the wake apparently has little effect on the surface static pressures in the far wake region. Little insight into the structure of the wake can be gained from the static pressure measurements and it is felt that the oil-flow photographs and fluctuating pressure measurements are more definitive of the wake structure.

A cursory examination of the effects of Reynolds number and protuberance size on the perturbed flow field was made utilizing the static pressure measurements. The effects of Reynolds number were evaluated using the 8-inch diameter protuberance results for unit Reynolds number conditions of 1.5, 3.0 and 4.5 million per foot. Corresponding Reynolds numbers, based on protuberance diameter, are 1.0, 2.0, and 3.0 million. Representative axial distributions of static pressure coefficient are presented for $h/D = 2.0$ and Mach numbers from 0.60 to 1.60 in Figure 32. The effect of Reynolds number variations appear to be small, although there are some noticable deviations in the data. In general, variations in Reynolds number primarily affected the static pressure distributions in the wake region at subsonic Mach numbers (although a consistent trend was not evident); whereas, at $M_\infty \geq 1.20$, the effects appeared to be more predominant upstream of the protuberance. Increasing the Reynolds number at supersonic Mach numbers appeared to cause a slight enlargement of the upstream separated flow region. The effects of protuberance size variations were determined by comparing axial distributions of static pressure coefficient for the 2- and 4-inch diameter protuberances with Reynolds number, based on protuberance diameter, held constant at 0.5 million (Figure 33). Further, a similar comparison was made between the 4- and 8-inch diameter protuberances for a Reynolds number, based on protuberance diameter, of 1.0 million (Figure 34). These data represent the $h/D = 2.0$ condition for Mach numbers ranging from 0.60 to 1.60. Small variations in static pressure coefficient were observed in both the upstream and wake regions due to protuberance size variations with the most significant effects occurring in the wake region at subsonic Mach numbers and in the upstream separated flow region at supersonic Mach numbers. The most noticeable effect of increasing the protuberance size was to cause a slight enlargement of the normalized upstream separated flow region at supersonic Mach numbers (particularly for $Re_D = 0.5 \times 10^6$).

The pressure distributions over the wall of the 8-inch diameter protuberance are exhibited by variations of C_p with vertical location, y_p/D for various polar angles around the protuberance. Test results are presented for a range of protuberance heights and Mach numbers in Figures 35-40. A high density of static pressure orifices were present along the vertical rays and thus provided good definition of the pressure variations associated with the various flow fields to which the protuberance was exposed. Flow fields impinging on the upstream half of the protuberance ($\theta^+ < 90$ degrees) which appear to be evident in the static pressure measurements are: 1) the separated shear layer (base region) near the base of the protuberance, 2) the two-dimensional cross flow (central region) near the middle of the protuberance, and 3) the end effect (tip region) near the top of the protuberance. The vertical extent of these regions naturally vary with h/D. For $h/D \geq 1.5$, all three regions are clearly defined in the vertical pressure distributions. The tip region is characterized by a combination of flow around the protuberance and over the top of the protuberance. The resulting three-dimensional relief afforded to the flow causes a reduction in pressure in comparison to the pressures for two-dimensional flow as encountered by an infinite cylinder in cross flow. At supersonic Mach numbers, the bow shock generated by the cylinder is curved in the vicinity of the tip region as discussed in References 17 and 18. The tip region extends downward from the top of the protuberance for approximately 0.4 diameters for $h/D \geq 1.5$. The central region is characterized by nearly parallel or two-dimensional flow around the protuberance. In the central region, the wall pressure is approximately constant along vertical rays and the flow exhibits characteritistics similar to that of an infinite cylinder in cross flow. The central region is located between the tip region and the base region and its vertical extent varies noticeably with h/D. The base region is characterized by the interaction of the separated flow, which is induced upstream of the protuberance, with the protuberance. The presence of reverse flow in the separated flow region is evidenced by the low pressures measured just above the base of the protuberance. For $M_\infty \geq 1.0$, the growth of the separated flow region is exhibited by the upward movement of the pressure defect in the vertical pressure distributions. For $M_\infty < 1.0$, the pressure defect associated with the base flow is poorly defined due to the small extent of the separated flow region. Further, the region of constant pressure normally associated with the central region is not exhibited in the results for $M_\infty < 1.0$ due to the extremely thick inflowing boundary layer for $M_\infty = 0.60$ and 0.80. The boundary layer velocity profile shape in the region of $y_p/D < 1.0$ results in a loss of total pressure and, thus, a decrease in the surface pressures measured over the front half of the cylinder.

Over the aft half of the cylinder ($\theta^+ > 90$ degrees) small variations in pressure over the wall of the cylinder were observed for $M_\infty > 0.60$. This is explained by the separation of the cylinder boundary layer near the $\theta^+ = 90$-degree ray. This characteristic is clearly evident in the test results for $M_\infty \geq 1.0$. For a Mach number of 0.60, large variations in the protuberance wall pressures were observed over the wall of the cylinder at the $\theta^+ = 90$-degree ray. Apparently the flow exhibits irregular separation along the 90-degree ray due to the variation in the flow upstream of the protuberance in the vertical direction.

6.3.2 Protuberance Induced Fluctuating Pressure Field

Overall Levels

Of particular interest during the present study was the fluctuating pressure field induced by the cylindrical protuberances. The overall fluctuating pressure levels associated with the perturbed flow field are presented as variations of the RMS coefficient of fluctuating pressure along the test panel longitudinal centerline in Figures 41-43. Test results are presented, separately, for the 2-, 4-, and 8-inch diameter protuberances for ranges of protuberance height and Mach number which are consistent with the presentation of static pressure results discussed in the preceding section. Here again, the results for the 2-, 4-, and 8-inch diameter protuberances represent varying degrees of definition of the perturbed flow field ranging from a general overview as exhibited by the 2-inch diameter protuberance results to a detailed, near field, study as exhibited by the 8-inch diameter protuberance results.

Certain characteristics of the fluctuating pressure field are immediately obvious from an examination of these results. The fluctuating pressure field induced by the protuberances corresponds closely with the region of perturbed flow as exhibited by the static pressure results. Two distinct regions of perturbed flow are exhibited by the fluctuating pressure results - one corresponding to the upstream separated flow region and the other corresponding to the downstream wake region. It is evident from the fluctuating pressure measurements that significant fluctuating pressures occurred in both the upstream and downstream environments. In general, the most severe fluctuating pressures were encountered in the wake region for $M_\infty < 1.0$ and large h/D; whereas, for other test conditions, the separated flow upstream of the protuberance caused the most severe fluctuating pressures. It is convenient to discuss the separated and wake flow regions separately.

In the separated flow region, the fluctuating pressure field is characterized by a gradual increase in overall level as the field is observed in the direction of the free-stream. Near the mid-point in the separated flow region, the fluctuating pressure reaches a maximum value which ranged from 12 to 17 percent of the free-stream dynamic pressure. The peak is followed, in general, by a decrease in fluctuating pressure level. This decrease appears to become less drastic with increasing Mach number such that, at $M_\infty = 1.60$, a peak plateau level of fluctuating pressure occurs near the protuberance. For $M_\infty = 1.40$ and 1.60, a small peak in fluctuating pressure occurs upstream of the separation point and corresponds to the mean location of the shock wave. Levels of fluctuating pressure for the shock wave are approximately the same as observed for two-dimensional protuberances (forward facing steps); however, the levels within the separated flow region are considerably greater than for the two-dimensional case. Immediately, it becomes obvious that the unsteady mechanisms within the three-dimensional separated region are significantly different than the two-dimensional case and, further, the three-dimensional flow generates more severe fluctuating pressures.

Increasing either protuberance height or free-stream Mach number results in increasing the area of the unsteady perturbed flow field upstream of the protuberance. For the range of test variables of the present study, increasing the protuberance height did not alter the peak level of the fluctuating pressures in the upstream separated flow region with any consistent trend and, in general, there appears to be only a slight increase in the peak level of the fluctuating pressure with increasing Mach number. However, the most significant and important trend is the increase in area which is subjected to the high levels of fluctuating pressure within the separated flow region for increasing protuberance height and free-stream Mach number.

The fluctuating pressure field associated with the wake of the protuberance extended over a relatively large axial distance for all protuberance heights and Mach numbers as is shown in Figures 41-43. Very large fluctuating pressures were encountered at subsonic Mach numbers, and in certain cases, the levels exceeded those encountered upstream of the protuberance. Of particular interest are the results for $M_\infty = 0.80$ and $h/D = 1.5$ and 2.0, Figure 43b. For these conditions, the peak levels in the wake ranged from 18 to 22 percent of the free-stream dynamic pressure. For the unit Reynolds number of 3×10^6, the corresponding overall sound pressure level ranges from 166 to 168 dB. These values were the largest encountered in the perturbed flow field along the longitudinal centerline of the test panel for the range of test variables investigated. As previously mentioned, it was difficult to distinguish the neck region of the wake at $M_\infty \leq 1.20$; however, there are indications that the neck occurs further downstream than the location of the peak levels of fluctuating pressure for $M_\infty = 0.80$. (Some evidence of this is given by the cross-spectra results as discussed in later paragraphs.) For certain conditions (for example, $M_\infty = 1.00$, $h/D = 2.0$) the peak levels in the fluctuating pressures associated with the wake occurred 3 or 4 diameters aft of the protuberance. It is difficult to define consistent trends in the wake results, and perhaps this confusion is a result of the complex flow structure that exists in the wake and the way in which it changes with variations in both Mach number and protuberance height. Additional discussion on this point is presented in the section on the power spectra.

The general trend in the axial distributions of the fluctuating pressures in the wake consists of a moderate increase to peak levels followed by a gradual decrease to the unperturbed flow level as the flow field is examined in the direction of the free-stream. Both the location and the width of the peak varies with free-stream Mach number and protuberance height. Further, for $M_\infty \geq 1.0$, there appeared to be a general reduction in the overall fluctuating pressures in the wake with increasing Mach numbers. Also a gradual aft movement and decrease in level of the peak fluctuating pressures occurred with increasing protuberance height.

A comparison of the axial distributions of overall fluctuating pressure level for the 2-, 4-, and 8-inch diameter protuberances is shown in Figure 44. All of the protuberances exhibited similar trends in the axial distributions; however, some deviations in the levels were noted. These deviations are relatively small and may result from either Reynolds number (based on protuberance diameter) or protuberance size effects.

The fluctuating pressure field over the surface of the protuberance is exhibited by measurements taken over the wall of the 8-inch diameter protuberance, Figures 45-50. These data are presented as variations of RMS fluctuating pressure coefficient along circumferential rays with $\theta^- = 0$ degree corresponding to the upstream centerline and $\theta^- = 180$ degrees corresponding to the downstream centerline. It will be noted that a range of circumferential rays are presented for various heights above the test panel surface. For $h/D = 1.0$, the surface measurements were contained within the perturbed flow field of the test panel (base region); whereas, for $h/D = 2.0$, the surface measurements were above the perturbed flow field of the test panel and should closely approximate the characteristics of an infinite cylinder in cross flow (central region). In general, flow around the cylinder is characterized by attached flow over approximately the forward half of the cylinder and separated flow over the aft half. The separation of the flow from the wall of the cylinder occurred near the 90-degree polar location. For $M_\infty = 0.60$, $h/D = 2.0$, extremely large fluctuating pressures (in excess of 170 dB) resulted from the unsteadiness of the separation line (see Figure 45a). These data were rechecked following the initial discovery of the large levels to verify their accuracy. Further, it should be noted that these results are consistent with the location of the separation line as observed in the static pressure results. Some evidence of flow separation near $\theta^- = 90$ degrees is given by the peak in the circumferential distributions at this location for all $M_\infty \leq 1.00$; whereas, for $M_\infty > 1.00$, it is felt that separation occurs slightly downstream of the 90-degree location. Due to the present model design, a continuous survey of the polar distribution could not be made. For $h/D = 2.0$, little variation with vertical location was observed in the fluctuating pressure levels except for the $M_\infty = 0.60$

condition. Further, the wake region ($\theta^{-} > 90$ degrees) appeared to exhibit larger fluctuating pressure levels than did the upstream region at subsonic Mach numbers. For $h/D = 1.0$, the effect of the perturbed flow field around the base of the protuberance is evidenced by the large fluctuating pressures in this region. For $M_{\infty} \geq 1.20$, the fluctuating pressure levels over the front half of the cylinder appeared to decrease with an increase in polar angle. It is interesting to note the drastic reduction in fluctuating pressures for the rear half of the protuberance at $M_{\infty} \geq 1.20$. These data appear to be consistent with an overall change in the wake structure at supersonic Mach numbers as observed in the oil flow studies and static and fluctuating pressure measurements taken over the test panel. Further, the test panel data for microphones near the protuberance appear to agree reasonably well with the protuberance data at $\theta^{-} = 0$ degree and 180 degrees as shown in Figures 45-50.

Power Spectra

Power spectra represent the distribution of the mean square energy of the fluctuating pressure with frequency. In general, power spectra of most fluctuating pressure environments are found to scale on a Strouhal number basis; that is, the frequency is non-dimensionalized by multiplying a typical length and dividing by a typical velocity. The advantages of using normalized spectra are obvious since it enables similar, homogeneous, flow fields to be represented by a single spectrum regardless of the scale of the flow field or the free-stream velocity. Numerous studies have been made to determine the proper parameters to be used to non-dimensionalize the spectra for various aero-acoustic environments. Unfortunately, the choice of parameters which best collapses the data appear to be dependent on the nature of the fluctuating pressure environment. In general, free-stream velocity is used as the normalizing velocity parameter, although a typical eddy convection velocity (itself a function of frequency) has been used occasionally. The local convection velocity appears to correspond more closely with the physical situation for fluctuating pressures due to turbulent eddies. For simplicity, free-stream velocity has been adopted for the power spectra presented herein since the three-dimensional protuberance flow field is a non-homogeneous environment with widely varying convection velocity characteristics.

Selection of a typical length is more difficult. For both undisturbed boundary layer flow and two-dimensional separated flow, typical dimensions of the undisturbed boundary layer such as boundary layer thickness, displacement thickness, and momentum thickness, have all been used by various authors. For transonic flow, the typical boundary layer lengths vary only slightly, but no final conclusion can be drawn on the relative merits of the collapse for any particular length. The most generally used typical length is the boundary layer displacement length, δ^*, and this parameter is used herein. An important typical length parameter for the protuberance flow field is the protuberance diameter, particularly for the region of the wake. It is evident from the test results presented herein that the scale of the perturbed flow field varies in proportion to the protuberance diameter. Thus it must be concluded that the power spectra of the fluctuating pressures would depend to some degree on the size of the protuberance. However, since test results are presented for the 8-inch diameter protuberance only, the use of protuberance diameter as a typical length parameter will be withheld until the power spectra for the other size protuberances are reduced. These data will be forthcoming in a later report.

Power spectra representing the frequency characteristics of the protuberance induced fluctuating pressures are presented for both upstream and downstream flow fields in Figures 51-62. It will be noted that test results are presented for the Mach number range from 0.60 to 1.60 and protuberance heights of 1.0 and 2.0 diameters. These data were obtained for the 8-inch diameter protuberance configuration and, thus, provide a detailed study of the protuberance induced flow field for the region in close proximity to the protuberance. It is impractical to discuss all of the frequency characteristics of the flow as exhibited by the power spectra; however, some general features should be pointed out. The data for the upstream and downstream flow fields will be discussed separately.

For the upstream flow field, test results are presented only for the microphone locations which appeared to have been within the perturbed region (Figures 51-56). All of the spectra appear to exhibit the same general characteristics when presented in terms of normalized power spectral density. For the present discussion, it suffices to note that a high concentration of energy was present at low frequencies with a roll-off at the high frequencies. For the region of the most intense fluctuating pressures upstream of the protuberance at $M_\infty \leq 1.0$, the roll-off appeared to be approximately two orders of magnitude per decade. This is equivalent to 20 dB per decade or 6 dB per octave band. For $M_\infty \leq 1.0$, there appears to be relatively little variation in the shape of the spectra within the separated flow region, although there is some change from the perturbed flow region upstream of separation to the region within the separated flow field. For the perturbed flow field upstream of the separation point, the spectra appear to roll-off less rapidly at the high frequencies. For $M_\infty > 1.0$, the separated flow field is sufficiently large in comparison with the microphone spacing to enable a trend in spatial variation of the power spectra to be established. Of particular interest is the plateau in the power spectra in the vicinity of $r/D = -1.00$ to -1.25 for $h/D = 1.0$, $M_\infty = 1.40$ and 1.60 and in the vicinity of $r/D = -1.125$ to -1.500 for $h/D = 2.0$, $M_\infty = 1.40$ and 1.60. This region corresponds to the inner separated flow field in the vicinity of the peak levels of fluctuating pressure (see Section 6.4). The plateau indicates an increase in fluctuating pressure energy at the mid and high frequencies when compared to the spectra for other regions of the separated flow field.

Another important characteristic of the perturbed flow field is exhibited by the power spectra associated with the shock wave at $M_\infty = 1.40$ and 1.60, $h/D = 1.0$. At the mean location of the shock wave ($r/D = -1.25$), the flow is disturbed as a result of the shock wave impinging on, and interacting with the attached boundary layer. The power spectra for these data (Figures 55a and 56a) exhibited a sharp reduction in energy with increasing frequency starting at relatively low frequencies. The transition in spectra shape is evident also as the fluctuating pressure field is examined moving aft of the shock wave. The transition is characterized by a reduction in low frequency energy and an increase in high frequency energy.

Clearly, the power spectra show a large spatial variation in the fluctuating pressure characteristics as was observed in the overall fluctuating pressure levels. The upstream perturbed flow field is obviously non-homogeneous in space in both overall level and frequency characteristics. However, it is interesting to note that variations in protuberance height and free-stream Mach number did not appear to have any gross effect on the general shape of the power spectra for a given region in the perturbed flow field. Although a direct comparison is not presented, a cursory examination of the data suggests that spectra for the same values of r/ℓ_s would agree at least in trend for the various h/D and M_∞ conditions. This characteristic will be evaluated in detail in a subsequent report and, if correct, it will be a strong argument for the similarity of the upstream separated flow fields for various Mach numbers and protuberance heights.

The power spectra for the wake, Figures 57-62 exhibit the characteristics of a non-homogeneous flow field which is gradually changing in space. It is difficult to determine precise trends in the data with variations in either Mach number, protuberance height, or axial location. The general trend is that the spectra appear to roll-off less rapidly at the higher Mach numbers. Also, the spectra for supersonic Mach numbers have appreciably less low frequency energy than the subsonic data. One interesting feature of the wake spectra is the peak which occurs at certain conditions. For example, the spectra for $h/D = 1.0$, $M_\infty = 1.20$ (Figure 60a) show a peak at $f\,\delta^*/U_\infty = 0.013$ for all axial locations. The corresponding Strouhal number, based on protuberance diameter, is 0.28. The peak generally occurs at the same Strouhal number for other conditions; however, the peak does not occur at all conditions. Further, the value of 0.28 is larger than the Strouhal number for vortex shedding from an infinite cylinder in cross flow which has a value of 0.21 for the Reynolds number range of the present test. However, it is probable that the peaks observed in the present spectra are due to vortex shedding from the cylinder at a Strouhal frequency of 0.28.

Cross-Spectra

Considerable insight into the unsteady mechanisms at work in a fluctuating pressure field can be gained by studying the relationship between data observed at two different points in the field. For a number of years, investigators involved in turbulence and unsteady-fluid dynamic research have utilized cross-correlation techniques to describe, on the average, the mutual statistical dependence of the signals at two different points. From such studies, the correlation patterns, convection velocities, and other features of the flow have been evaluated. One useful technique which has been adopted in recent years is the cross-spectral density function. The cross-spectral density function and the better known cross-correlation function are Fourier transform pairs. The primary advantage of using the cross-spectral density function is that the correlation can be expressed directly as a function of frequency. The mathematics involved in deriving the cross-spectral density function by taking the Fourier transform of the cross-correlation function is well documented and will not be repeated here. It suffices to state that the resulting cross-spectral density function is a complex quantity composed of real and imaginary parts. The real component, denoted as the co-spectral density, is derived by solving the complex function for a time displacement of $\tau = 0$. Thus, the co-spectral density represents a description of the in-phase components of the fluctuating pressure field and is equivalent to the narrow-band spatial correlation function. The imaginary component, denoted as the quad-spectral density, is derived by solving the complex function for a time displacement of $\tau = 1/4f$ and represents a description of the out-of-phase components of the fluctuating pressure field.

The microphone measurements for locations along the test panel longitudinal centerline were analyzed for cross-spectral density characteristics. The method of analysis consisted of digitizing successive pairs of microphones in both the upstream and wake regions. For the present analysis, no attempt was made to perform cross-spectral density analyses for varying separation distance between microphones except for those where the separation between neighboring microphones as installed in the test panel varied. Since the majority of the microphones along the longitudinal centerline were separated by one inch, most of the analyses were performed for the one-inch separation distance. The microphones for the most upstream pair were separated by two inches, and the microphones for the two most downstream pairs were separated by two inches and four inches. Thus, these microphone pairs are the only ones for which cross-spectral densities were computed with separation distances greater than one inch. The purpose of this approach was to obtain maximum correlation between the fluctuating pressure measurements. Further, the overall fluctuating pressure measurements indicated that the protuberance flow field was significantly non-homogeneous in space, particularly for the upstream separated flow region, and it was felt that the correlation lengths would be relatively short.

Cross-spectral density results for the 8-inch diameter protuberance are presented as normalized co- and quad-spectra in Figures 63-68. These results represent areas of maximum correlation between neighboring microphones located in the upstream separated flow and downstream wake regions for free-stream Mach numbers of 1.2, 1.4 and 1.6 and protuberance heights of 1.0 and 2.0 diameters. It will be noted that the region of maximum coherence of the fluctuating pressures for the protuberance induced separated flow region (Figures 63-65) occurred between the point of separation and the point of maximum fluctuating pressure. Further, the trend in the quad-spectral density and the negative values of the normalized frequency parameter show the presence of negative convection velocities, thus indicating that the disturbances are convected counter to the direction of the free stream. In the wake, maximum coherence was observed in the neck and far wake regions. Results presented in Figures 66-68 represent the neck region since, here, the separation between microphones was a minimum of one inch. In the far wake, microphones which were paired for the analysis were separated by 2 and 4 inches and some loss of coherence was observed at the lower frequencies as discussed later. In general, the wake was characterized by positive convection velocities as exhibited by positive values of the normalized frequency parameter and the trend in the quad-spectral density.

A comparison of the various cross-spectra results shows a definite dependency on both free-stream Mach number and protuberance height-to-diameter ratio. In general, the larger values of M_∞ and h/D exhibited the greater coherence of the fluctuating pressure environment.

It will be noted that results are not presented for $M_\infty \leq 1.0$. For this Mach number range, the upstream separated flow region was confined to a region in close proximity to the protuberance, and the 1-inch separation of the microphones appeared to be small relative to the structure of the fluctuating pressure mechanisms. This will become clear from the discussion of the model of the separated flow field which is presented in Section 6.4. In the wake region, the near wake appeared to extend further downstream for $M_\infty \leq 1.0$, than for $M_\infty > 1.0$. As a result, the region of maximum coherence was near or downstream of the most aft microphones and the cross-spectra were poorly defined. Thus, the 4-in. diameter protuberance results will be used to analyze the wake environments for $M_\infty \leq 1.0$; however, these data are not available for the present report.

Narrow-Band Convection Velocity

Before discussing the narrow-band convection velocity results, distinction is made between a fluctuating pressure field which is composed of vorticity (or turbulence) mode disturbances and that which is composed of acoustic (or sound) mode disturbances. Vorticity mode disturbances result from a turbulent flow structure which is convected at some fraction of the local mean flow velocity. Further, the convection velocity is in the same direction as the mean velocity of the turbulent environment. On the other hand, acoustic mode disturbances consist of sound waves which propagate in the fluid medium. The propagation velocity relative to the fluid is at the local speed of sound with a direction independent of the local velocity. Propagation in the direction of the mean flow will have a propagation velocity of the speed of sound plus the mean speed; whereas, propagation counter to the flow direction will have a propagation velocity equal to the difference between the local speed of sound and the local velocity. Obviously, acoustic mode disturbances cannot propagate upstream in a supersonic flow.

For the present computation of the narrow-band convection velocities, use was made of the narrow band phase angle, $\alpha(\xi, f)$, as shown in Equation 4.27. Thus, the resulting velocities are in actuality the narrow band phase velocities which are the same as the true convection velocities only if the turbulence structure is frozen in the moving frame of reference. The idea of a velocity of convection of turbulent fluctuations stems originally from Taylor's work on grid turbulence (Reference 36). Taylor pointed out that, if the turbulence level was low, the time variation in the velocity u observed at a fixed point in the flow would be approximately the same as those due to the convection of an unchanging, frozen, spatial pattern past a fixed point with the mean flow velocity U, i.e., that $u(x,t) \approx u(x - Ut, 0)$ where x and t represent distance measured downstream in the mean flow direction and time, respectively. This is known as Taylor's hypothesis. Lin (Reference 37) has shown that this hypothesis is valid only if the turbulence level is low, viscous forces are negligible, and the mean shear is small. It is unreasonable to expect the hypothesis to apply to the high intensity perturbed flow field induced by the protuberance. For the present computation, measurements for a constant separation, ξ, was used and the results represent the broad band in wave number. A discussion on convection velocities using wave number spectra is given in Reference 38. Due to the non-homogeneous nature of the flow field, computations of convection velocity for varying ξ did not seem practical, particularly for the upstream separated flow field.

The variations of the normalized narrow band convection velocity, $U_c(f)/U_\infty$, with normalized frequency, $f\xi/U_\infty$, are presented in Figures 69-74. These data correspond to the locations in the perturbed flow field and the test conditions for which cross-spectra results are presented. Also presented in Figures 69-74 are the estimated maximum local velocities which were computed based on free-stream speed of sound, free-stream total pressure and local static pressure. Pitot pressure measurements were not taken in the perturbed flow field near the protuberance, and consequently, the values of local convection velocity are only crude estimates of the maximum values. These estimates are conservative in that the local total pressure was probably significantly less than the free-stream total pressure and thus would give a lower local velocity.

For the upstream separated flow region (Figures 69-71) the narrow band convection velocities were negative indicating that the disturbances were generally convected (or propagated) counter to the direction of the free-stream. At low values of the frequency parameter (low frequencies since ξ was held constant for the present analysis), the convection velocity was a small fraction of the free-stream velocity. However, the convection velocity approaches the free-stream value at high frequencies, and in certain cases, exceeded the free-stream velocity. In every case, the estimated local velocity was exceeded at the high frequencies. This suggests that appreciable non-frozen turbulence and/or acoustic mode disturbances were present in the perturbed flow field upstream of the protuberances at the high frequencies. The broad-band convection velocity, indicated by the broken line in each figure, was either less than or approximately equal to the estimated maximum local velocity. It will be noted that the broad band convection velocities are heavily weighted to the high frequencies. This characteristic results from the broader bandwidths associated with the high frequency data points (see Equation 4.23). It should be noted that the convection velocity data do not reflect the power spectral density of the fluctuating pressure energy. Thus, a comparison of the power spectra with the narrow band convection velocities will reveal that most of the fluctuating pressure energy is convected at a small fraction of the free-stream velocity in a direction counter to the free stream. Thus, the true convection velocity from the standpoint of convected energy corresponds to the low frequency values.

In the wake, the narrow-band convection velocities were generally positive indicating that the disturbances are convected (or propagated) in the same direction as the free stream. Appreciable acoustic mode disturbances appear to be present in the mid- and high-frequency ranges as indicated by the large peaks in the narrow-band convection velocity curves (Figures 72-74). For certain frequency bands, negative convection velocities were computed from the fluctuating pressure measurements which further suggests the presence of acoustic mode disturbances in the wake. These data are not plotted; however, the frequencies at which they occurred are indicated by broken lines between neighboring data points in Figures 72-74.

6.4 Analysis of the Protuberance Induced Flow Field

Most of the technical effort underlying this report has been concentrated in developing data reduction techniques and computer programs, reducing the data to tabulation and plot form, and evaluating the accuracy of the final values. For this reason, a comprehensive analysis of the results in regard to the development of mathematical models has not been made. At the present time, additional test results are being reduced which will provide more insight into the three-dimensional protuberance flow field, and it is felt that these data are required before a comprehensive analysis of the flow can be made - particularly in regard to the specification of empirical prediction formula. For this reason, only a cursory analysis of the protuberance induced flow field is presented in this section.

A composite schematic showing typical axial distributions of static pressure coefficient and root-mean-square fluctuating pressure coefficient, and a possible model of the flow field upstream of the protuberance is presented in Figure 75. Sufficiently upstream of the protuberance, the flow is attached which results in static pressure coefficients of approximately zero, and fluctuating pressure coefficients of approximately 0.01. The latter results primarily from tunnel background noise as discussed in Section 5.0. For the case shown, which is the $M_\infty = 1.60$, $h/D = 2.0$ condition, the most upstream boundary of the perturbed flow is the shock wave. The shock wave induces a nonlinear increase in static pressure coefficient and a relatively small peak in the fluctuating pressure coefficient. The mean shock wave location corresponds to the inflection point in the static pressure data. Immediately aft of the shock wave, the boundary layer undergoes separation which, in turn, results in a region of relatively constant, plateau, static pressure. In the plateau region, a gradual increase in fluctuating pressure level with decreasing distance from the protuberance is observed. In contrast to these data, the two-dimensional protuberance (or step) case shows a region of plateau fluctuating pressure corresponding to the region of plateau static pressure (see References 27 and 35 for examples). This latter discrepancy between two- and three-dimensional separated flows is the first indication (as the flow is examined moving downstream toward the protuberance) of dissimilarities between the two cases. Further, the fluctuating pressure levels for the three-dimensional case are an order of magnitude greater than that for the two-dimensional separated flow region. Immediately downstream of the plateau region, the flow exhibits a sudden reduction in static pressure, and the beginning of this sudden reduction corresponds to a peak in the fluctuating pressure level. Corresponding to the region of low static pressure is, what may be envisioned as a plateau region of fluctuating pressure for the $M_\infty = 1.60$ condition; however, this is not typical of all Mach numbers. For lower Mach numbers, the fluctuating pressure decreases toward the protuberance for the region of low static pressure as discussed in Section 6.3.2. The distinct nature of the sudden static pressure reduction and the strong levels of fluctuating pressure are unique to the three-dimensional separated flow case. Before describing the model of the separated flow region, some additional features of the flow field as given by oil flow patterns of the separated region will be discussed.

A typical oil flow picture, Figure 26, was discussed briefly in Section 6.3. Colored oil was injected into the attached boundary layer upstream of the perturbed flow region as well as in close proximity to the protuberance. The oil from the three upstream orifices flowed aft and was deflected around the protuberance by the separated flow field. The oil injected into the separated flow region, flowed in a direction counter to the free stream - indicating a reverse flow region, as well as transverse to the free stream - indicating side relief due to the three-dimensional nature of the flow field. The important feature of the oil flow pattern in the separated flow region is the concentration of oil along a secondary front which is downstream of the front caused by separation of the boundary layer. This suggests a condition of low velocity at angles perpendicular to the secondary front. The presence of this low velocity region imbedded within the separated flow has not been observed in two-dimensional separated flow and is apparently unique to the three-dimensional case. The oil flow pictures also reveal the flow patterns in the wake region; however, an adequate discussion of this region was presented in Section 6.3.

Based on the characteristics of the induced separated flow as exhibited by the static pressures, fluctuating pressures, and oil flow pictures, a model of the upstream perturbed flow can be postulated. Consider a system of horse-shoe vortices, which, when viewed in the plane of symmetry appear as shown in Figure 75. Two major vortices are assumed to be rotating such that a condition of reverse flow exists near the wall of the test panel with a third, smaller, vortex trapped near the wall between the two major vortices and rotating in the opposite direction. Thus, the boundary conditions at the inner region of the separated shear layer and within the separated flow are satisfied. Also observe that the upstream vortex may be elongated which would result in a relatively constant static pressure, plateau, region. The aft vortex, because of the geometry of the flow, may be more circular which would induce a nonlinear variation of the wall pressures as observed in the static pressure distribution. Further, because of the different static pressure levels associated with the two vortices, it may be postulated that the inner vortex has a higher tangential velocity at the wall than does the forward, elongated vortex. Finally, the shearing mechanism that would result due to the opposite velocity vectors in the region between the two vortices would cause a discontinuity in the wall shear stress which would enable oil to be trapped in this region (corresponding to the secondary front noted in the oil flow pictures) and also noise resulting from the shear interaction could generate high level fluctuating pressures as noted in the axial distribution of ΔC_p(RMS), Figure 75. The direction of rotation of the vortices is verified from the oil flow patterns over the surface of the test panel (Figure 26) as well as in photographs of titanium dioxide studies of the protuberance flow pattern, Figure 76. It is interesting to note that the titanium dioxide flow patterns (side view) shows the separation of the flow from the wall of the protuberance near the 90-degree ray very clearly as was observed in the static and fluctuating pressure measurements over the wall of the 8-inch diameter protuberance.

Other data which substantiates the assumption of a double vortex system are the 1/3-octave spectrums. It was pointed out that, based on the static pressure levels, the aft vortex appears to have the greater rotational velocity. Thus, fluctuating pressures being convected past the microphones in the region of the aft vortex would be expected to have energy concentrated at higher frequencies than those associated with the upstream vortex. Typical 1/3-octave spectra show this trend as shown in Figure 77. Further, cross-spectral densities for microphone pairs located beneath the separated flow were obtained at various locations in the separated flow regions and these data yield even greater insight into the mechanism of the flow. If the postulated model is accurate, good coherence should be shown for microphone pairs located in either of the two regions, i.e., microphone pairs located either upstream or downstrem of the peak ΔC_p(RMS). However, poor coherence should be evident from cross-spectral densities for microphone pairs which are separated by the peak since the microphones would sense fluctuating pressures from two separate vortex systems.

Cross-spectra for a representative condition ($M_\infty = 1.60$, $h/D = 2.0$) are presented in Figure 78. It will be noted that reasonably good correlation is shown for microphone pairs located beneath the forward vortex, poor coherence for microphone pairs located near the region between the two major vortices, and fair correlation for microphone pairs located in the region of the inner vortex. It will be noted that disturbances generated in the region of interaction between the two major vortices would not be convected directly across the microphones near the protuberance because of the direction of rotation of the inner vortex. Thus, some loss of coherence (compared to that for the outer vortex system) may be expected.

One final sample of data which adds support to the validity of the postulated model of the upstream separated flow is presented in Figure 79. Here, the flow pattern upstream of a cylindrical protuberance has been photographed using thin filaments of smoke for flow visualization (from Reference 39). The multiple vortex pattern upstream of the protuberance is clearly defined. This condition was extremely low speed (on the order of 5 ft/sec); however, the present data suggests that the basic features of the flow field remain unchanged at transonic Mach numbers.

The flow structure in the wake consists of a converging flow region, a neck region of nearly parallel flow, and a diverging flow region when viewed in the plane of the test panel. This flow field is further complicated by the flow over the top of the protuberance, particularly for $h/D \leq 1.0$. The characteristics of the fluctuating pressure field have been previously discussed; however, some additional insight can be gained from the cross-spectra for various locations in the wake, Figure 80. In the near wake, $r/D < 1.00$, the cross-spectra decay very rapidly and in general show poor correlation. The correlation increases to a maximum in the neck region and this is attributed to the non-dispersive nature of the parallel flow in this region. In the far wake, the flow has a diverging pattern; however, good correlation was still attained. The larger separation of the microphones in the far wake resulted in a loss of coherence in the low frequency components.

In summary, the preliminary analysis of the test results have revealed some important characteristics of the static- and fluctuating-pressure environments induced by three-dimensional protuberances. Based on this analysis, some conclusions have been drawn in regard to the perturbed flow field and areas for further, expanded, studies have been defined. These points are discussed in the next section.

7.0 CONCLUDING REMARKS

7.1 Conclusions

A wind tunnel investigation has been conducted to study the flow field induced by three-dimensional protuberances at transonic Mach numbers. Selected results for the generalized protuberance - which consisted of right circular cylinders - have been presented and discussed. In particular, the static pressure field, the fluctuating pressure field, and general features of the perturbed flow have been evaluated. From this study, the following conclusions have been made.

7.1.1 General Characteristics of the Protuberance Induced Flow Field

1. The protuberance flow field consisted of two predominant regions - an upstream separated flow region and a downstream wake region. The upstream separated flow region was composed of a complex, multiple, vortex flow structure. This flow structure appears to be unique to the three-dimensional separated flow case and has little similarity to the two-dimensional, step induced, flow structure. A postulated model of the three-dimensional separated flow region consists of two major vortices rotating in the same direction with velocity vectors at the wall which are counter to the free-stream direction. Static- and fluctuating-pressure measurements and oil-flow patterns appear to agree with the postulated flow structure. The wake region consisted of a near wake of converging flow, a neck region of approximately parallel flow, and a far wake of diverging flow. For small ratios of protuberance height to diameter, the wake flow structure was complicated by the flow over the top of the protuberance which appeared to re-attach on the surface supporting the protuberance in the vicinity of the neck of the wake.

2. Increasing either protuberance height or free-stream Mach number caused an increase in the upstream separation length and a corresponding growth of the separated flow structure.

3. The perturbed flow field scales approximately with protuberance diameter, although some trends in the normalized data with protuberance size and Reynolds number were detected in the static- and fluctuating-pressure measurements.

7.1.2 Protuberance Induced Static Pressure Field

1. The protuberance induced static pressure field upstream of the protuberances exhibited the following characteristics:

   a. There was an increase in static pressure at the outer extremities of the upstream perturbed flow field that induced boundary layer separation. At $M_\infty < 1.20$, the pressure gradient was relatively small; whereas, at $M_\infty \geq 1.20$, the pressure gradient was large and resulted from the pressure discontinuity of the shock wave.

   b. The initial pressure gradient was followed by a region of nearly constant, plateau, static pressure which corresponded to the outer region of the separated flow field.

   c. A region of low static pressure (below the plateau level) was exhibited by the inner region of the separated flow field.

   d. At the base of the protuberance, maximum static pressure was reached.

   e. Variations in protuberance height and free-stream Mach number caused similar variations in the region exposed to the protuberance induced static pressure field. An increase in the test variables caused an increase in the area of the protuberance induced static pressure field.

2. The protuberance induced negative static pressure coefficients immediately downstream of the protuberance which corresponded to the near wake and neck regions of the wake flow field. Approximately free-stream static pressure was measured in the far wake.

3. The static pressure field over the wall of the protuberance exhibited noticeable variations in both the vertical and circumferential directions over the forward half of the cylinder. Variations in the vertical direction corresponded to the various flow regimes of the inflowing perturbed flow field. Circumferential variations indicated that the flow separated from the wall of the protuberance near the 90-degree ray.

4. Variations in Reynolds number and protuberance size caused small variations in the wake pressures at subsonic Mach numbers, and small, but consistent, variations in the upstream pressures at supersonic Mach numbers.

7.1.3 Protuberance Induced Fluctuating Pressure Field

1. The protuberance induced fluctuating pressure field upstream of the protuberances exhibited the following characteristics:

   a. There was a gradual increase in fluctuating pressure in the axial direction which started at the outer extremity of the perturbed flow field and reached a peak near the mid-point of the separated flow region. The peak levels of fluctuating pressure corresponded to a region between two major vortices and appeared to result from the shear interaction of the vortices. Peak levels were in the range from 12 to 17 percent of the free stream dynamic pressure and are an order of magnitude greater than that observed for two-dimensional separated flows.

b. The inner region of the separated flow field exhibited a high level of fluctuating pressure which corresponded to the inner vortex system. For $M_\infty = 1.60$, the fluctuating pressure levels for the inner region were approximately constant and equal to the peak level in the separated flow field. For $M_\infty < 1.60$, the fluctuating pressure levels in the inner region decreased below the peak level.

c. For $M_\infty = 1.40$ and 1.60, shock-boundary interaction upstream of the separation point resulted in a small peak in the fluctuating pressure levels for the region beneath the shock wave.

d. Variations in protuberance height and free-stream Mach number caused similar variations in the extent of the separated flow field, i.e., increasing test variables caused an increase in the size of the separated flow field and, thus, the region exposed to protuberance induced fluctuating pressures. Otherwise, the separated flow structure and the corresponding fluctuating pressure field appeared to remain relatively invariant with changes in protuberance height and free-stream Mach number.

e. The power spectra corresponding to the peak levels of fluctuating pressure exhibited a high energy level at low frequencies with a roll-off at high frequencies of approximately 6 dB per octave.

f. Maximum correlation of the fluctuating pressures within the separated flow field corresponded to the region of the outer vortex system.

g. Fluctuating pressures within the separated flow field were convected in a direction counter to that of the free stream.

h. The fluctuating pressure field was largely non-homogeneous and this is attributed to the complex vortex structure of the separated flow field.

2. Fluctuating pressures over the wall of the protuberance exhibited peak values in the region of separation of the flow from the wall of the protuberance and in the wake region of the protuberance at subsonic Mach numbers. At supersonic Mach numbers, maximum levels of fluctuating pressure occurred over

the front half of the protuberance corresponding to the region of impingement of the upstream separated flow field. At $M_\infty = 0.60$, the flow separated from the wall of the protuberance at the 90-degree ray and resulting fluctuating pressures exceeded 170 dB.

3. The protuberance induced fluctuating pressure field downstream of the protuberances exhibited the following characteristics:

   a. There was a moderate increase in fluctuating pressure levels in the axial direction within the near wake, peak levels of fluctuating pressure in the neck region and gradually decreasing fluctuating pressure levels in the far wake.

   b. Power spectra of the fluctuating pressures revealed discrete frequency energy at certain protuberance heights and Mach numbers. The Strouhal number, based on protuberance diameter, associated with the peaks in the power spectra was approximately 0.28.

   c. Maximum correlation of the fluctuating pressures within the wake flow field corresponded to the neck and far wake regions.

   d. The fluctuating pressure characteristics of the wake appeared to vary with both protuberance height and Mach number.

7.2 Areas for Further Study

Based on the foregoing analysis of the test results, important areas requiring further analysis can be defined. These areas are as follows:

1. A more extensive study of the spectra and cross spectra of the fluctuating pressures recorded by the centerline distribution of microphones. These data will be analyzed to define the structure of both the upstream separated flow (i.e., verification or disproval of the postulated model of the separated flow) and the wake flow aft of the protuberance.

2. Examination of the microphone and static pressure data for locations around the protuberance in the plane of the test panel. These data will be analyzed to define the generating mechanisms associated with the three-dimensional flow around the protuberances that caused differences between two- and three-dimensional flow patterns as observed in the centerline axis data. It is felt that the transverse velocity and acceleration components induced by the three-dimensional protuberance shape are the key to the multiple vortex flow pattern which has been postulated. These data will also provide a basis for the development of prediction techniques for the steady and fluctuating air loads around the protuberances.

3. Further examination of the microphone and static pressure data recorded for sensors distributed over the wall of the 8-inch diameter protuberances. These data will be analyzed to define the steady and fluctuating air loads on protuberances and to assist in defining the three-dimensional flow patterns.

4. A more detailed study of the effects of Reynolds number and protuberance scale on the flow field particularly for the fluctuating pressure environment.

5. An evaluation of the free-interaction hypothesis as it applies to three-dimensional flows. This hypothesis, advanced by Chapman, Kuehn and Larson, Reference 2, suggests that turbulent boundary layers undergo separation in a manner independent of the detailed geometry of the cause. Although proven for two-dimensional separated flows, its application to three-dimensional flows has not been verified. If the hypothesis is true for the three-dimensional case, prediction of protuberance flow fields for specific geometries can be made based on data obtained for generalized protuberance shapes. Further, this hypothesis applies only to the upstream separated flow region. It is also of interest to determine if the free-interaction concept can be applied to the wake region as well.

In addition to those described, it is anticipated that other areas requiring study will become evident during the course of the analysis.

REFERENCES

1. Reich, J.R., "Saturn V External Protuberances, Cavities, and Corrugations," Lockheed Missiles and Space Company, Huntsville Technical Memorandum, TM-54/50-43, May 1966.

2. Chapman, D.R., Kuehn, D.M., and Larson, H.K., "Investigation of Separated Flows in Supersonic and Subsonic Streams with Emphasis on the Effects of Transition," NACA Report 1356.

3. Voitenko, D.M., et al., "Supersonic Gas Flow Past a Cylindrical Protuberance on a Plate," AD 650 960, January 1967.

4. Halprin, R.W., "Study of the Separated Regions Caused by Two-Dimensional and Cylindrical Steps Mounted on a Flat Plate in a Supersonic Turbulent Flow," Master's Thesis, University of California, Los Angeles, 1964.

5. Couch, L.M., et al., "Heat Transfer Measurements on a Flat Plate with Attached Protuberances in a Turbulent Boundary Layer at Mach Numbers of 2.49, 3.51, and 4.44," NASA TN D-3736, December 1966.

6. Burbank, P.B., Strass, K.H., "Heat Transfer to Surfaces and Protuberances in a Supersonic Turbulent Boundary Layer," NACA RM L58E 1a, July 14, 1958.

7. Burbank, P.B., et al., "Heat Transfer and Pressure Measurements on a Flat-Plate Surface and Heat Transfer Measurements on Attached Protuberances in a Supersonic Turbulent Boundary Layer at Mach Numbers of 2.65, 3.51, and 4.44," NASA TN D-1372, December 1962.

8. Price, E.A., and Stalling, R.L., Jr., "Investigation of Turbulent Separated Flows in the Vicinity of Fin Type Protuberances at Supersonic Mach Numbers," NASA TN D-3804, February 1967.

9. Miller, W.H., "Pressure Distributions on Single and Tandem Cylinders Mounted on a Flat Plate in Mach Number 5.0 Flow," University of Texas Defense Research Laboratory Report 538, (N66-28598), June 1966.

10. Westkaemper, J.C., "The Drag of Cylinders All or Partially Immersed in a Turbulent Supersonic Boundary Layer," University of Texas Defense Research Laboratory Report 549, AD 813 886, March 1967.

11. Sykes, D.M., "The Supersonic and Low-Speed Flows Past Circular Cylinders of Finite Length Supported at One End," Journal of Fluid Mechanics, Vol. 12, Part 3, March 1962.

12. Lucero, E.F., "Turbulent Boundary Layer Separation Induced by Three-Dimensional Protuberances on a Flat Plate," Master's Thesis, University of Maryland, 1966.

13. Walthrup, P.J., et al., "Flow Field in the Vicinity of Circular Protuberances on a Flat Plate in Supersonic Flow," Journal of Spacecraft and Rockets, Vol. 5, No. 1, pp. 127-128.

14. Bogdonoff, S.M., and Kepler, C.E., " Separation of a Supersonic Boundary Layer," Journal of the Aeronautical Sciences, June 1955.

15. Uselton, J.C., "Fin Shock/Boundary-Layer Interaction Tests on a Flat Plate with Blunted Fins at $M_D = 3$ and 5," Arnold Engineering Development Center Test Report 67-113, June 1967 (AD 815 760).

16. Zukoski, E.E., "Turbulent Boundary Layer Separation in Front of a Forward-Facing Step," AIAA Journal, Volume 5, No. 10, pp. 1746-1753, October 1967.

17. Dendrinos, S. Jr., "Prediction of Mean Flow Characteristics About Three-Dimensional Protuberances in Supersonic Flow," Wyle Laboratories Research Staff Report WR 67-19, November 1967.

18. Dendrinos, S. Jr., "Static and Relative Fluctuating Pressure Results of a Wind Tunnel Investigation of Subsonic and Supersonic Separated Flow About Cylindrical and Saturn V Model Protuberances," Wyle Laboratories Research Staff Report WR 68-13, June 1968.

19. Robertson, J.E., "Experimental Program for the Investigation of Transonic Flow Around Protuberances in the AEDC-16T Wind Tunnel Facility," Wyle Laboratories - Research Staff Technical Memorandum 68-6, 1968.

20. Chevalier, H.L., "Calibration of the 16-Foot Transonic Circuit with a Modified Model Support System and Test Section," AEDC-TN-60-164, AD 241 735, August 1960.

21. Riddle, C.D., "An Investigation of Free-Stream Fluctuating Pressures in the 16-Foot Tunnels of the Propulsion Wind Tunnel Facility, AEDC-TR-67-167, August 1967.

22. Bies, D.A., "A Review of Flight and Wind Tunnel Measurements of Boundary Layer Pressure Fluctuations and Induced Structural Response," NASA CR-626, October 1966.

23. Jolly, A.C., "Computer Programs for the Calculation of Direct and Cross-Power Spectral Density of Discrete Random Data," Wyle Laboratories - Research Staff Report WR 69-1, January 1969.

REFERENCES (Continued)

24. Jolly, A.C., "Estimation of Direct and Cross-Power Spectral Density of Discrete Data Using the Fast Fourier Transform," Wyle Laboratories - Research Staff Report WR 69-4, March 1969.

25. Brice, T.R., "Determination of Flow-Field Characteristics Around Generalized and Specific Protuberances at Mach Numbers 0.60 through 1.60," AEDC-TR-68-186, September 1968.

26. Lowson, M.V., "Prediction of Boundary Layer Pressure Fluctuations," Wyle Laboratories - Research Staff Report WR 67-15, 1967.

27. Chyu, Wei J., and Hanly, Richard D., "Power- and Cross-Spectra and Space-Time Correlations of Surface Fluctuating Pressures at Mach Numbers Between 1.6 and 2.5," AIAA Preprint No. 68-77, Paper presented at the AIAA 6th Aerospace Sciences Meeting, New York, New York, January 22-24, 1968.

28. White, Pritchard H., "Effect of Transducer Size, Shape, and Surface Sensitivity on the Measurement of Boundary Layer Pressures," Journal of the Acoustical Society of America, Vol. 41, No. 5, 1967.

29. Skudrzyk, E.J., and Haddle, G.P., "Noise Production in a Turbulent Boundary Layer by Smooth and Rough Surfaces," Journal of the Acoustical Society of America, Vol. 32, No. 1, 1960.

30. Lyamshev, L.M., and Salosina, S.A., "Influences of the Pickup Dimensions on Measurements of the Spectrum of Wall Pressure Fluctuations in a Boundary Layer," Soviet Physics - Acoustics Vol. 12, No. 2, 1966.

31. Willmarth, W.W., and Roos, F.W., "Resolution and Structure of the Wall Pressure Field Beneath a Turbulent Boundary Layer," Journal of Fluid Mechanics, Vol. 22, Part 1, 1965.

32. Corcos, G.M., "Resolution of Pressure in Turbulence," Journal of the Acoustical Society of America, Vol. 35, No. 2, 1963.

33. Gilchrist, Richard B., and Strauderman, Wayne A., "Experimental Hydrophone Size Correction Factor for Boundary Layer Pressure Fluctuations," Journal of the Acoustical Society of America, Vol. 38, No. 2, 1965.

34. Bendat, Julius S., and Piersol, Allan G., <u>Measurement and Analysis of Random Data</u>, John Wiley and Sons, Inc., New York, New York, 1966.

35. Speaker, W.V., and Ailman, C.M., "Spectra and Space-Time Correlations of the Fluctuating Pressures at a Wall Beneath a Supersonic Turbulent Boundary Layer Perturbed by Steps and Shock Waves," NASA CR-486, May 1966.

REFERENCES (Continued)

36. Taylor, G.I., Proceedings of the Royal Society, A, 174, 476, 1938.

37. Lin, C.C., Quarterly of Applied Mathematics, Vol. 18, 295, 1952.

38. Wills, J.A.B., "On Convection Velocities in Turbulent Shear Flows," Journal of Fluid Mechanics, Vol. 20, Part 3, 1964.

39. Incompressible Aerodynamics, Oxford at the Claredon Press, 1960.

APPENDIX A

DATA REDUCTION EQUATIONS FOR MEAN FLOW PARAMETERS

The parameters used in the specification of the mean flow characteristics are presented in terms of the measured static and total pressures as follows.

1. Local Static Pressure Coefficient

$$C_p = \frac{P_\ell - P_\infty}{q_\infty} \tag{A-1}$$

where P_ℓ and P_∞ are the local and free-stream static pressures, respectively, and q_∞ is the free stream dynamic pressure.

2. Boundary Layer Profile Mach Number (Computed at Both Forward and Aft Rake Positions)

For $P_g/P_{t_n} \leq 0.528$, the Rayleigh Pitot Equation was solved for Mach numbers as follows:

$$\frac{P_{t_n}}{P_s} = \left[\frac{6\,M_n^2}{5}\right]^{7/2} \left[\frac{6}{7\,M_n^2 - 1}\right]^{5/2} \tag{A-2}$$

where P_s is the test panel static pressure nearest the rake and P_{t_n} is the pitot pressure measured by the rake.

For $P_s/P_{t_n} > 0.528$, the standard compressible flow equation was solved, i.e.,

$$M_n = \sqrt{5\left[\frac{1}{(P_s/P_{t_n})^{2/7}} - 1\right]} \tag{A-3}$$

3. Boundary Layer Profile Velocity Ratio (Computed at Both Forward and Aft Rake Positions)

$$\frac{U_n}{U_s} = \frac{M_n}{M_s}\sqrt{\frac{1 + 0.2\,M_s^2}{1 + 0.2\,M_n^2}} \tag{A-4}$$

where U_s and M_s are the velocity and Mach number corresponding to the local static pressure P_s, and U_n and M_n are the profile velocities and Mach numbers corresponding to the measured pitot pressures, P_{t_n}.

4. Boundary Layer Displacement Thickness (Computed at Both Foreward and Aft Rake Positions)

$$\delta^* = \int_0^{\delta} \left[1 - \frac{\rho_n}{\rho_s}\,\frac{U_n}{U_s}\right] dy \tag{A-5}$$

where δ is the y position for the pitot probe that is the furtherest from the test panel for each rake. ρ_n and ρ_s are densities corresponding to P_s and P_{t_n}.

5. Boundary Layer Momentum Thickness (Computed at Both Forward and Aft Rake Positions)

$$\theta = \int_0^{\delta} \frac{\rho_n}{\rho_s}\,\frac{U_n}{U_s}\left[1 - \frac{U_n}{U_s}\right] dy \tag{A-6}$$

6. Empirical Boundary Layer, Displacement and Momentum Thicknesses (Computed at Model Station Zero)

$$\delta^* = \frac{X\,[1.3 + 0.43\,M_\infty^2]\;[\delta/X]}{10.4 + 0.5\,M_\infty^2\;[1 + (2)\,(10^{-8})\;Re_\infty \cdot X]^{1/3}} \tag{A-7}$$

where

$$\delta/X = 0.37\;[Re_\infty \cdot X]^{-1/5}\left[1 + \left(\frac{Re_\infty \cdot X}{6.9 \cdot 10^7}\right)^2\right]^{1/10} \tag{A-8}$$

$$X = 124.36 \text{ inches}$$

and

$$\theta = \frac{\delta^*}{1.3 + 0.43\,M_\infty^2} \tag{A-9}$$

```
 TEST      PART       POINT      TIME        DATE                                               AEDC PROPULSION WIND TUNNEL
 TF-184     154          5        251       6- 7-68                                                    TRANSONIC 16T

   M1      PT1    P1     C1      2P    RX10-6  NCN   PTA     PTB     PCA     PCB     PTI     W9     TPR   WA/WT TH-E TH-W TTA TTB
 1.5985 1572.1  370.7  663.0  41227   3.000   45 1572.1 1572.3  384.5   384.3 1060.0  225.2  1.483 0.0480 0.51 0.51 112 104

  K1       K2       K3       K4       K5       K6       K7       K8       K9       K10         CONF
 0.2083   0.2094   0.2120   0.2094   0.2094   0.2035   0.0000   0.0000   0.0000   0.2037        03

                                  TWO-INCH PROTUBERANCE      XOD= 2.00             CORRECTED
     PHI      0       15      30      45     67.5     90    112.5    135     150    157.5    165     170     175     180     270
     R
    1.75    1.581   1.583   1.589   1.596   1.512   1.306   0.908   0.591   0.507   0.483   0.437   0.421   0.572   0.630
            0.332   0.335   0.336   0.341   0.296   0.175  -0.053  -0.234  -0.287  -0.300  -0.329  -0.334  -0.250  -0.215

    2.75    1.253   1.229   1.177   1.176   1.209   1.232   1.040   0.697   0.547   0.494   0.449   0.509   0.647   0.735
            0.146   0.130   0.101   0.102   0.119   0.133   0.023  -0.175  -0.262  -0.293  -0.320  -0.282  -0.202  -0.153

    3.75    1.504   1.489   1.457   1.397   1.254   1.088   1.061   0.738   0.551   0.479   0.486   0.613   0.670   0.738
            0.282   0.278   0.261   0.227   0.145   0.050   0.034  -0.151  -0.260  -0.295  -0.294  -0.219  -0.188  -0.148

    4.75    1.314   1.466   1.453   1.446   1.355   1.207   1.036   0.903   0.533   0.453   0.532   0.633   0.697   0.767   1.189
            0.165   0.245   0.239   0.235   0.187   0.110   0.019  -0.057  -0.249  -0.290  -0.249  -0.197  -0.160  -0.132   0.101

    5.50    1.073   1.374   1.383   1.389   1.340   1.232   1.031   0.790   0.533   0.454   0.624   0.703   0.795   0.840   1.232
            0.038   0.194   0.200   0.205   0.180   0.123   0.017  -0.112  -0.249  -0.289  -0.199  -0.155  -0.108  -0.090   0.123

    6.50    1.003   1.137   1.170   1.270   1.320   1.243   1.055   0.806   0.549   0.462   0.776   0.874   1.009   0.996   1.235
            0.002   0.071   0.090   0.141   0.168   0.128   0.029  -0.102  -0.239  -0.287  -0.118  -0.066   0.005  -0.002   0.125

    7.50    1.007   1.012   1.010   1.089   1.241   1.231   1.087   0.804   0.540   0.629   0.959   1.018   1.068   1.105   1.244
            0.003   0.006   0.005   0.046   0.126   0.122   0.046  -0.102  -0.247  -0.197  -0.021   0.009   0.036   0.059   0.127

    8.50    1.004   1.008   1.001   1.014   1.145   1.240   1.132   0.808   0.593   0.858   1.018   1.075   1.062   1.081   1.232
            0.002   0.004   0.000   0.007   0.075   0.125   0.069  -0.101  -0.216  -0.076   0.009   0.039   0.033   0.046   0.120

    9.50    1.006   1.006   0.991   0.998   1.051   1.217   1.145   0.822   0.591   0.914   1.028   1.055   1.070   1.067   1.201
            0.003   0.003  -0.005  -0.001   0.027   0.113   0.075  -0.094  -0.219  -0.046   0.015   0.030   0.038   0.038   0.112

   10.50    0.998   1.005   1.004   1.010   1.019   1.191   1.148   0.856   0.671   0.941   1.044   1.062   1.051   1.056   1.170
           -0.001   0.002   0.002   0.005   0.010   0.097   0.077  -0.075  -0.177  -0.032   0.023   0.033   0.028   0.032   0.086

   11.50    0.995   1.006   0.998   1.003   1.008   1.157   1.153   0.855   0.817   0.953   1.023   1.060   1.061   1.054   1.121
           -0.002   0.003  -0.001   0.002   0.004   0.080   0.080  -0.077  -0.098  -0.025   0.012   0.032   0.033   0.031   0.061

   12.50    1.011   1.006   1.014   0.997   1.003   1.085   1.157   0.671   0.863   0.975   1.028   1.037   1.055   1.051   1.072
            0.006   0.003   0.007  -0.002   0.002   0.044   0.081  -0.069  -0.074  -0.013   0.015   0.019   0.029   0.029   0.036

   13.50    1.002   1.007   0.994   1.002   0.993   1.060   1.146   0.876   0.890   0.981   1.018   1.038   1.047   1.041   1.078
            0.001   0.003  -0.003   0.001  -0.004   0.031   0.076  -0.065  -0.059  -0.010   0.009   0.020   0.025   0.023   0.039

   14.50    1.000   1.044   0.993   0.997   1.006   1.037   1.149   0.893   0.914   0.994   1.024   1.024   1.036   1.040   1.024
           -0.000   0.022  -0.004  -0.002   0.003   0.019   0.076  -0.057  -0.046  -0.003   0.013   0.013   0.019   0.022   0.012

   15.50    1.003   1.144   0.985   1.006   1.008   0.992   1.139   0.904   0.926   1.003   1.025   1.026   1.040   1.042   1.027
            0.001   0.072  -0.007   0.003   0.004  -0.004   0.069  -0.051  -0.039   0.002   0.013   0.013   0.021   0.023   0.013

   16.50    1.006   1.477   0.978   0.995   0.993   0.996   1.130   0.908   0.939   0.975   1.023   1.015   1.013   1.024   1.001
            0.003   0.249  -0.011  -0.002  -0.004  -0.002   0.065  -0.049  -0.032  -0.013   0.012   0.010   0.007   0.013   0.000
```

```
 TEST    PART    POINT
  184     154       5

           R= 17.50  18.50  19.50  20.50  21.50  22.50  23.50  24.50  25.50  26.50  28.00

  PHI =0      1.006  1.005  0.987  0.999  1.004  1.006  0.999  0.995  0.999  0.995
              0.003  0.002 -0.006 -0.000  0.002  0.003 -0.001 -0.003 -0.001 -0.002

  PHI =180    1.020  1.016  1.015  1.021  1.016  1.024  1.019  1.019  1.024  1.023  1.025
              0.011  0.009  0.008  0.012  0.009  0.013  0.011  0.011  0.013  0.013  0.014

  PIN     11P     12P     13P     14P     15P     ****COMPARISON PRESSURES****    16P     17P     18P     19P     10P
  530.5   544.5   541.6   543.9   543.9   542.5                                  528.0    0.0     0.0     0.0   528.3

  PTOT    PS1     PS2
  368.2   371.4   374.9

                                                  FIXED RAKE (2)
  M1      M2      M3      M4      M5      M6      M7      M8      M9      M10     M11     M12     M13     M14     M15
 1.000   1.213   1.265   1.299   1.317   1.333   1.347   1.372   1.400   1.422   1.447   1.464   1.478   1.494   1.508

  M16     M17     M18     M19     M20     M21     M22     M23     M24     M25
 1.519   1.529   1.539   1.539   1.532   1.531   1.537   1.543   1.548   1.552

 U1/U    U2/U    U3/U    U4/U    U5/U    U6/U    U7/U    U8/U    U9/U    U10/U   U11/U   U12/U   U13/U   U14/U   U15/U
 0.702   0.820   0.847   0.864   0.872   0.881   0.887   0.899   0.912   0.923   0.934   0.942   0.948   0.955   0.961

 U16/U   U17/U   U18/U   U19/U   U20/U   U21/U   U22/U   U23/U   U24/U   U25/U
 0.966   0.971   0.975   0.975   0.972   0.972   0.974   0.977   0.979   0.981

    DISPLACEMENT THICKNESSES                                           MOMENTUM THICKNESSES
      1        2        3                                               1        2        3
  0.0000   0.2892   0.2987                                          0.0000   0.1961   0.1245
```

APPENDIX B

DATA REDUCTION EQUATIONS FOR UNSTEADY FLOW PARAMETERS

The statistical functions used in the specification of the fluctuating pressure characteristics of the unsteady flow field are presented in analog form. It is felt that the analog form of the descriptive statistical parameters will facilitate an understanding of the physical significance of the functions more so than the digital form. A comprehensive presentation of the digital equations used in the present digital computations are given in References 23 and 24. A brief discussion of the equations is presented in Section 4.4. The analog forms are as follows.

1. Overall RMS Fluctuating Pressure

$$\Delta P(\text{RMS}) = \left[\lim_{T \to \infty} \int_0^T P^2(t)\, dt \right]^{\frac{1}{2}} \tag{B-1}$$

where P(t) denotes the time history record of pressure.

2. Power Spectral Density

$$\phi(f) = \lim_{\substack{\Delta f \to 0 \\ T \to \infty}} \frac{1}{(\Delta f)\,T} \int_0^T P^2(t,f,\Delta f)\, dt \tag{B-2}$$

where $P(t,f,\Delta f)$ is the filtered portion of P(t) in the frequency range of $f - \Delta f/2$ to $f + \Delta f/2$.

3. Cross Spectral Density

$$G(\xi,f) = C(\xi,f) - i\, Q(\xi,f) \tag{B-3}$$

where $C(\xi,f)$ and $Q(\xi,f)$ denote the co-spectral density and quad-spectral density, respectively. The co- and quad-spectral densities are defined as follows:

$$C(\xi,f) = \lim_{\substack{\Delta f \to 0 \\ T \to \infty}} \frac{1}{(\Delta f)T} \int_0^T P(t,f,\Delta f)\, P_\xi(t,f,\Delta f)\, dt \tag{B-4}$$

and

$$Q(\xi,f) = \lim_{\substack{\Delta f \to 0 \\ T \to \infty}} \frac{1}{(\Delta f)\,T} \int_0^T P(t,f,\Delta f)\, P_\xi^*(t,f,\Delta f)\, dt \qquad \text{(B-5)}$$

where $P(t,f,\Delta f)$ and $P_\xi(t,f,\Delta f)$ pressure time histories taken at points separated in distance by ξ and $P_\xi^*(t,f,\Delta f)$ denotes a 90-degree phase shift from $P_\xi(t,f,\Delta f)$. The normalized co- and quad-spectral densities are given by:

$$c(\xi,f) = \frac{C(\xi,f)}{[\phi(f)\ \ \phi_\xi(f)]^{\frac{1}{2}}} \qquad \text{(B-6)}$$

and

$$q(\xi,f) = \frac{Q(\xi,f)}{[\phi(f)\ \ \phi_\xi(f)]^{\frac{1}{2}}} \qquad \text{(B-7)}$$

4. Phase Angle

$$\alpha(\xi,f) = \tan^{-1}\left[\frac{Q(\xi,f)}{C(\xi,f)}\right] \qquad \text{(B-8)}$$

5. Coherence

$$\gamma^2(\xi,f) = \frac{\left|G(\xi,f)\right|^2}{\left|\phi(f)\right|\,\left|\phi_\xi(f)\right|} \qquad \text{(B-9)}$$

6. Narrow-Band Convection Velocity

$$U_c(f) = \frac{2\pi\, f\, \xi}{\alpha(\xi,f)} \qquad \text{(B-10)}$$

```
              AVALOG REEL 192,  PN/TP=86/1  H/D=1,0  MACH NO.=1,6    10TH FILE DIG, REEL 16

            TAPE NUMBER TP16      MUX A     FILE NUMBER   10     OVERALL LEVEL =   35,02  P.S.F.            158,5  DB

            TAPE NUMBER TP16      MUX B     FILE NUMBER   10     OVERALL LEVEL =   36,84  P.S.F.            158,9  DB

  FREQ     FREQ     .....RMS.....        .........PSD.........     ................CROSS-PSD................     COHER-
   CPS     PARAM    MUXA      MUXB                                   CO          QUAD     TOTAL      PHASE      ENCE        UC

    25,0  -0,049    131,8     133,0      2,20E-05    2,89E-05        ,57        -0,18     1,50E-05    -17,8      ,355      -42,1
    31,5  -0,021    135,9     134,9      4,50E-05    3,60E-05        ,75        -0,10     3,06E-05     -7,6      ,576     -124,0
    39,7  -0,056    135,4     136,5      3,20E-05    4,12E-05        ,63        -0,23     2,43E-05    -20,2      ,447      -59,0
    50,0    ,055    137,2     139,0      3,81E-05    5,77E-05        ,78          ,28     3,90E-05     19,9      ,691       75,2
    63,0    ,031    138,1     138,9      3,75E-05    4,45E-05        ,75          ,15     3,12E-05     11,2      ,583      168,1
    79,4  -0,059    140,9     140,6      5,58E-05    5,23E-05        ,78        -0,31     4,55E-05    -21,3      ,709     -111,6
   100,0  -0,012    139,9     140,5      3,55E-05    4,03E-05        ,72        -0,05     2,72E-05     -4,3      ,517     -692,2
   126,0    ,049    139,6     140,4      2,62E-05    3,18E-05        ,49          ,16     1,49E-05     17,6      ,268      214,9
   158,8  -0,012    141,9     142,6      3,53E-05    4,17E-05        ,63        -0,05     2,44E-05     -4,2      ,403    -1136,4
   200,0    ,034    142,8     141,5      3,42E-05    2,55E-05        ,69          ,15     2,10E-05     12,2      ,506      491,4
   252,0    ,027    144,4     143,1      4,02E-05    2,93E-05        ,73          ,13     2,55E-05      9,8      ,553      767,7
   317,5    ,055    143,2     143,9      2,38E-05    2,80E-05        ,48          ,17     1,31E-05     19,7      ,259      482,5
   400,0    ,105    143,8     144,2      2,18E-05    2,38E-05        ,31          ,24     8,85E-06     37,7      ,151      318,6
   504,0    ,137    145,9     145,2      2,79E-05    2,40E-05        ,37          ,42     1,45E-05     49,1      ,314      307,6
   635,0    ,072    146,3     147,2      2,42E-05    3,03E-05        ,43          ,21     1,31E-05     26,1      ,233      730,4
   800,1    ,095    147,9     148,6      2,82E-05    3,29E-05        ,33          ,23     1,23E-05     34,1      ,163      704,1
  1008,0    ,126    147,9     148,3      2,23E-05    2,46E-05        ,28          ,29     9,46E-06     45,3      ,164      666,8
  1270,0    ,157    149,0     149,2      2,27E-05    2,41E-05        ,24          ,36     1,01E-05     56,6      ,188      673,5
  1600,1    ,183    148,8     150,3      1,74E-05    2,46E-05        ,20          ,44     9,88E-06     65,7      ,229      730,3
  2016,0    ,266    149,2     149,8      1,49E-05    1,72E-05      -0,05          ,47     7,61E-06     95,9      ,225      630,7
  2540,0    ,333    149,1     150,2      1,17E-05    1,50E-05      -0,19          ,32     4,96E-06    119,7      ,140      636,4
  3200,2    ,373    150,0     150,2      1,14E-05    1,19E-05      -0,25          ,26     4,23E-06    134,2      ,132      715,1
  4032,0  -0,399    148,3     149,7      6,15E-06    8,43E-06      -0,13        -0,10     1,17E-06   -143,5      ,027     -843,0
  5080,0  -0,286    149,0     149,7      5,72E-06    6,73E-06      -0,02        -0,11     6,79E-07   -103,1      ,012    -1478,4
  6400,4  -0,108    147,7     148,1      3,34E-06    3,63E-06        ,12        -0,10     5,44E-07    -38,8      ,024    -4949,6
  8064,0    ,182    146,4     146,6      1,96E-06    2,07E-06        ,06          ,14     3,08E-07     65,5      ,023     3693,4
 10160,0  -0,365    145,2     146,7      1,19E-06    1,68E-06      -0,04        -0,05     9,17E-08   -131,2      ,004    -2322,7
 12800,8    ,175    144,3     144,8      7,73E-07    8,62E-07        ,01          ,01     1,24E-08     63,0      ,000     6098,1
 16128,0    ,230    143,6     144,4      5,13E-07    6,15E-07        ,01          ,10     5,67E-08     82,9      ,010     5833,3
 20320,0  -0,473    144,2     143,4      4,68E-07    3,93E-07      -0,08        -0,01     3,33E-08   -170,3      ,006    -3579,2
```

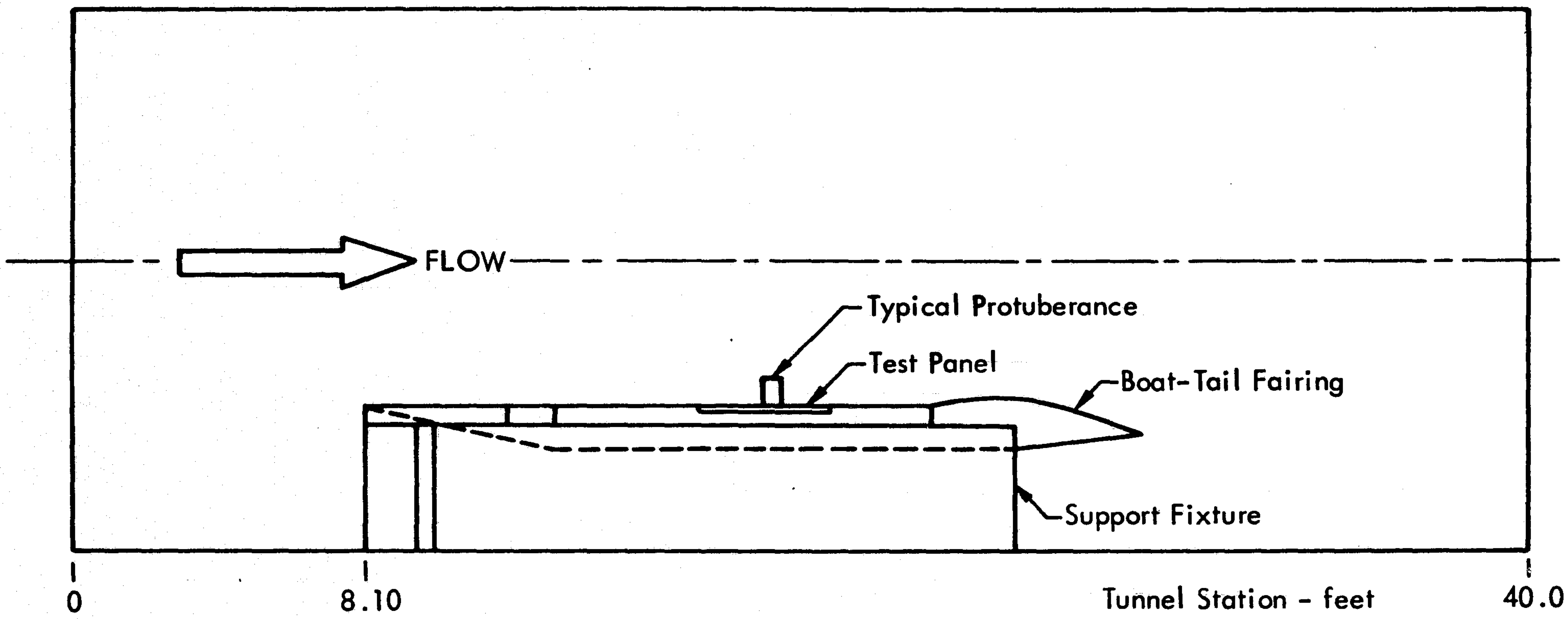

Figure 1. Schematic of the Test Article Installation in the AEDC - 16T Wind Tunnel Facility

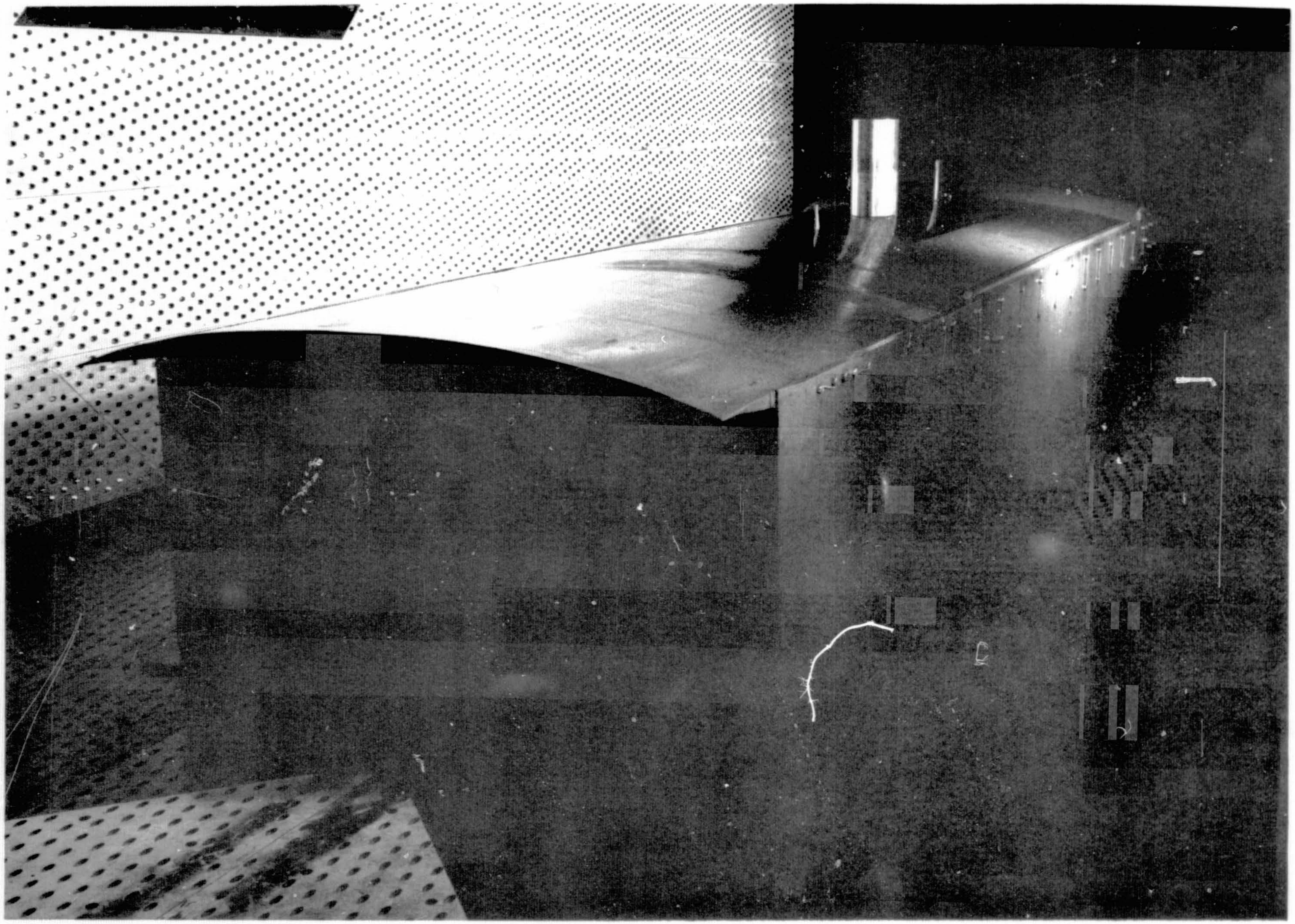

Figure 2. Photograph of the Model Installation in the AEDC-16T Wind Tunnel Facility

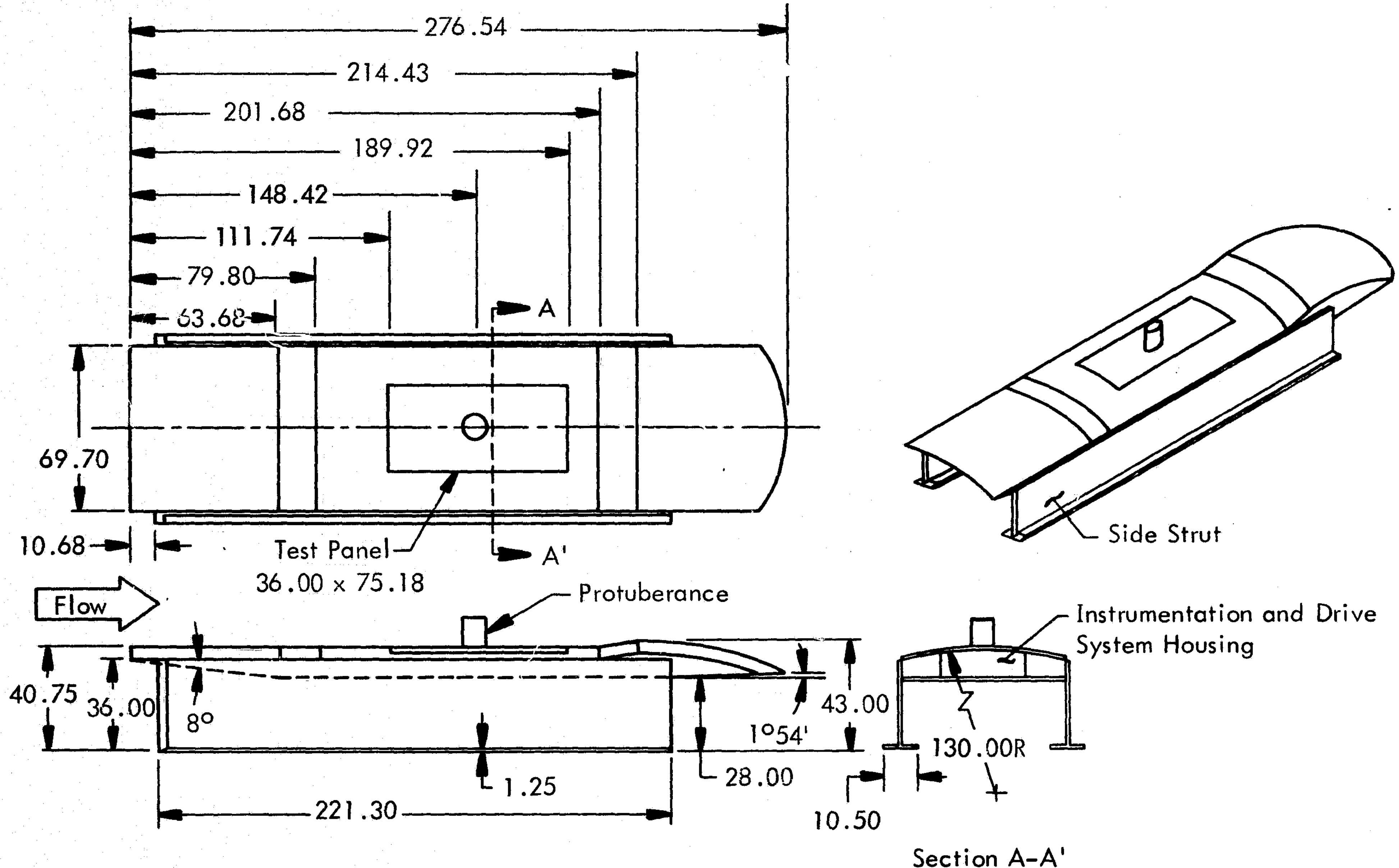

NOTE: Linear dimensions
in inches.

Figure 3. Details of the Test Article

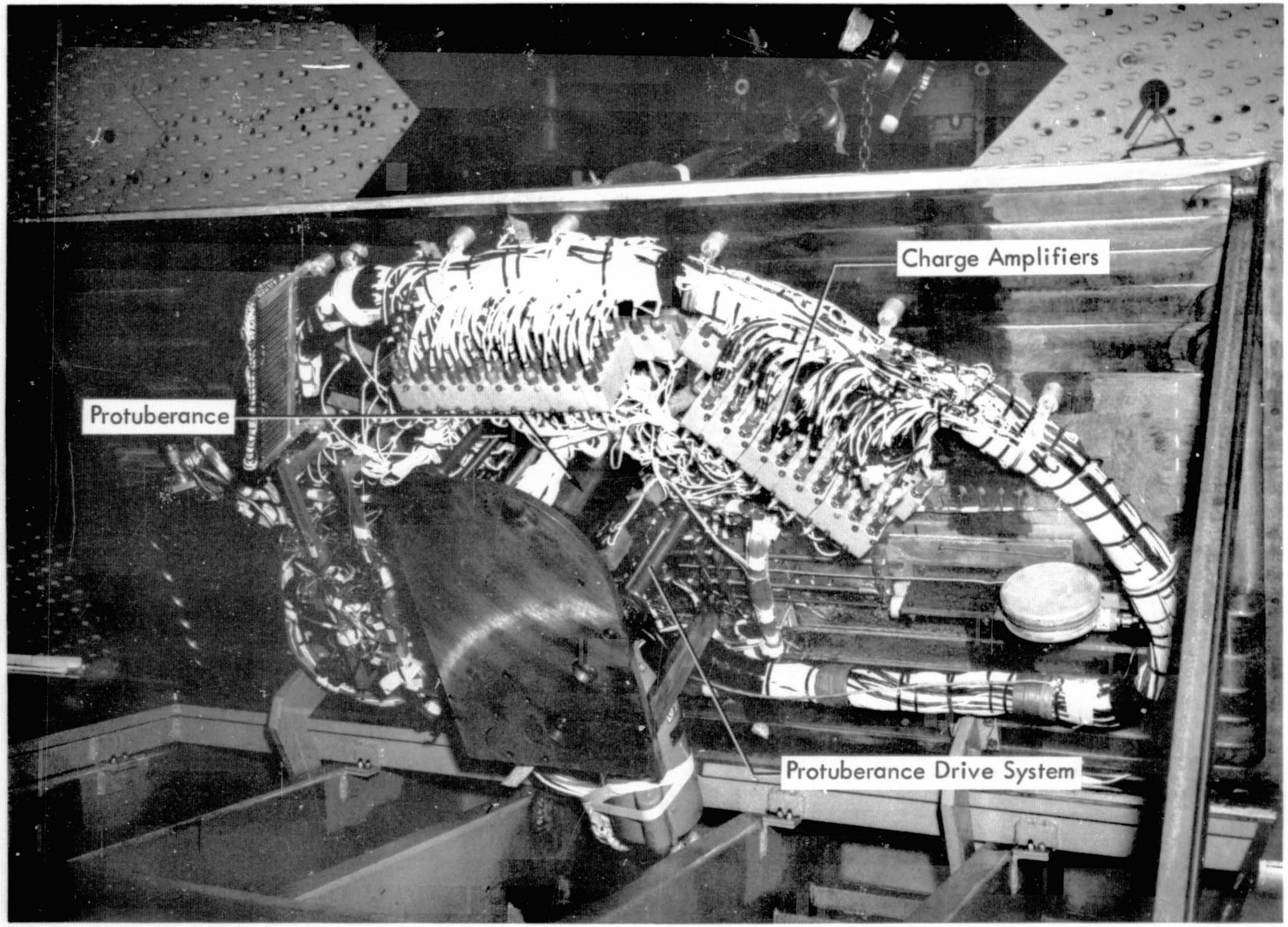

Figure 4. Photograph of the Protuberance Drive System and Instrumentation Supported Beneath the Test Panel

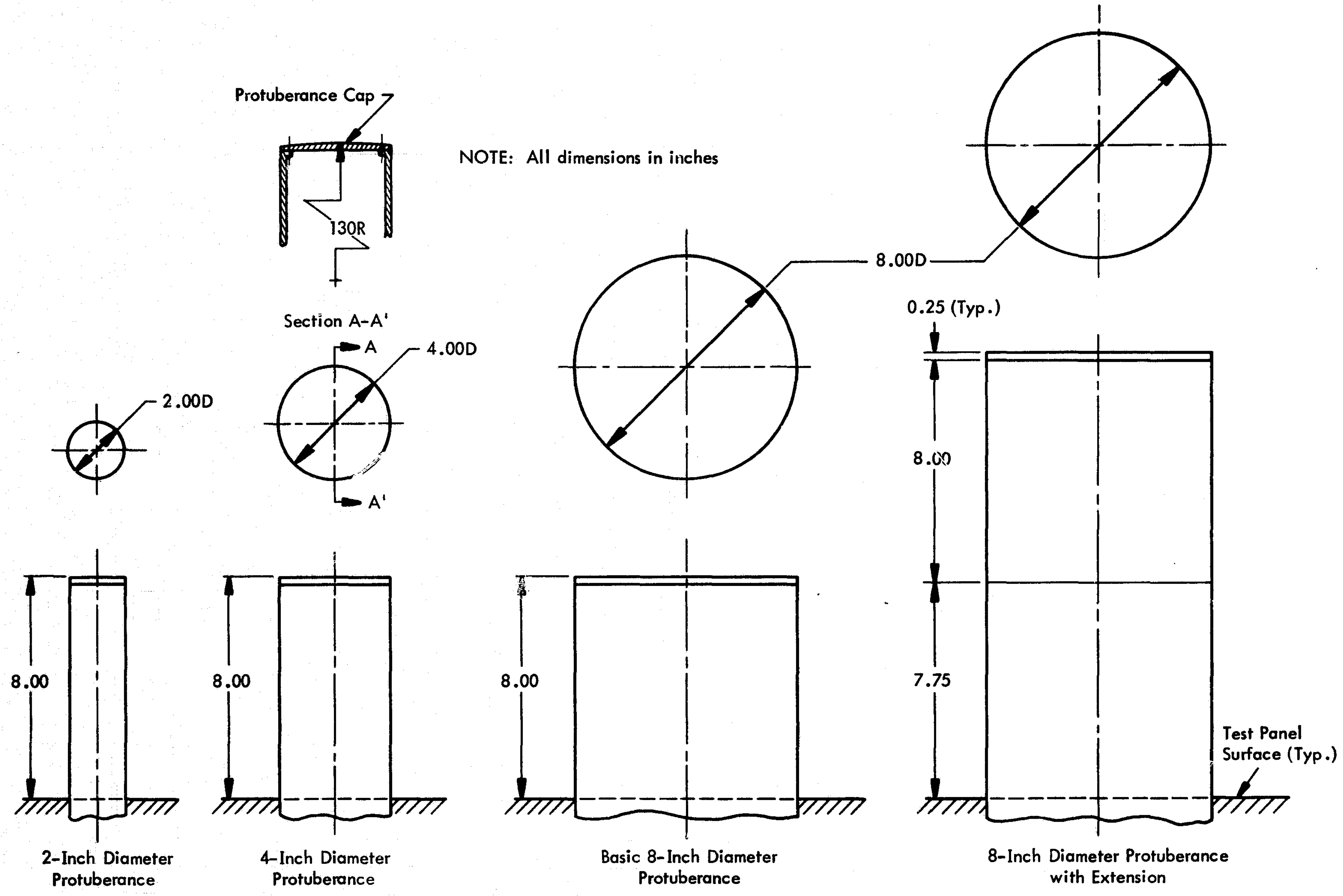

NOTE: All dimensions in inches

2-Inch Diameter Protuberance

4-Inch Diameter Protuberance

Basic 8-Inch Diameter Protuberance

8-Inch Diameter Protuberance with Extension

Figure 5. Details of the Cylindrical Protuberances

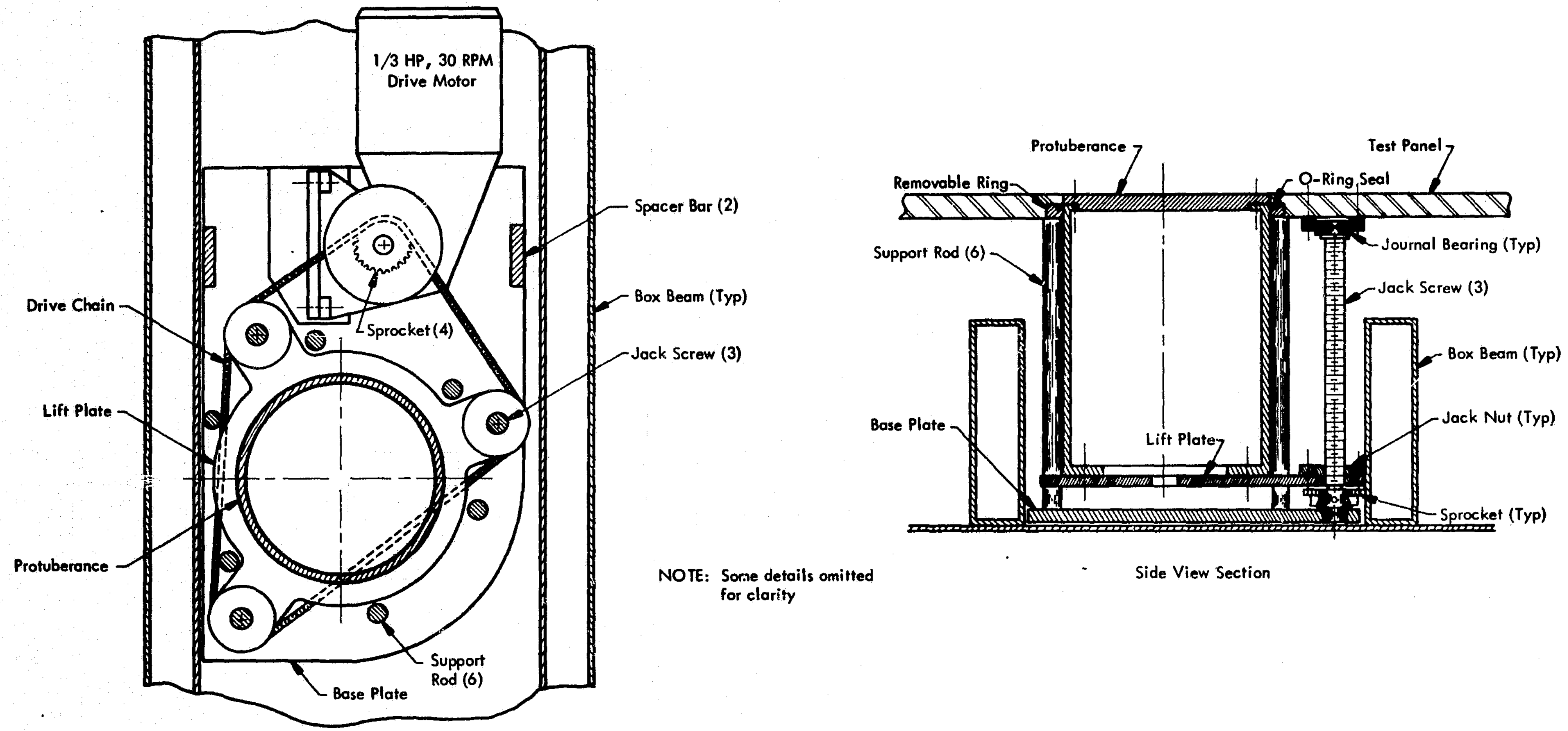

Top View Section

NOTE: Some details omitted for clarity

Side View Section

Figure 6. Details of the Cylindrical Protuberance Drive System

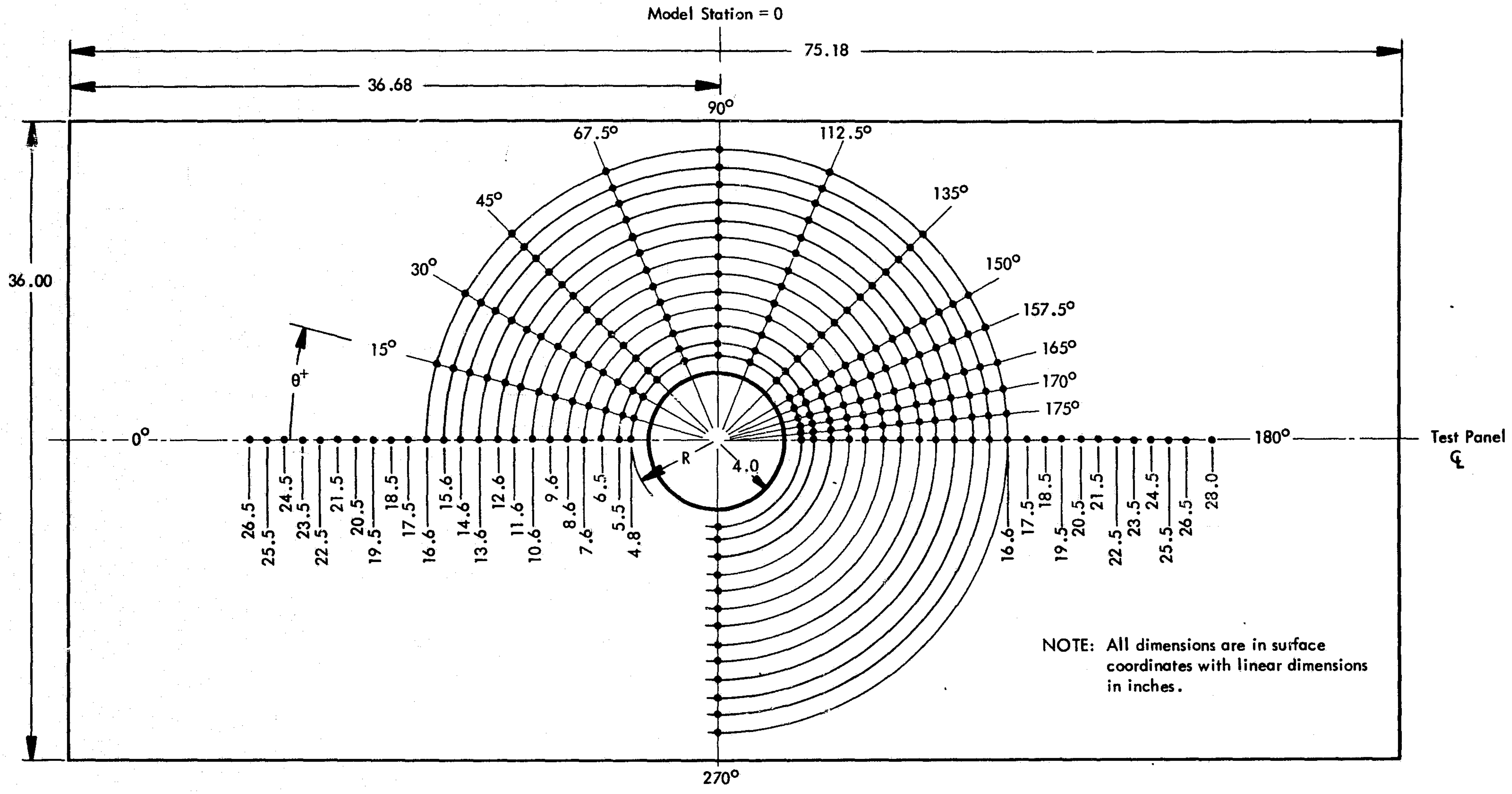

NOTE: All dimensions are in surface coordinates with linear dimensions in inches.

(a) Static Pressure Instrumentation

Figure 7. Instrumentation Location in the Test Panel

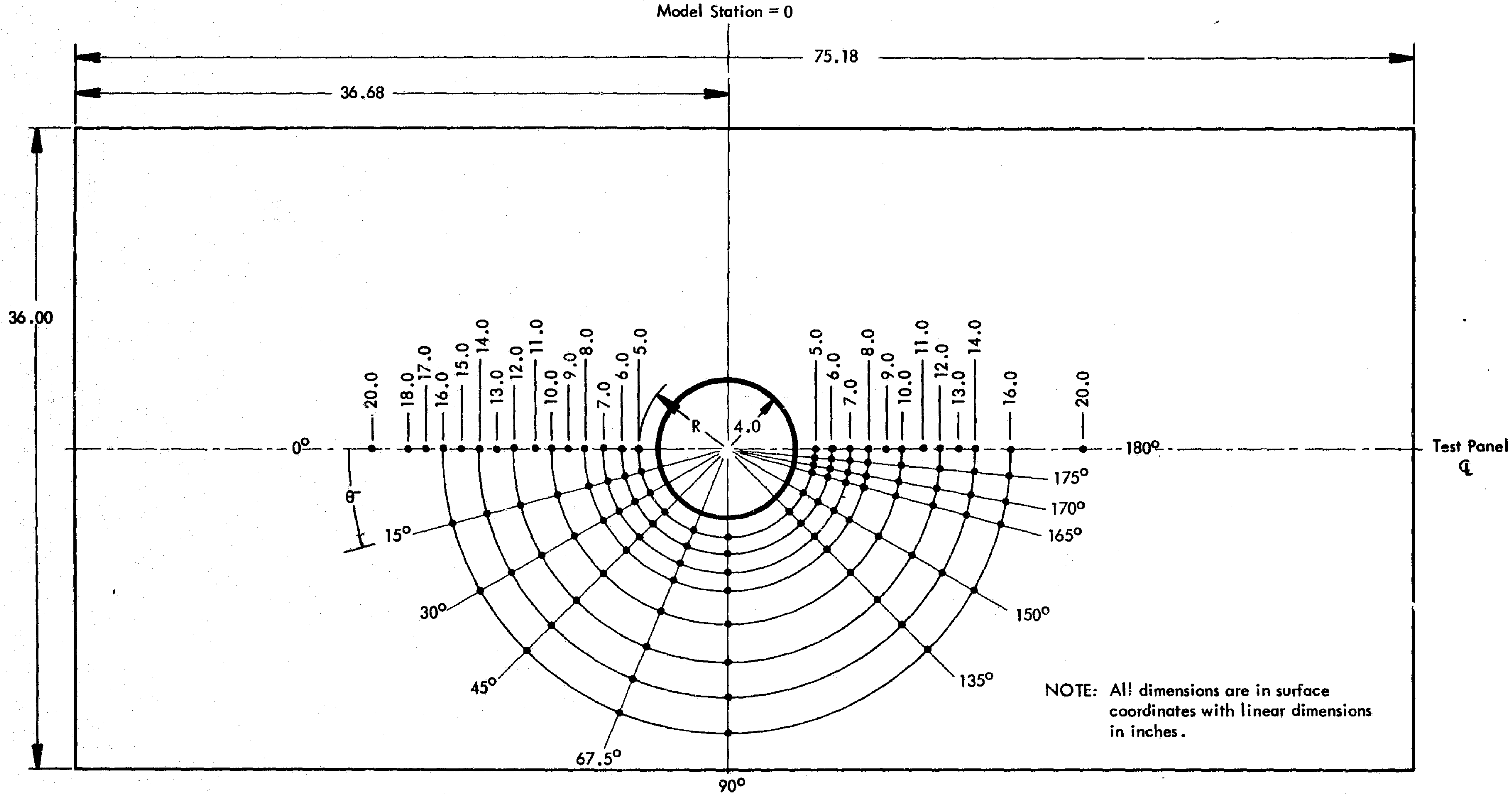

NOTE: All dimensions are in surface coordinates with linear dimensions in inches.

(b) Microphone Instrumentation

Figure 7. Concluded

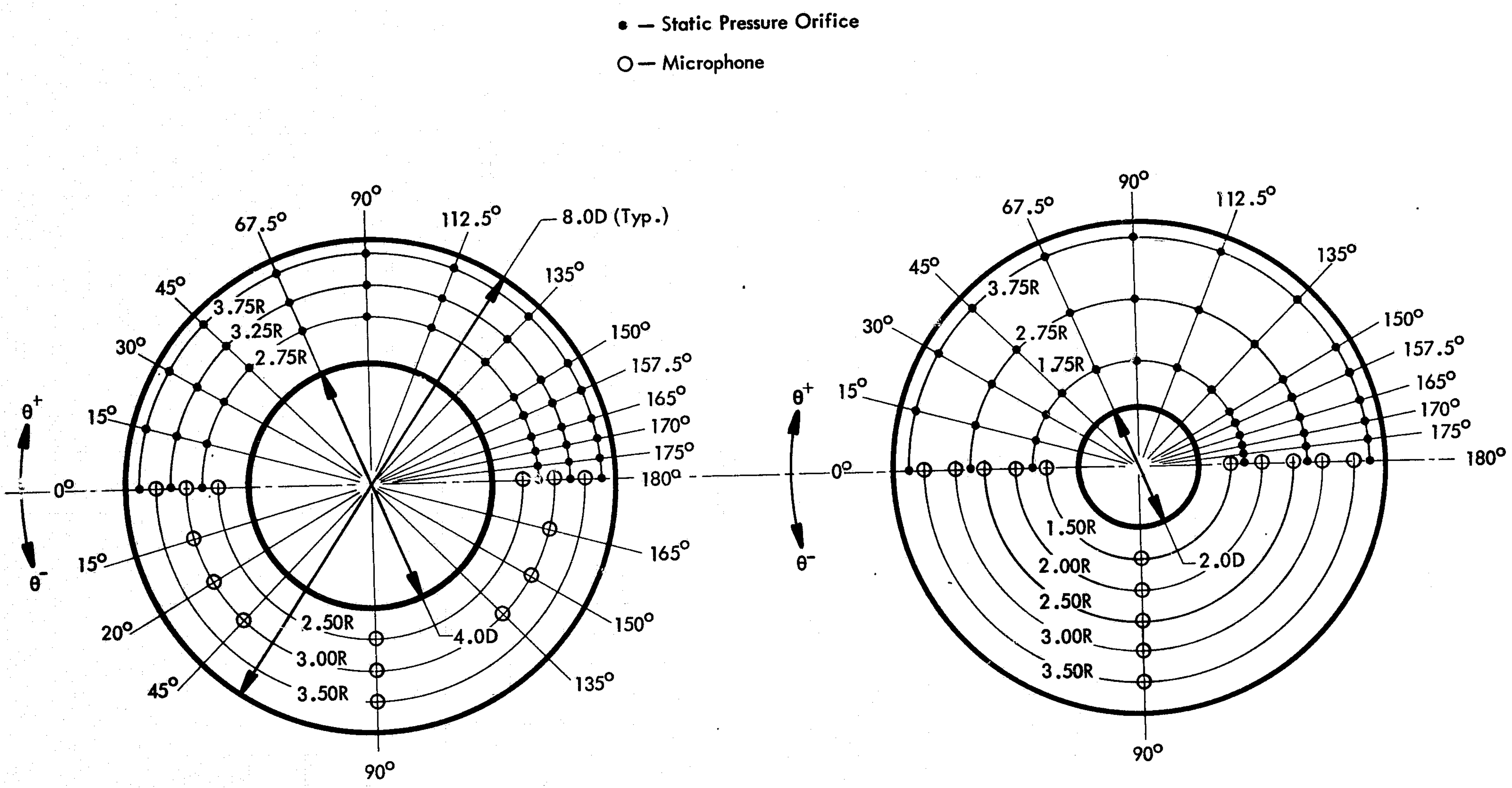

(a) Insert Plate for 4-Inch Diameter Protuberance

(b) Insert Plate for 2-Inch Diameter Protuberance

Figure 8. Instrumentation Locations in the Insert Panels

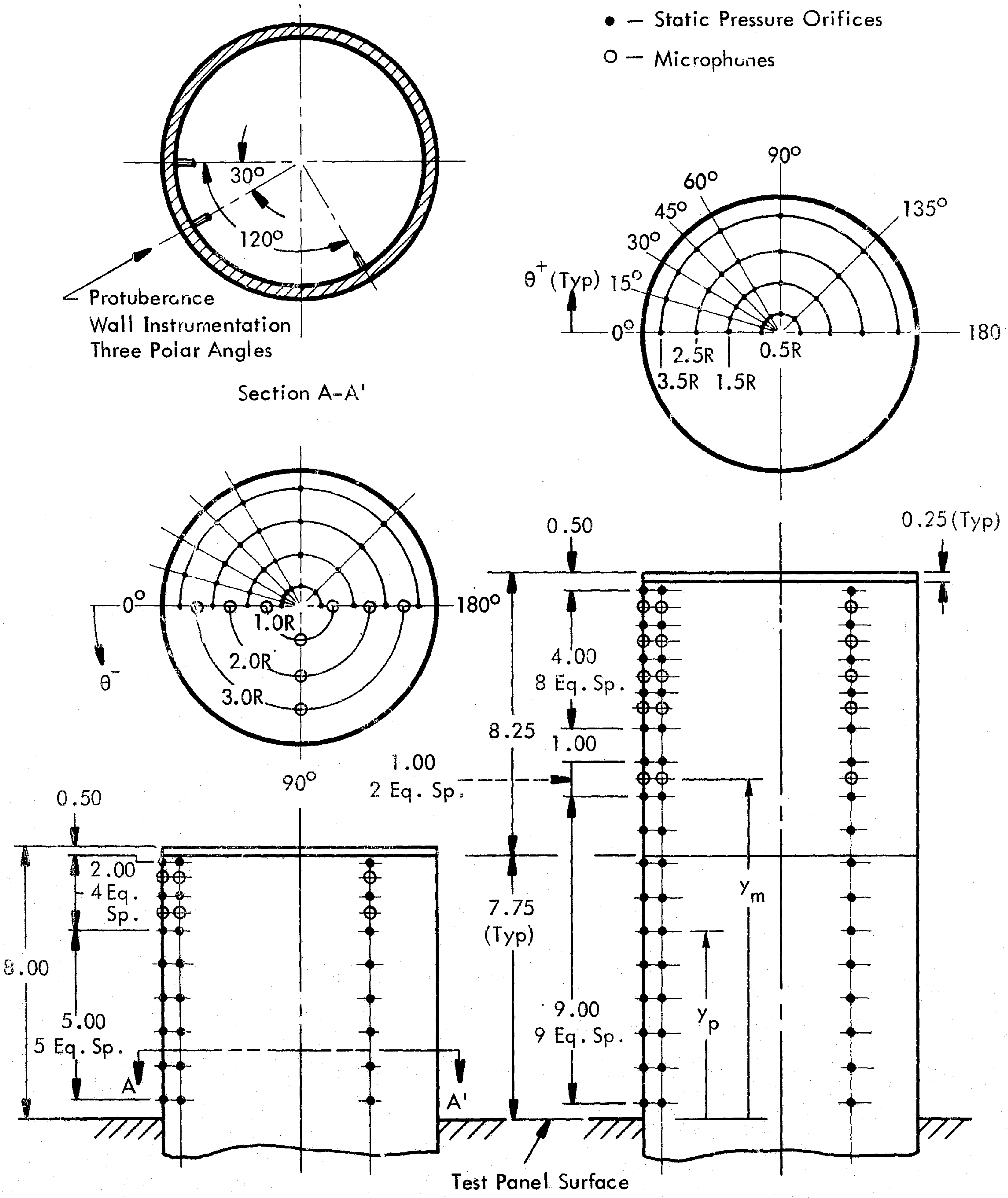

Basic 8-Inch Diameter Protuberance

8-Inch Diameter Protuberance with Extension

Figure 9. Instrumentation Location in the 8-Inch Diameter Protuberances

Probe	y
1	0.029
2	0.154
3	0.279
4	0.404
5	0.529
6	0.774
7	1.029
8	1.279
9	1.529
10	1.779
11	2.029
12	2.279
13	2.539
14	2.779
15	3.029

NOTE: Linear dimensions in inches.

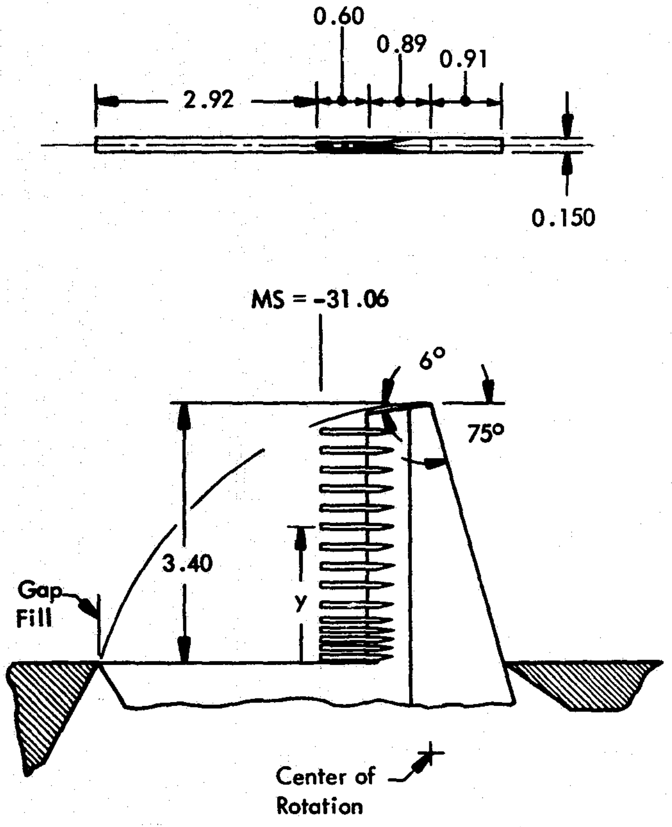

FORWARD RAKE

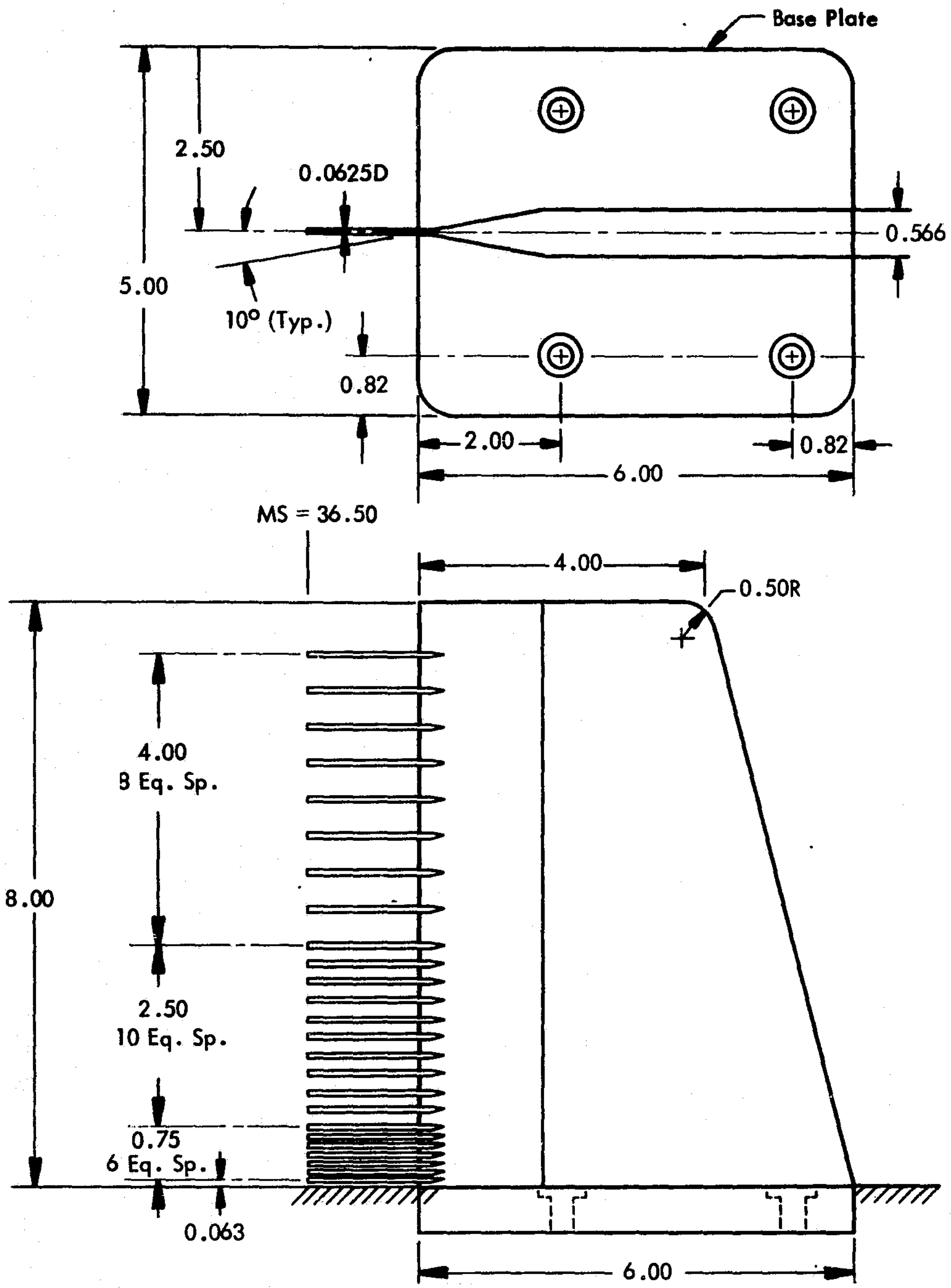

AFT RAKE

Figure 10. Details of the Boundary Layer Profile Rakes

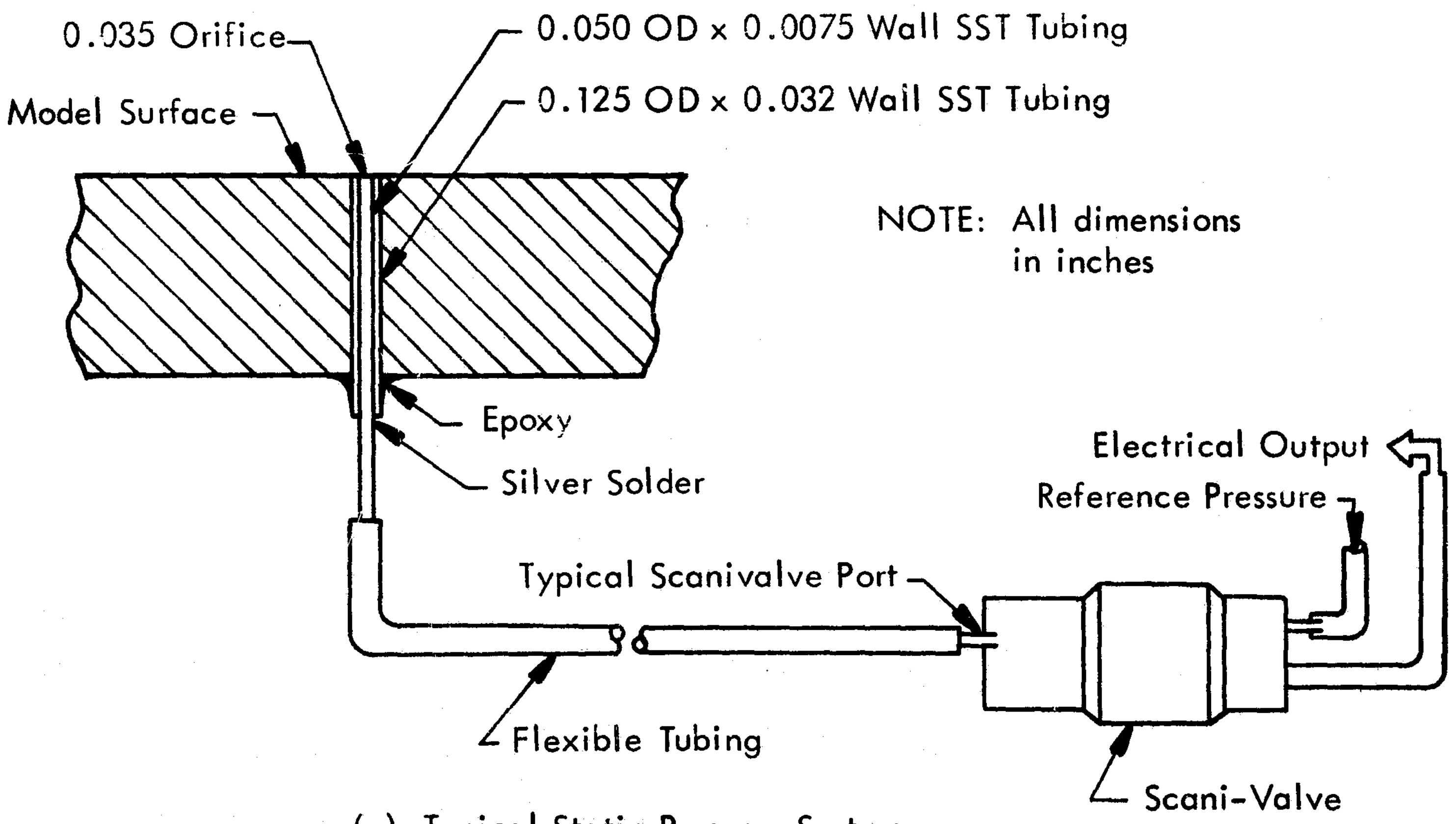

(a) Typical Static Pressure System

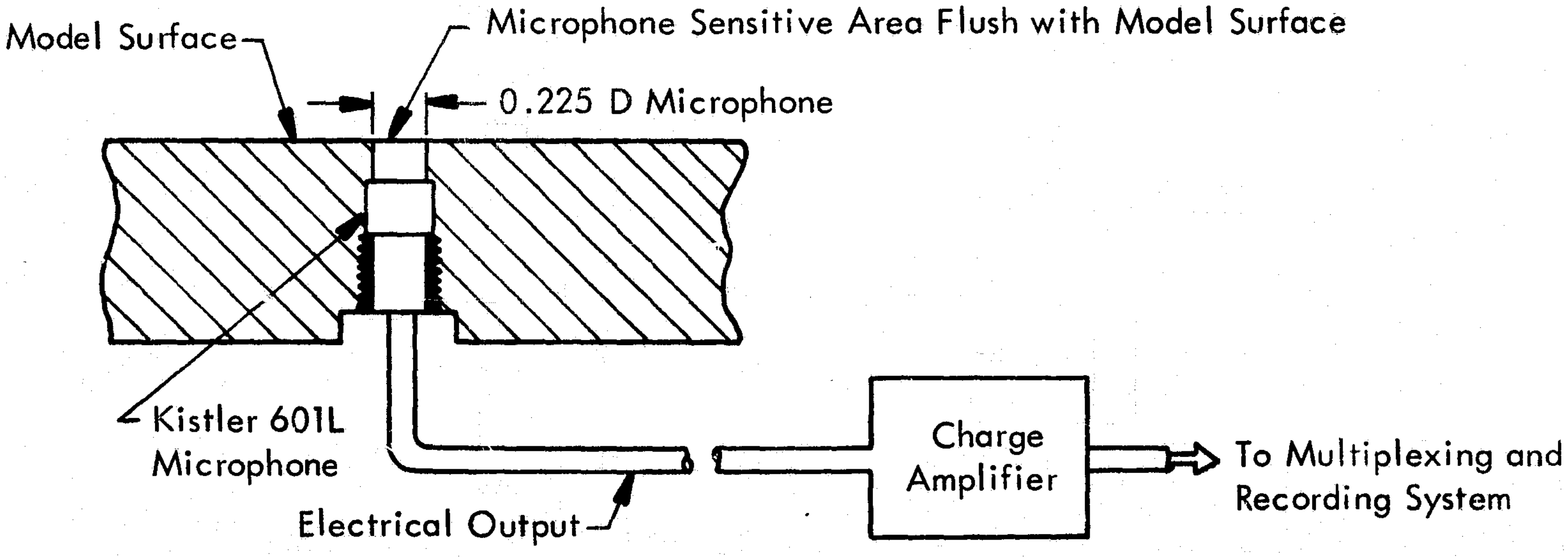

(b) Typical Microphone System

Figure 11. Details of Static Pressure and Microphone Systems

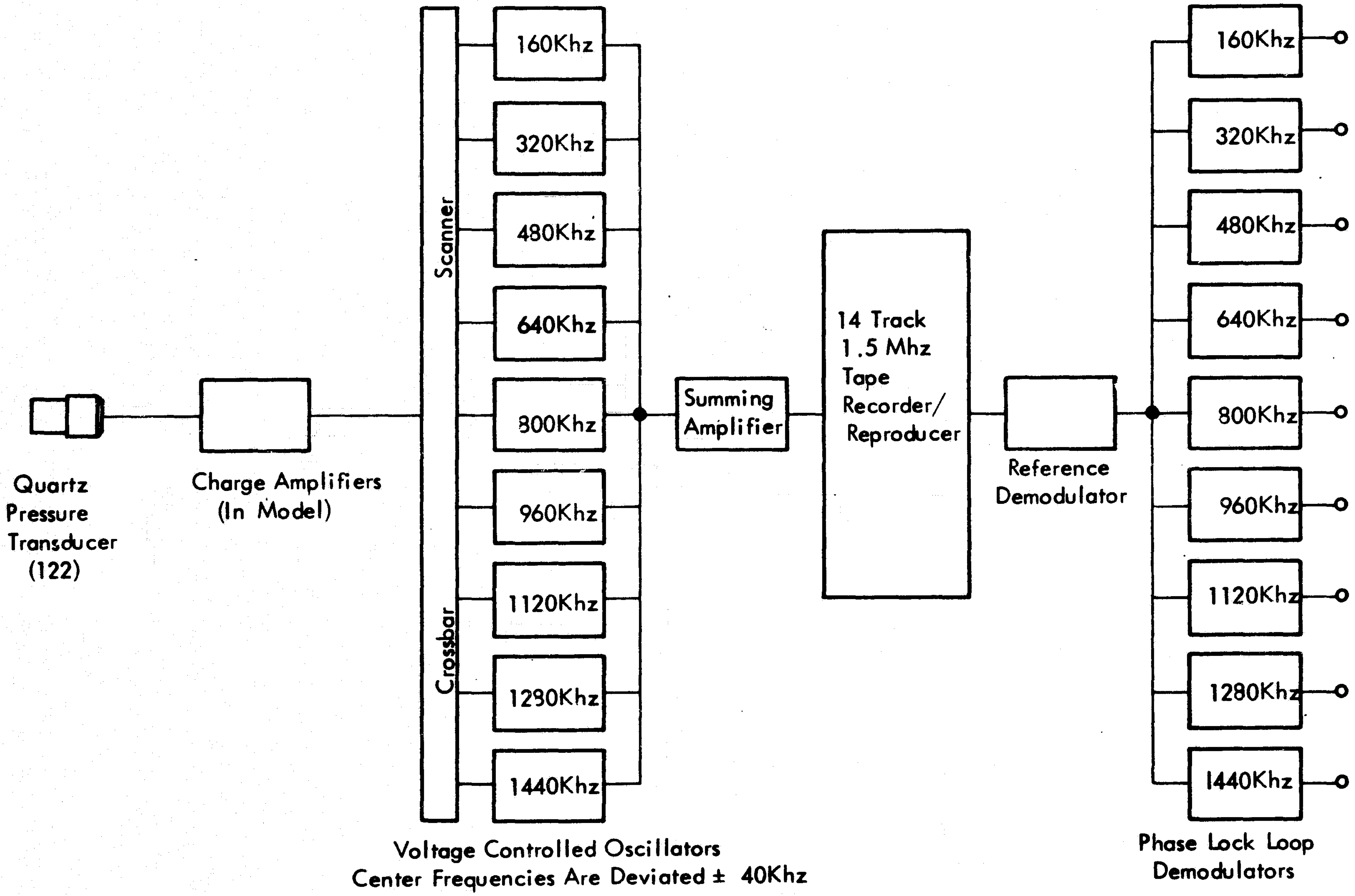

Figure 12. Block Diagram of Acoustic Recording System

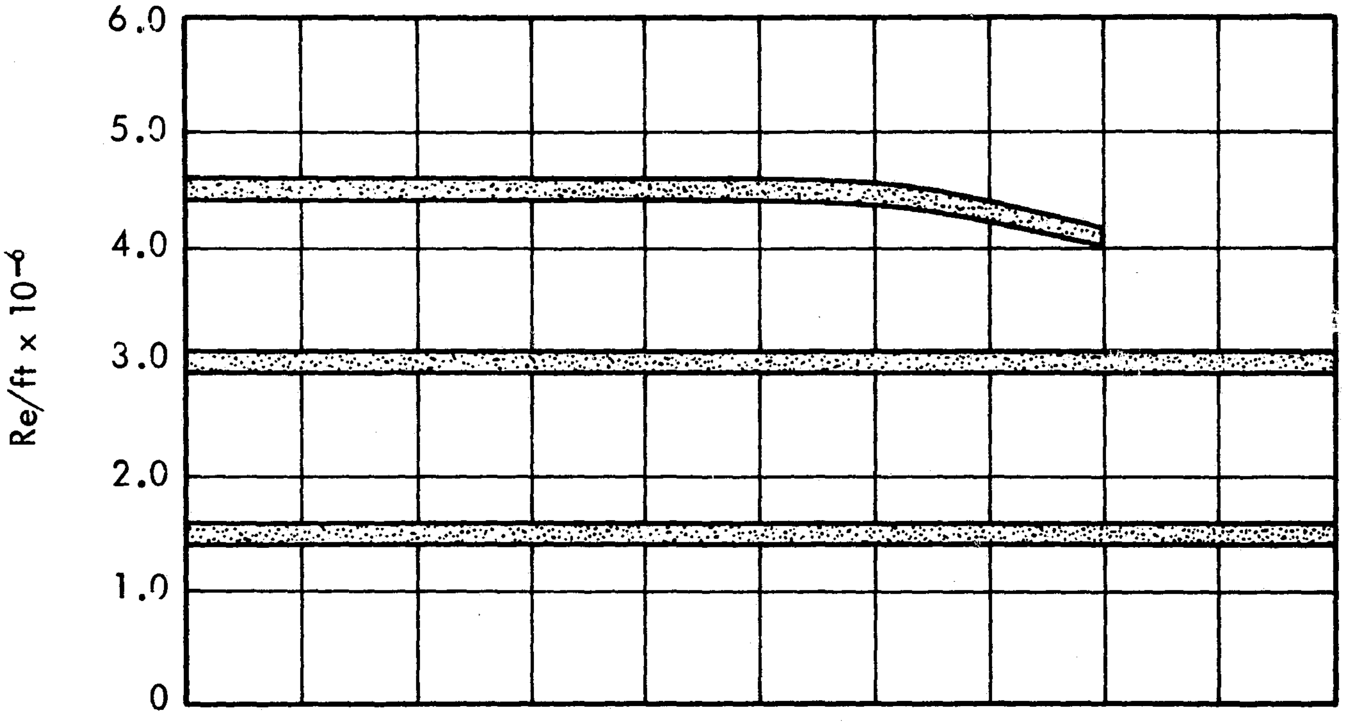

a. Unit Reynolds Number

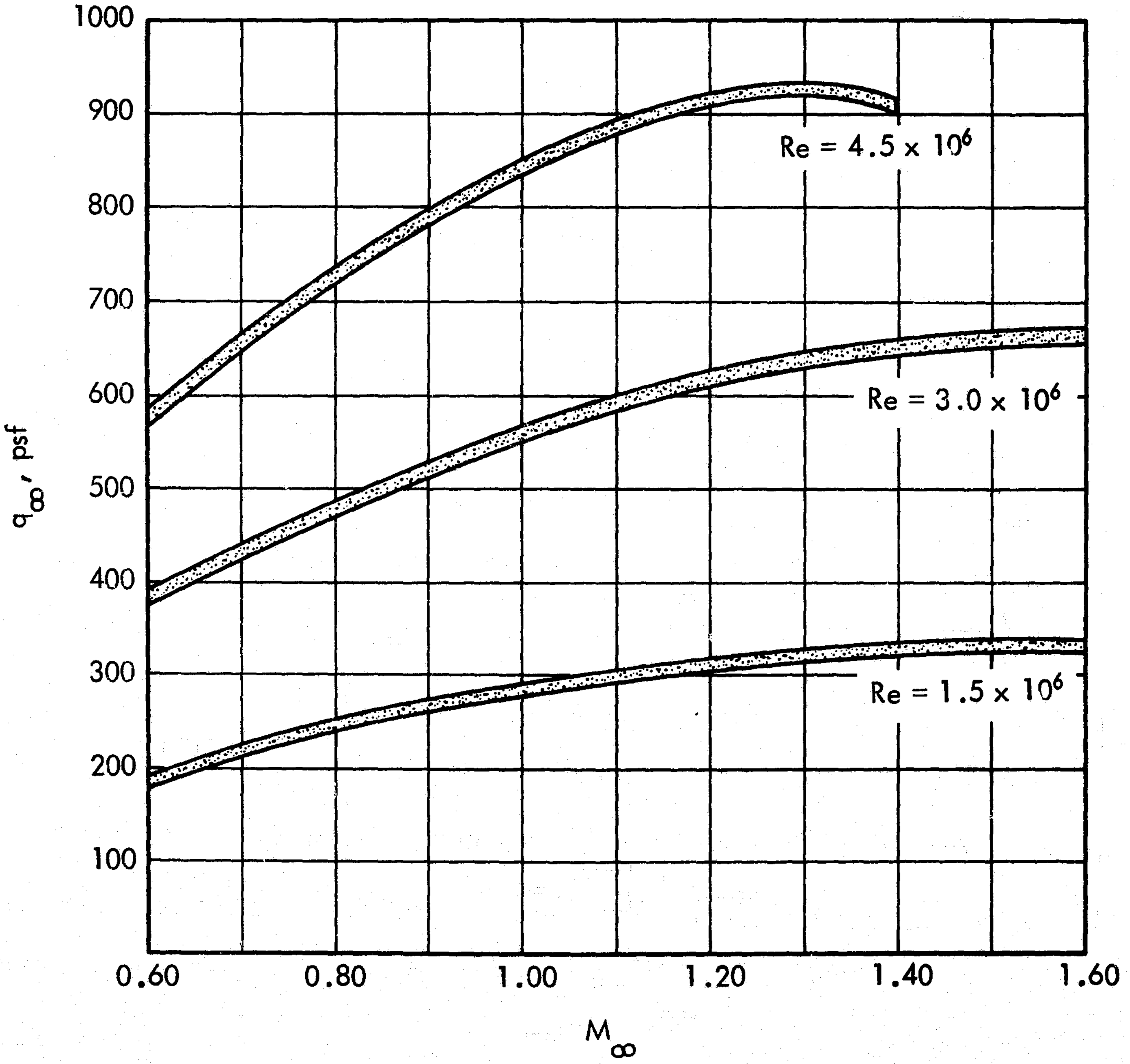

b. Dynamic Pressure

Figure 13. Variations of Unit Reynolds Number and Dynamic Pressure With Free-Stream Mach Number

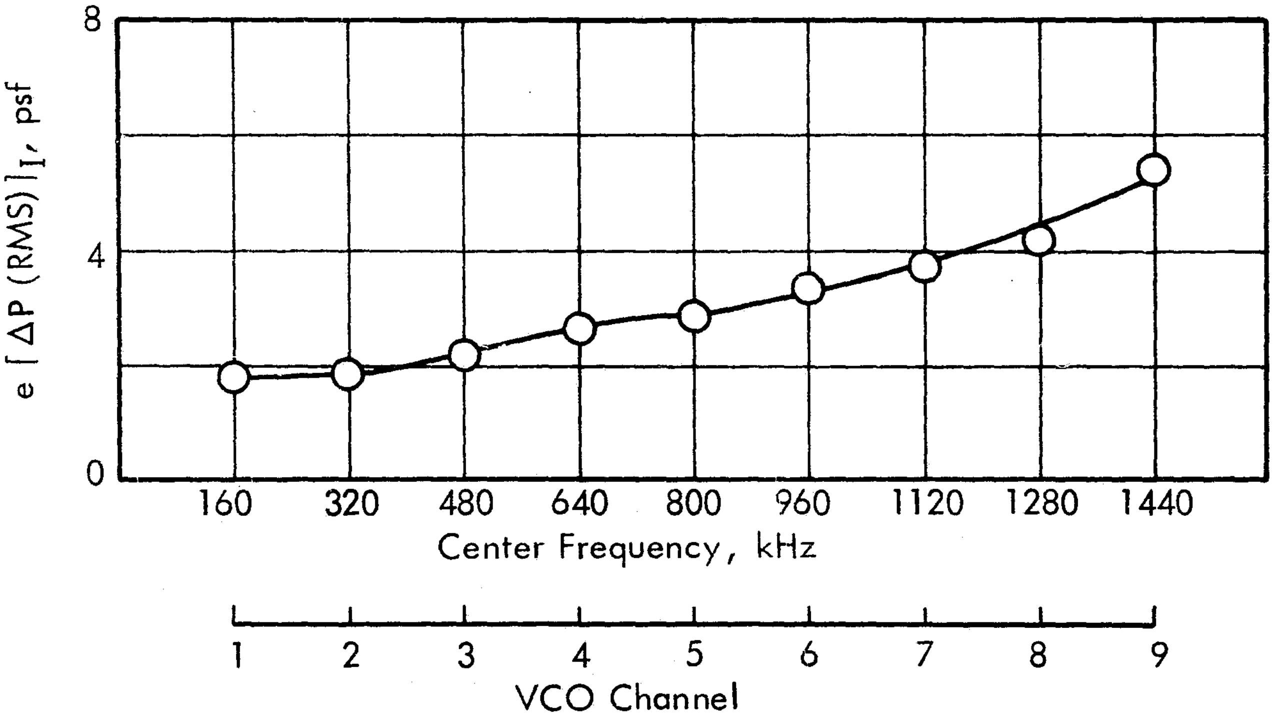

a. Overall Level

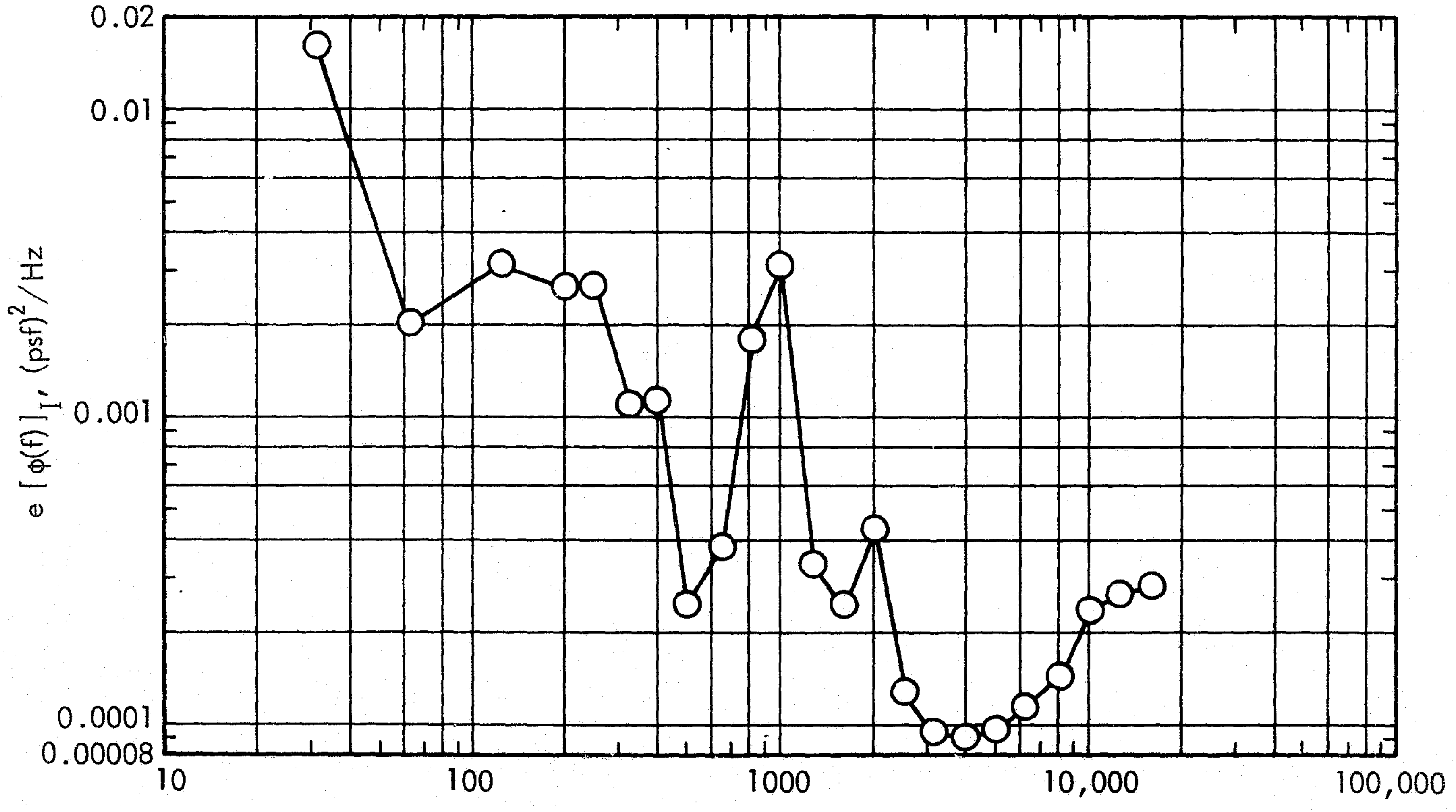

b. Mean Power Spectra

Figure 14. Characteristics of the Instrumentation System Noise

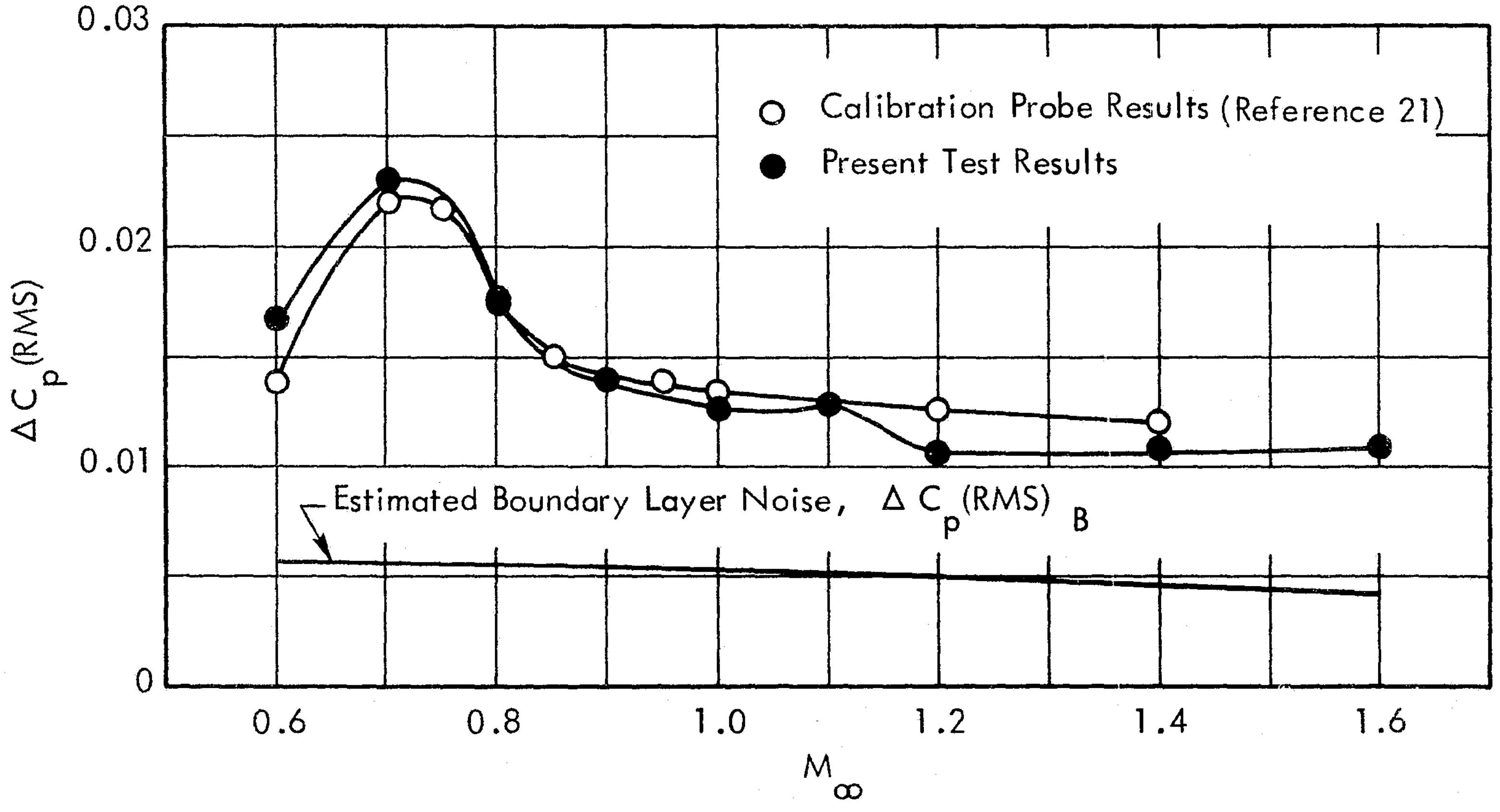

a. Undisturbed Flow Environments

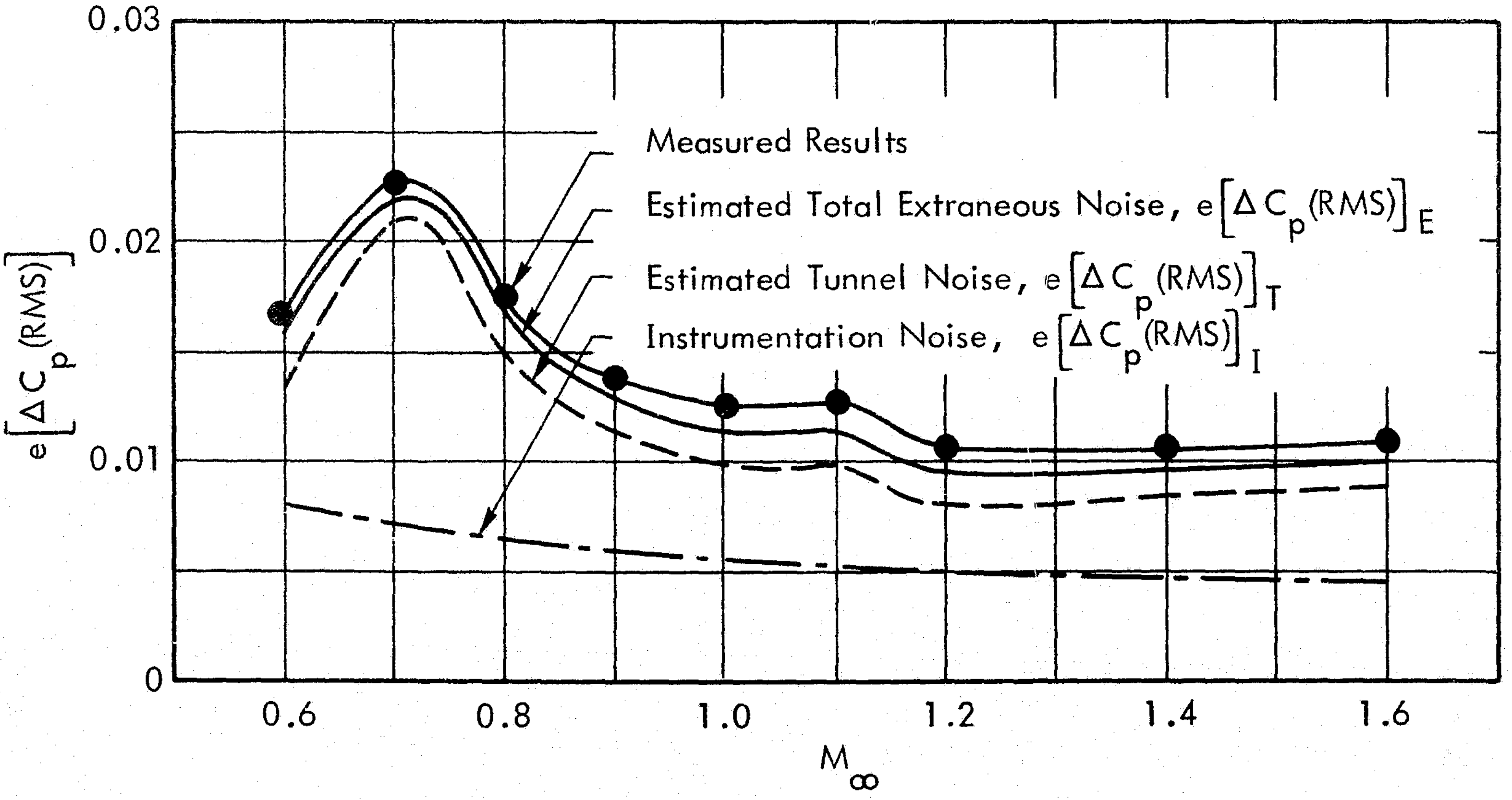

b. Extraneous Noise Contributions

Figure 15. Characteristics of the RMS Fluctuating Pressure Coefficient for the Undisturbed Flow Environments Showing the Contributing Sources

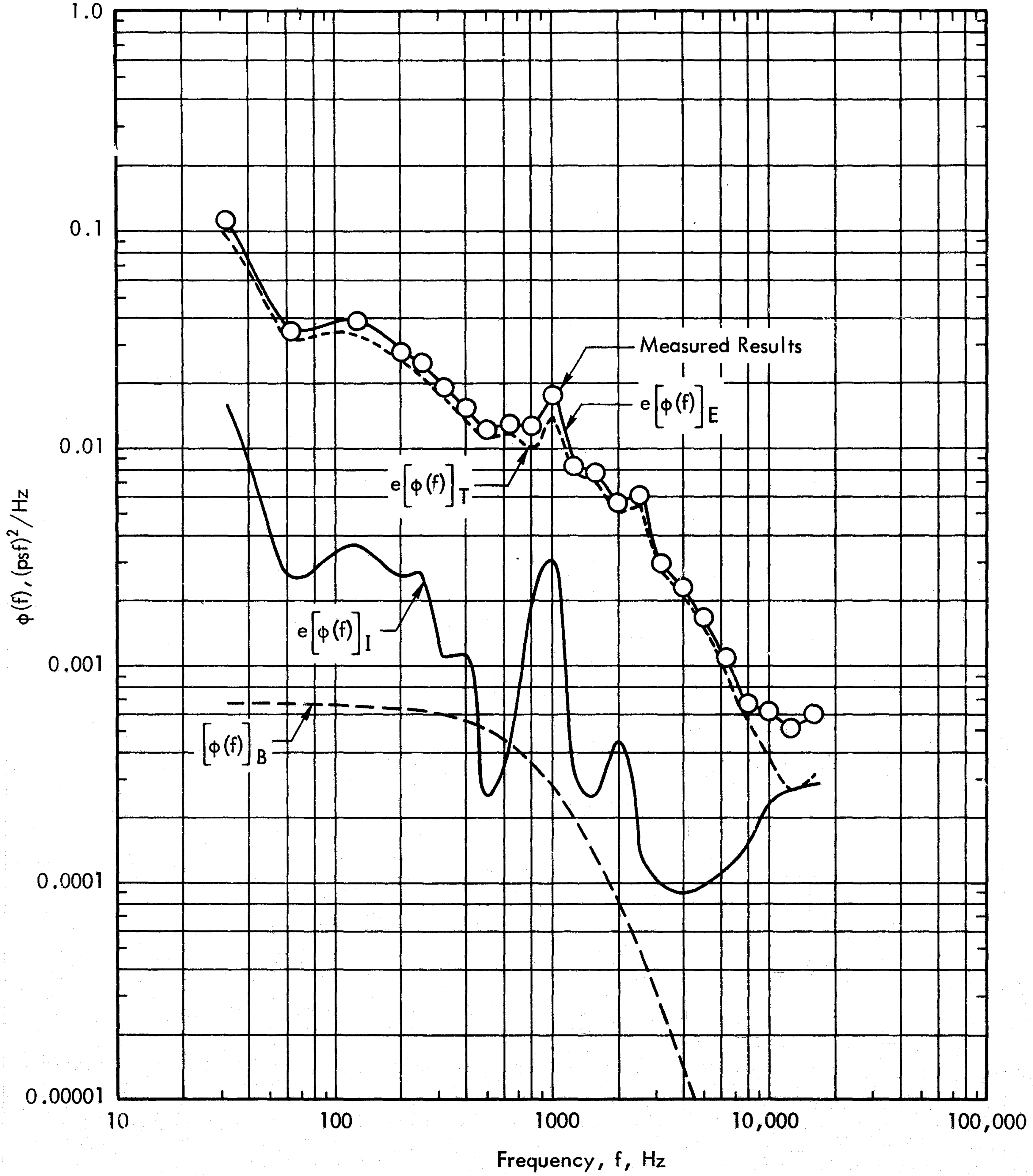

a. $M_\infty = 0.60$

Figure 16. Characteristics of the Power Spectra for the Undisturbed Flow Environments Showing the Contributing Sources

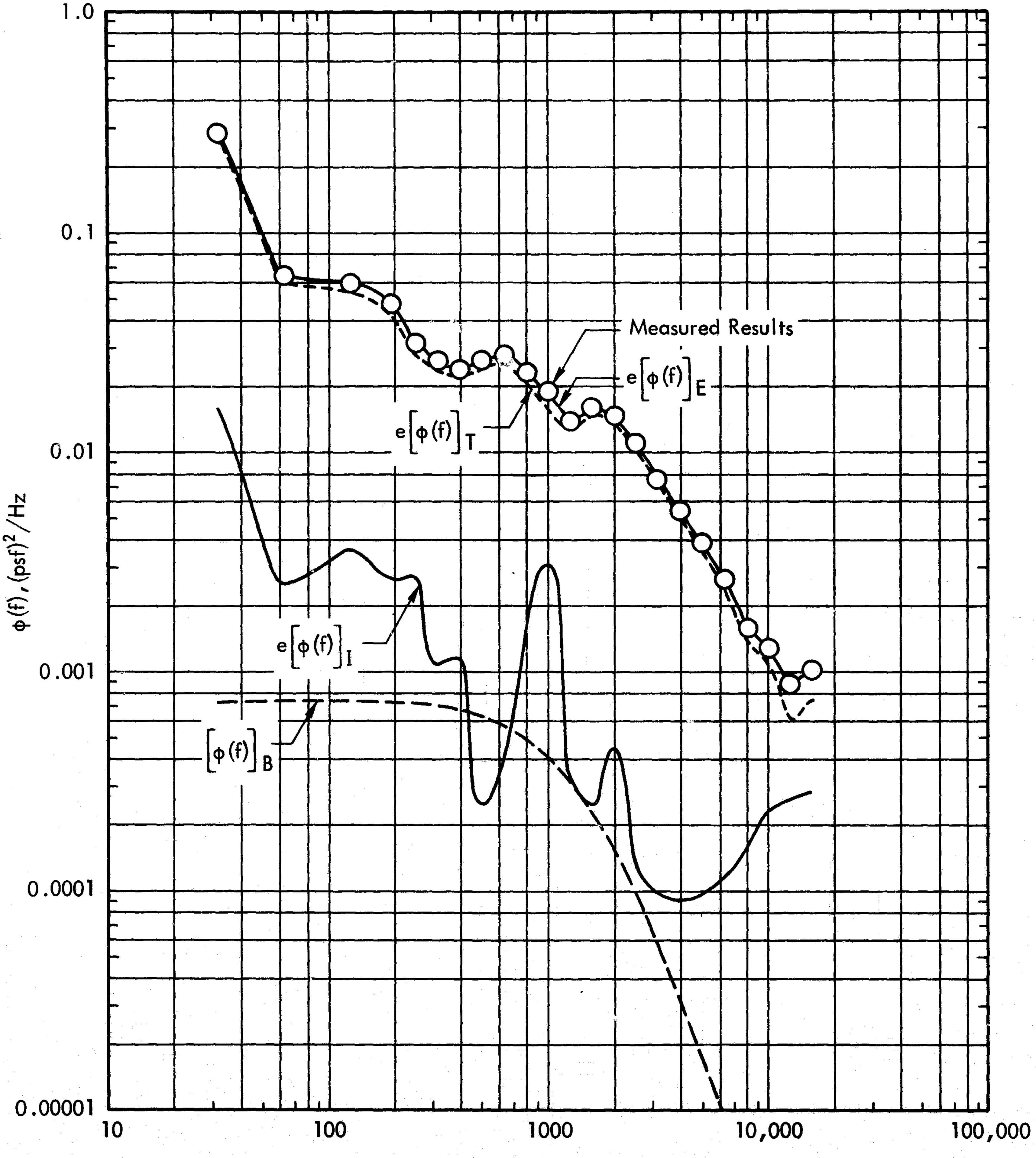

b. $M_\infty = 0.80$

Figure 16. Continued

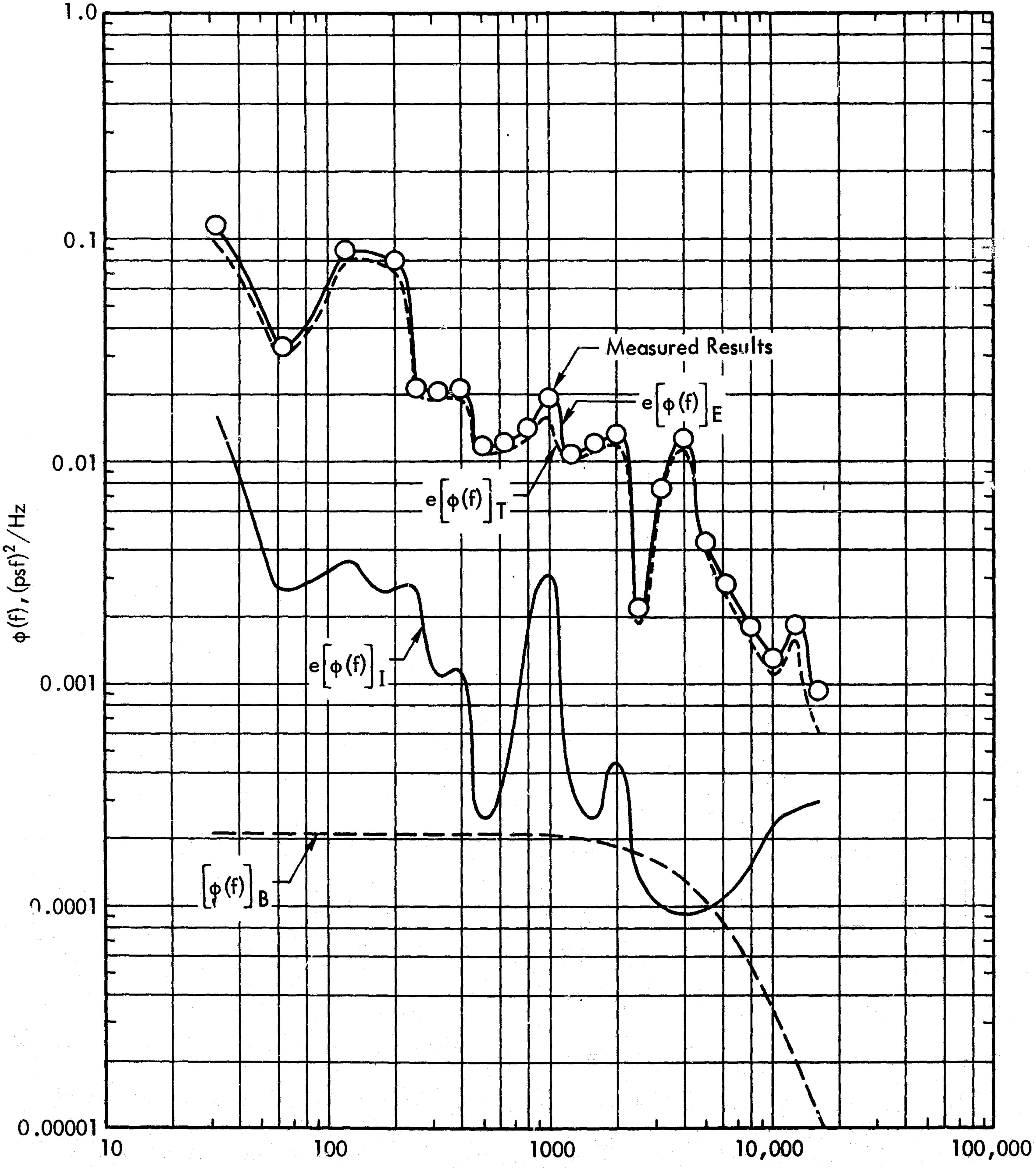

c. $M_\infty = 1.00$

Figure 16. Continued

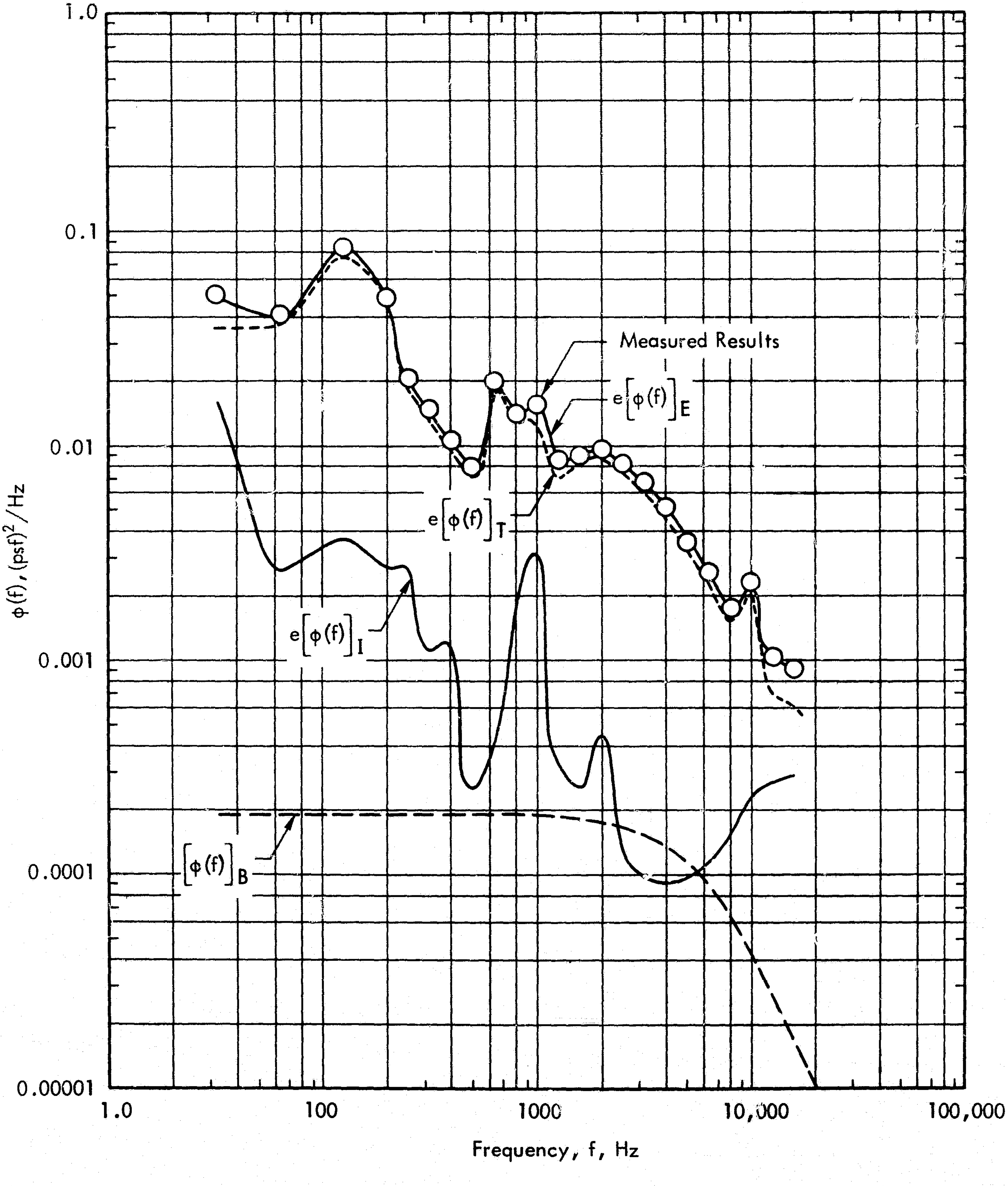

d. $M_\infty = 1.20$

Figure 16. Continued

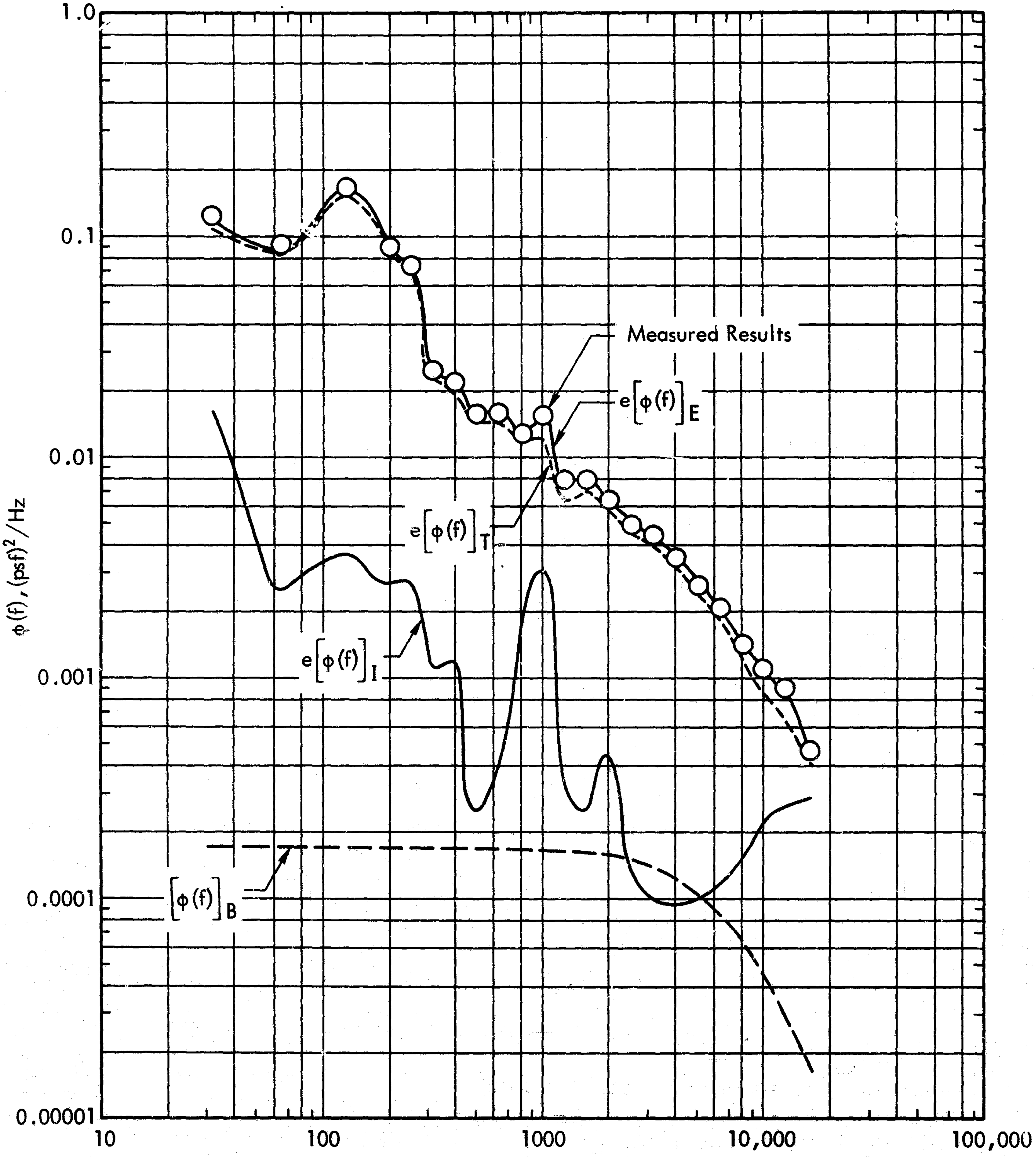

e. $M_\infty = 1.40$

Figure 16. Continued

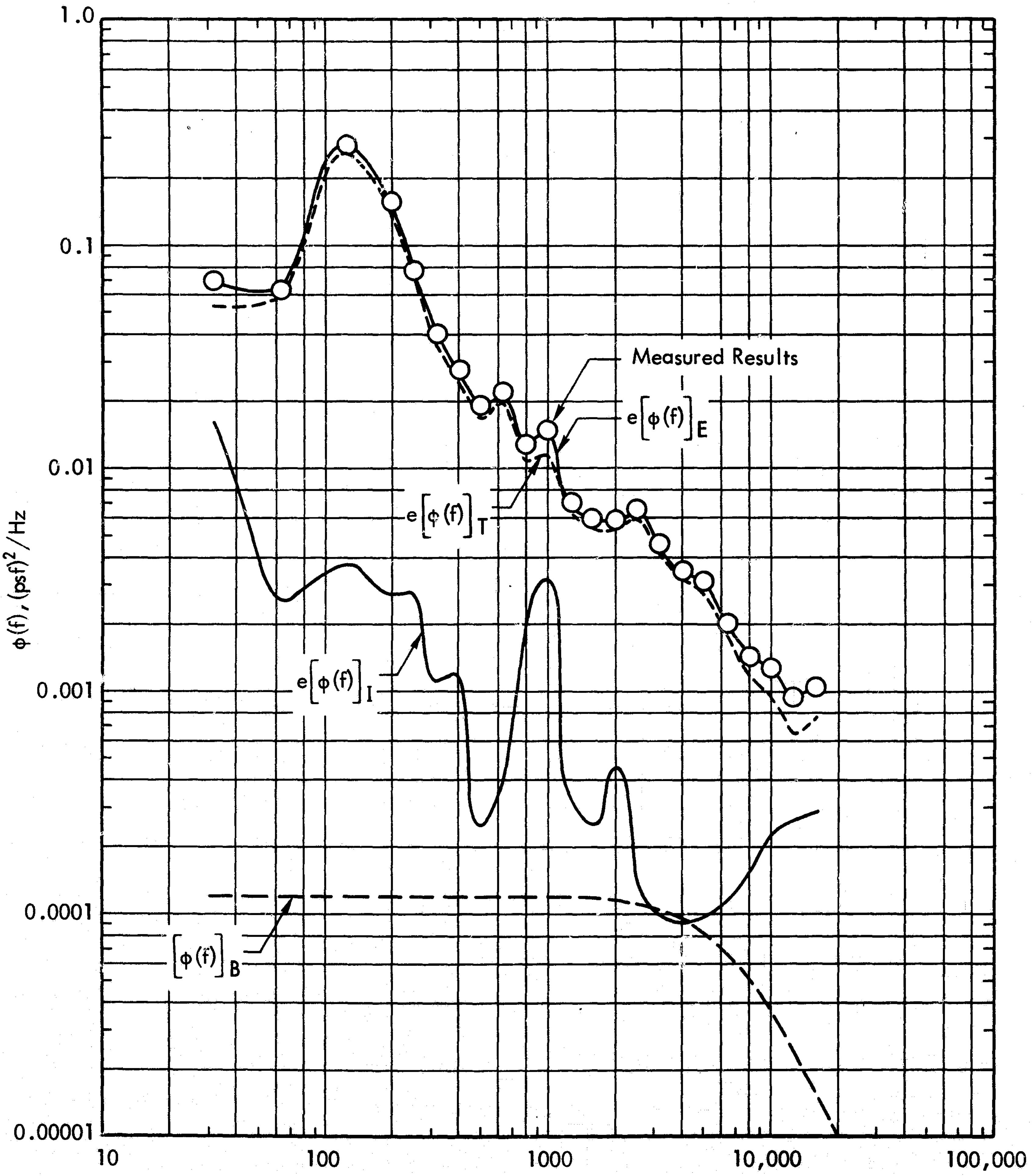

f. $M_\infty = 1.60$

Figure 16. Concluded

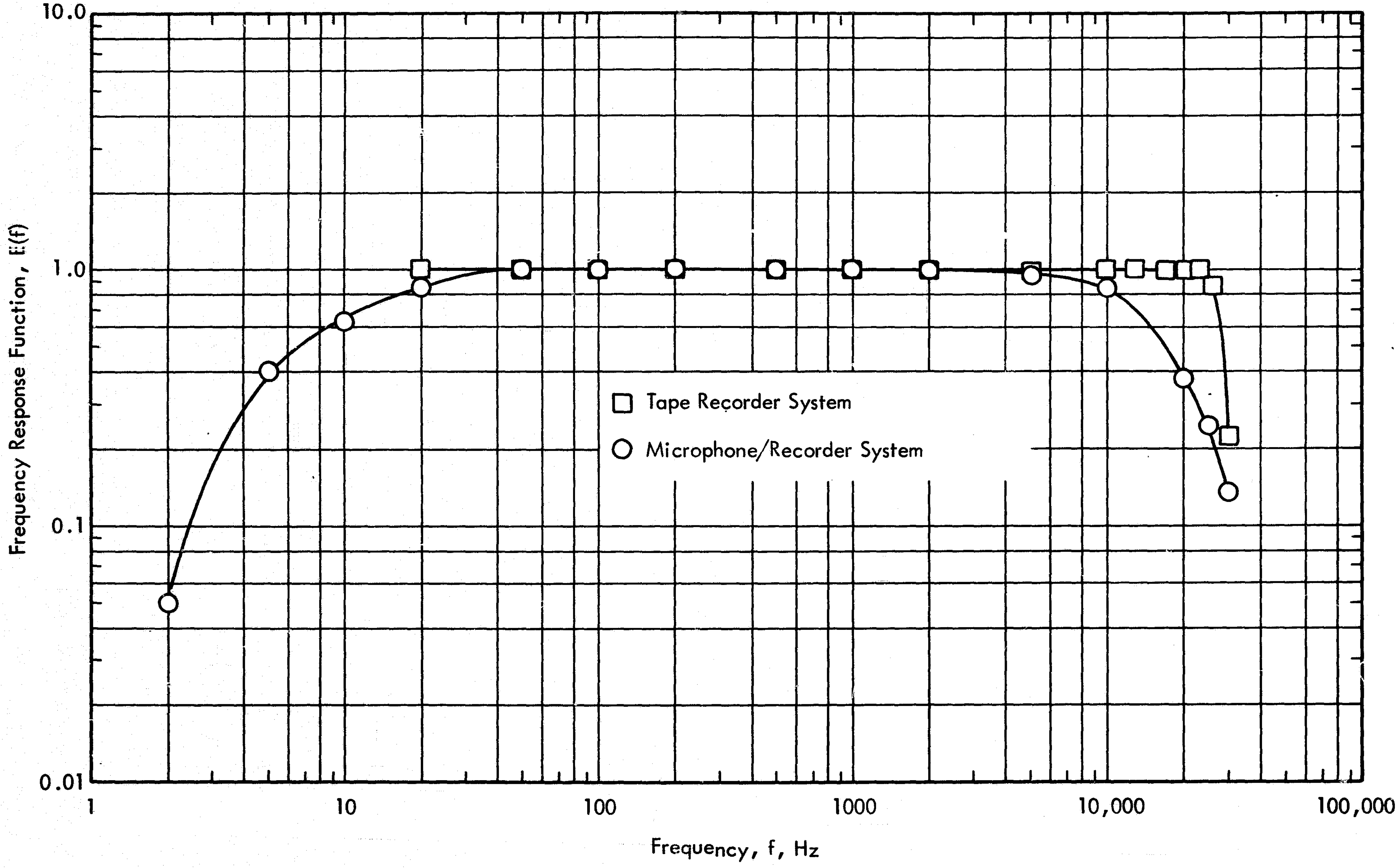

Figure 17. Frequency Response Characteristics of the Microphone/Data Acquisition System Electronics

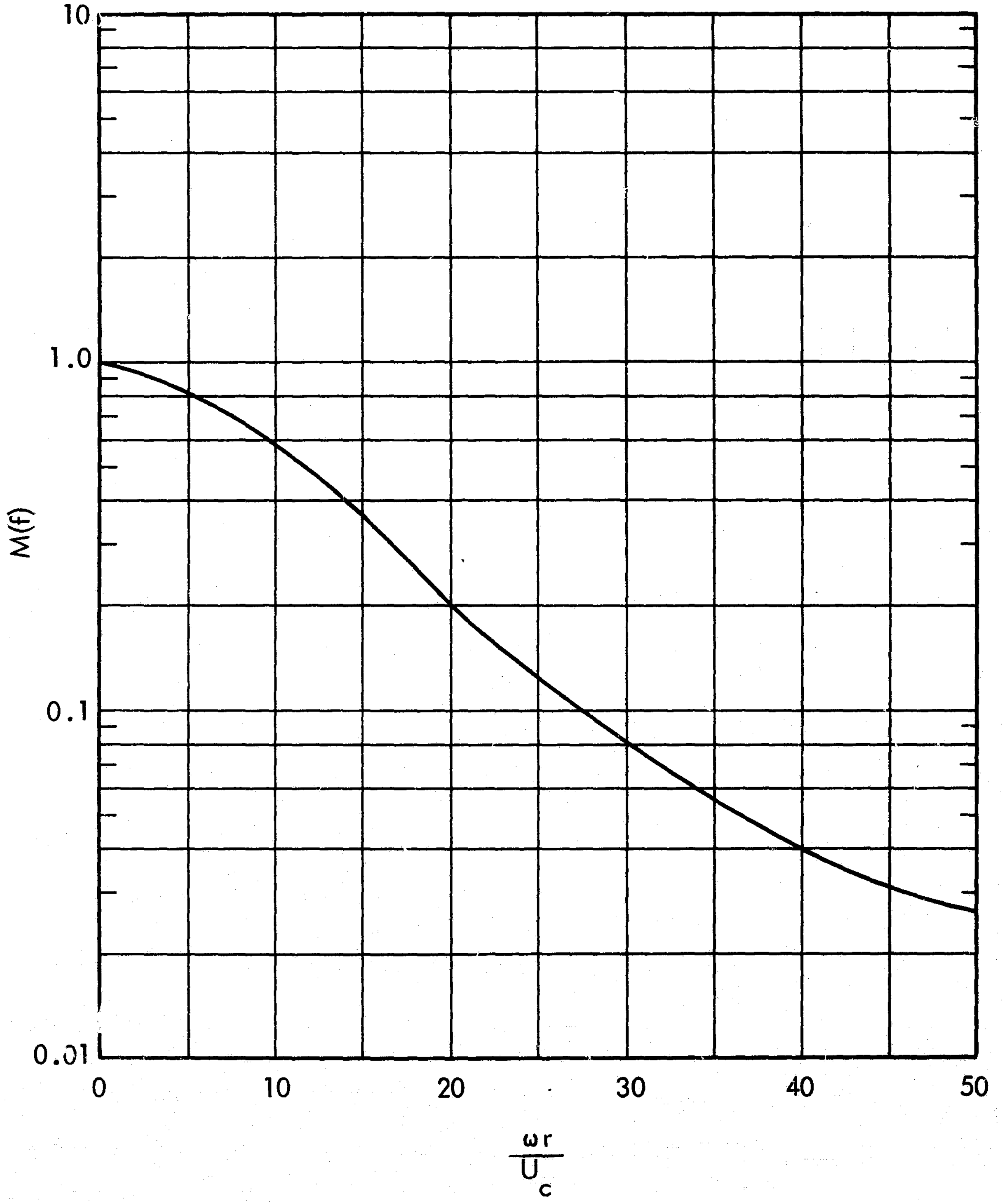

Figure 18. Estimated Frequency Response Characteristics Associated with the Effect of a Finite Microphone Size for the Three-Dimensional Protuberance Flow Field

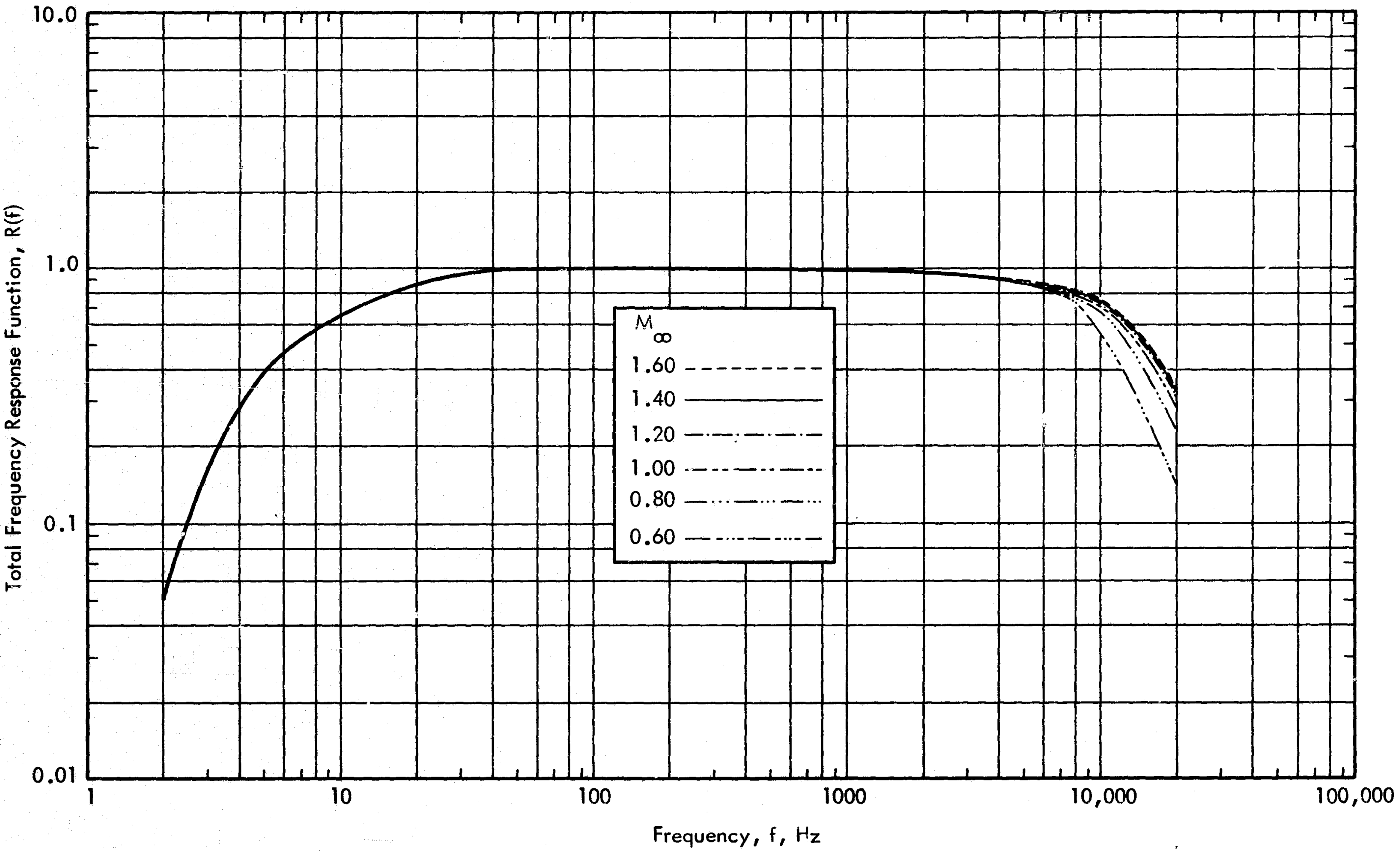

Figure 19. Estimated Overall Frequency Response Characteristics of the Instrumentation System

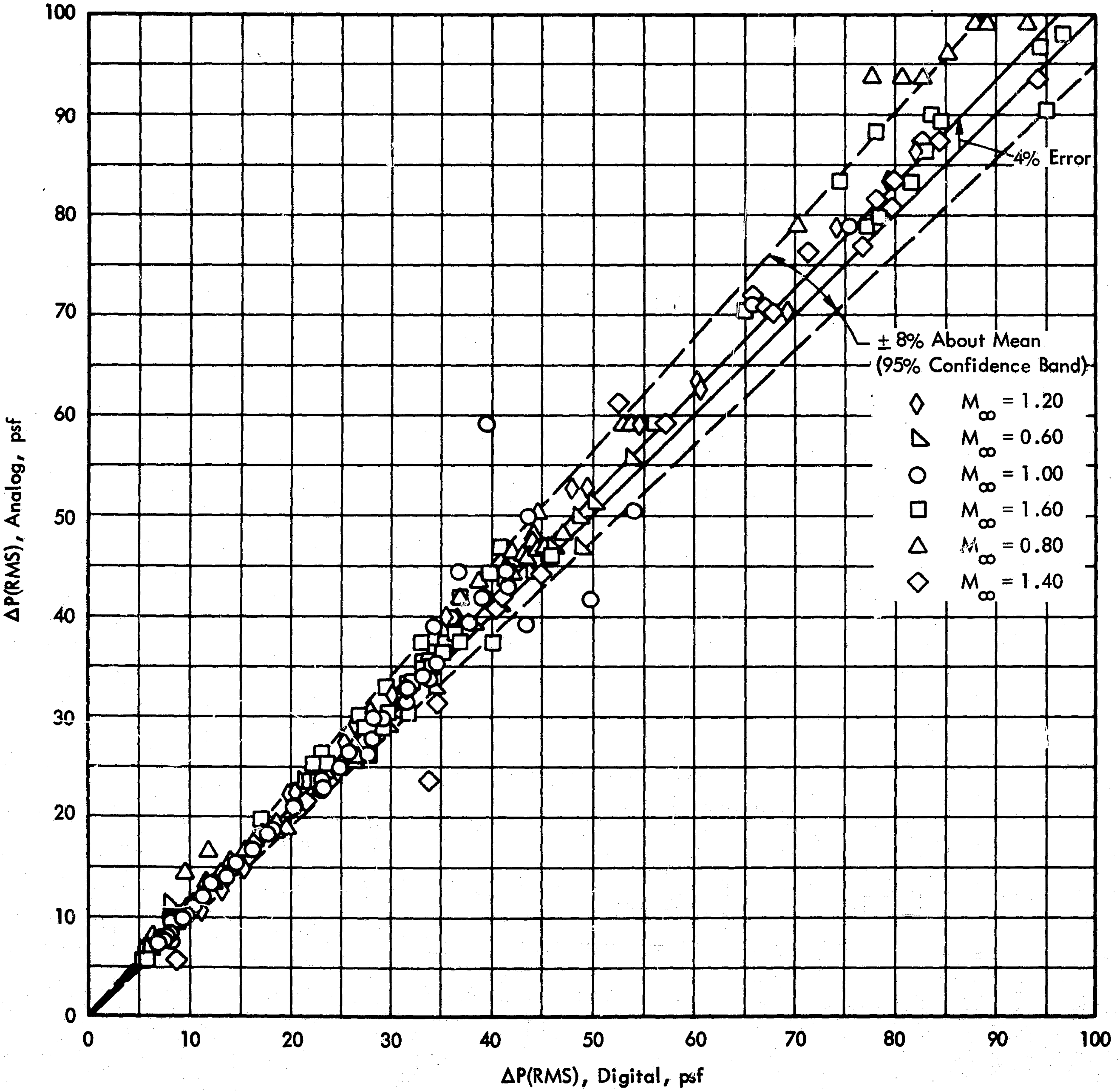

Figure 20. Comparison of the Analog and Digital Computations of RMS Fluctuating Pressure Level

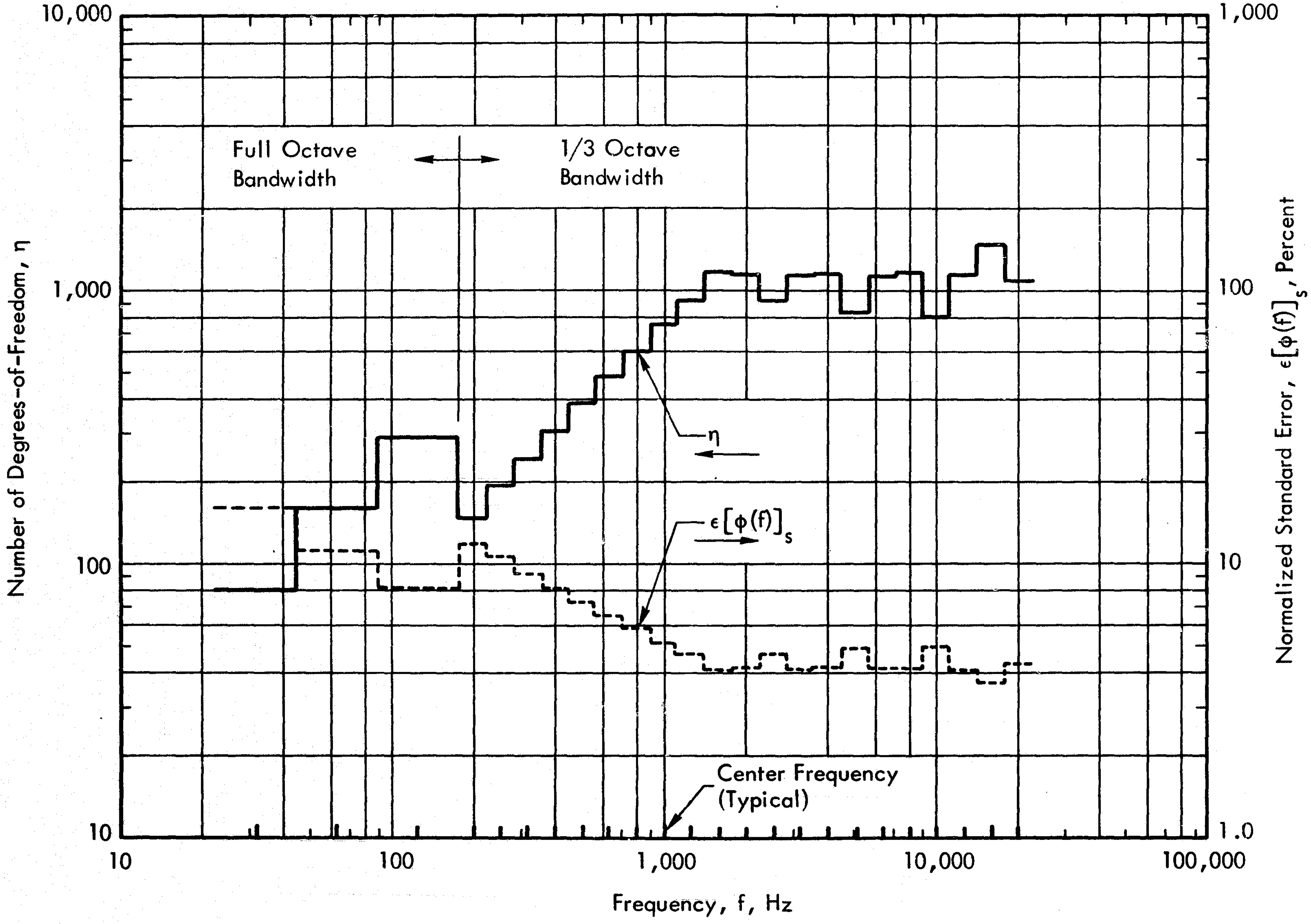

Figure 21. Variation of Statistical Accuracy Parameters with Frequency for the Present Digital Computation of Power Spectral Densities

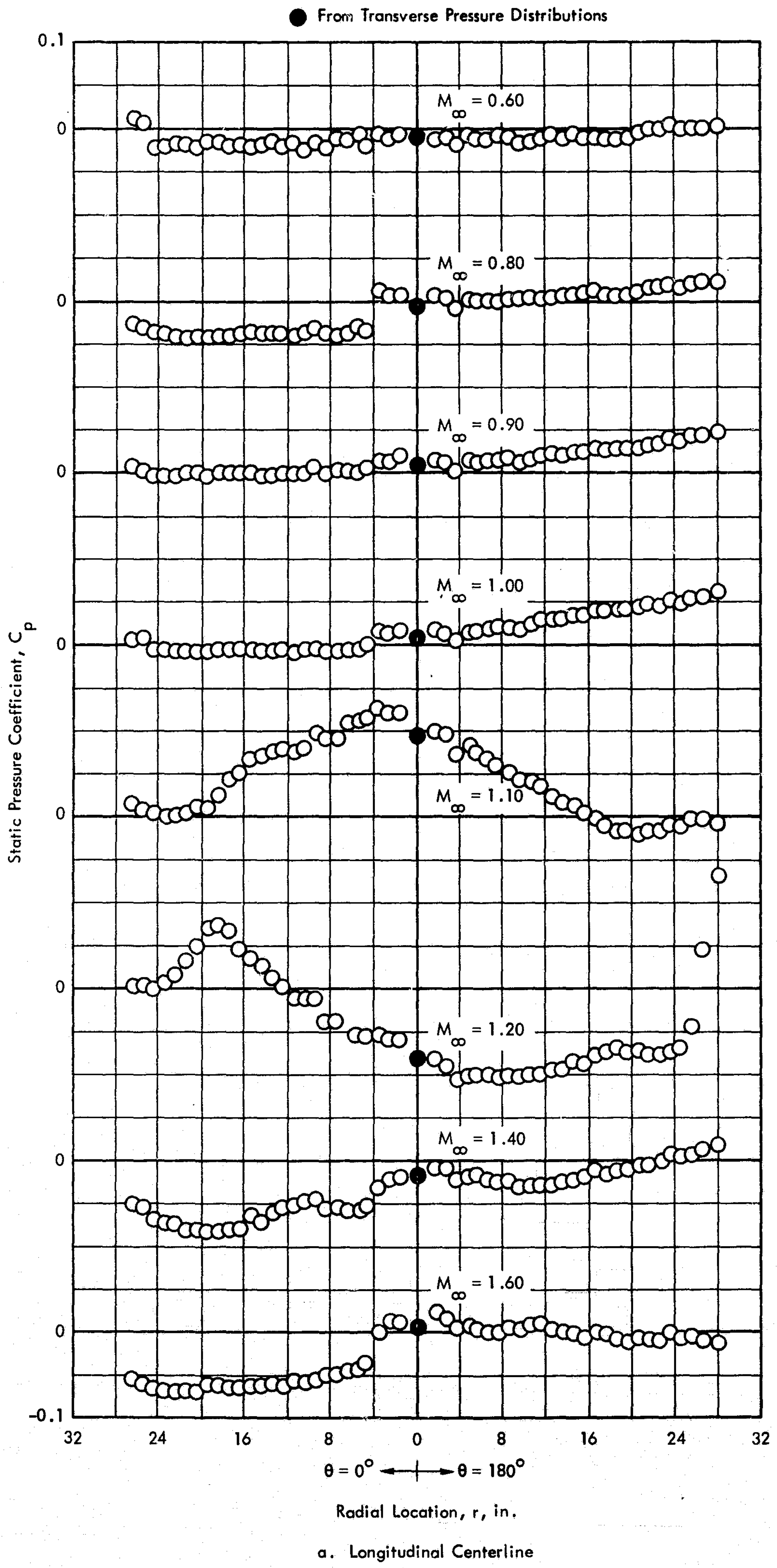

a. Longitudinal Centerline

Figure 22. Static Pressure Distributions Along the Longitudinal and Transverse Centerlines for Undisturbed Flow over the Test Panel, $Re/ft = 3 \times 10^6$

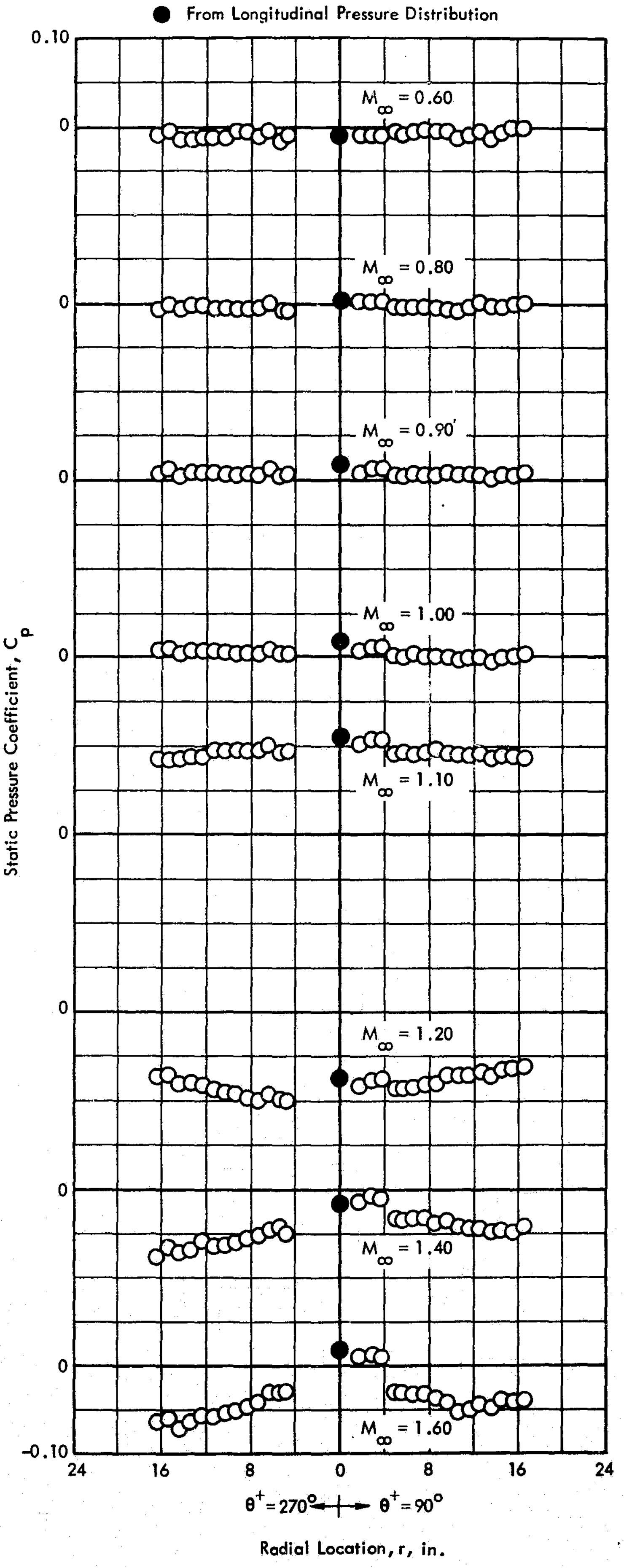

b. Transverse Centerline

Figure 22. Concluded

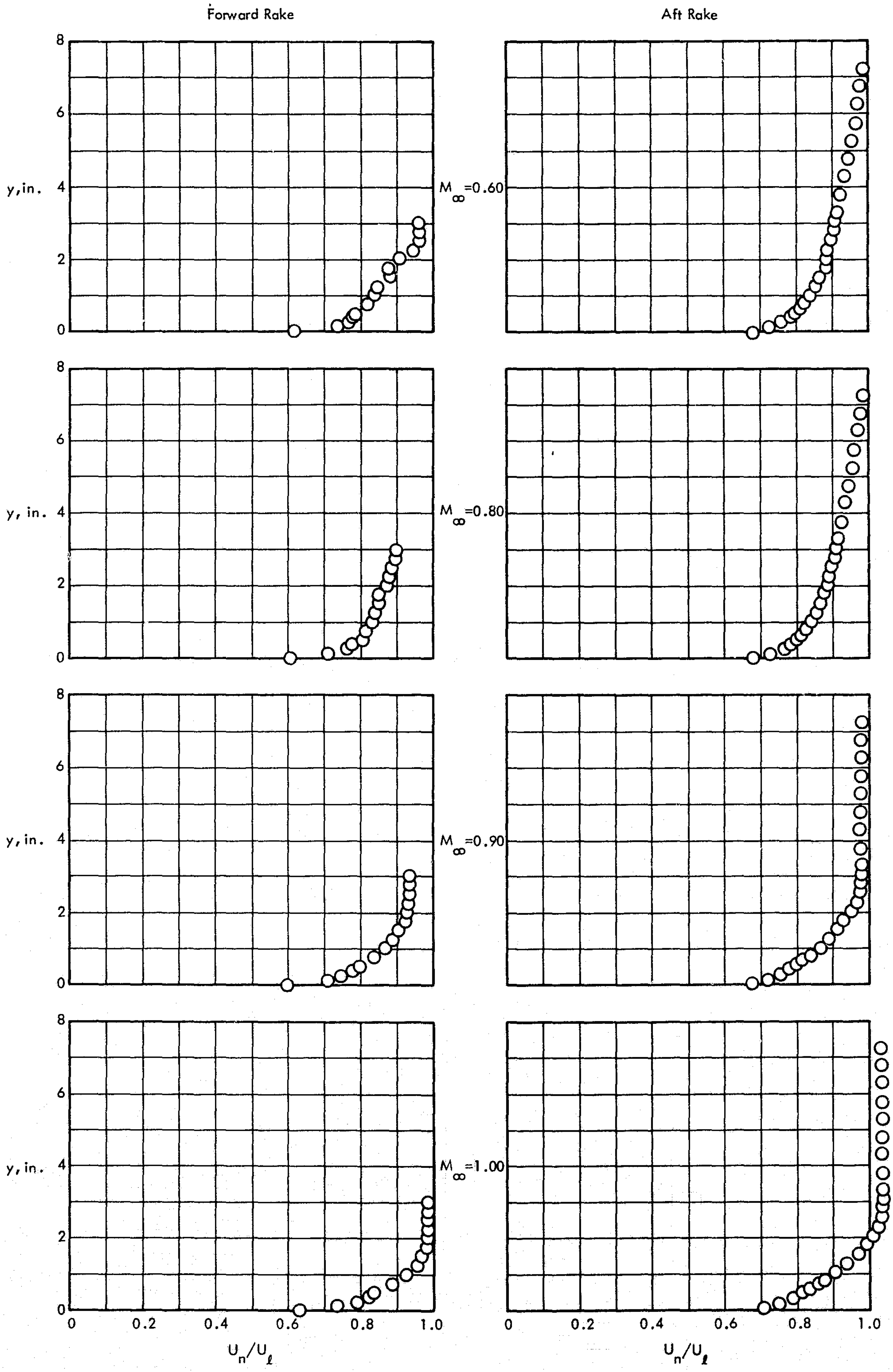

Figure 23. Boundary Layer Velocity Profiles at the Forward and Aft Rake Positions For Undisturbed Flow, re/ft = 3×10^6

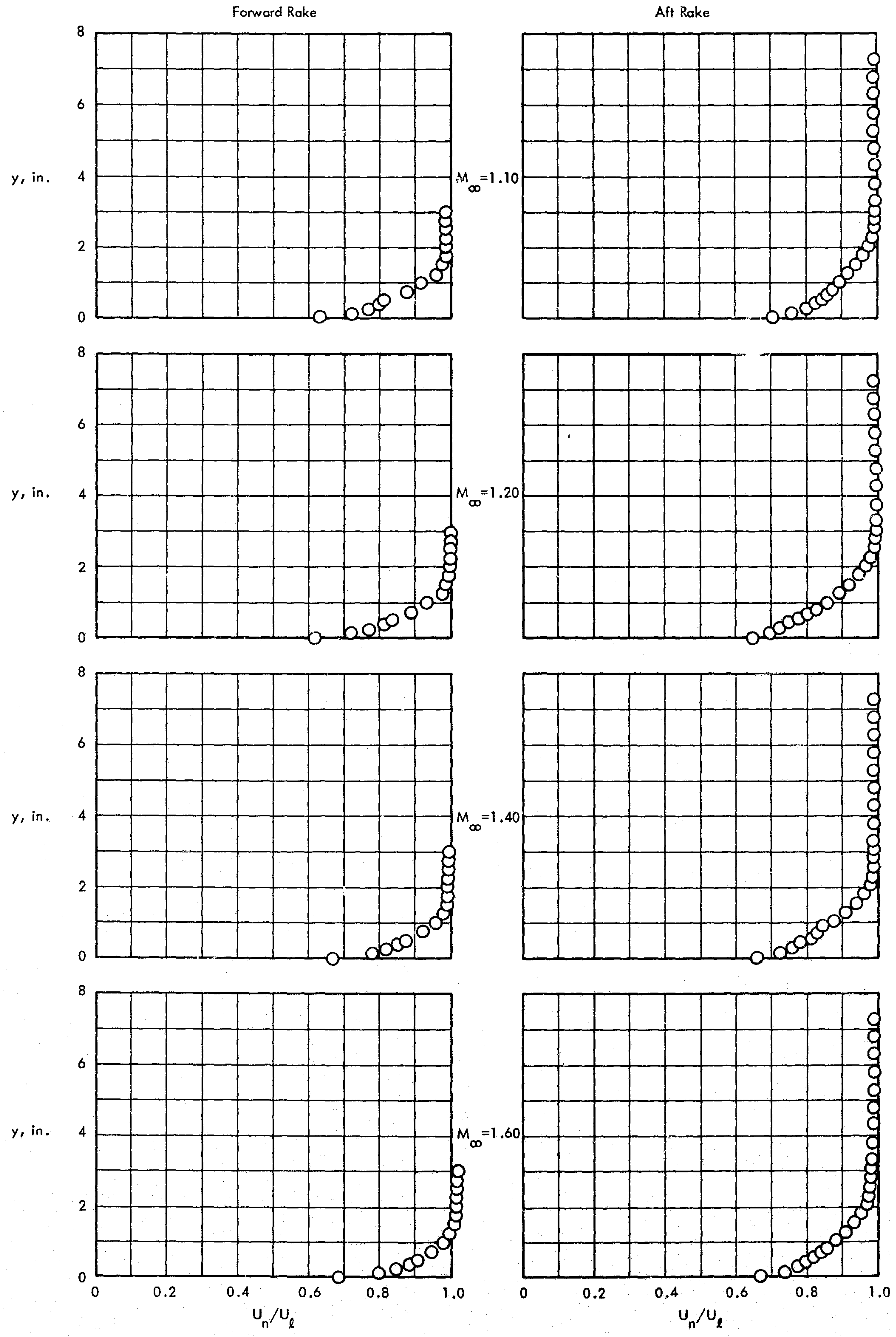

Figure 23. Concluded

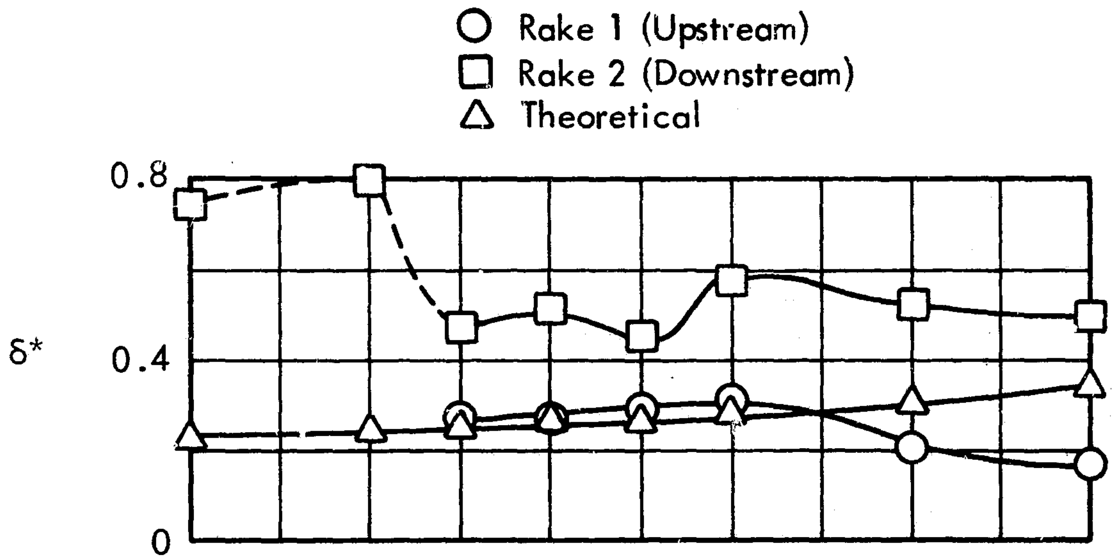

a. Re/ft = 1.5×10^6

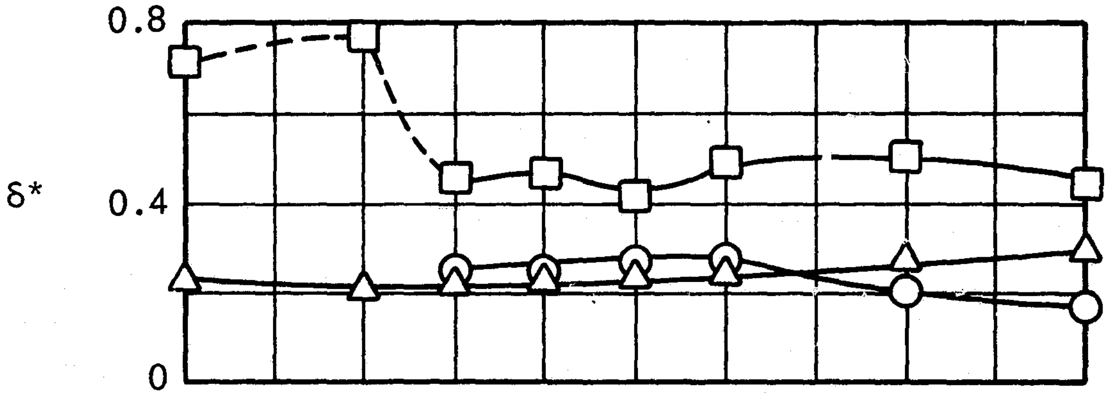

b. Re/ft = 3.0×10^6

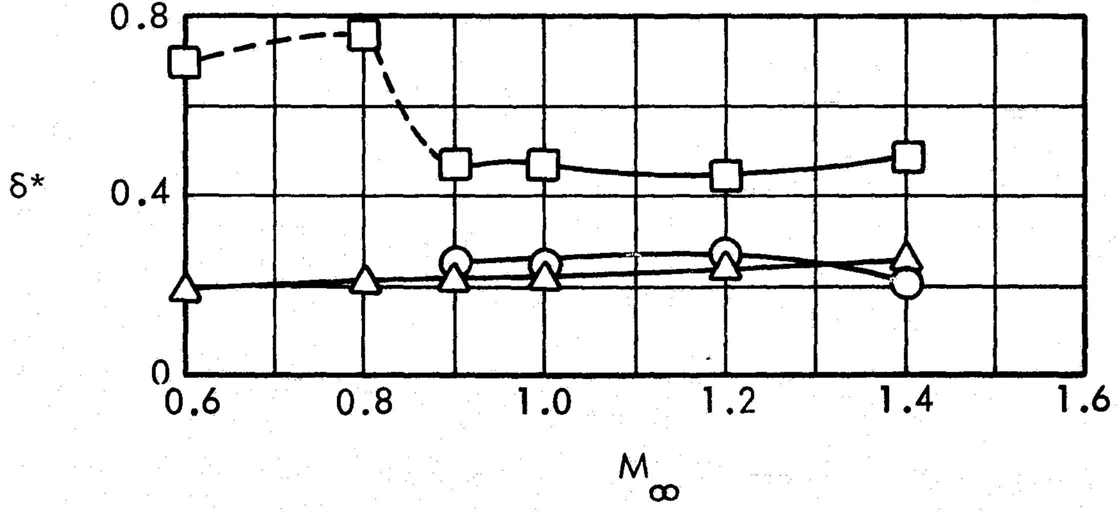

c. Re/ft = 4.5×10^6

Figure 24. Variation of Boundary Displacement Thickness With Mach Number for Undisturbed Flow

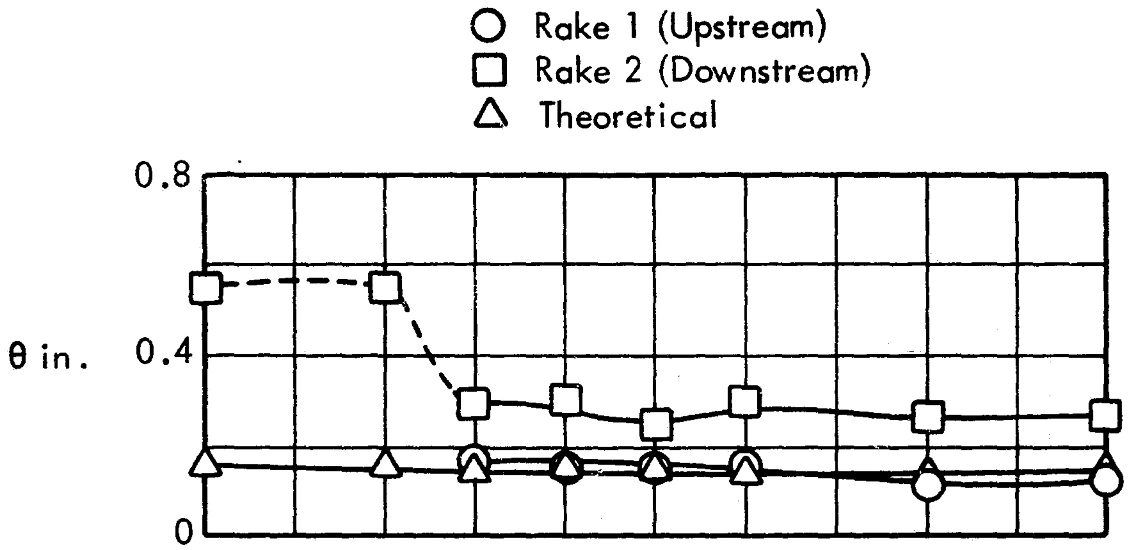

a. Re/ft = 1.5 x 10^6

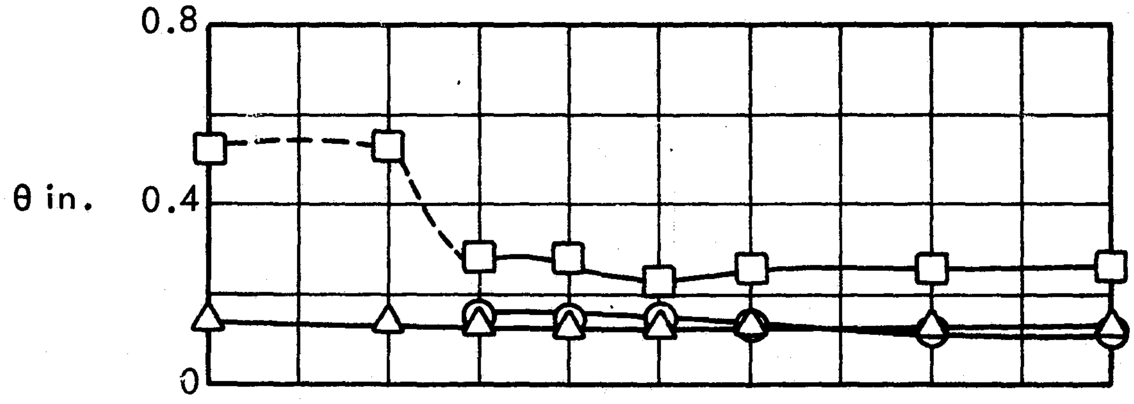

b. Re/ft = 3.0 x 10^6

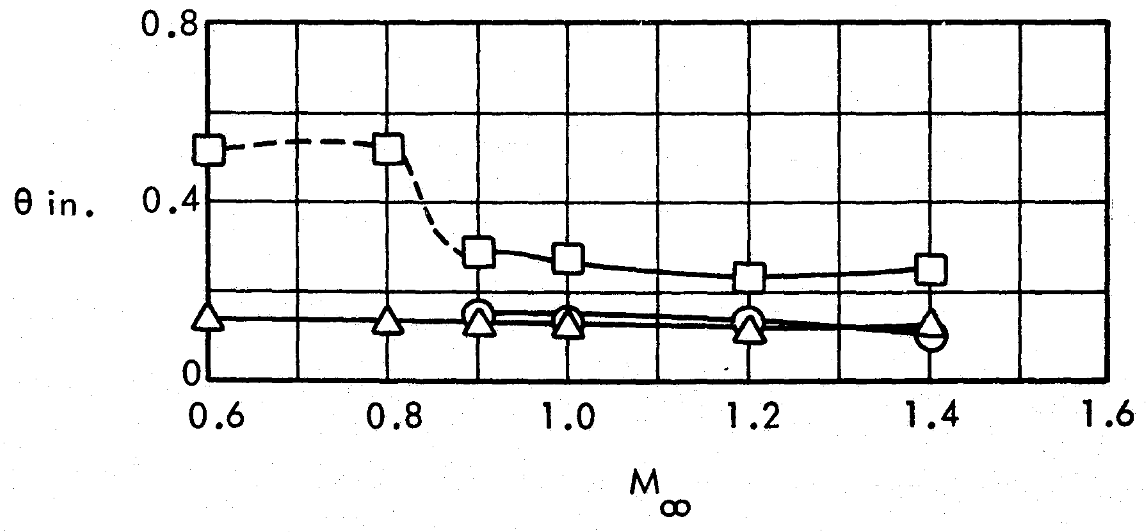

c. Re/ft = 4.5 x 10^6

Figure 25. Variation of Boundary Layer Momentum Thickness With Mach Number for Undisturbed Flow

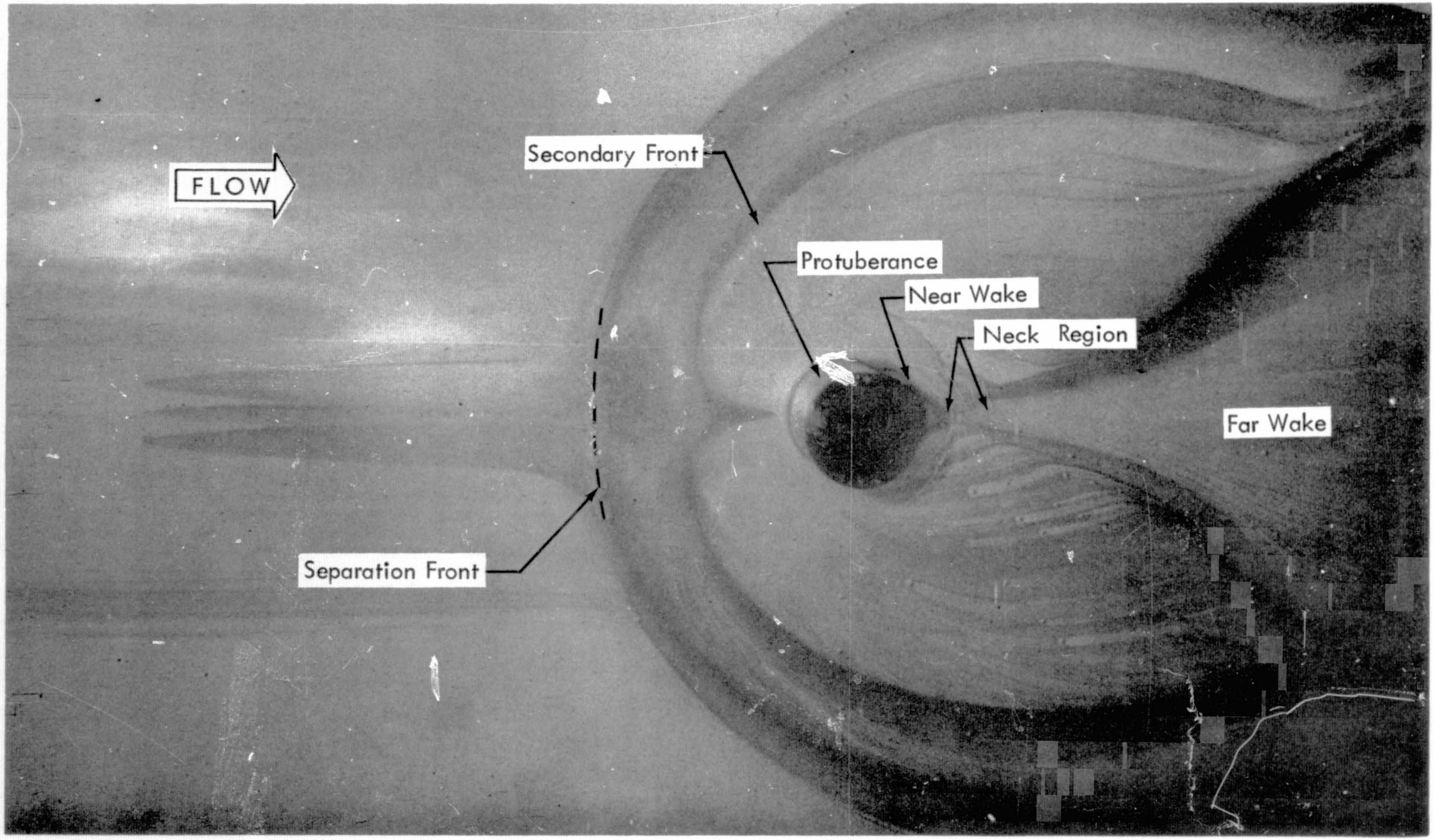

Figure 26. Typical Oil Flow Pattern of the Protuberance Flow Field

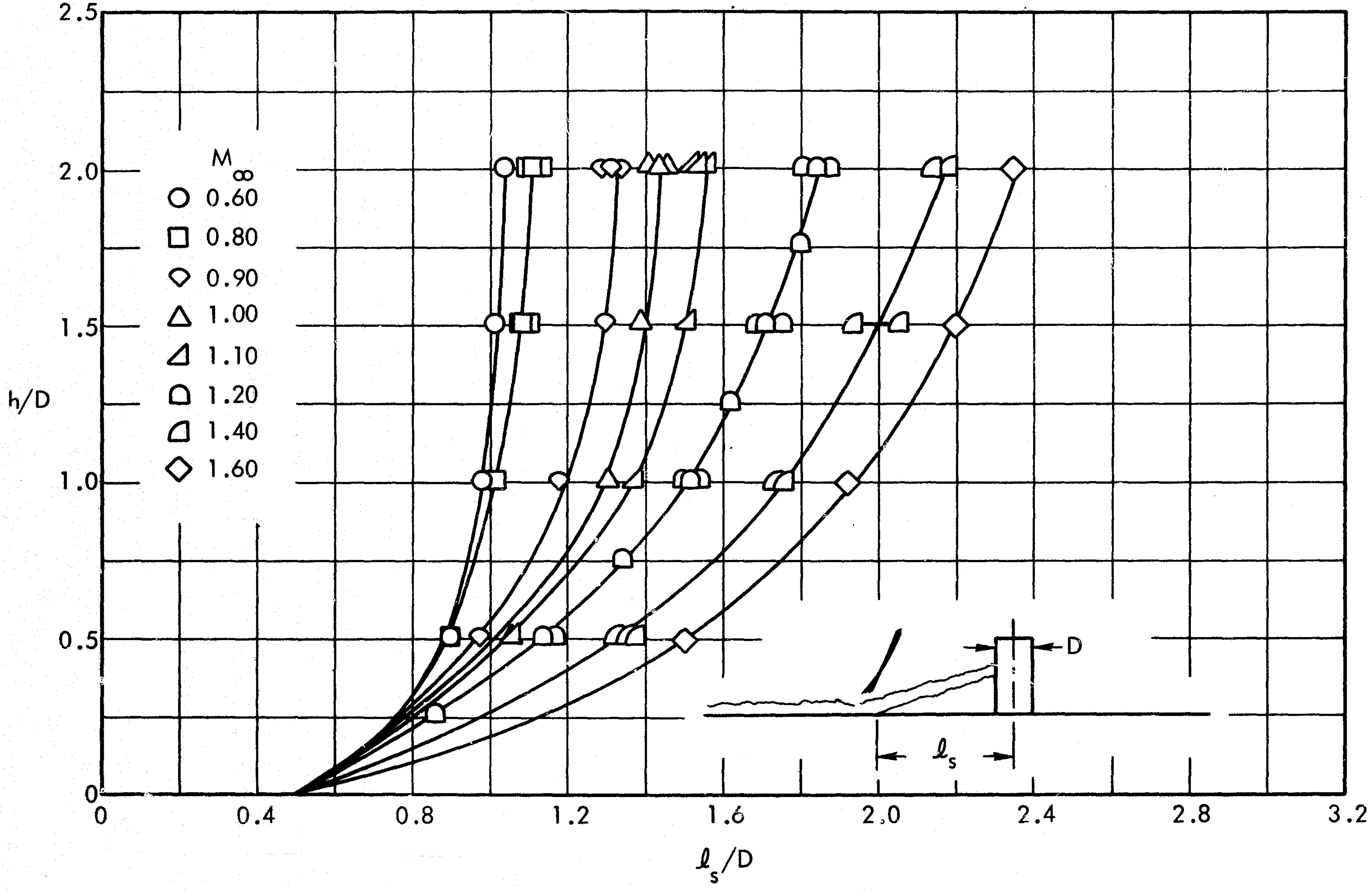

Figure 27. Variation of Separation Length with Protuberance Height

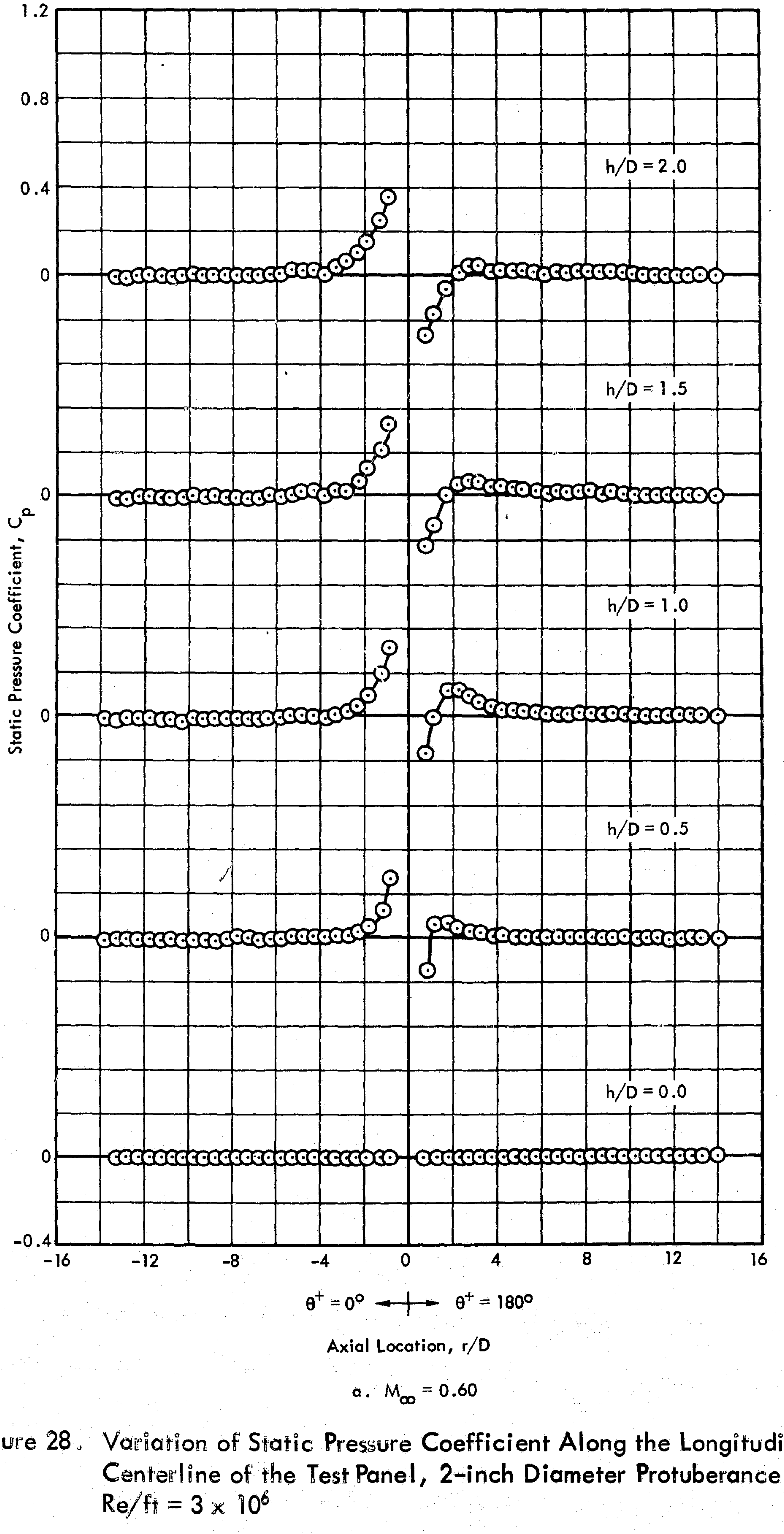

a. $M_\infty = 0.60$

Figure 28. Variation of Static Pressure Coefficient Along the Longitudinal Centerline of the Test Panel, 2-inch Diameter Protuberance, $Re/ft = 3 \times 10^6$

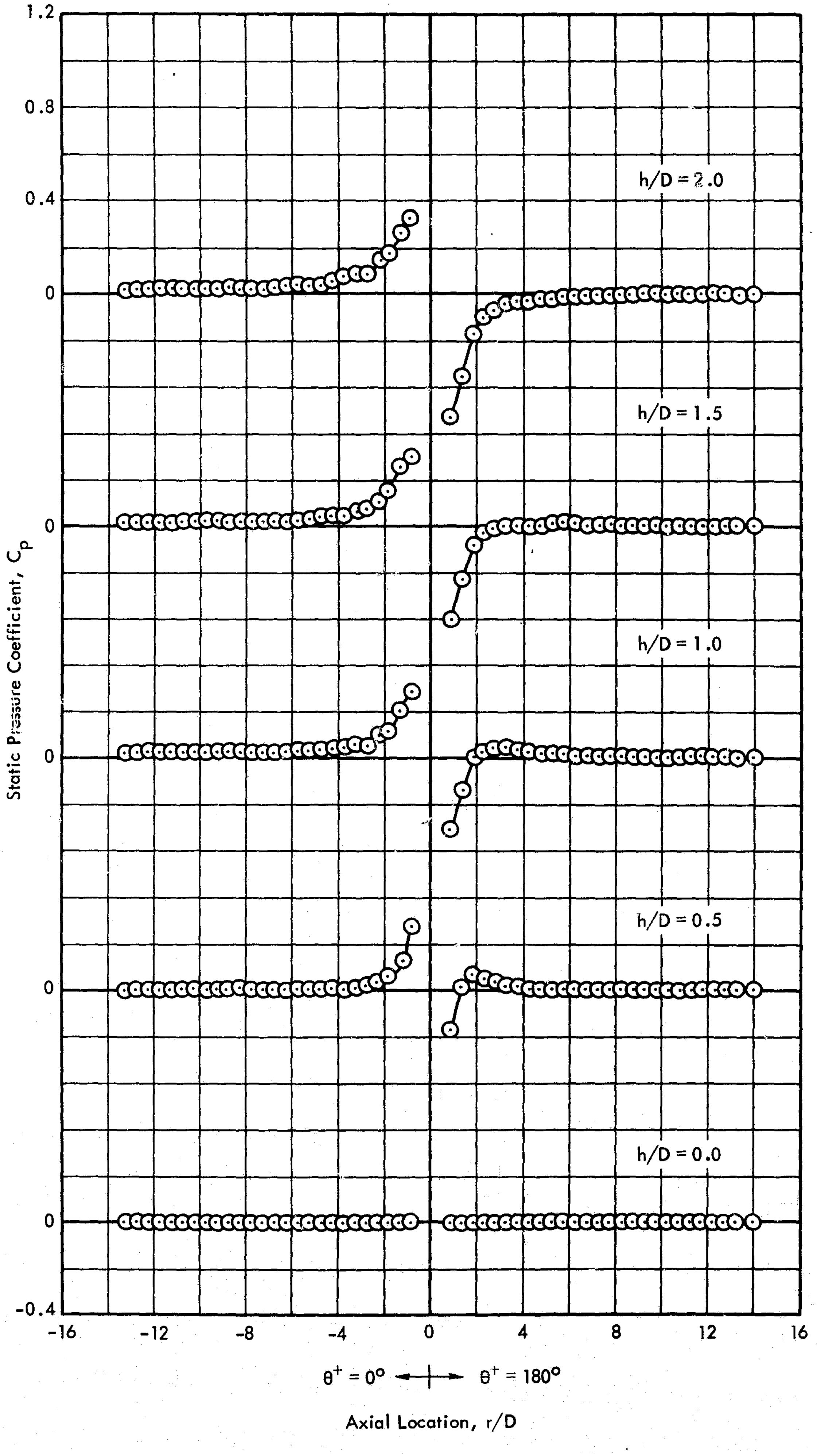

b. $M_\infty = 0.80$

Figure 28. Continued

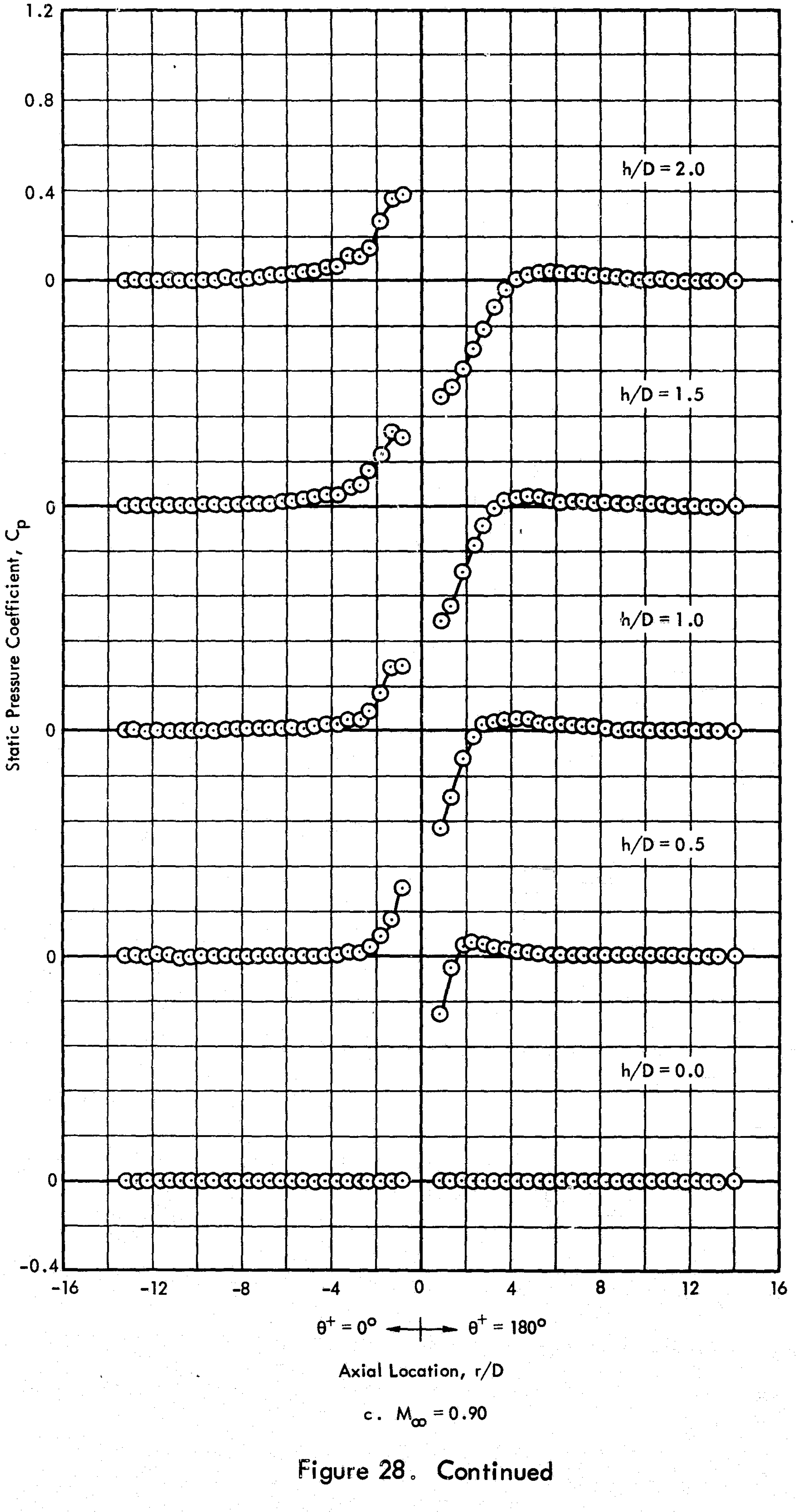

c. $M_\infty = 0.90$

Figure 28. Continued

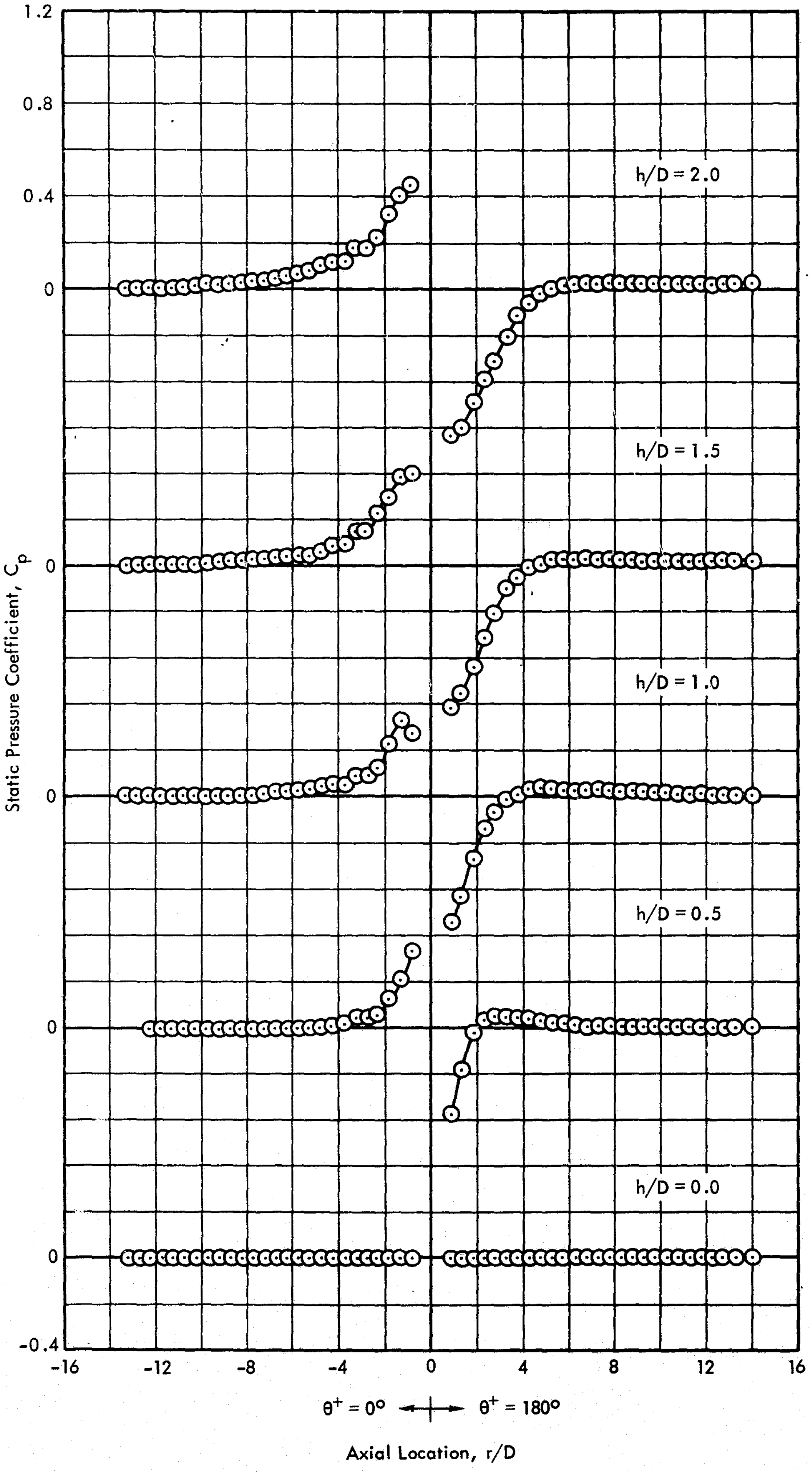

d. $M_\infty = 1.00$

Figure 28. Continued

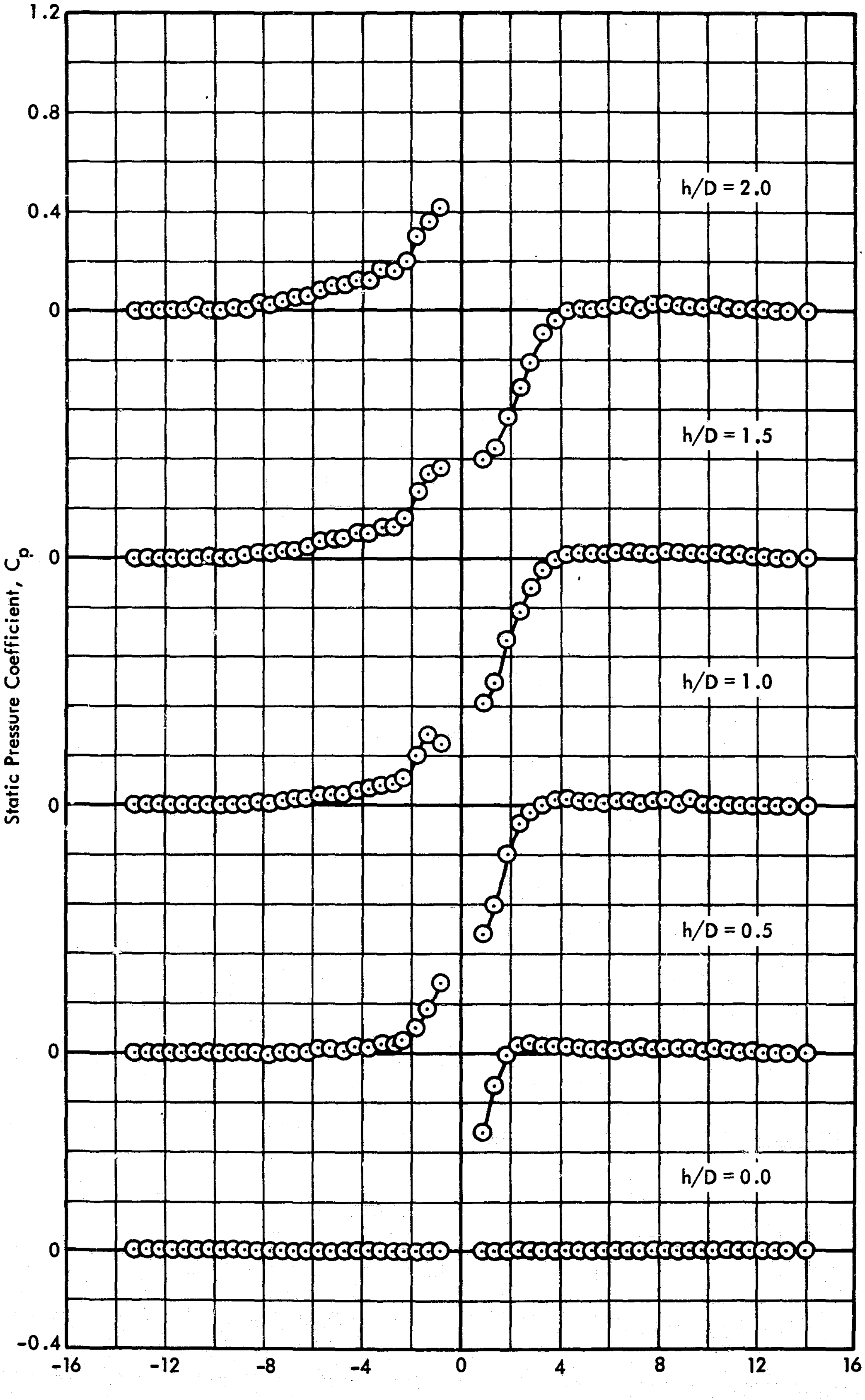

e. $M_\infty = 1.10$

Figure 28. Continued

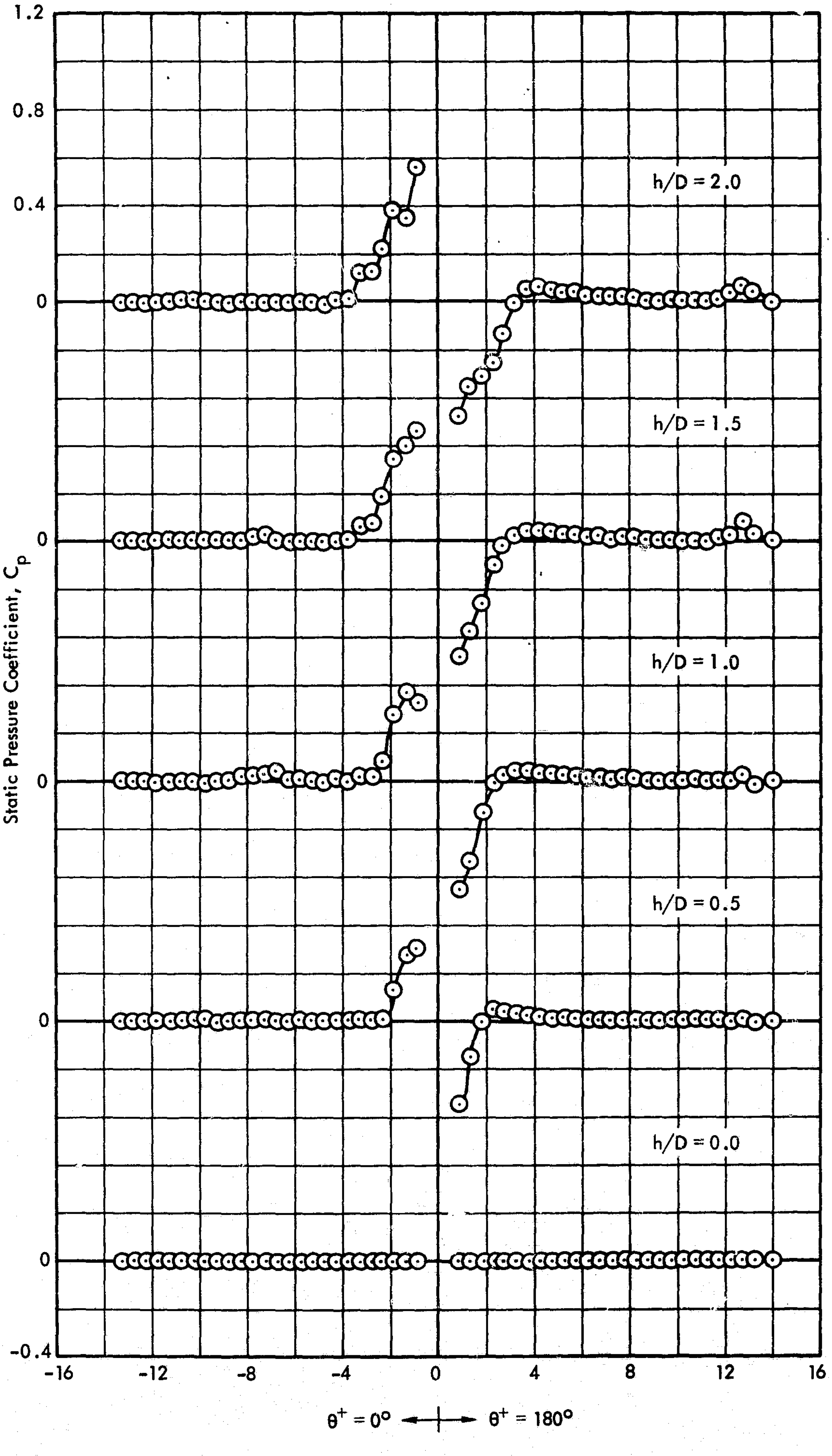

f. $M_\infty = 1.20$

Figure 28. Continued

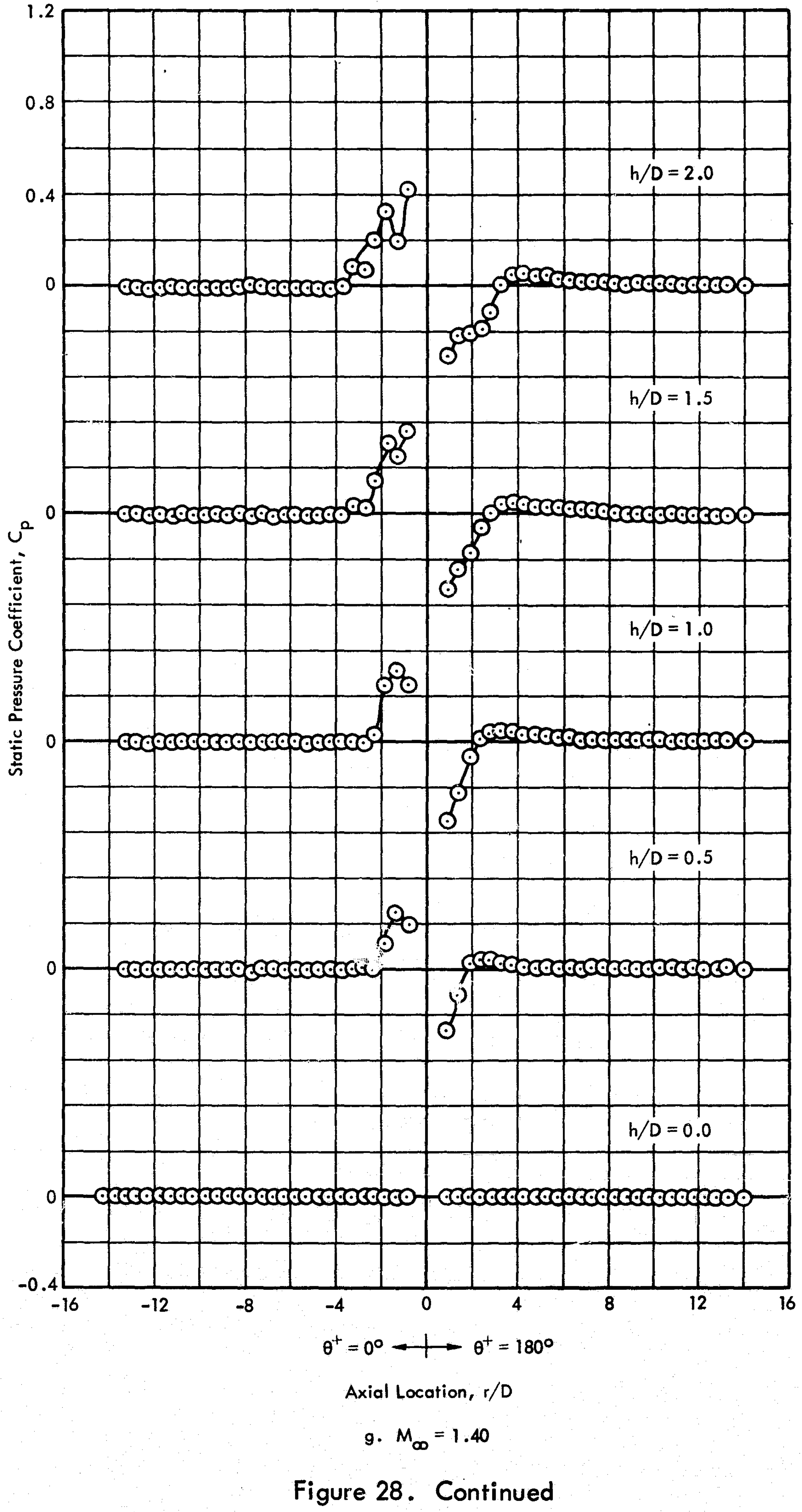

g. $M_\infty = 1.40$

Figure 28. Continued

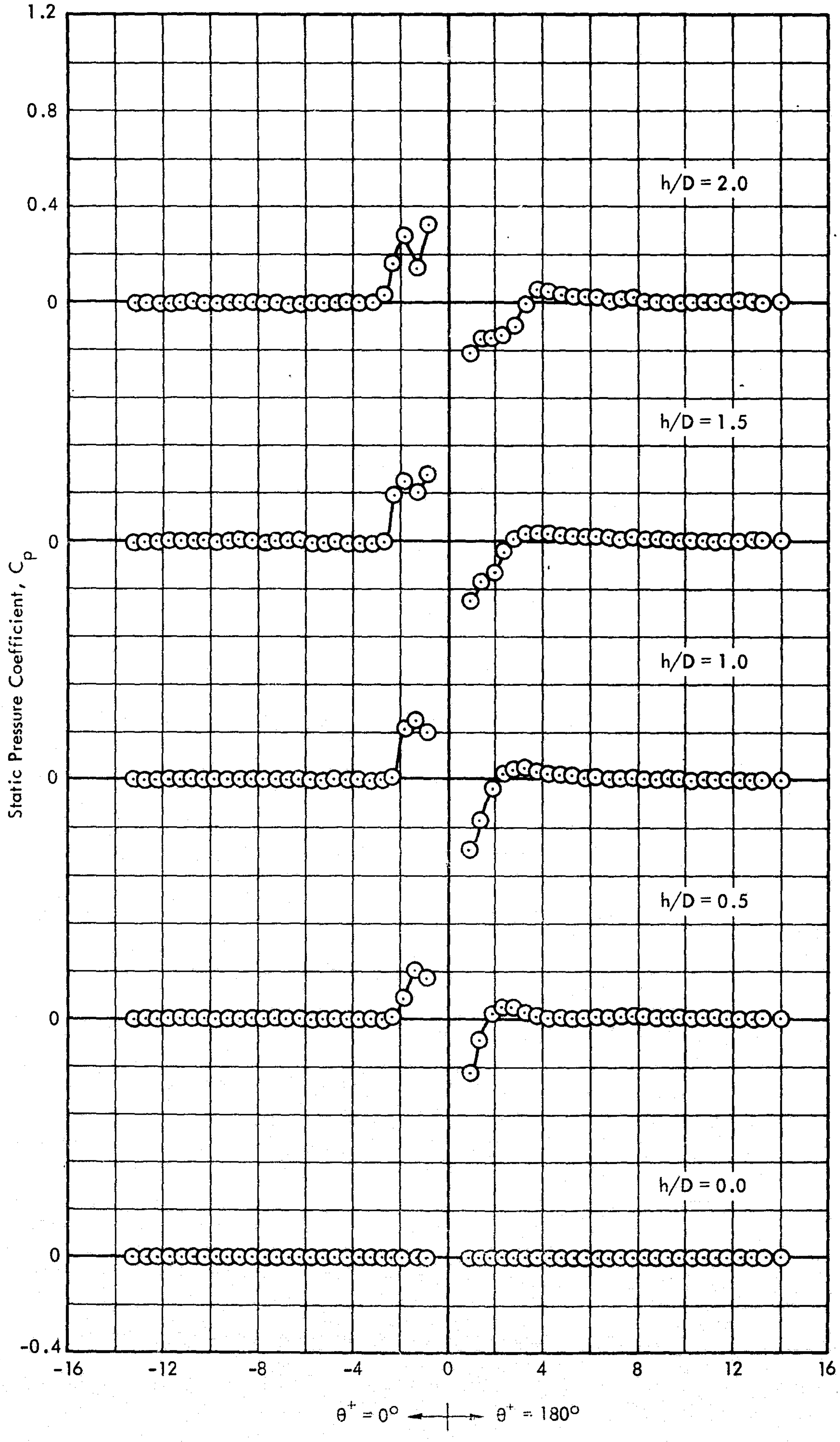

h. $M_\infty = 1.60$

Figure 28. Concluded

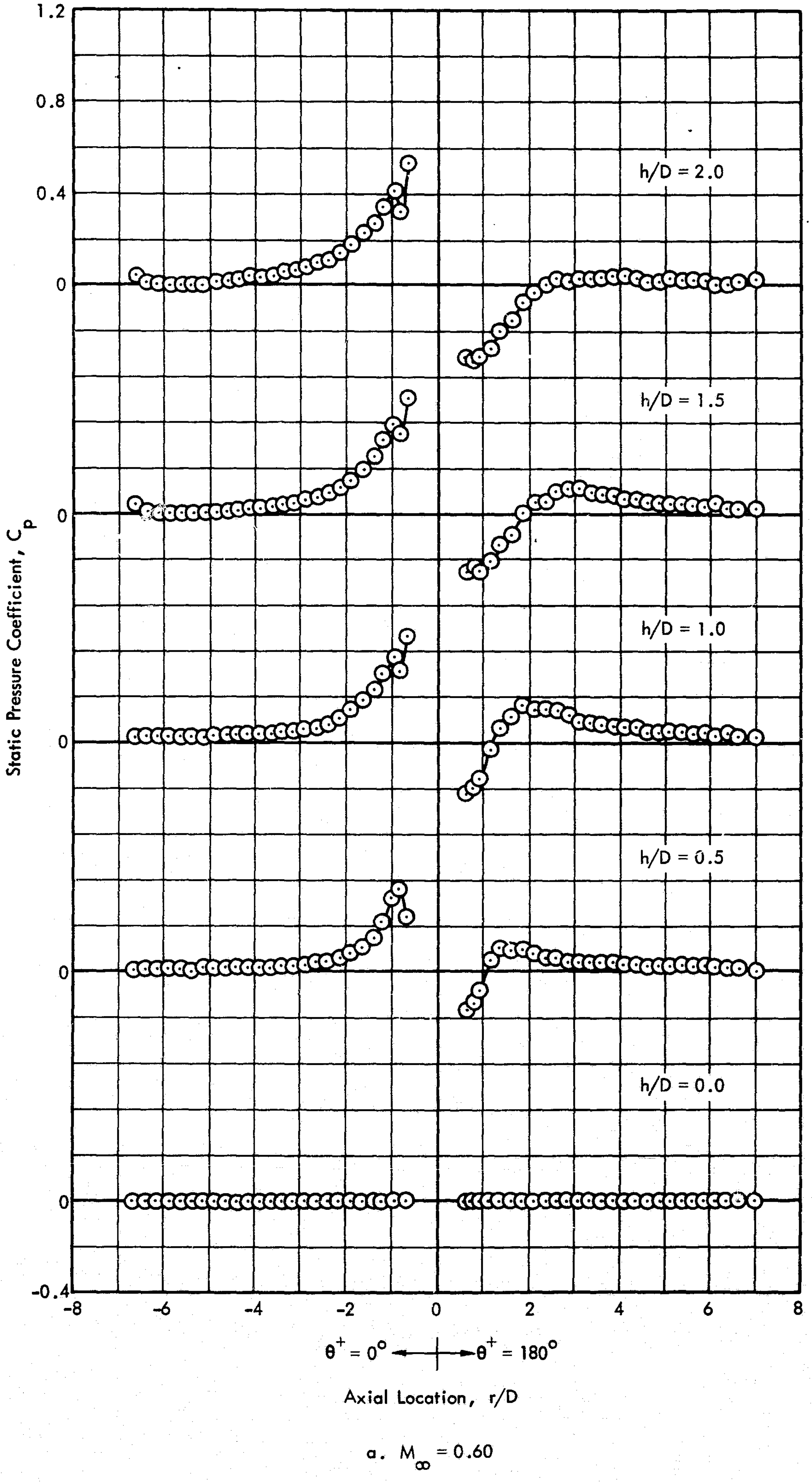

a. $M_\infty = 0.60$

Figure 29. Variation of Static Pressure Coefficient Along the Longitudinal Centerline of the Test Panel, 4-inch Diameter Protuberance, $Re/ft = 3 \times 10^6$

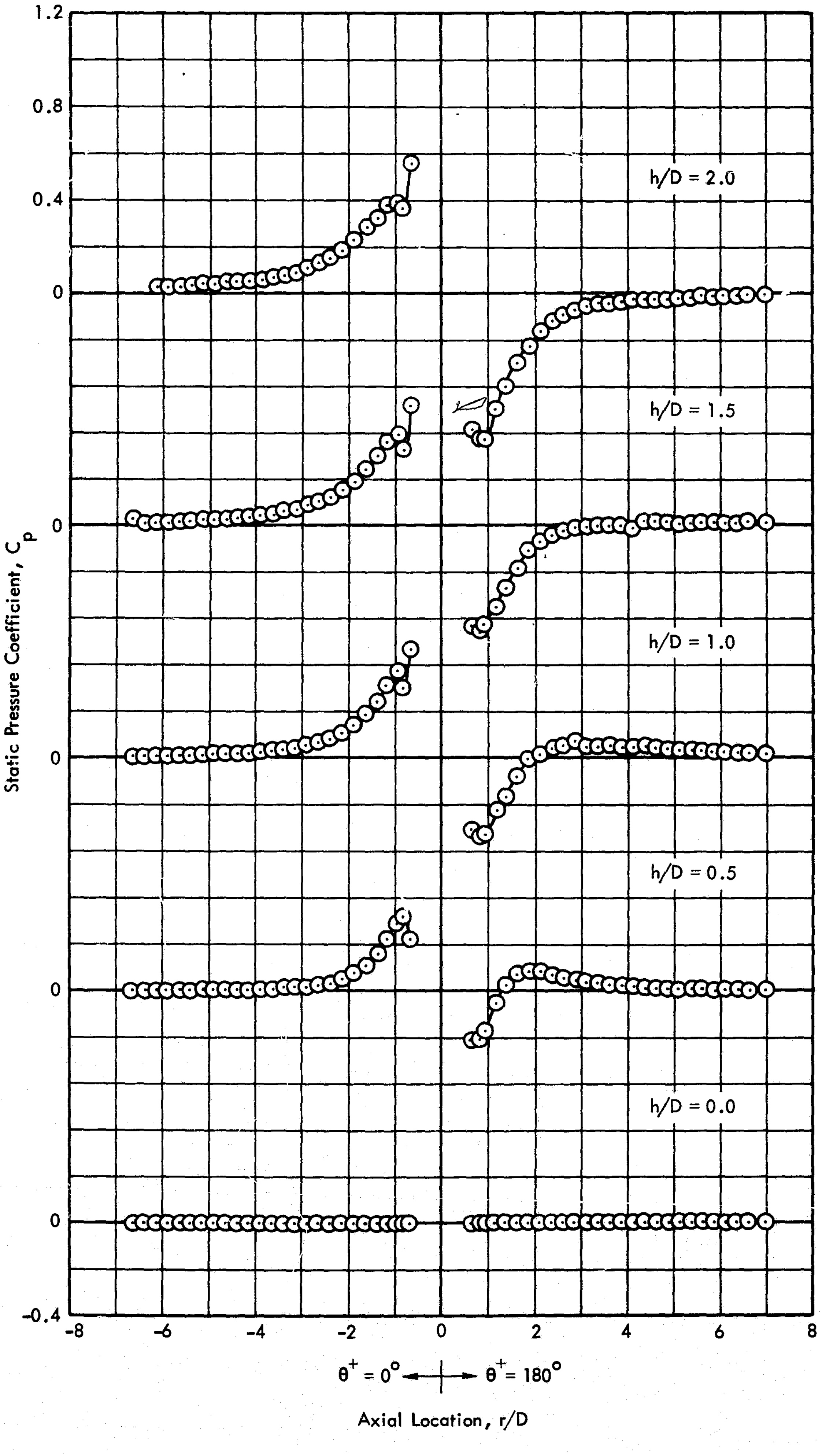

b. $M_\infty = 0.80$

Figure 29. Continued

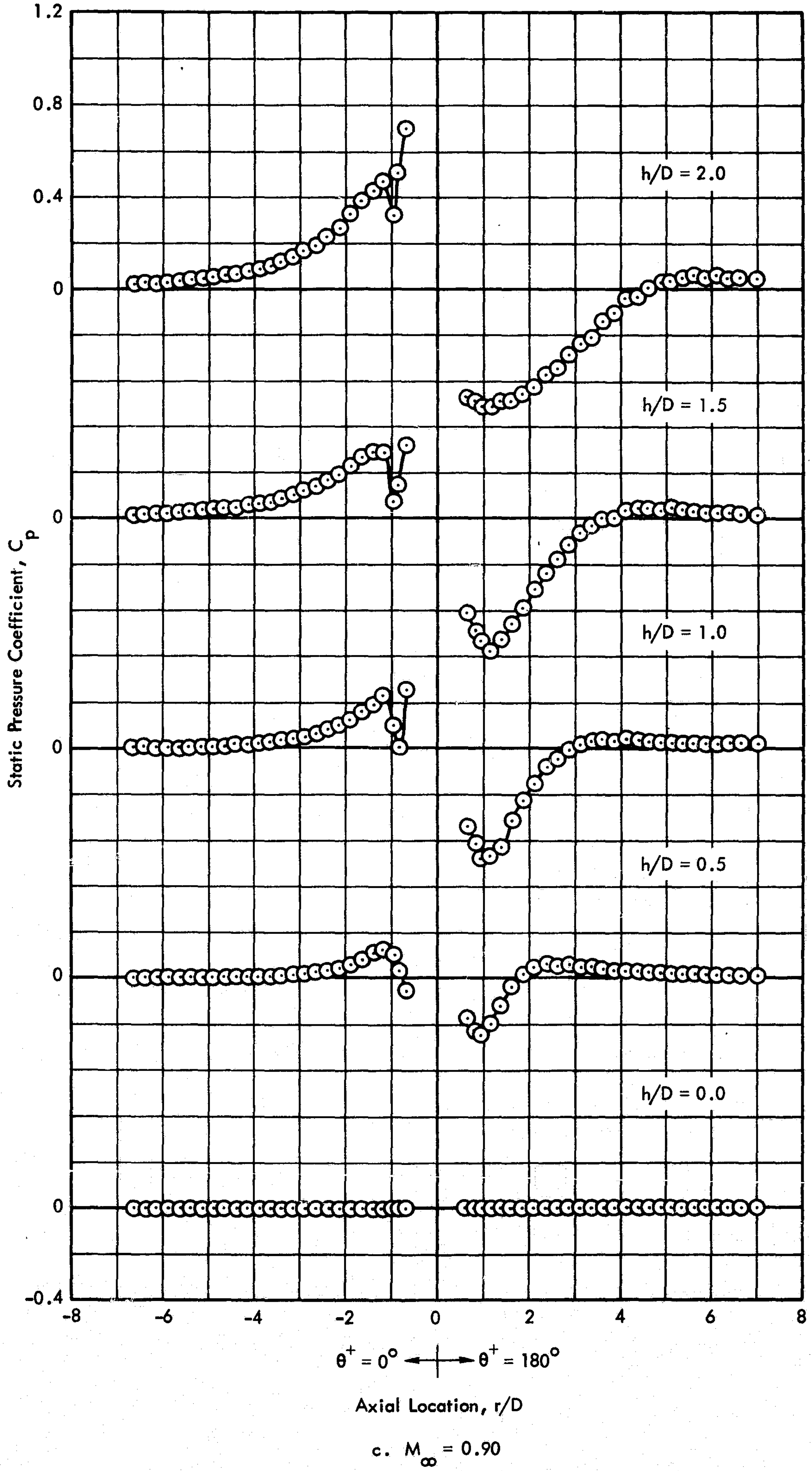

c. $M_\infty = 0.90$

Figure 29. Continued

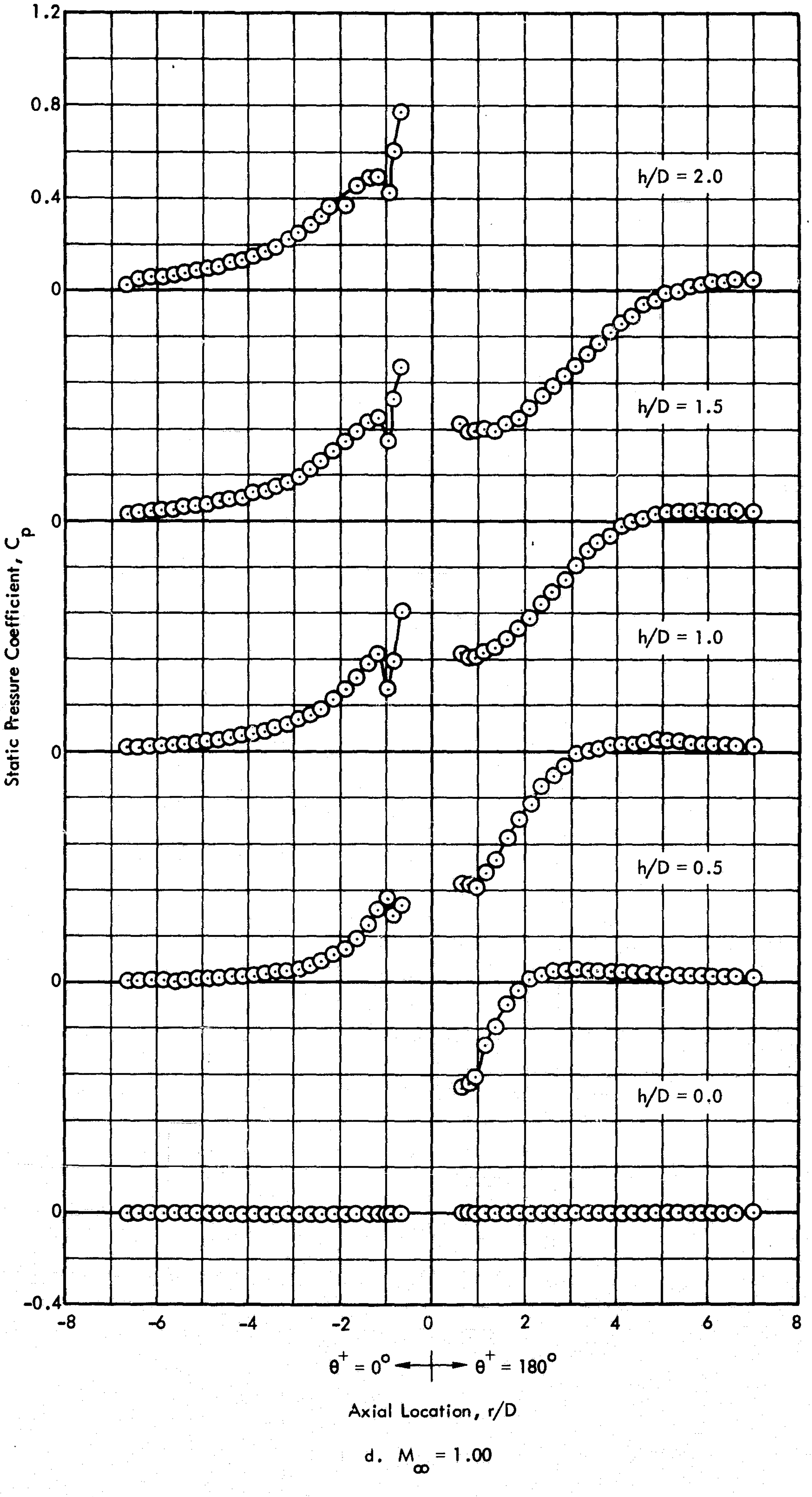

d. $M_\infty = 1.00$

Figure 29. Continued

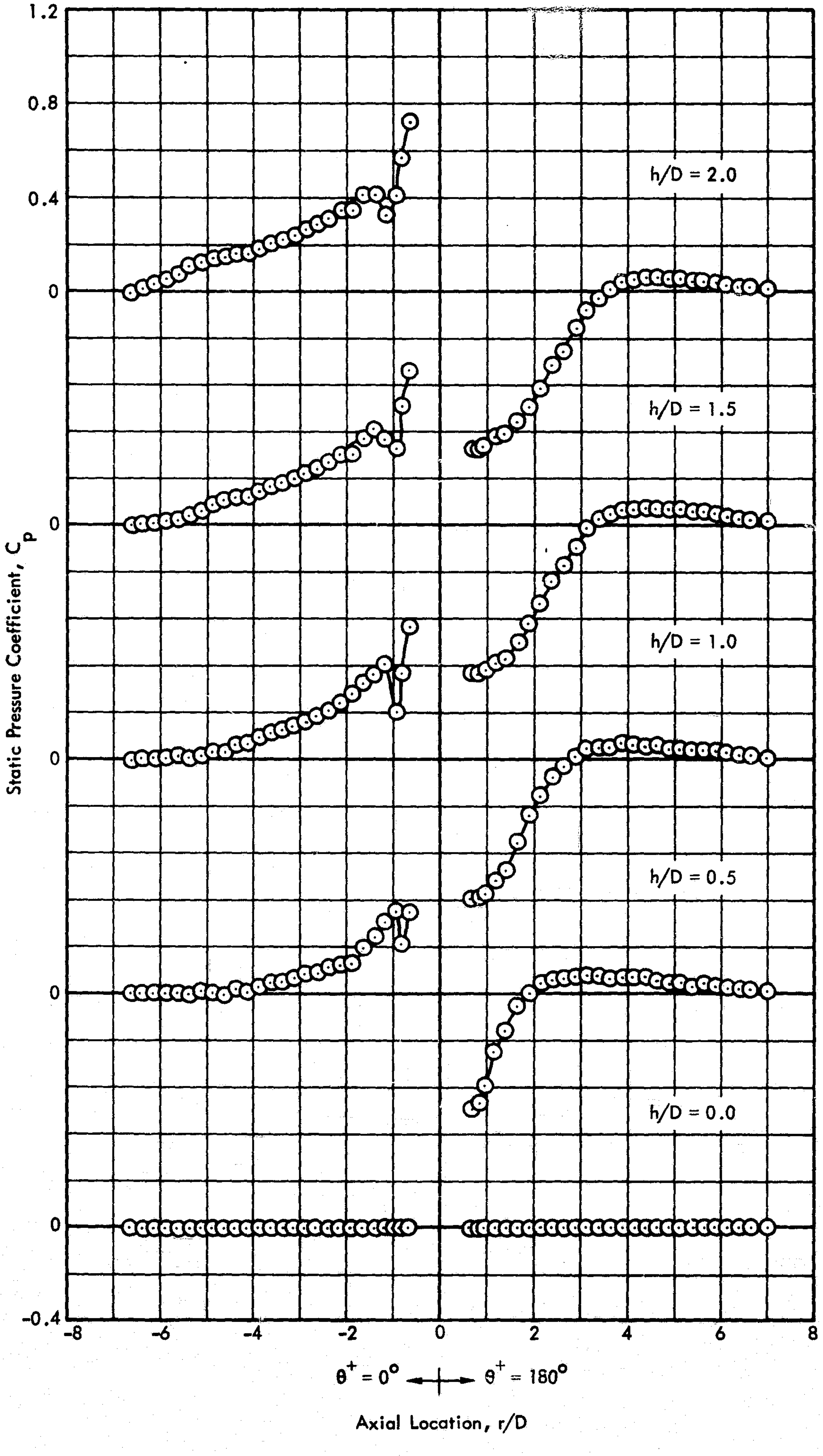

e. $M_\infty = 1.10$

Figure 29. Continued

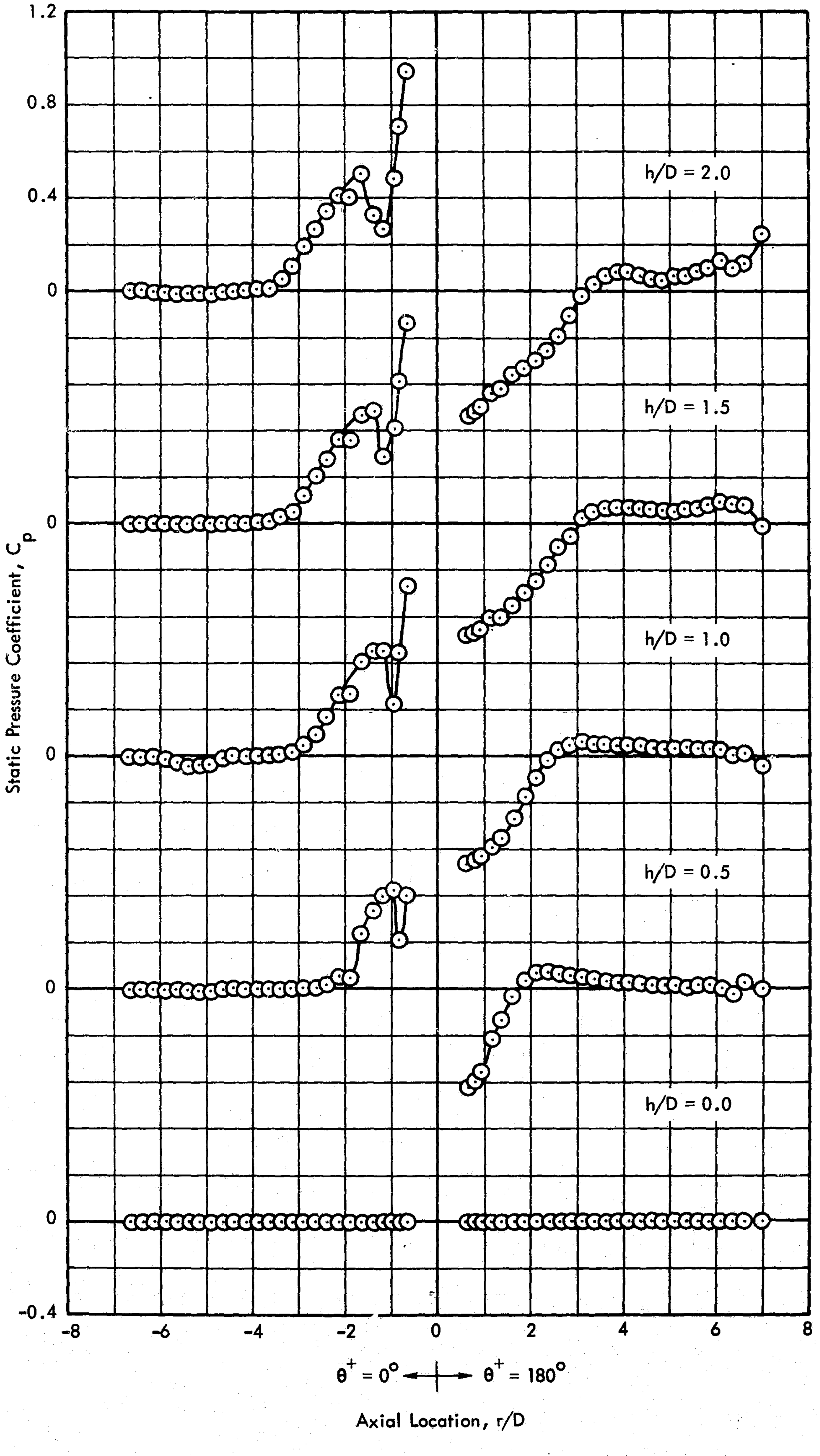

f. $M_\infty = 1.20$

Figure 29. Continued

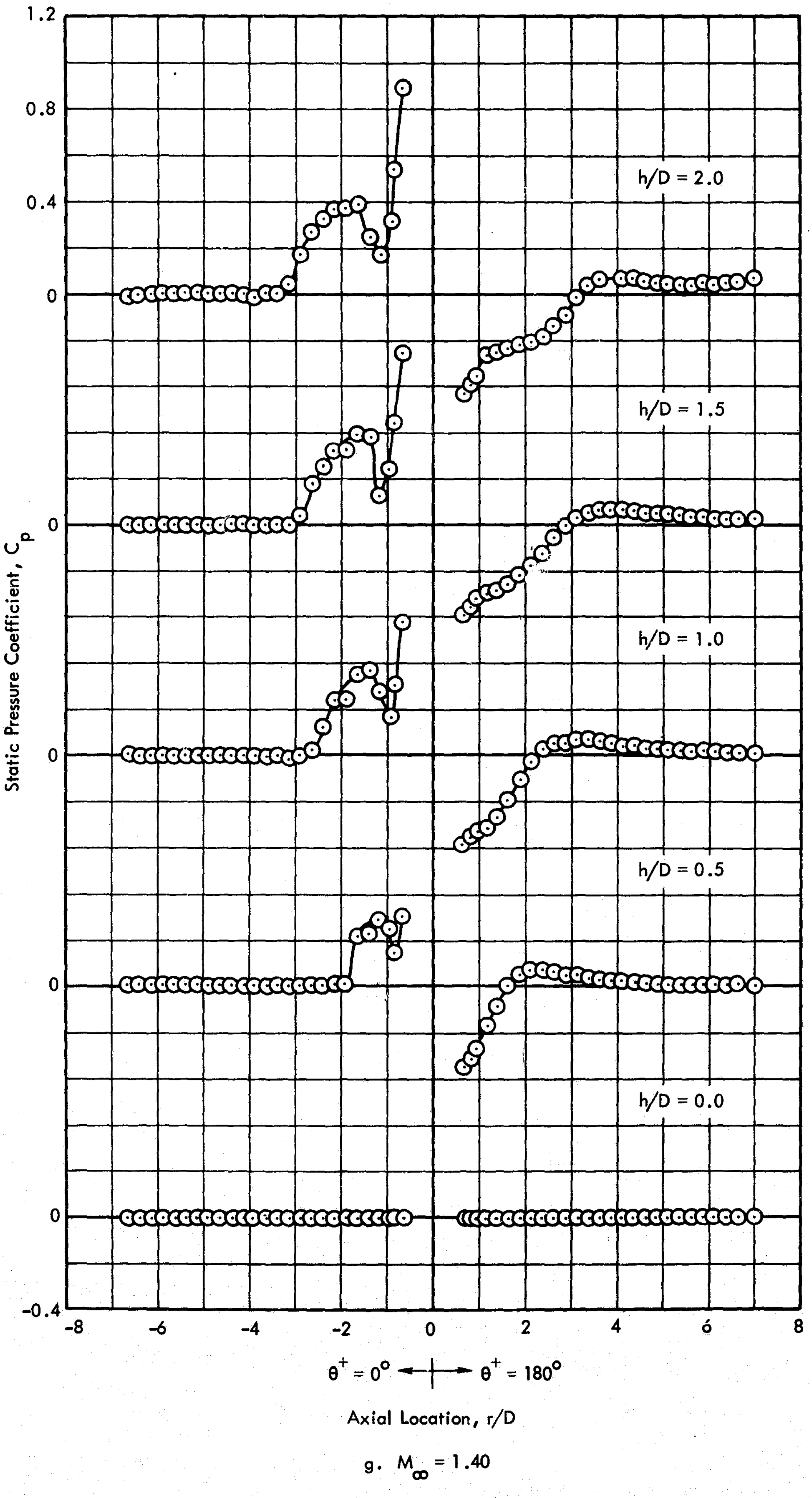

g. $M_\infty = 1.40$

Figure 29. Continued

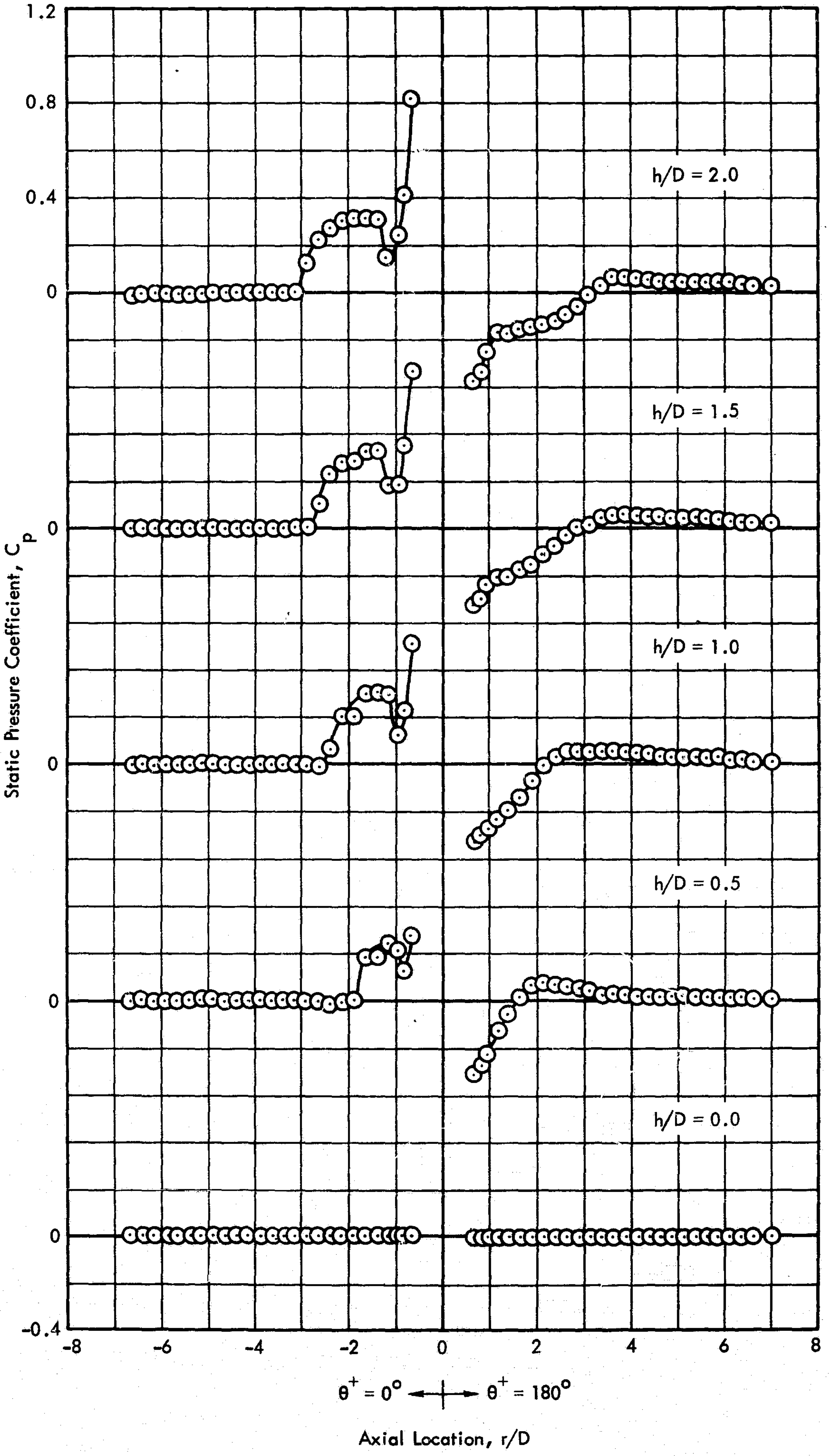

h. $M_\infty = 1.60$

Figure 29. Concluded

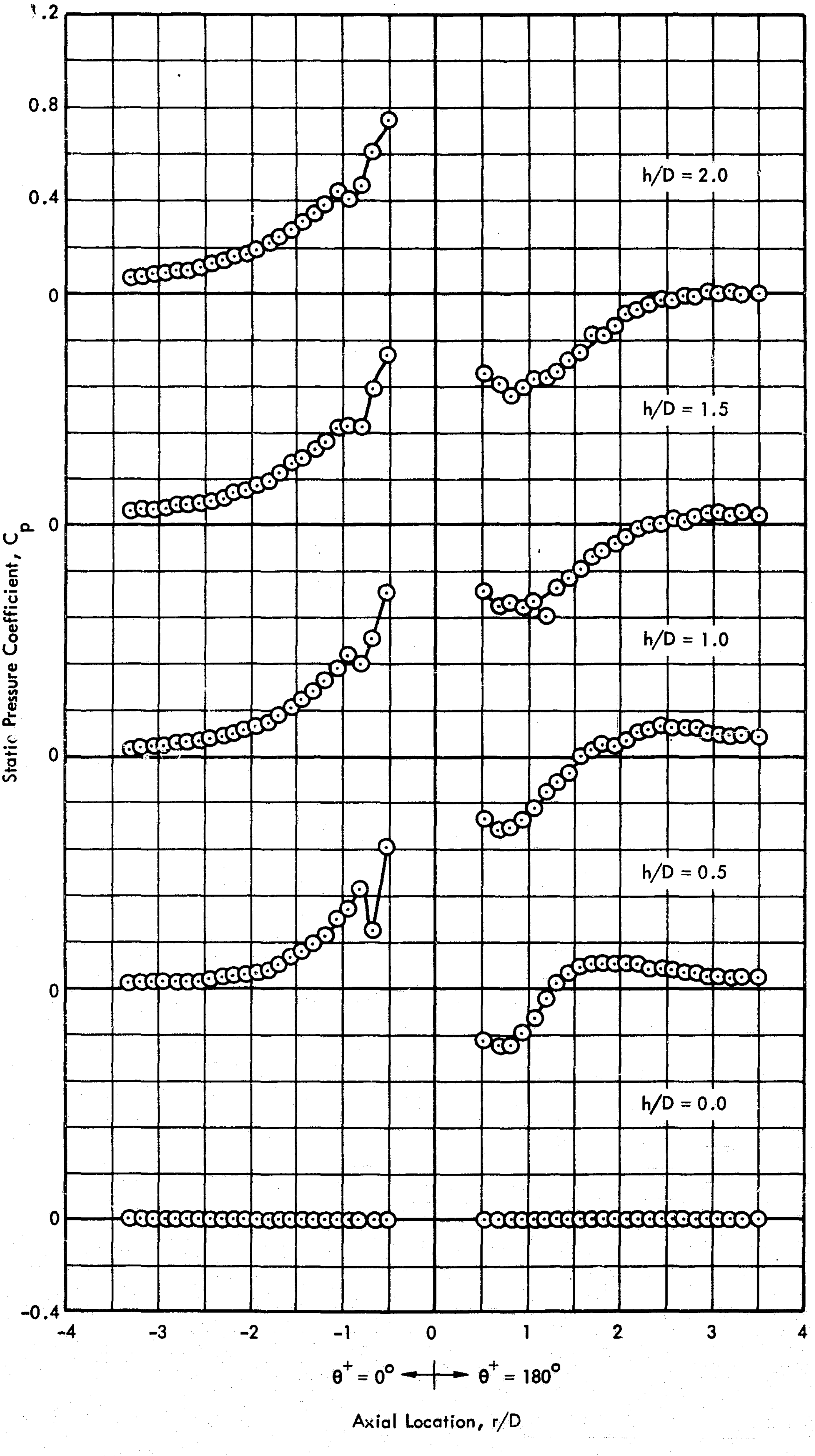

a. $M_\infty = 0.60$

Figure 30. Variation of Static Pressure Coefficient Along the Longitudinal Centerline of the Test Panel, 8-inch Diameter Protuberance, Re/ft = 3 × 10^6

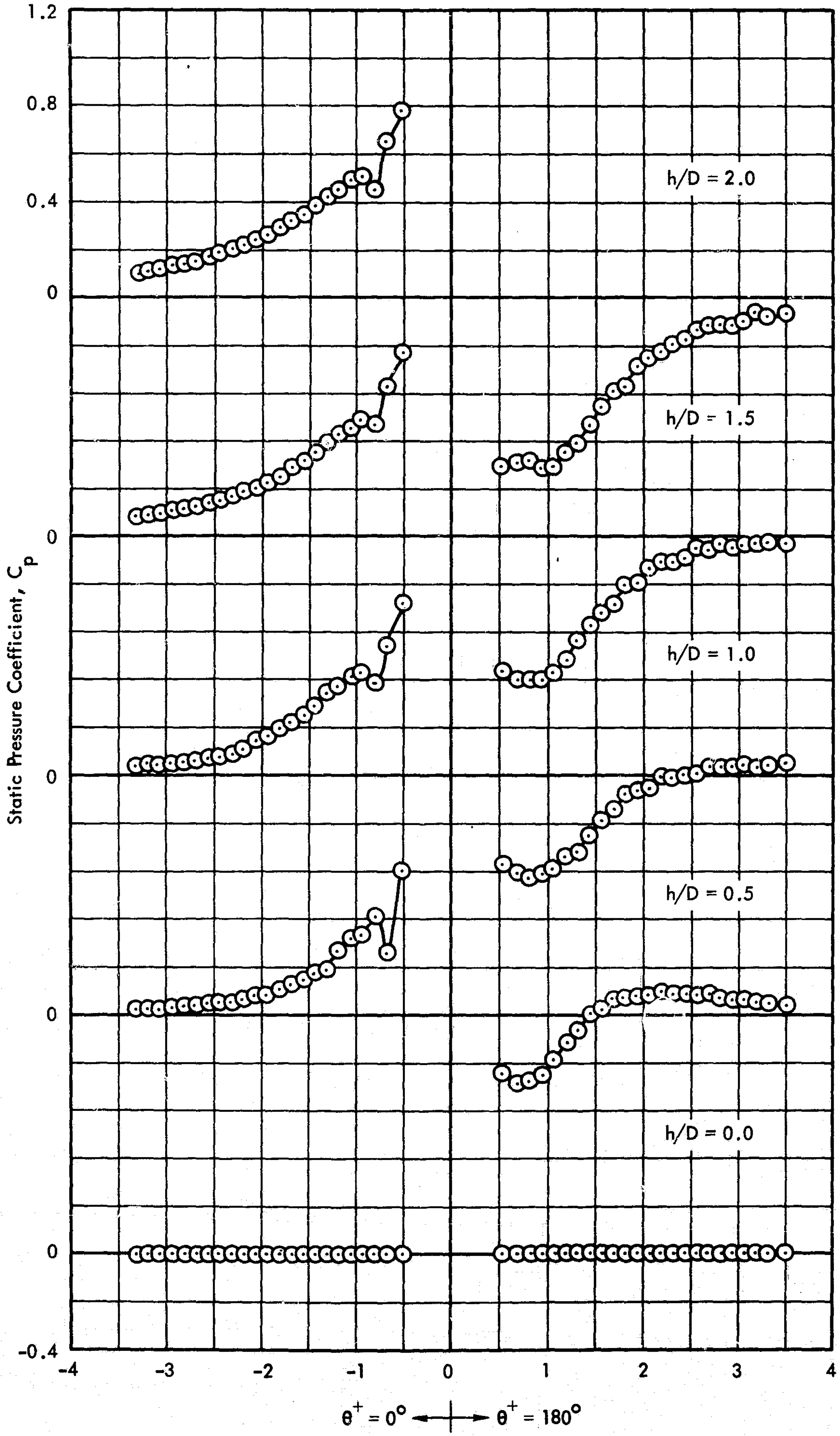

b. $M_\infty = 0.80$

Figure 30. Continued

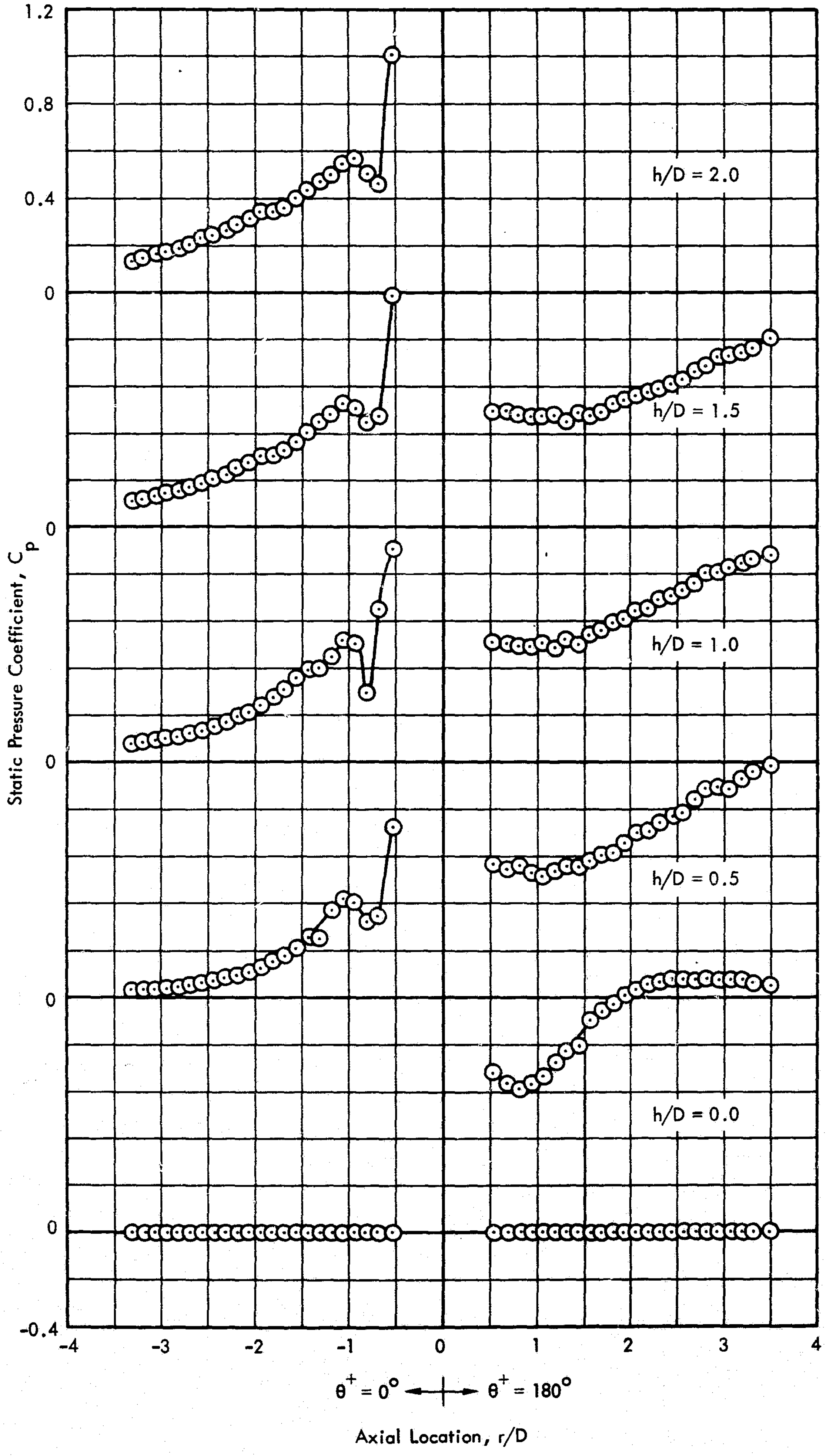

c. $M_\infty = 0.90$

Figure 30. Continued

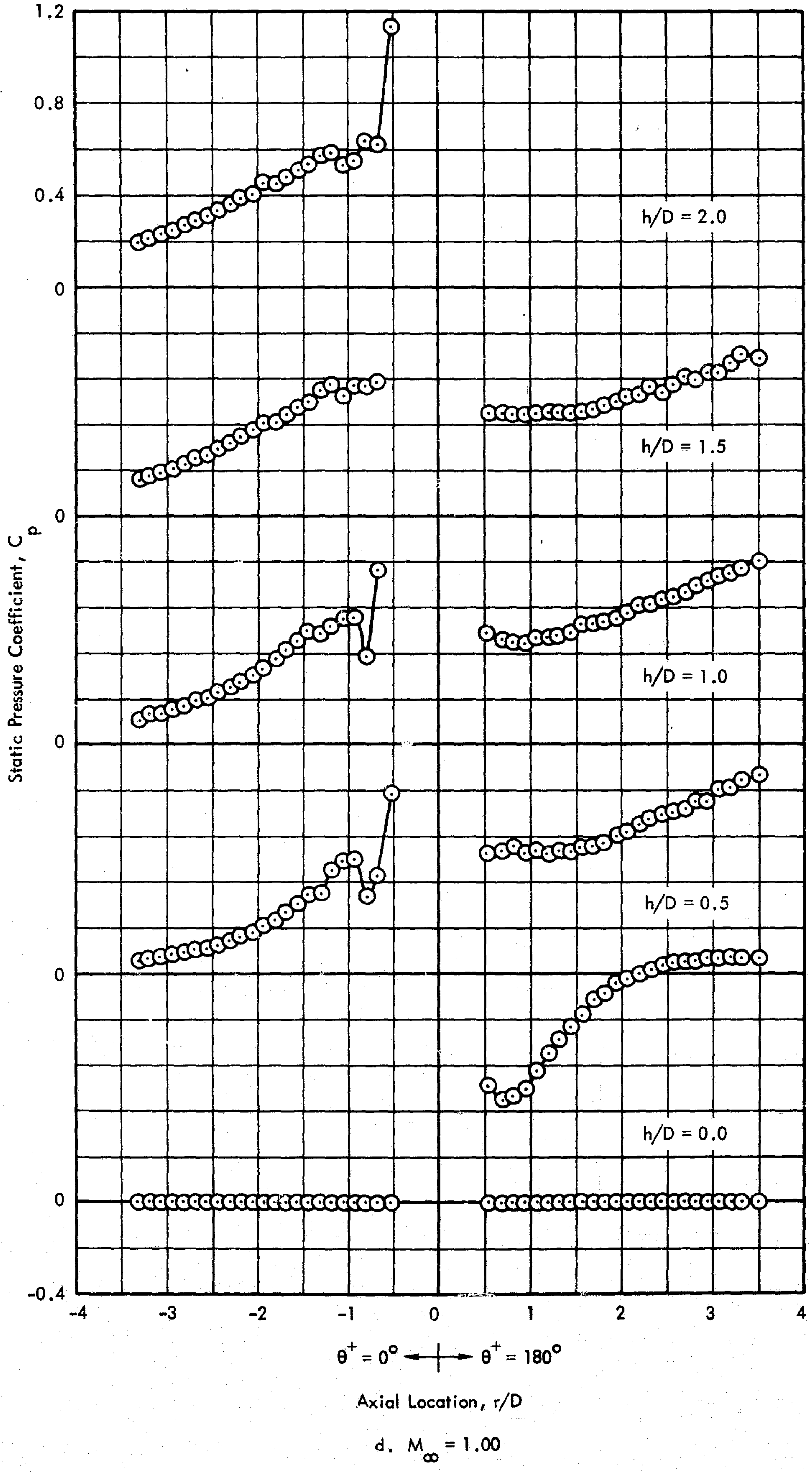

d. $M_\infty = 1.00$

Figure 30. Continued

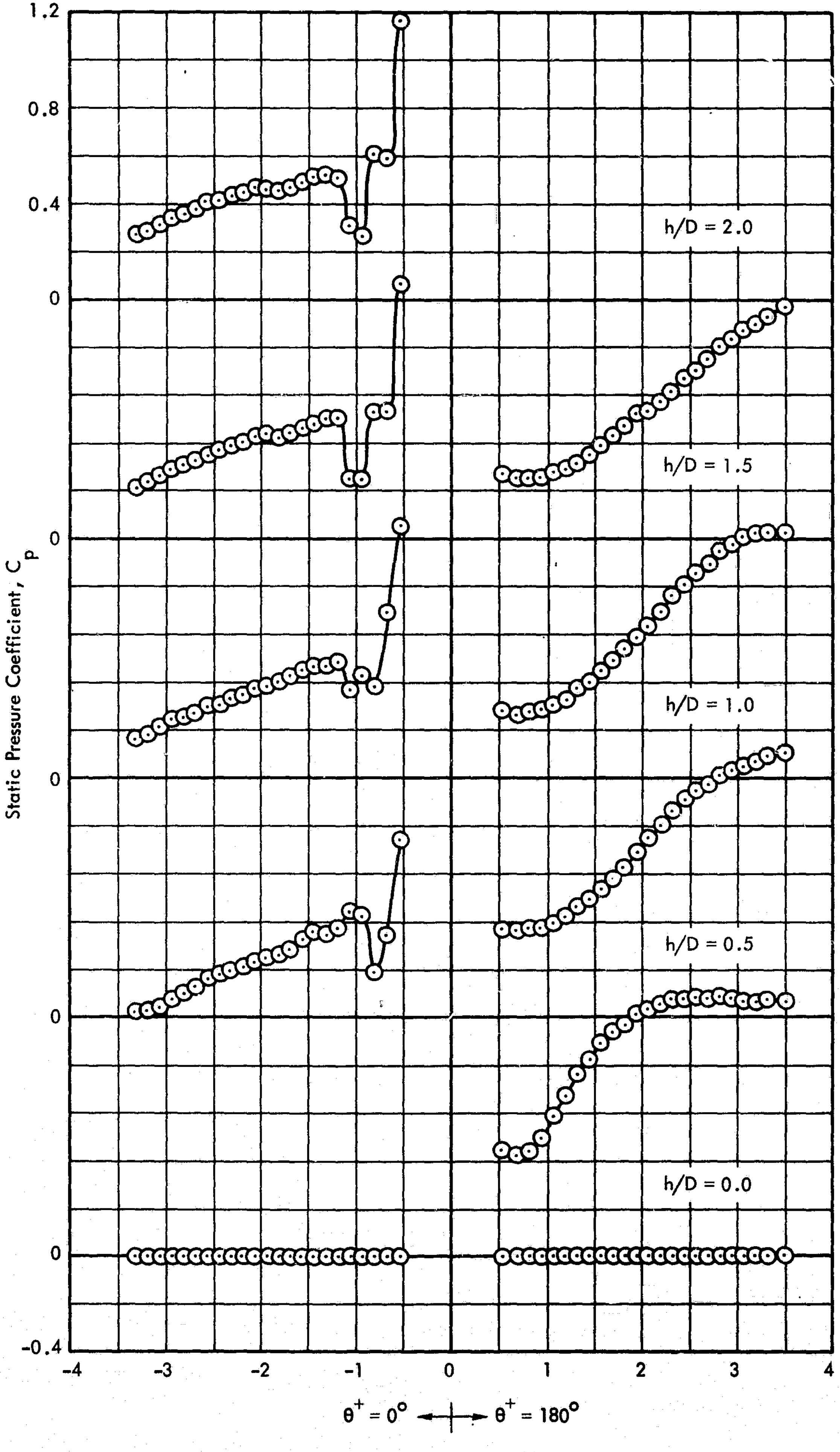

e. $M_\infty = 1.10$

Figure 30. Continued

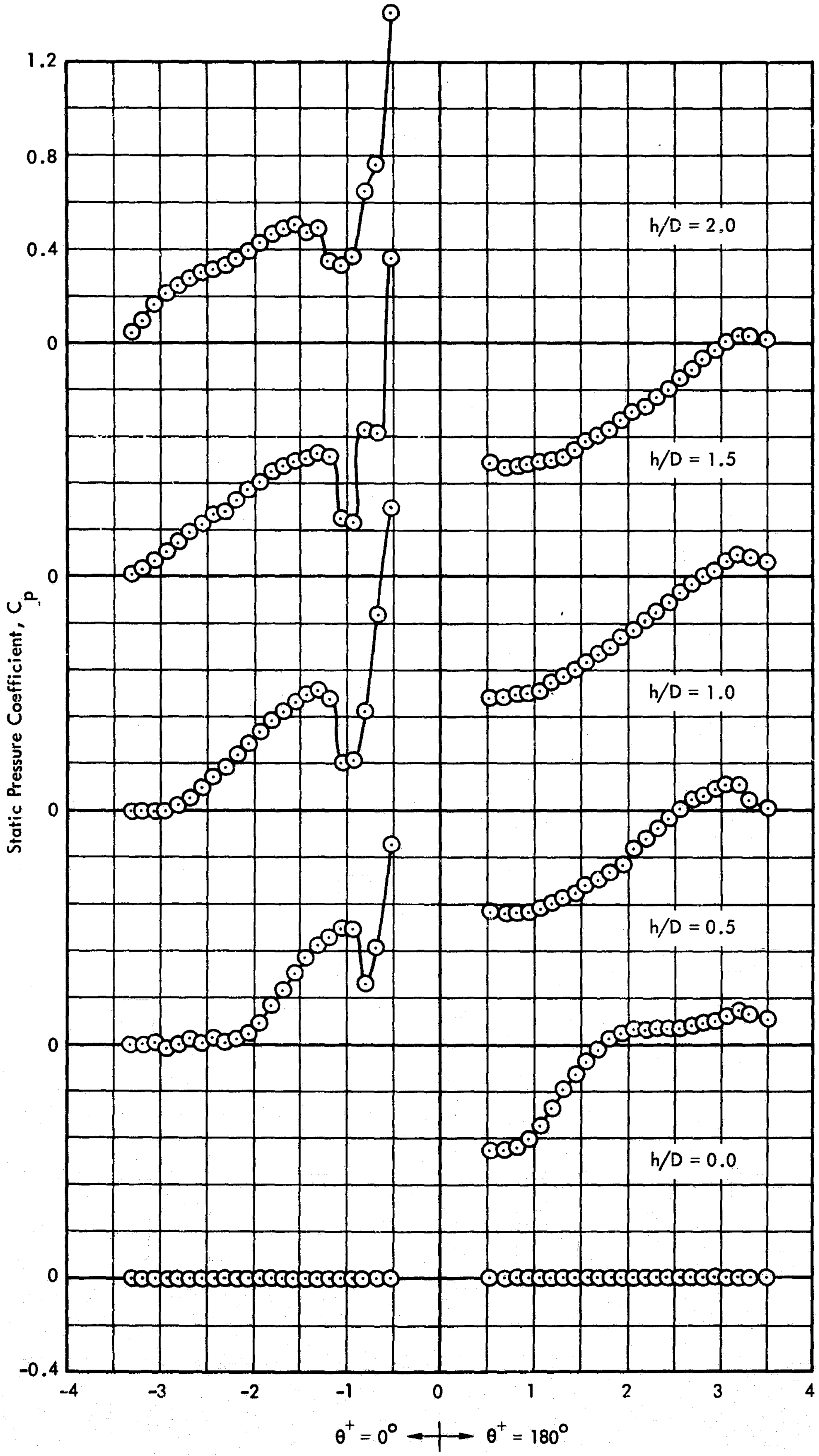

Axial Location, r/D

f. $M_\infty = 1.20$

Figure 30. Continued

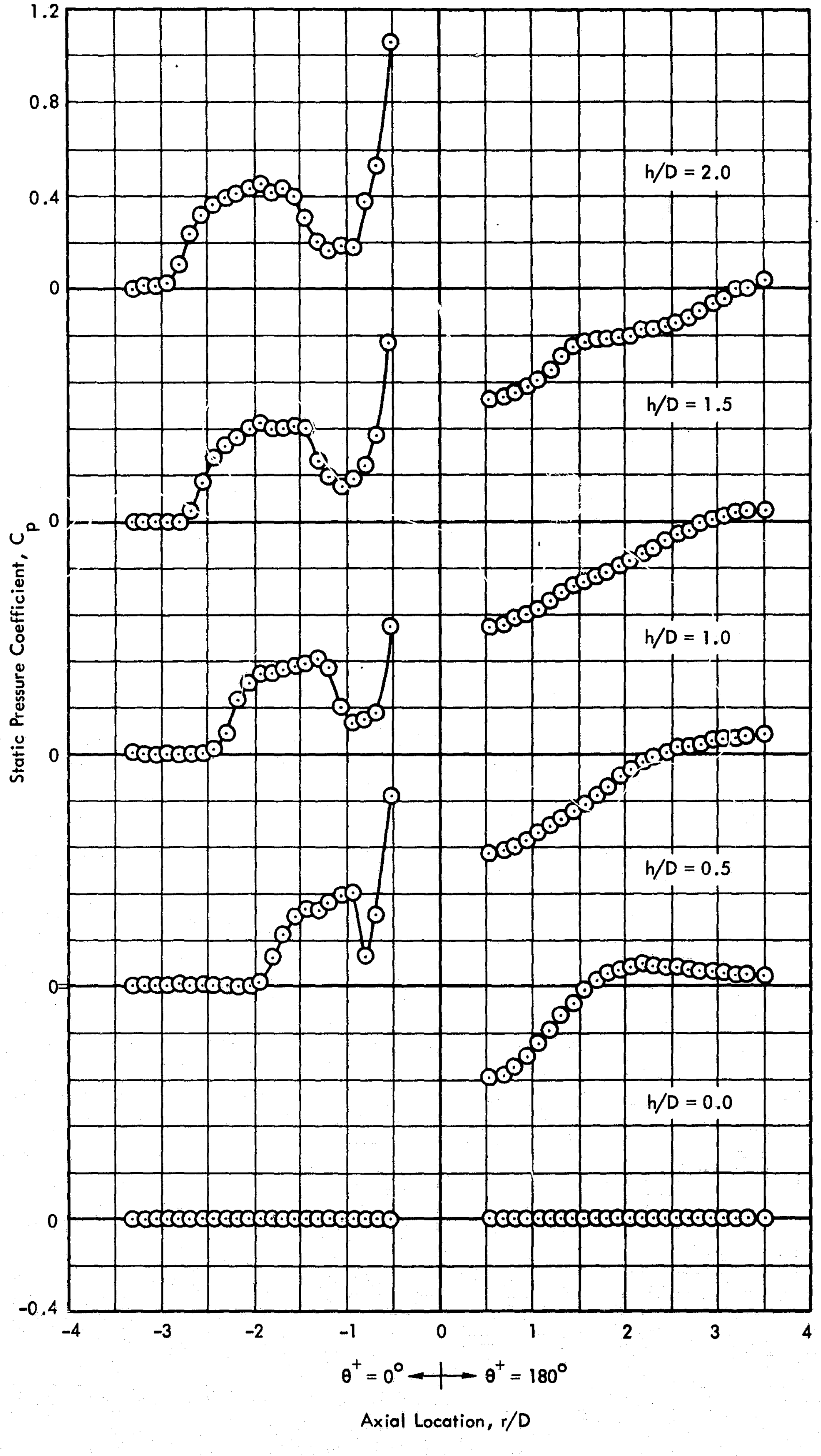

g. $M_\infty = 1.40$

Figure 30. Continued

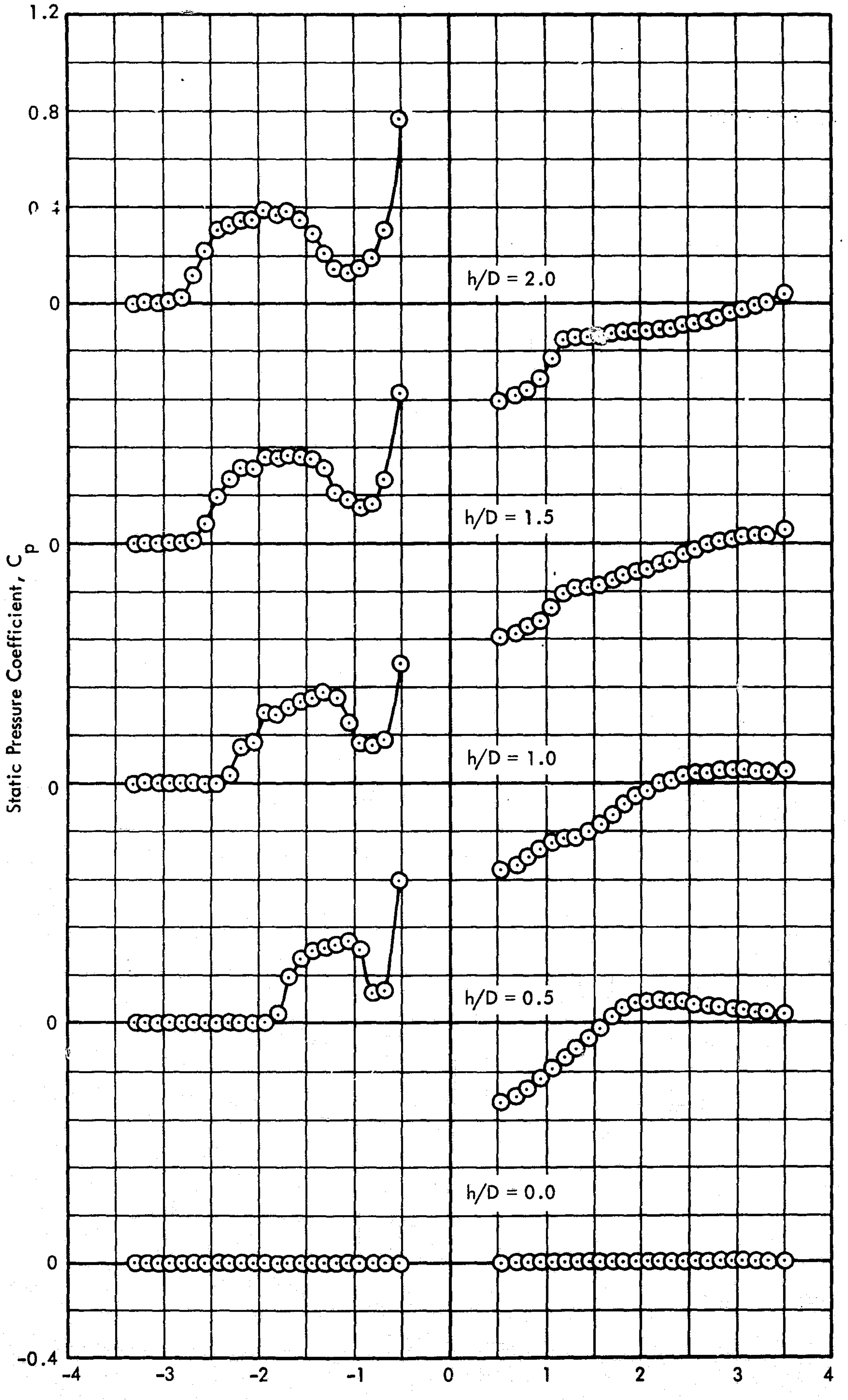

h. $M_\infty = 1.60$

Figure 30. Concluded

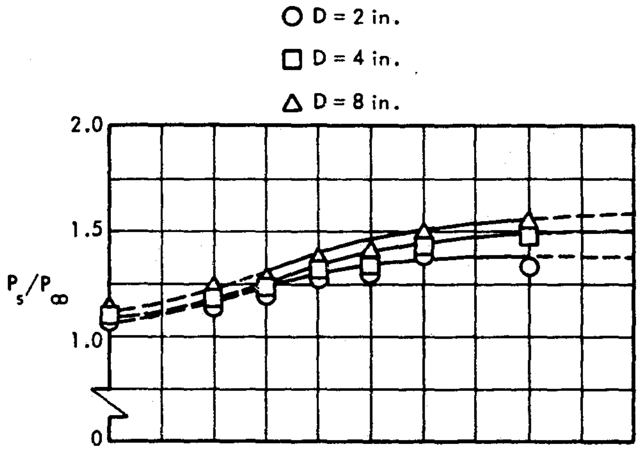

a. h/D = 2.0

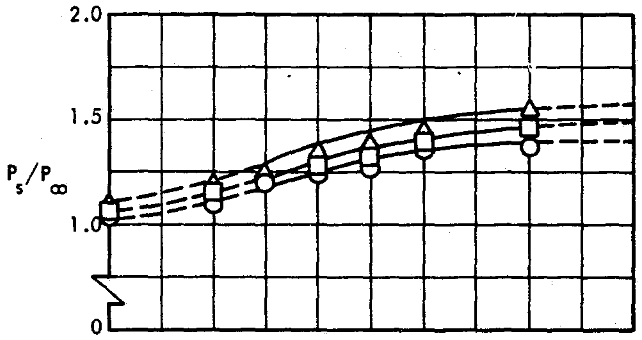

b. h/D = 1.5

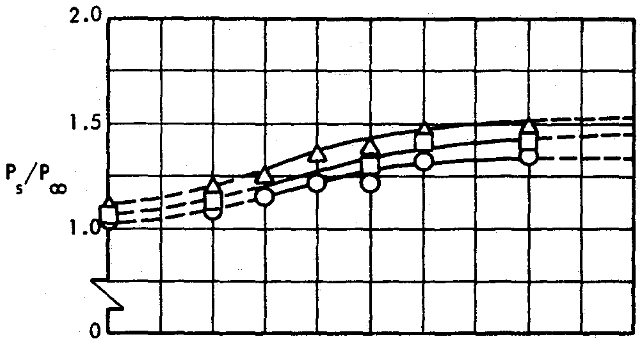

c. h/D = 1.0

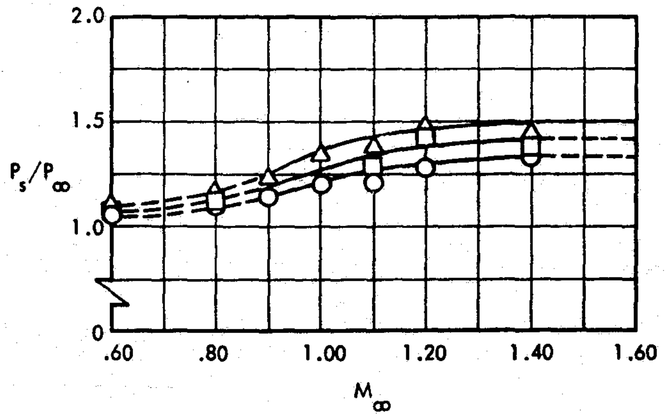

d. h/D = 0.5

Figure 31. Variation of the Separation-to-Free-Stream Pressure Ratio with Mach Number

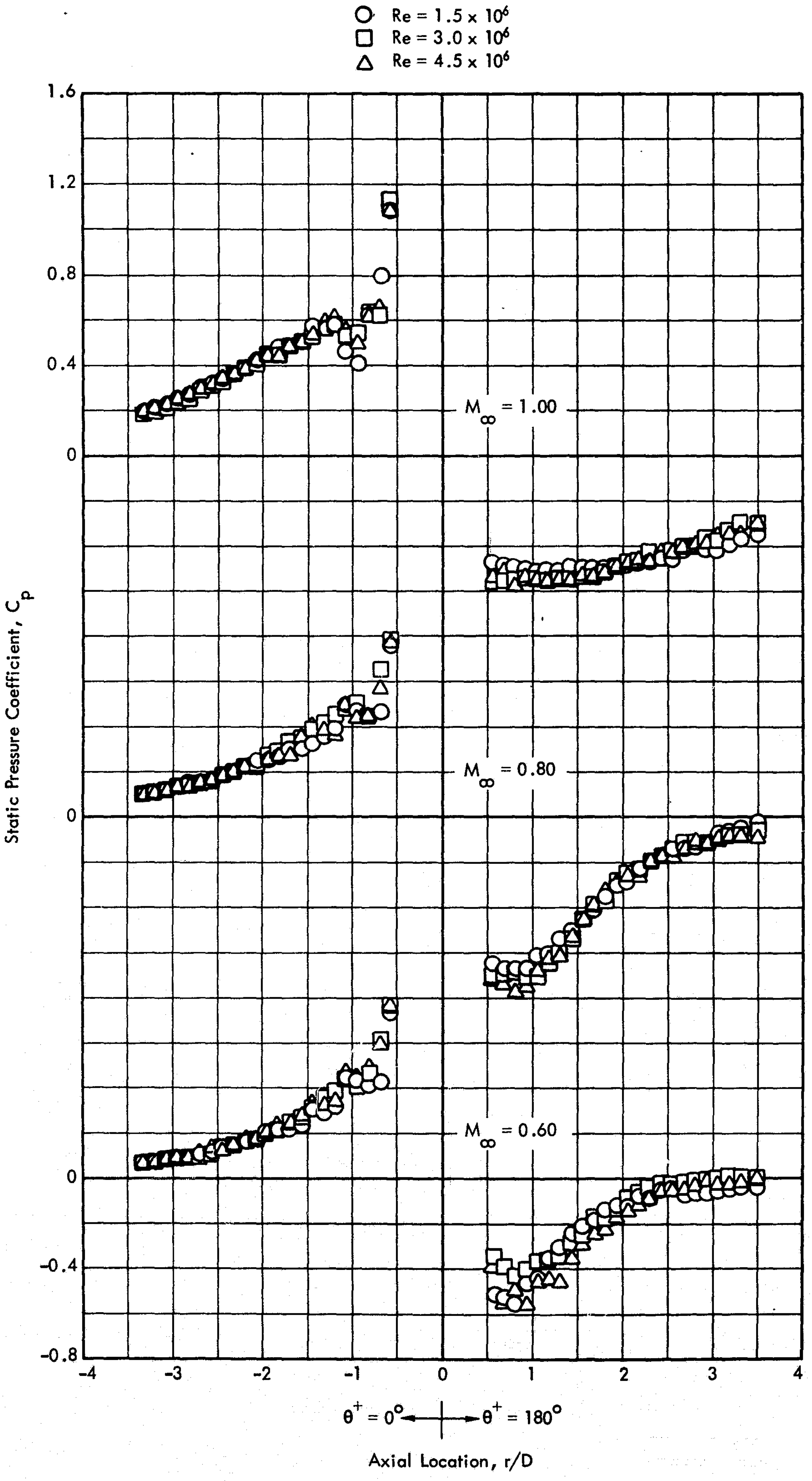

Figure 32. Effect of Reynolds Number on the Axial Distributions of Static Pressure Coefficient, 8-inch Diameter Protuberance, h/D = 2.0

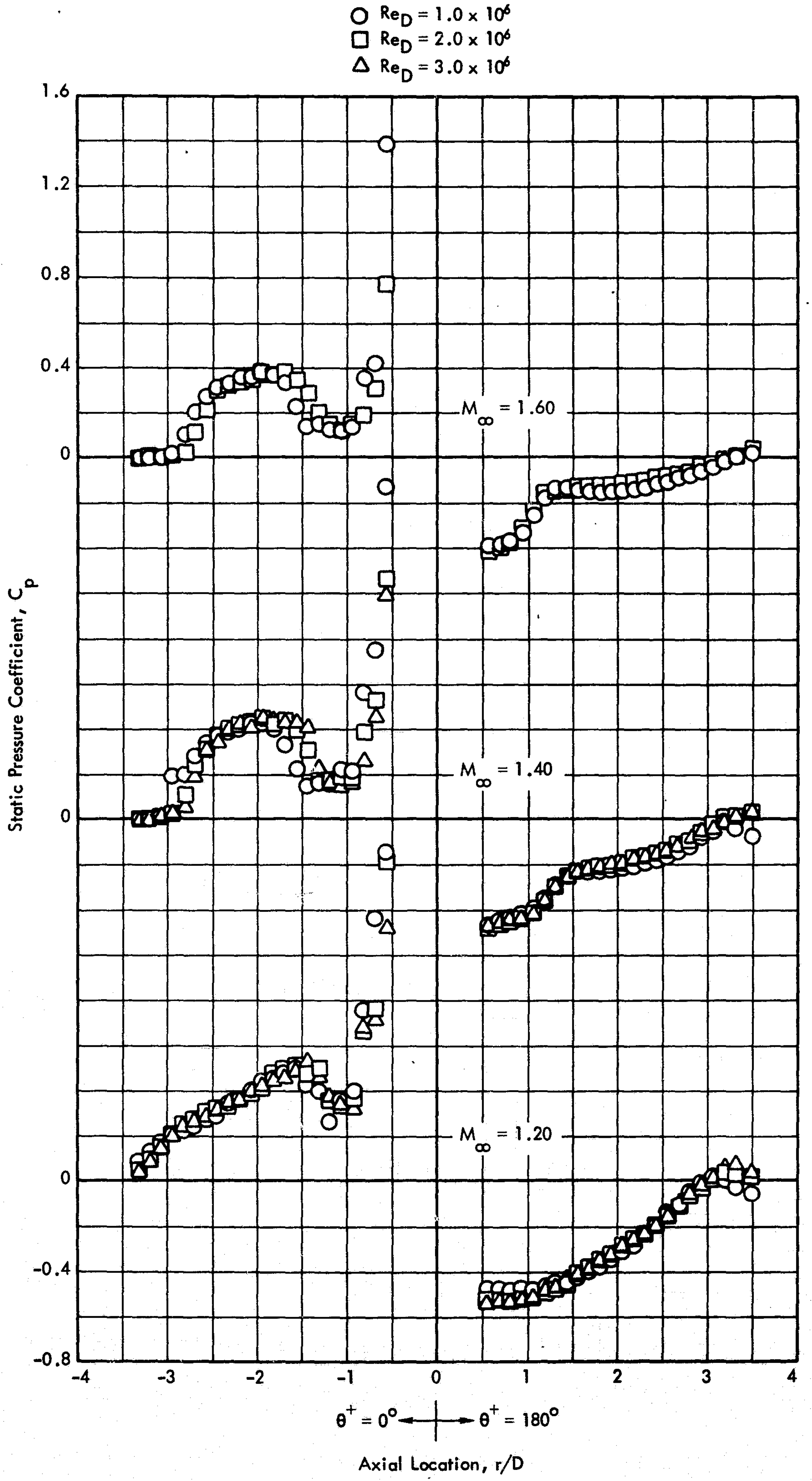

Figure 32. Concluded

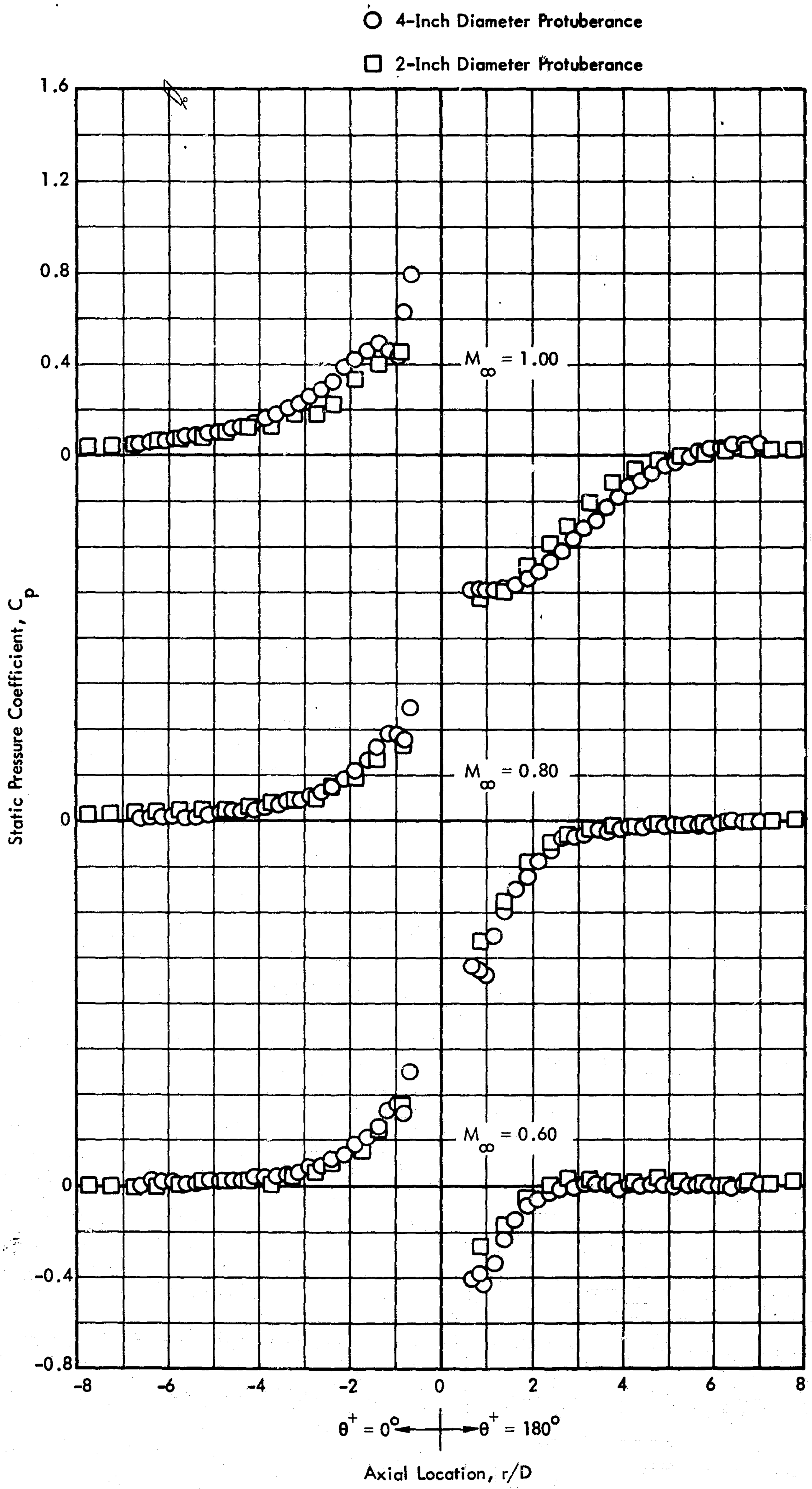

Figure 33. Effect of Protuberance Size on the Axial Distribution of Static Pressure Coefficient, $Re_D = 0.5 \times 10^6$, $h/D = 2.0$

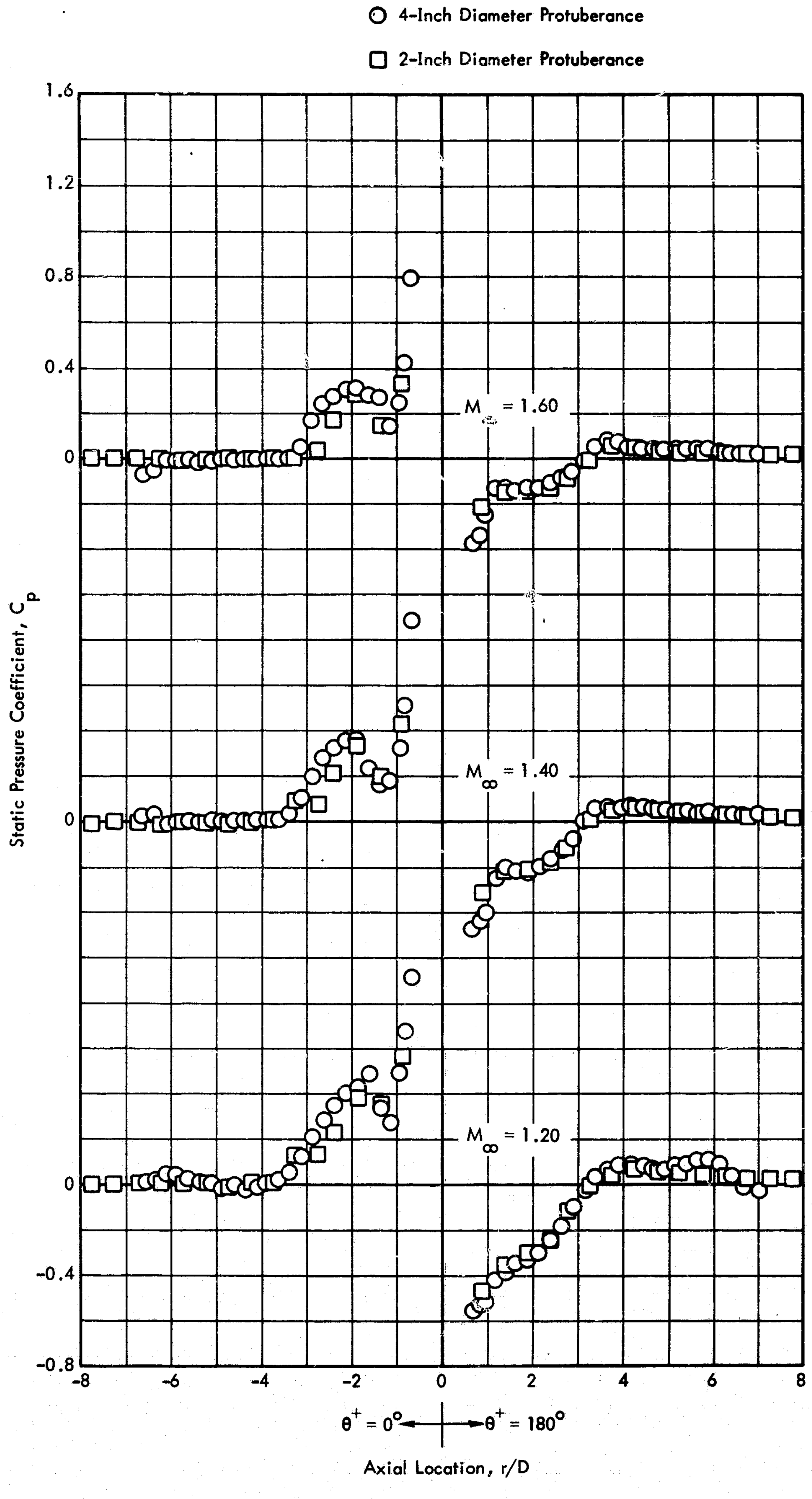

Figure 33. Concluded

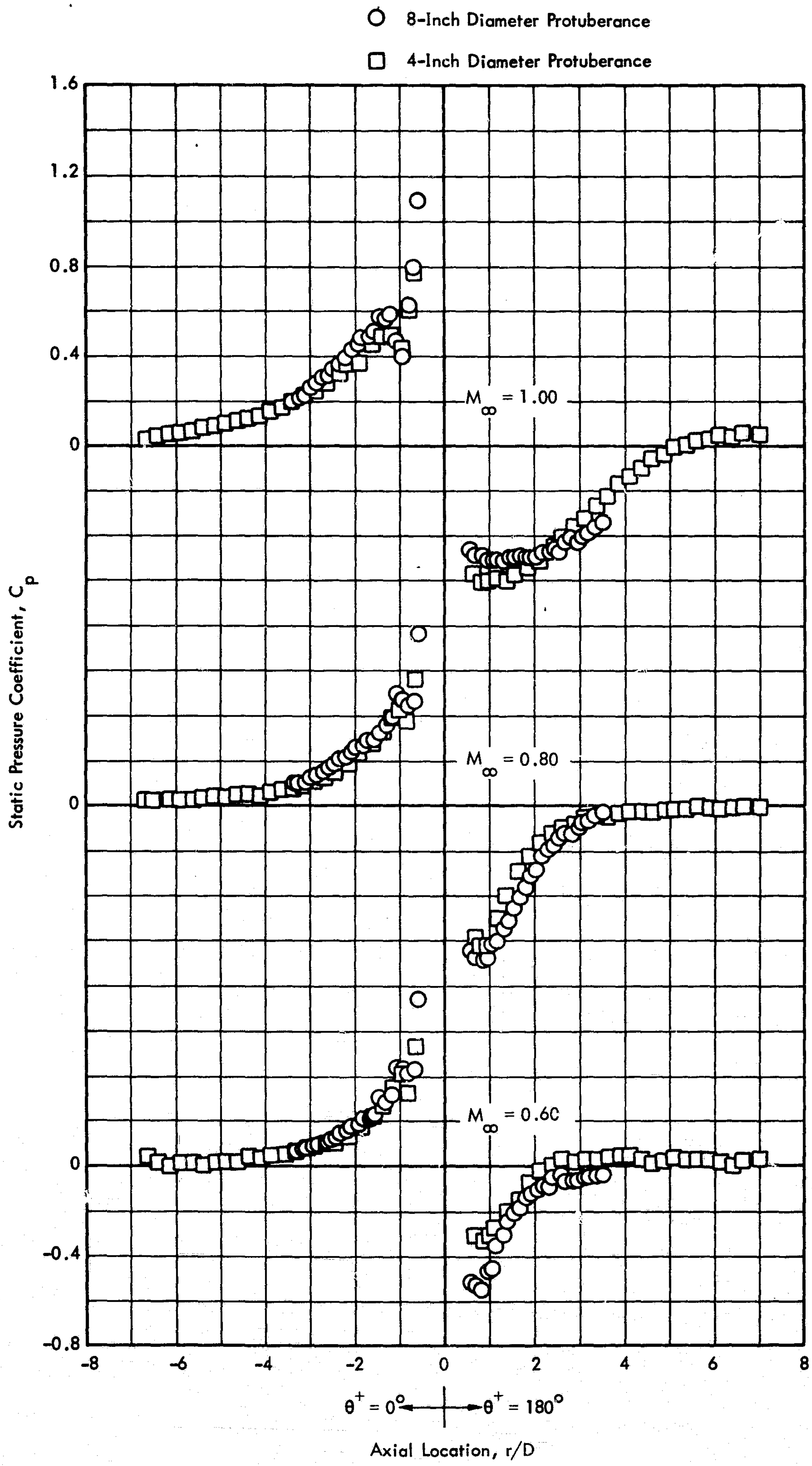

Figure 34. Effect of Protuberance Size on the Axial Distributions of Static Pressure Coefficient, $Re_D = 1.0 \times 10^6$, $h/D = 2.0$

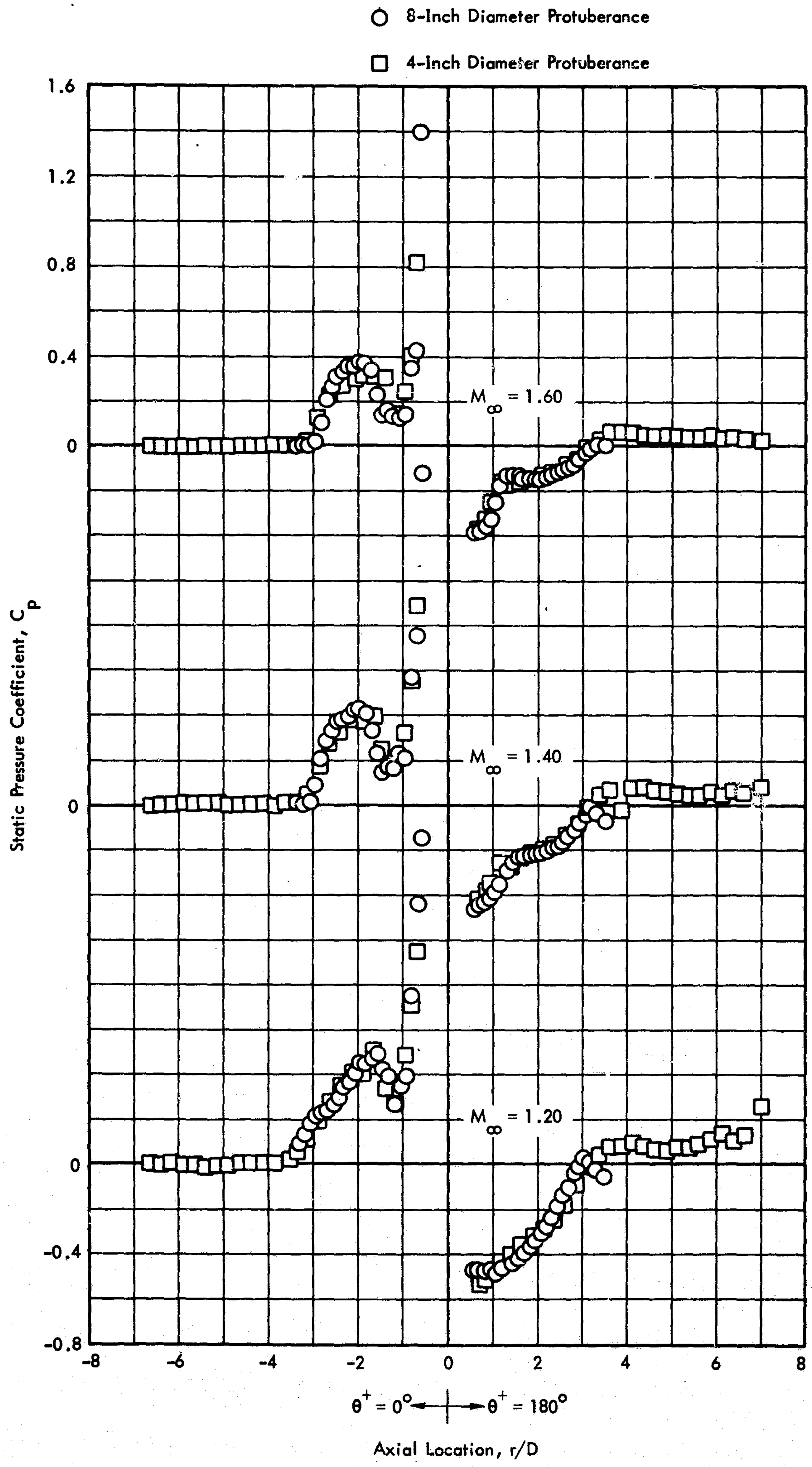

Figure 34. Concluded

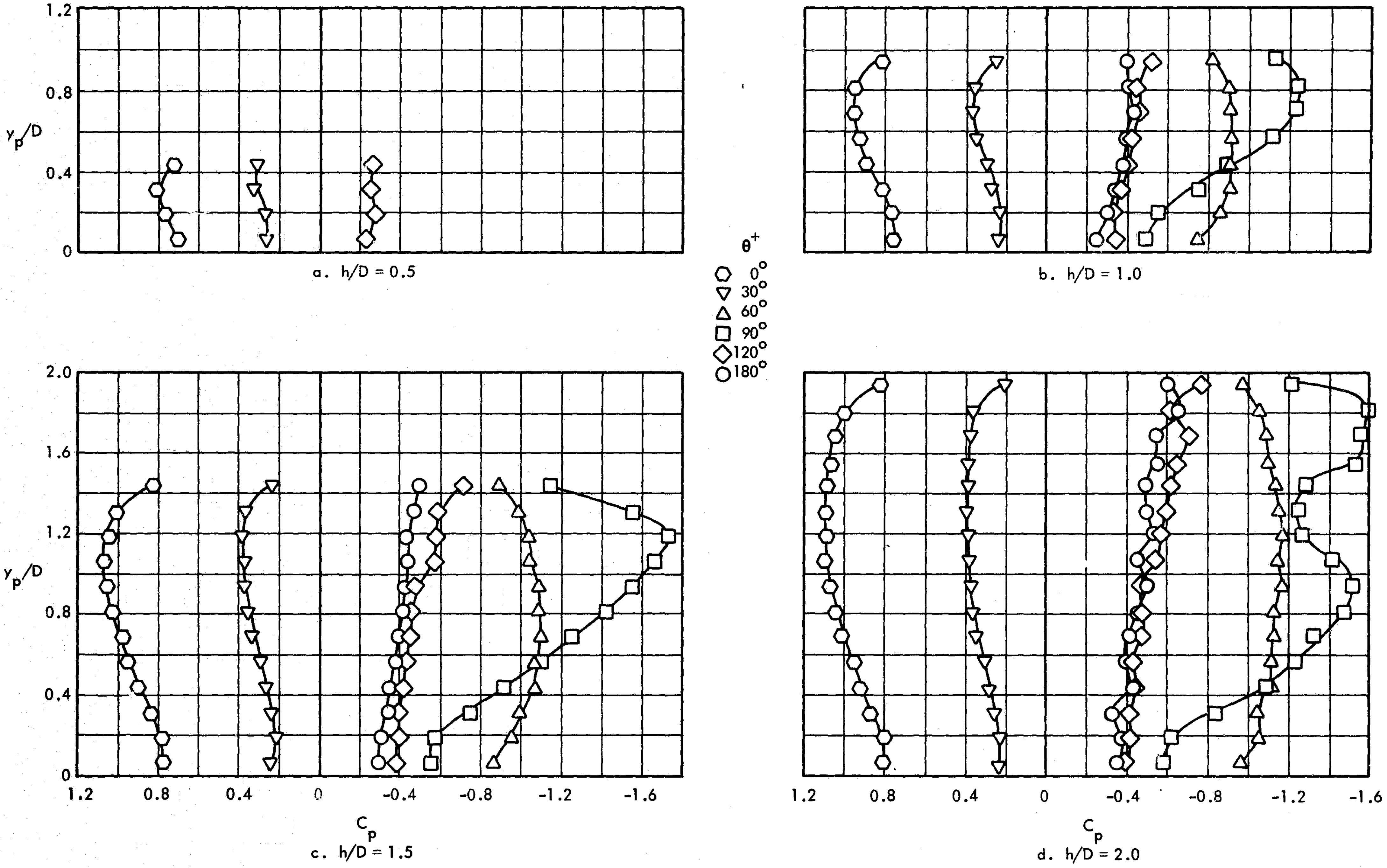

a. h/D = 0.5

b. h/D = 1.0

c. h/D = 1.5

d. h/D = 2.0

Figure 35. Variation of Static Pressure Coefficient Over the Wall of the 8-inch Diameter Protuberance, $M_\infty = 0.60$, $Re/ft = 3 \times 10^6$

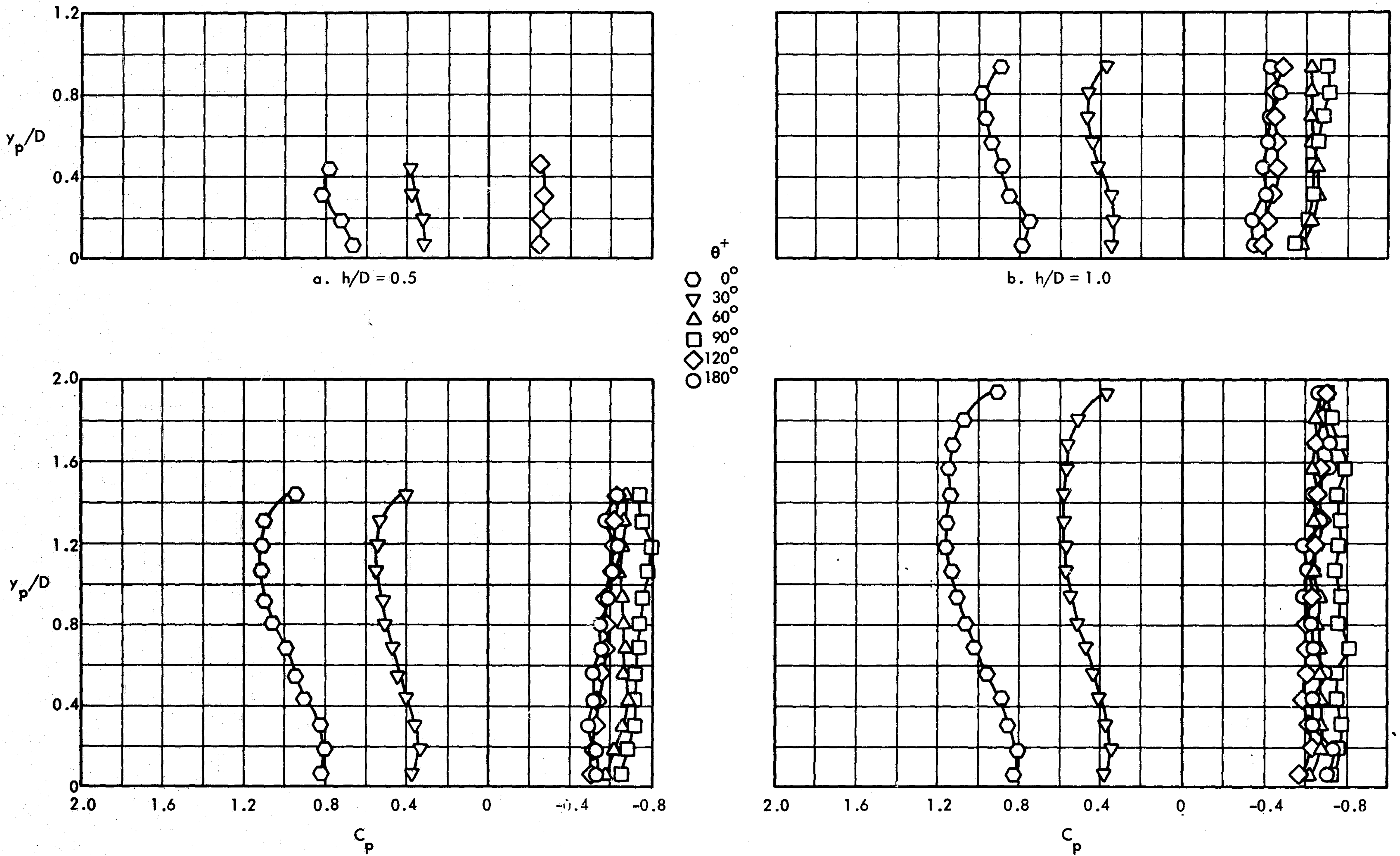

a. h/D = 0.5

b. h/D = 1.0

c. h/D = 1.5

d. h/D = 2.0

Figure 36. Variation of Static Pressure Coefficient Over the Wall of the 8-inch Diameter Protuberance, $M_\infty = 0.80$, Re/ft = 3×10^6

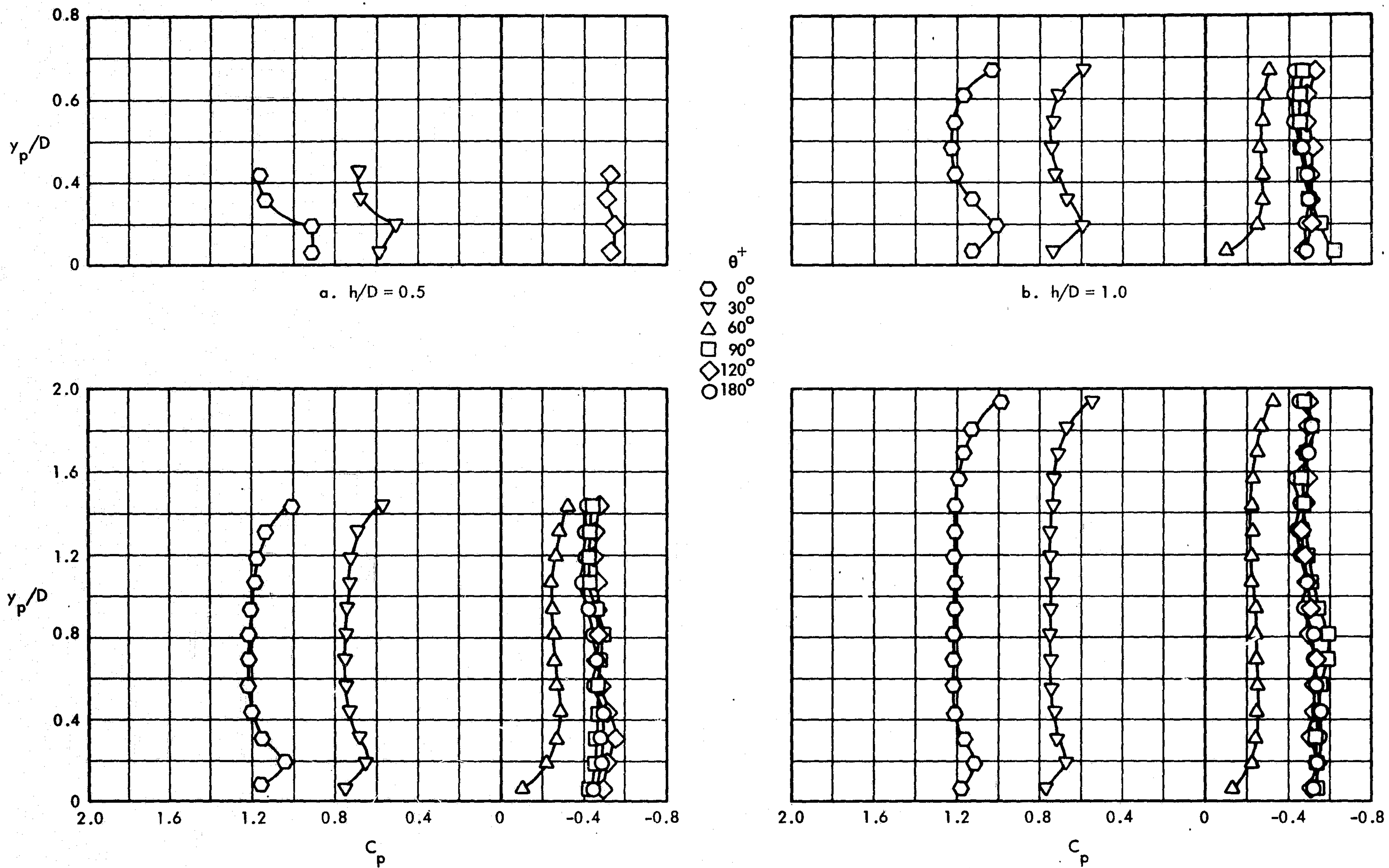

a. h/D = 0.5

b. h/D = 1.0

c. h/D = 1.5

d. h/D = 2.0

Figure 37. Variation of Static Pressure Coefficient Over the Wall of the 8-inch Diameter Protuberance, $M_\infty = 1.00$, $Re/ft = 3 \times 10^6$

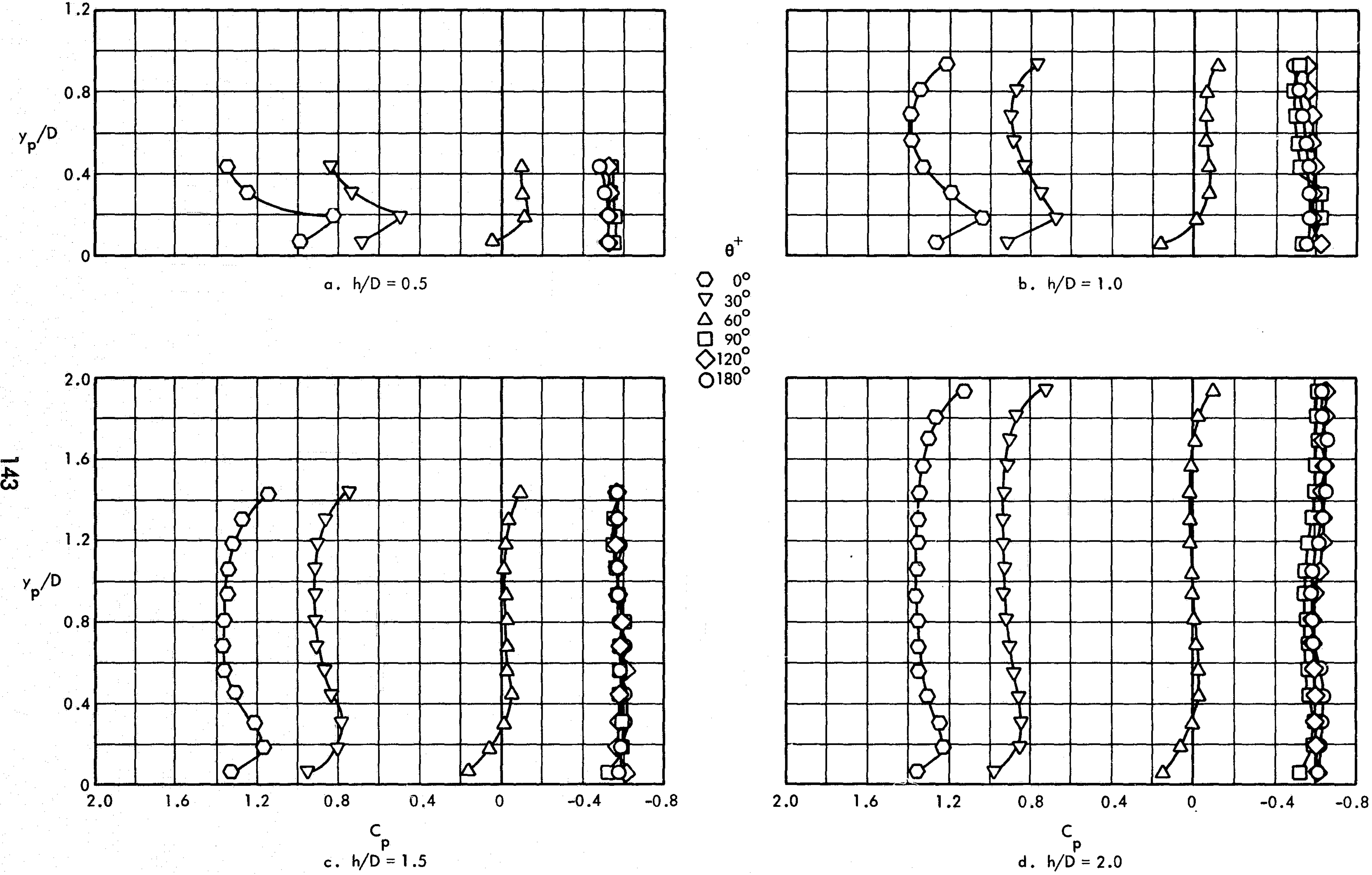

a. h/D = 0.5

b. h/D = 1.0

c. h/D = 1.5

d. h/D = 2.0

Figure 38. Variation of Static Pressure Coefficient Over the Wall of the 8-inch Diameter Protuberance, $M_\infty = 1.20$, Re/ft = 3×10^6

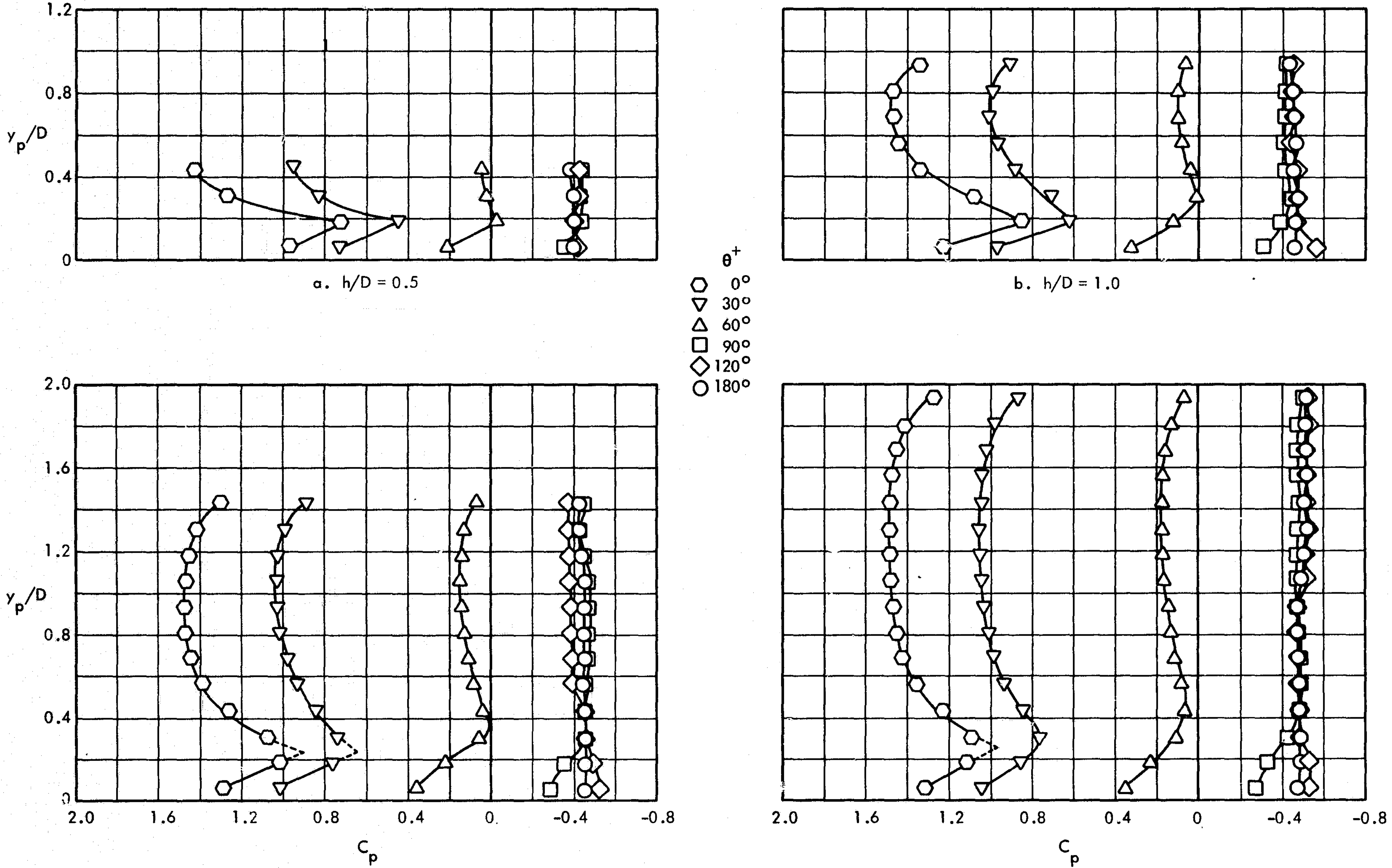

a. h/D = 0.5

b. h/D = 1.0

c. h/D = 1.5

d. h/D = 2.0

Figure 39. Variation of Static Pressure Coefficient Over the Wall of the 8-inch Diameter Protuberance, $M_\infty = 1.40$, Re/ft = 3×10^6

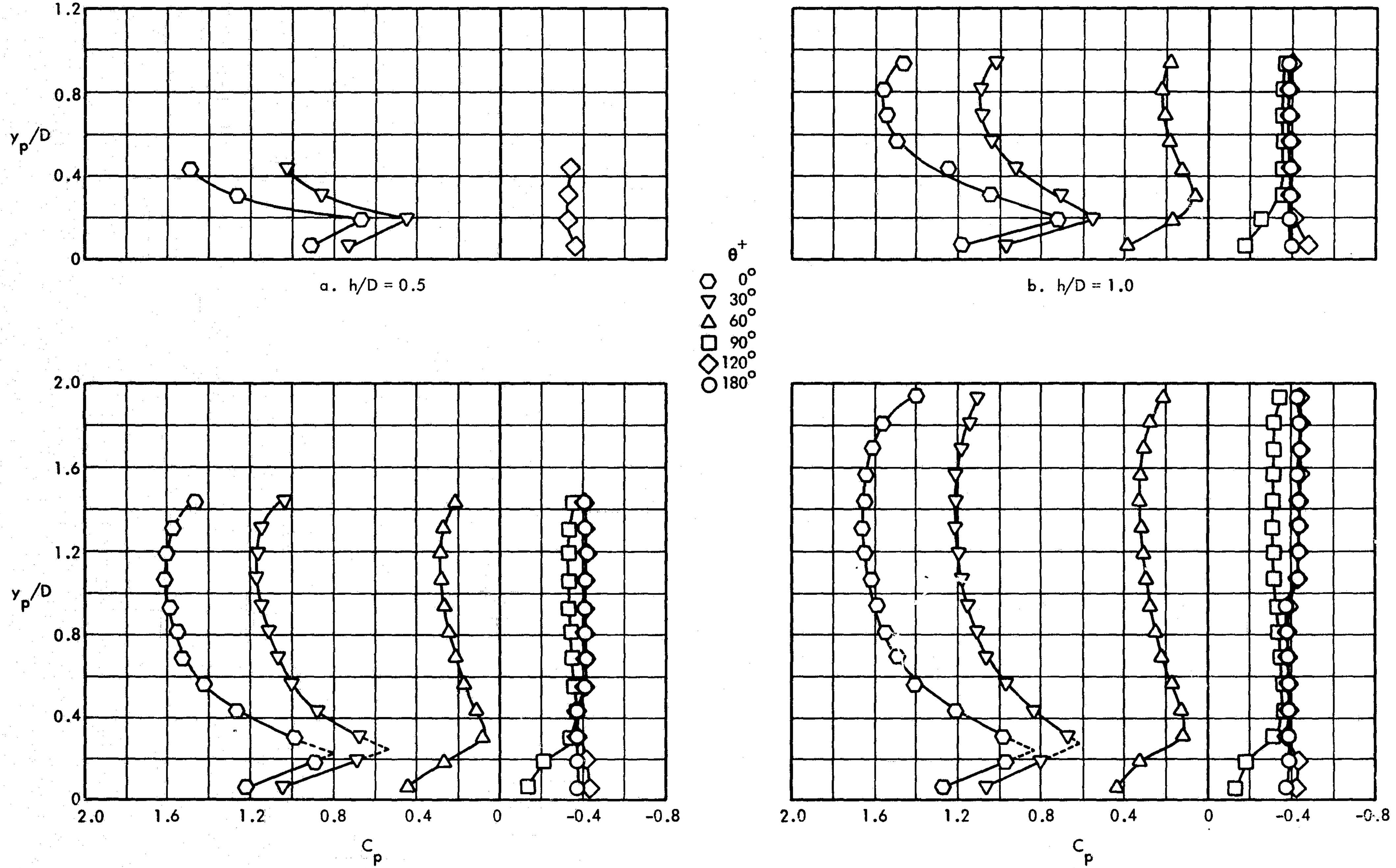

a. h/D = 0.5

b. h/D = 1.0

c. h/D = 1.5

d. h/D = 2.0

Figure 40. Variation of Static Pressure Coefficient Over the Wall of the 8-inch Diameter Protuberance, $M_\infty = 1.60$, $Re/ft = 3 \times 10^6$

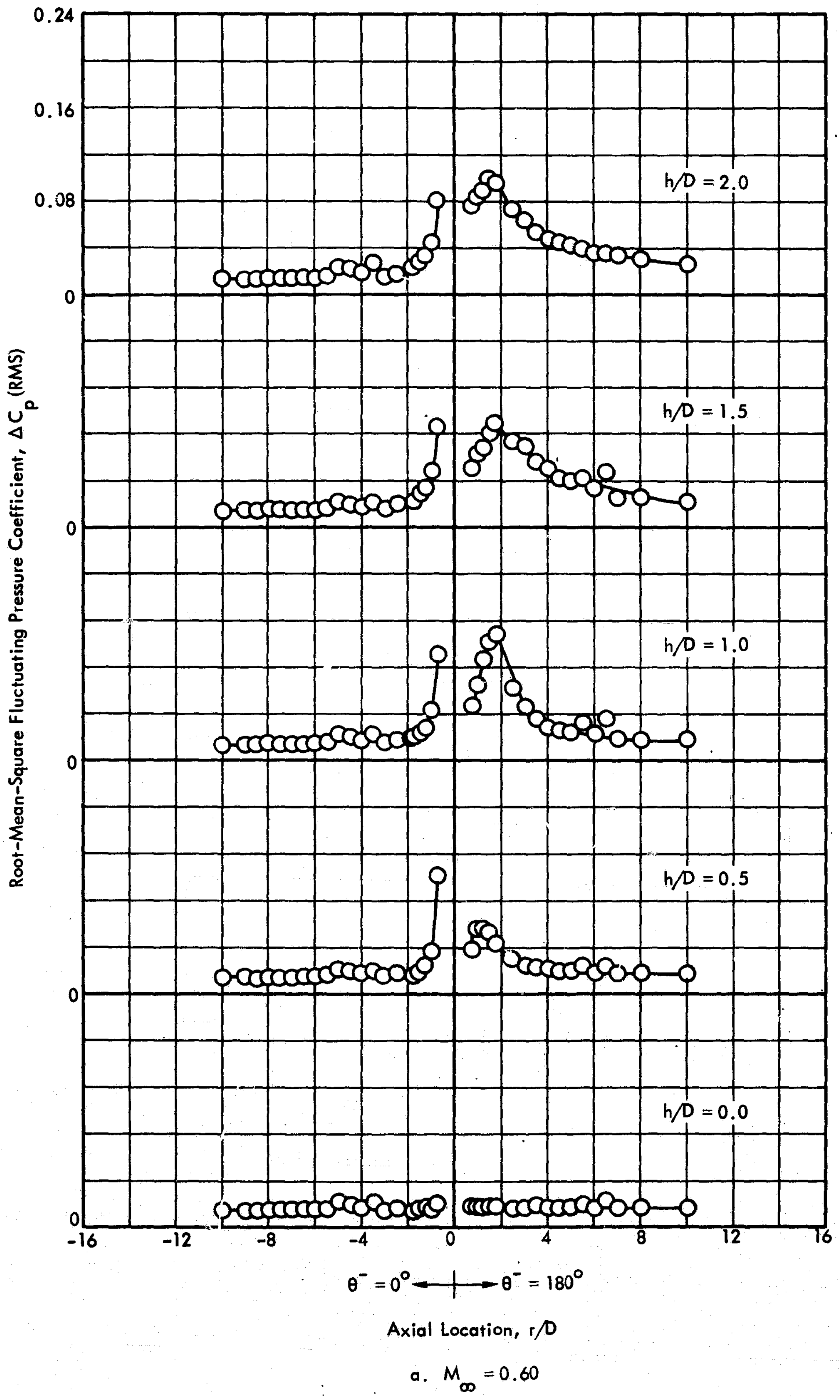

a. $M_\infty = 0.60$

Figure 41. Variation of the RMS Fluctuating Pressure Coefficient Along the Longitudinal Centerline of the Test Panel, 2-inch Diameter Protuberance, $Re/ft = 3 \times 10^6$

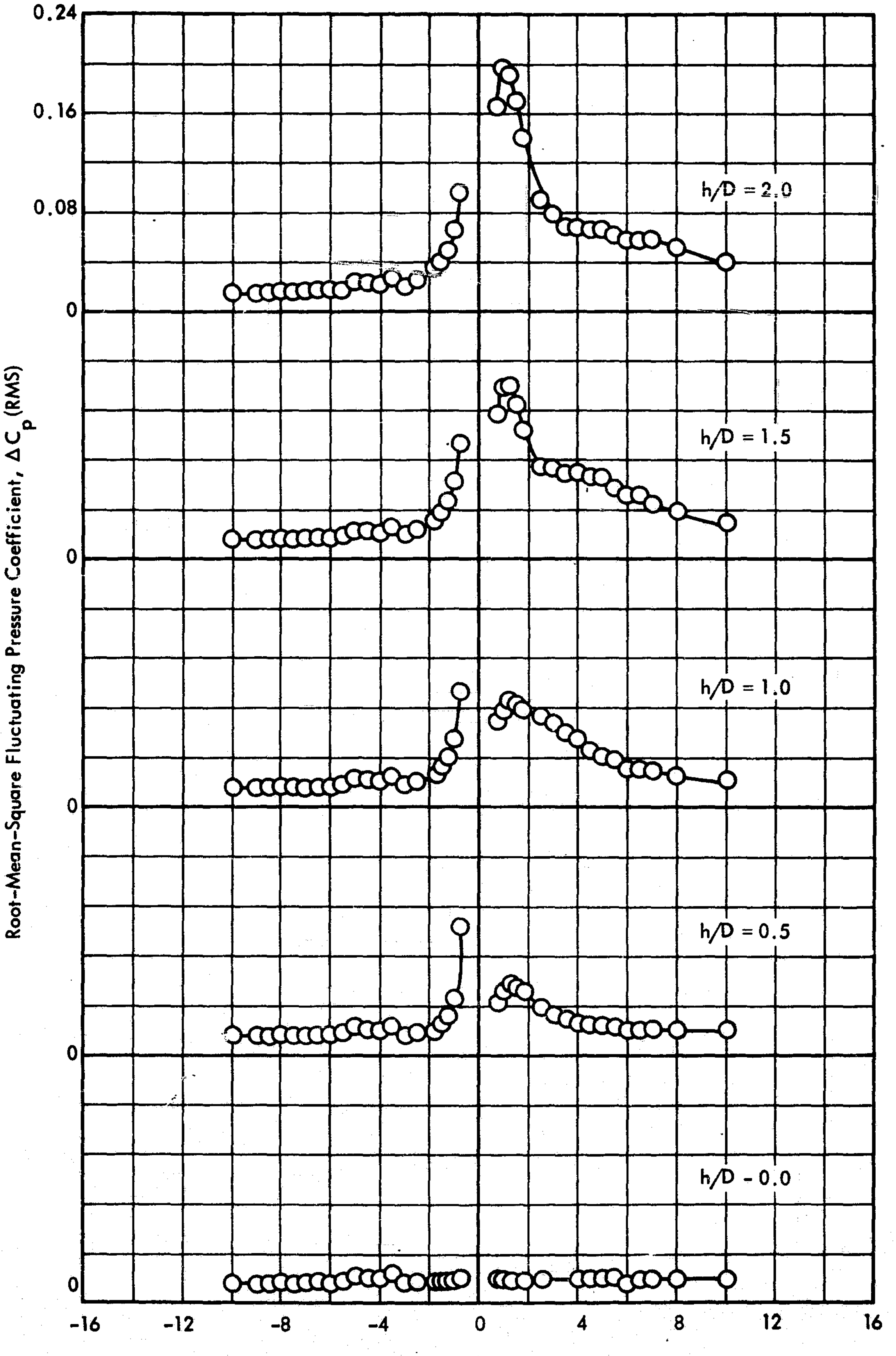

b. $M_\infty = 0.80$

Figure 41. Continued

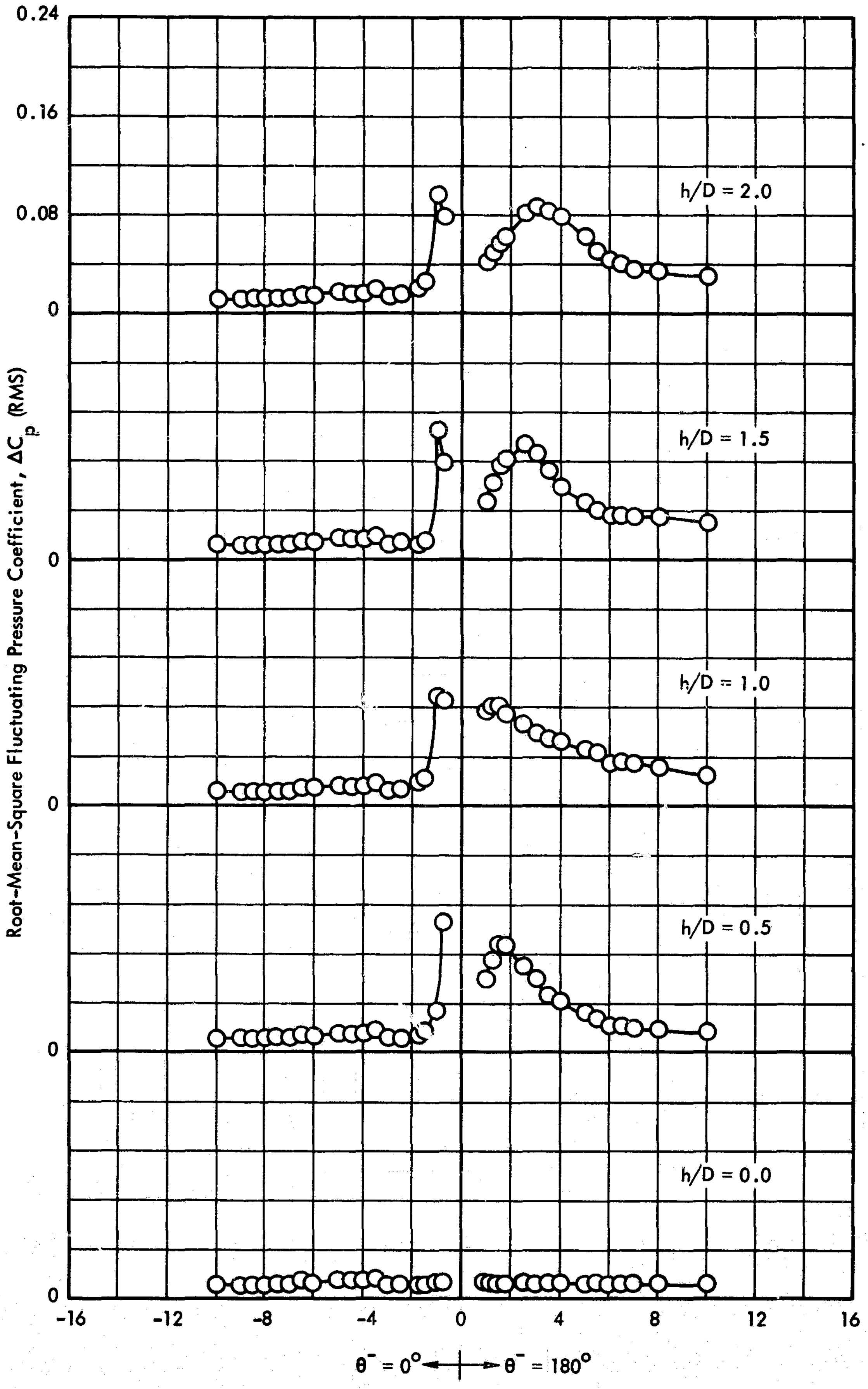

c. $M_\infty = 1.00$

Figure 41. Continued

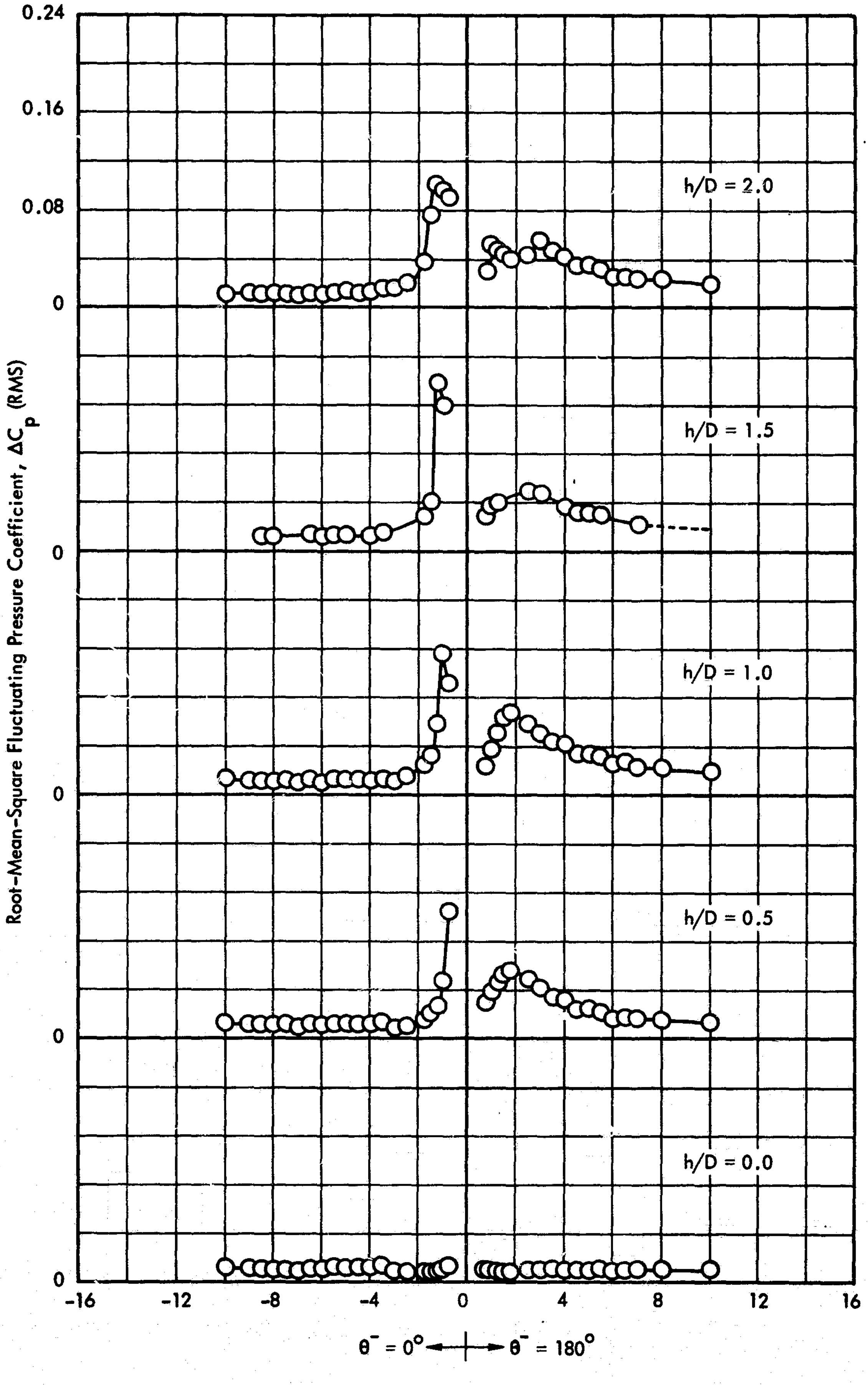

d. $M_\infty = 1.20$

Figure 41. Continued

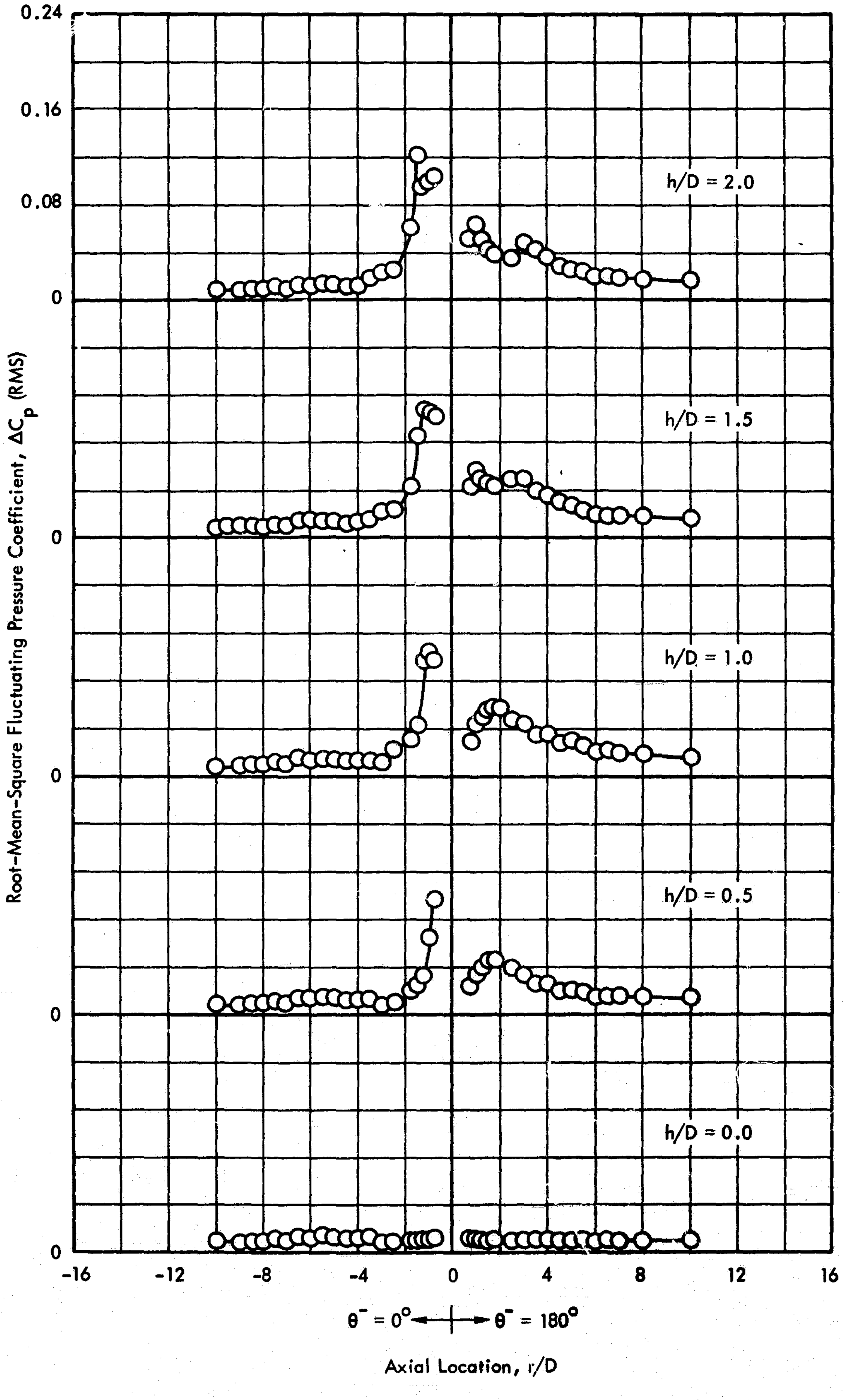

e. M_∞ = 1.40

Figure 41. Continued

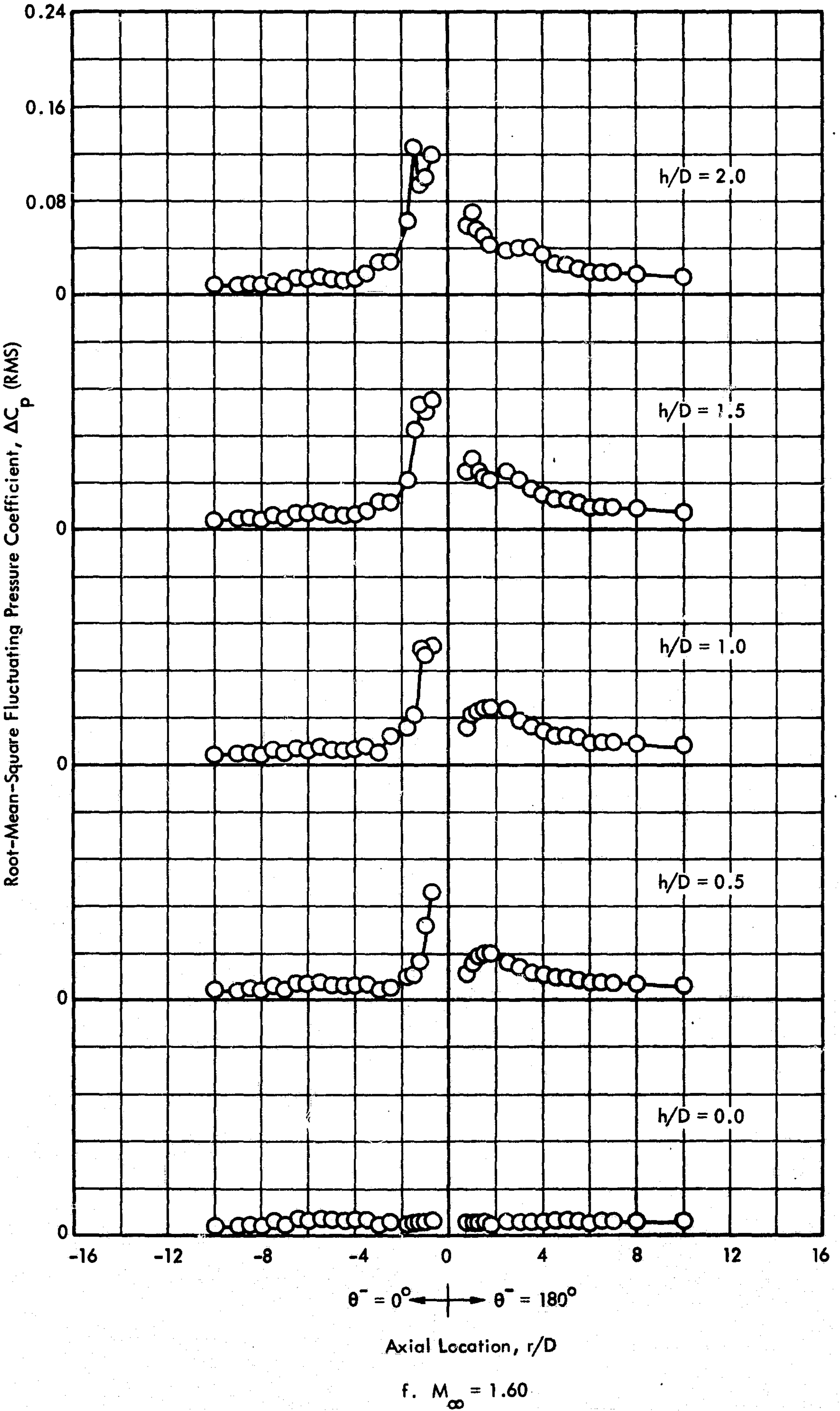

f. $M_\infty = 1.60$

Figure 41. Concluded

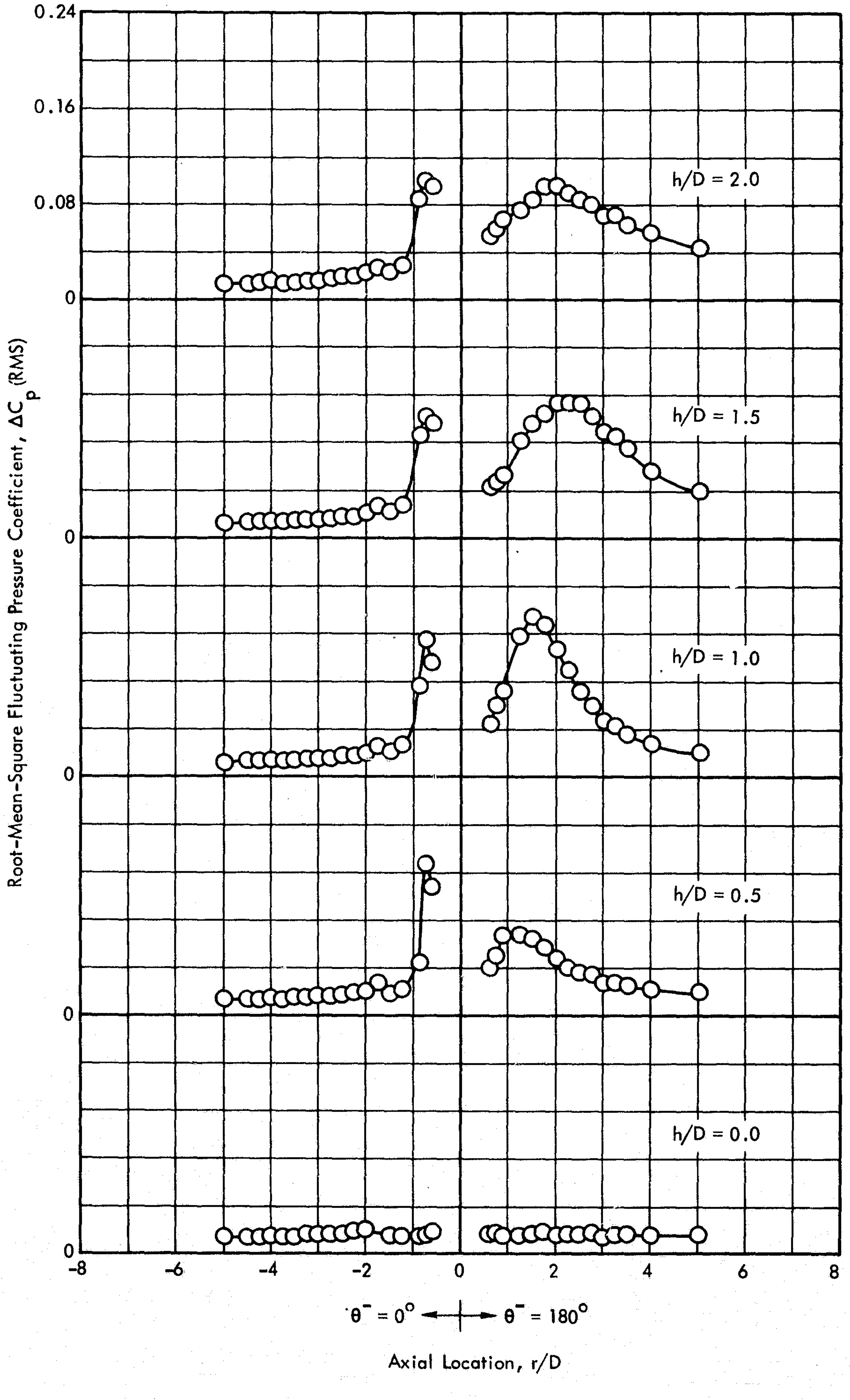

a. $M_\infty = 0.60$

Figure 42. Variation of the RMS Fluctuating Pressure Coefficient Along the Longitudinal Centerline of the Test Panel, 4-inch Diameter Protuberance, Re/ft = 3×10^6

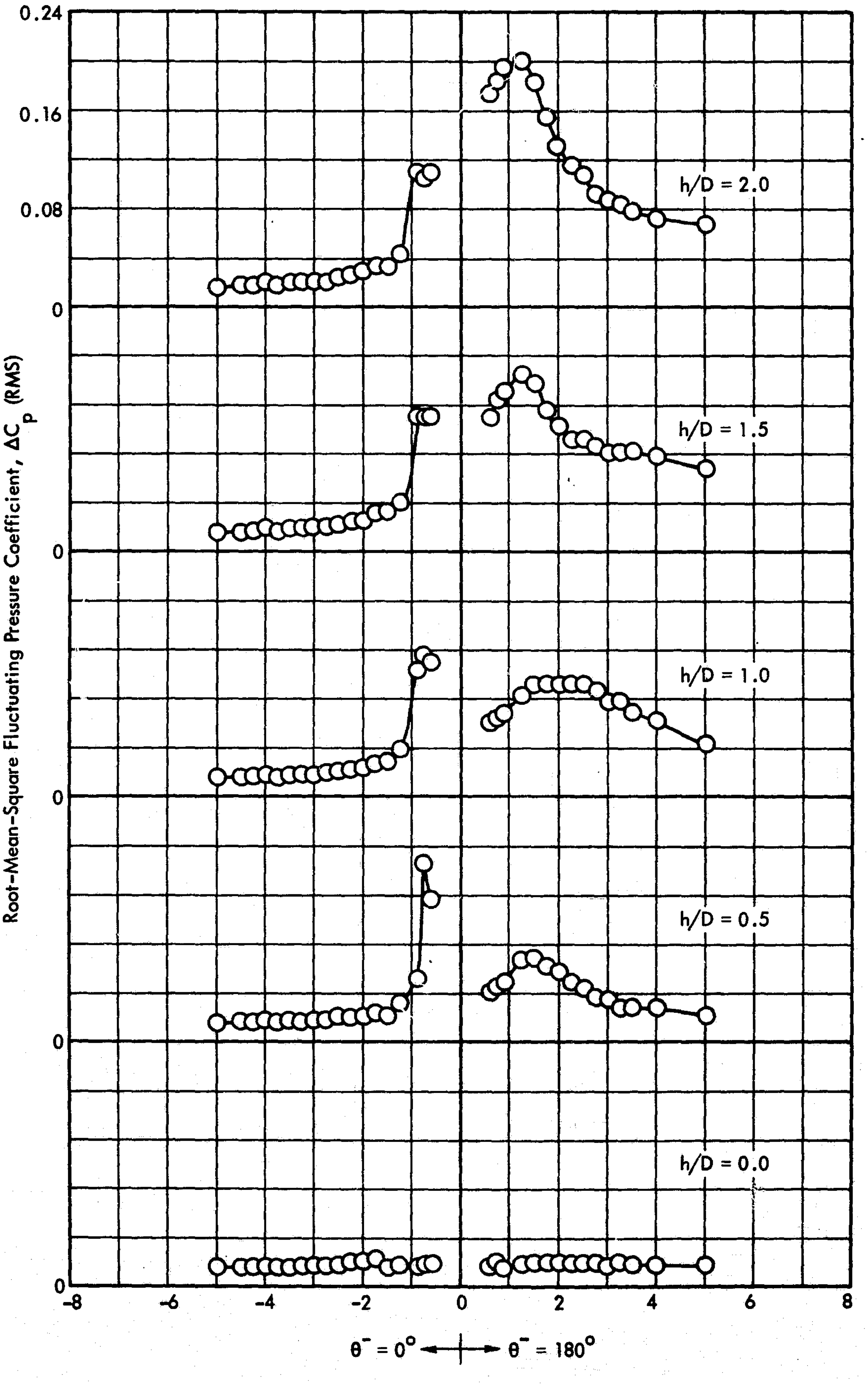

b. $M_\infty = 0.80$

Figure 42. Continued

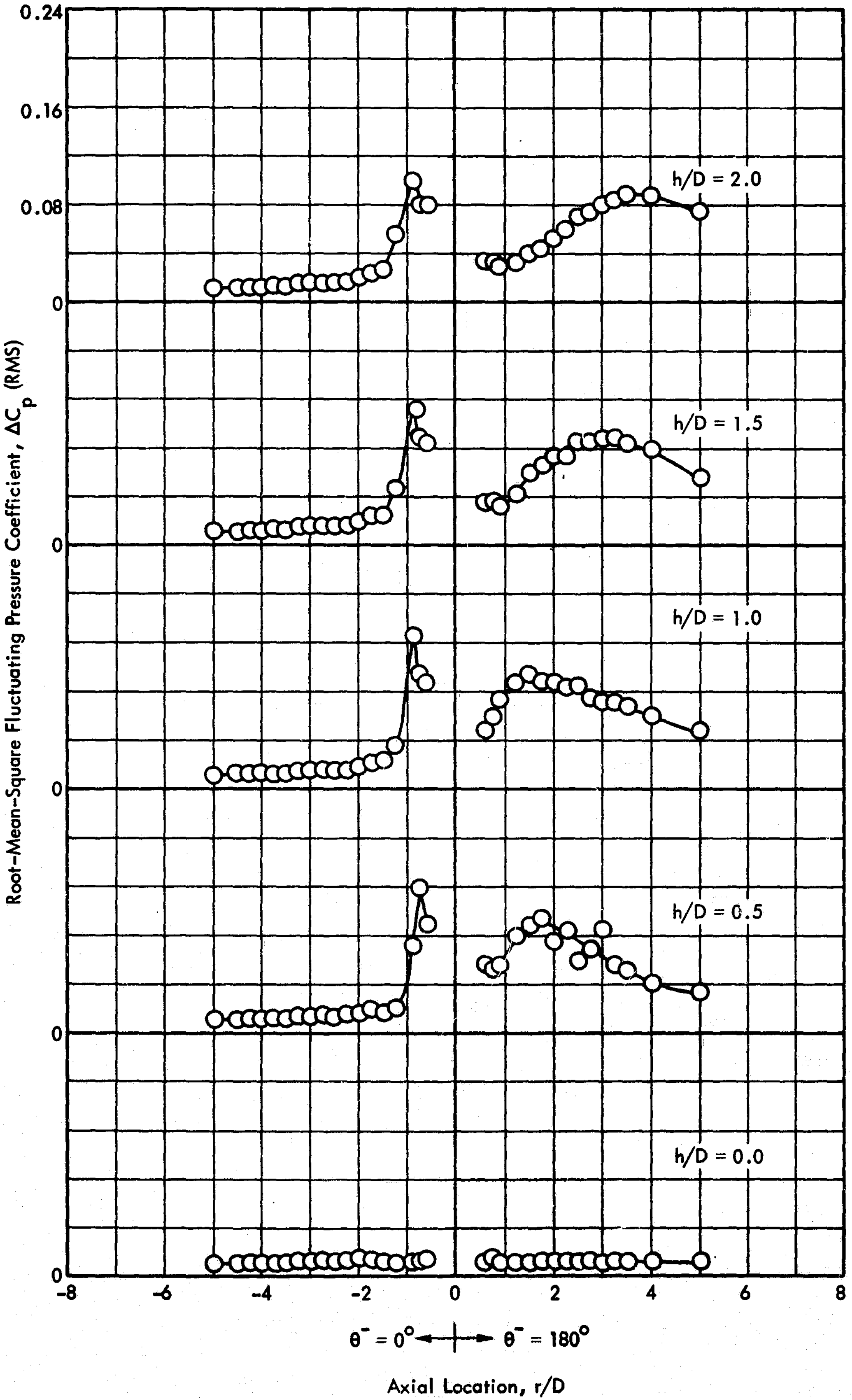

c. $M_\infty = 1.00$

Figure 42. Continued

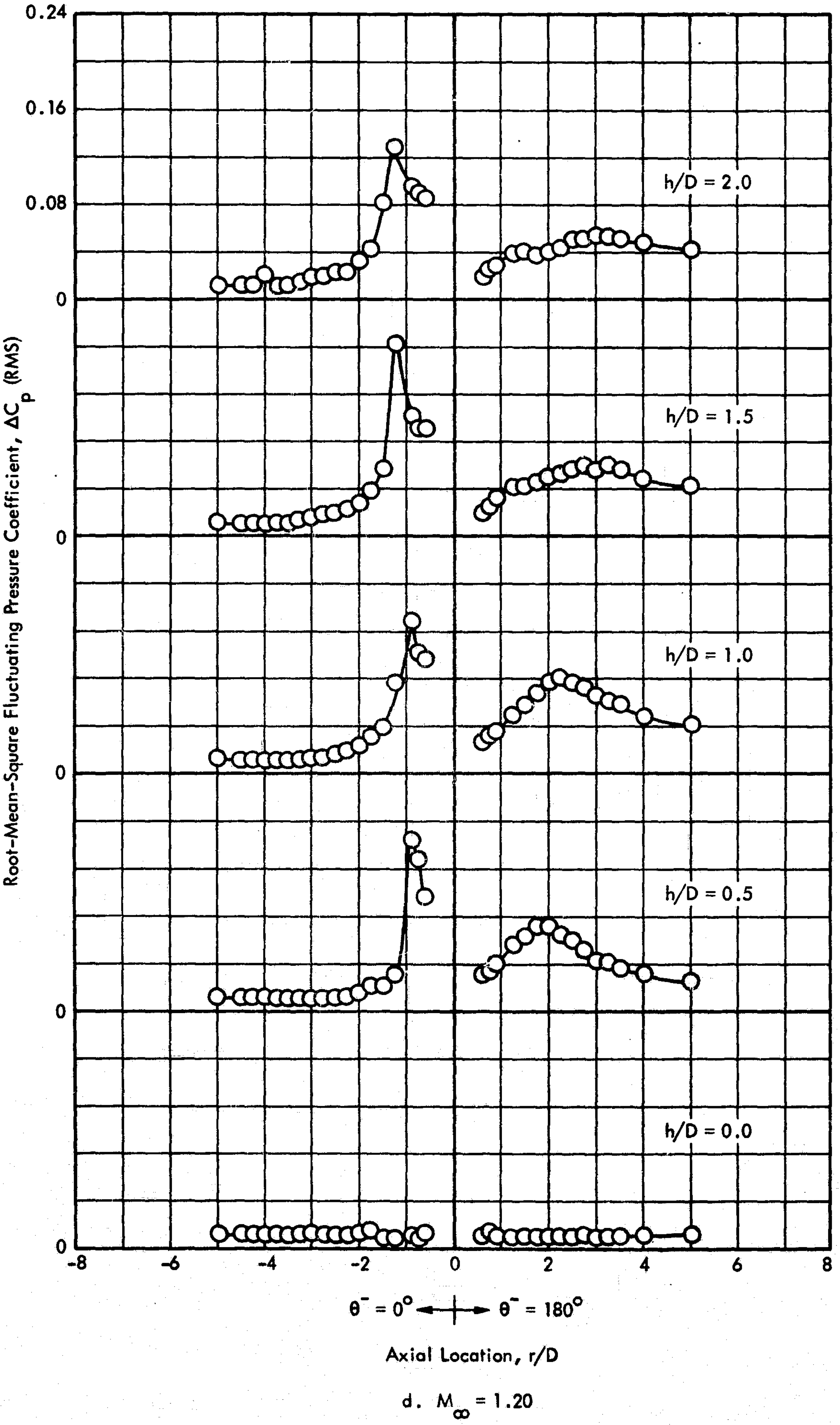

d. $M_\infty = 1.20$

Figure 42. Continued

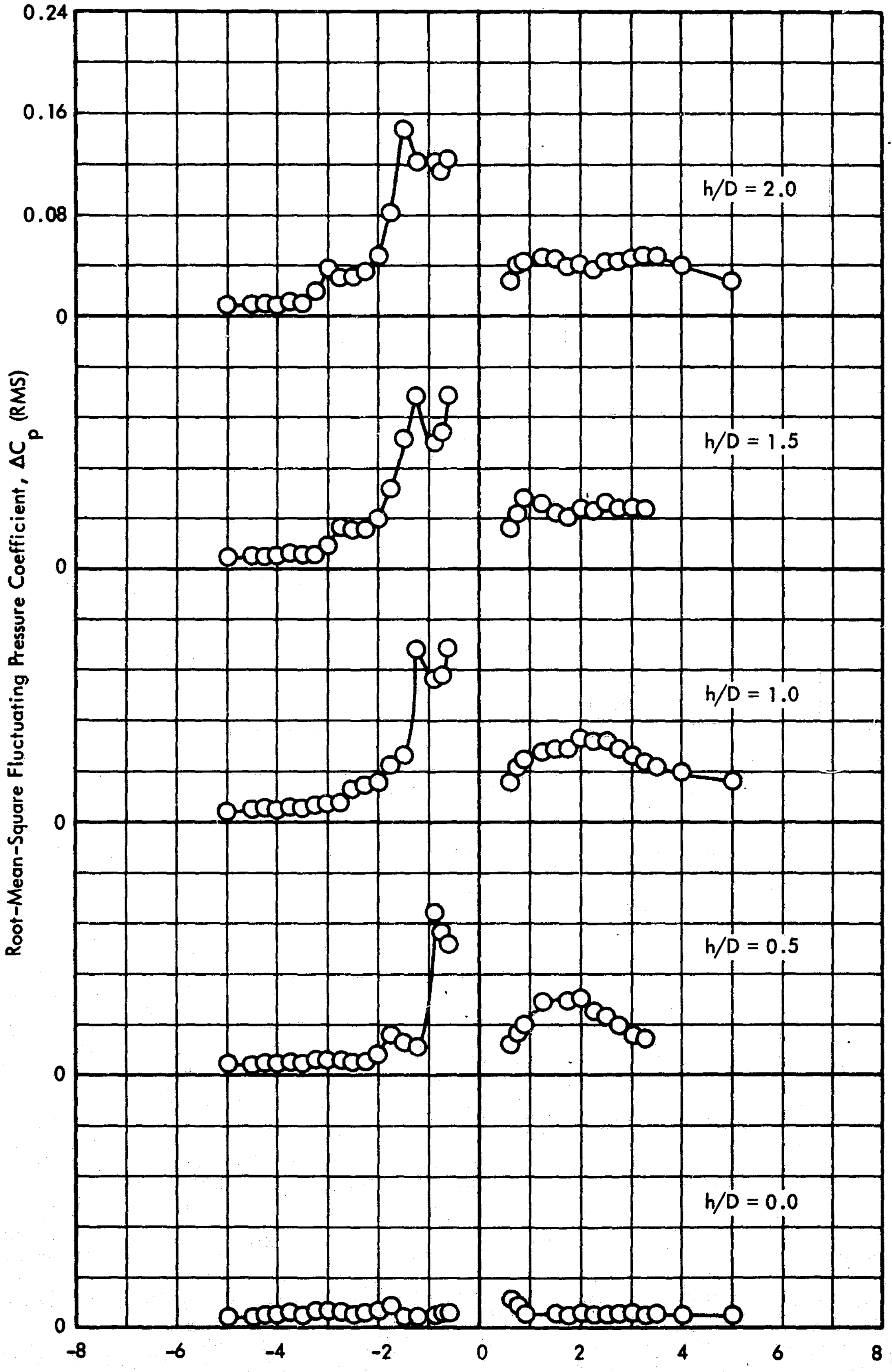

e. $M_\infty = 1.40$

Figure 42. Continued

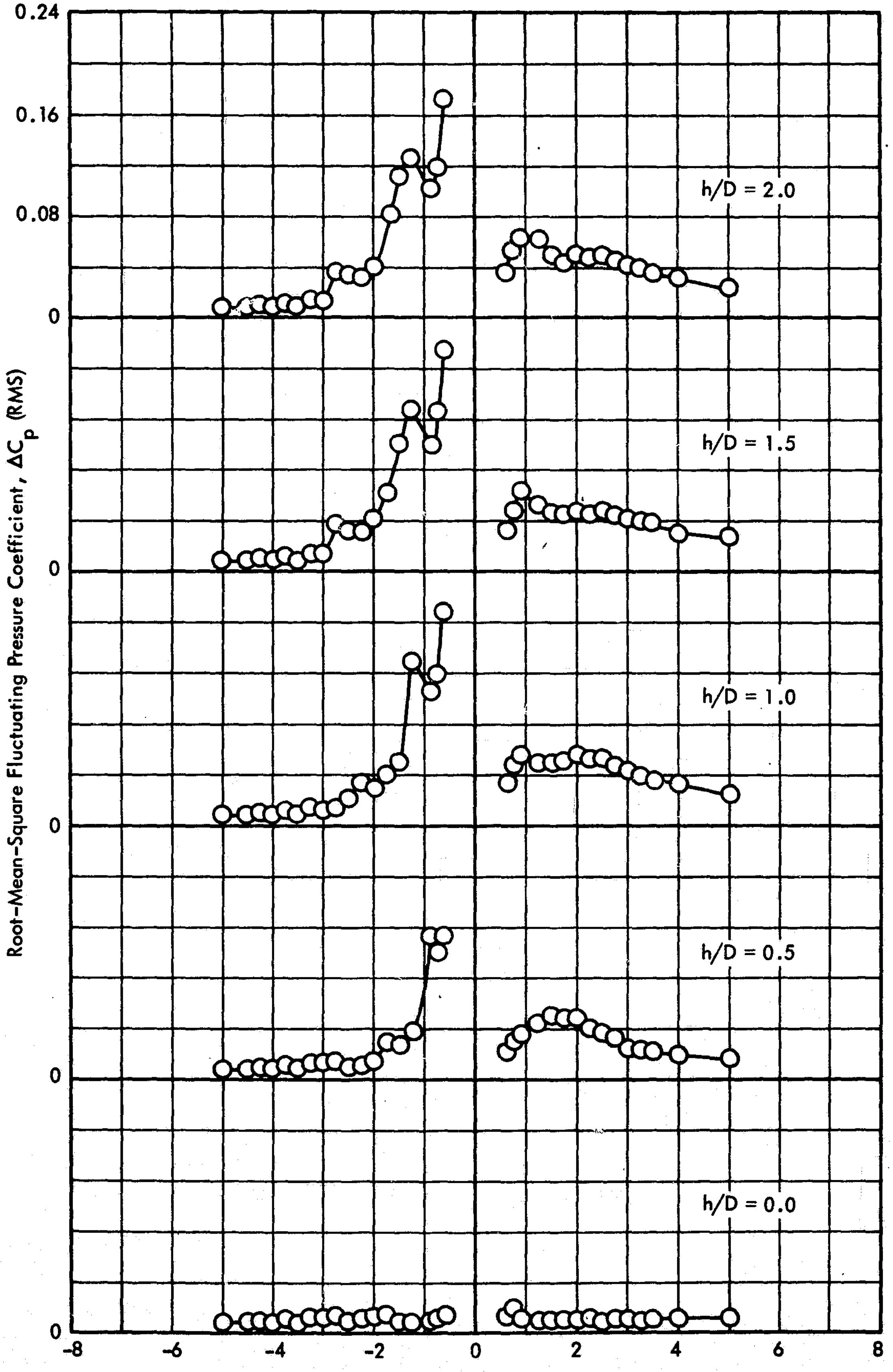

f. $M_\infty = 1.60$

Figure 42. Concluded

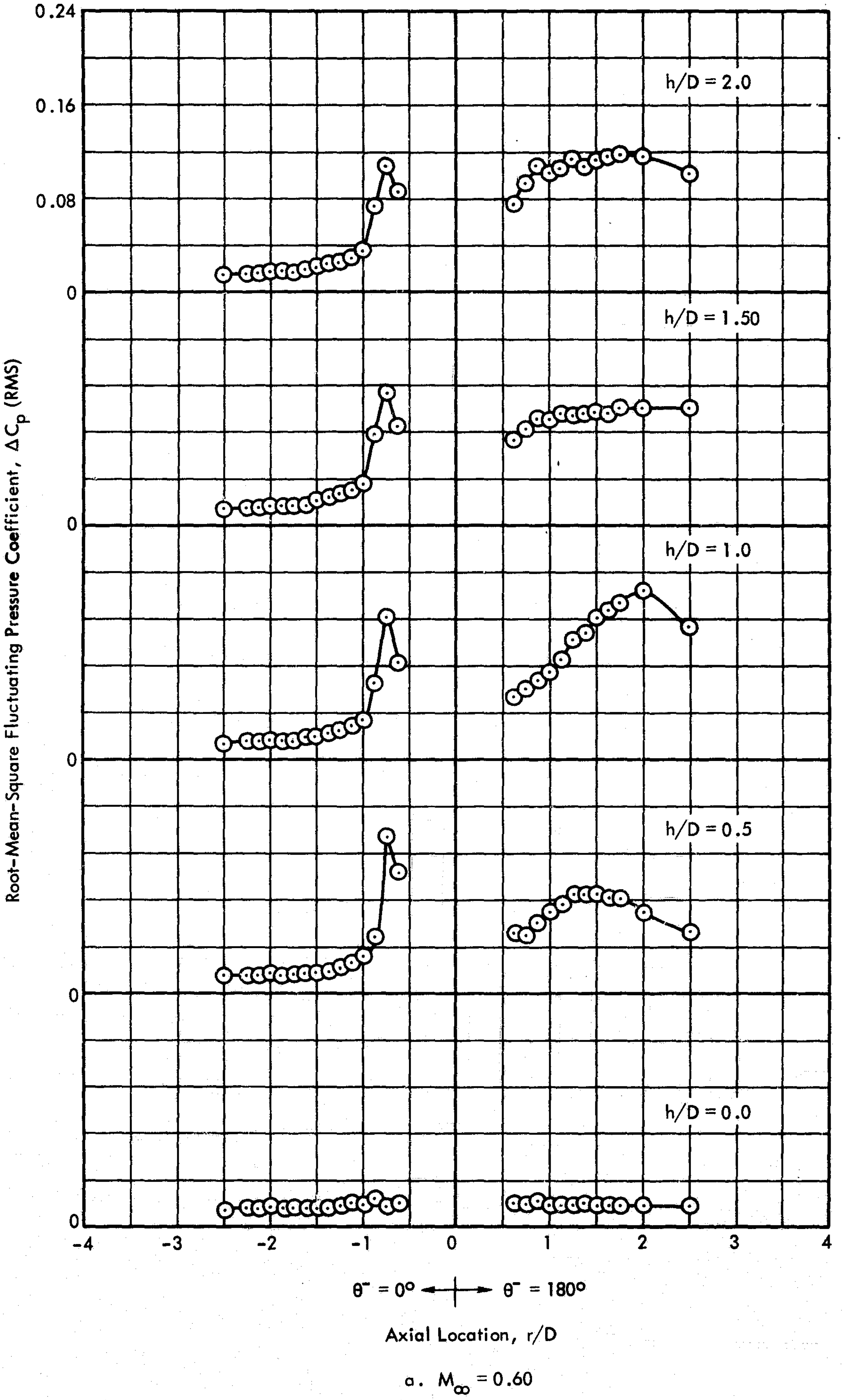

Figure 43. Variation of the RMS Fluctuating Pressure Coefficient Along the Longitudinal Centerline of the Test Panel, 8-inch Diameter Protuberance, Re/ft = 3×10^6

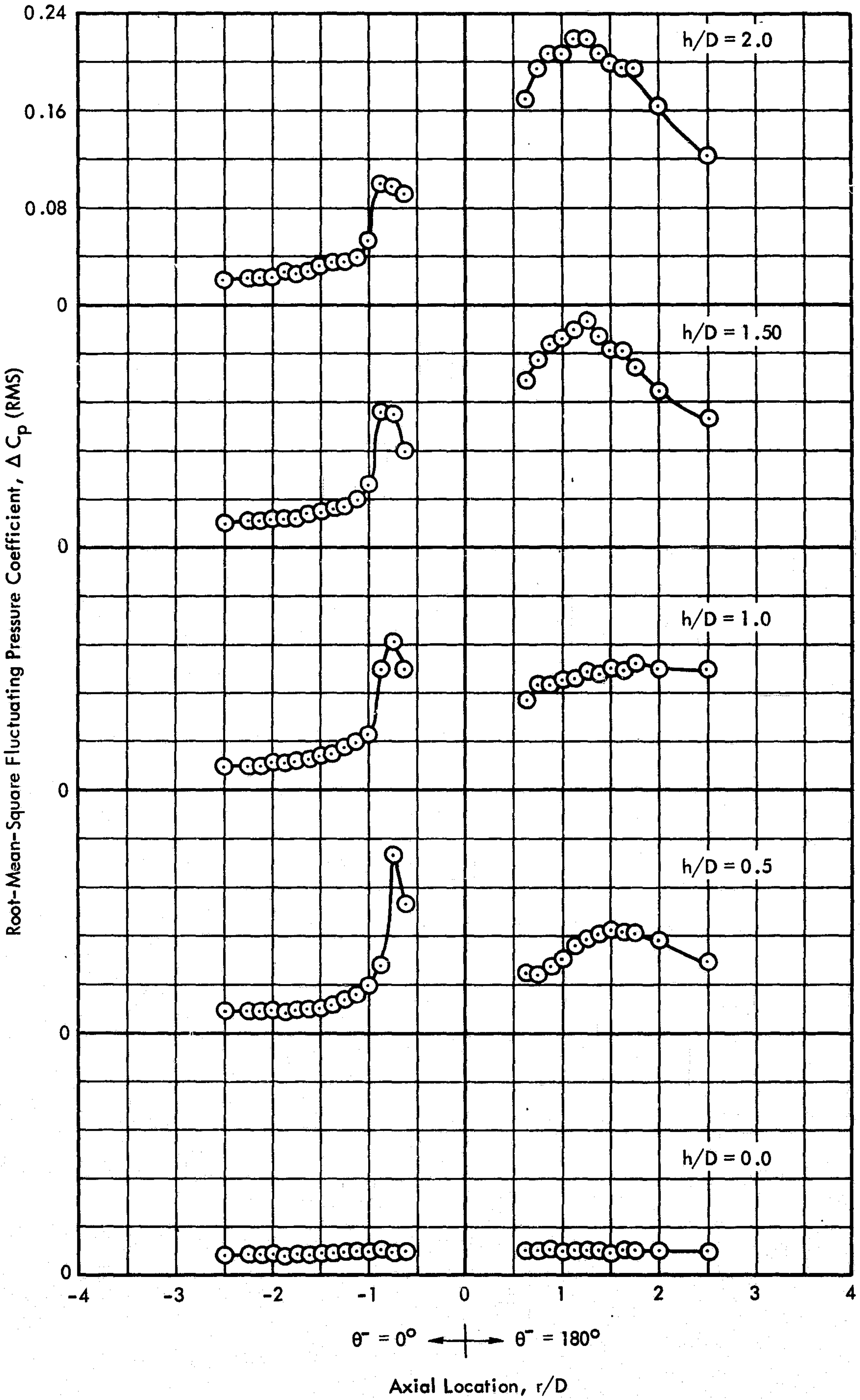

b. $M_\infty = 0.80$

Figure 43. Continued

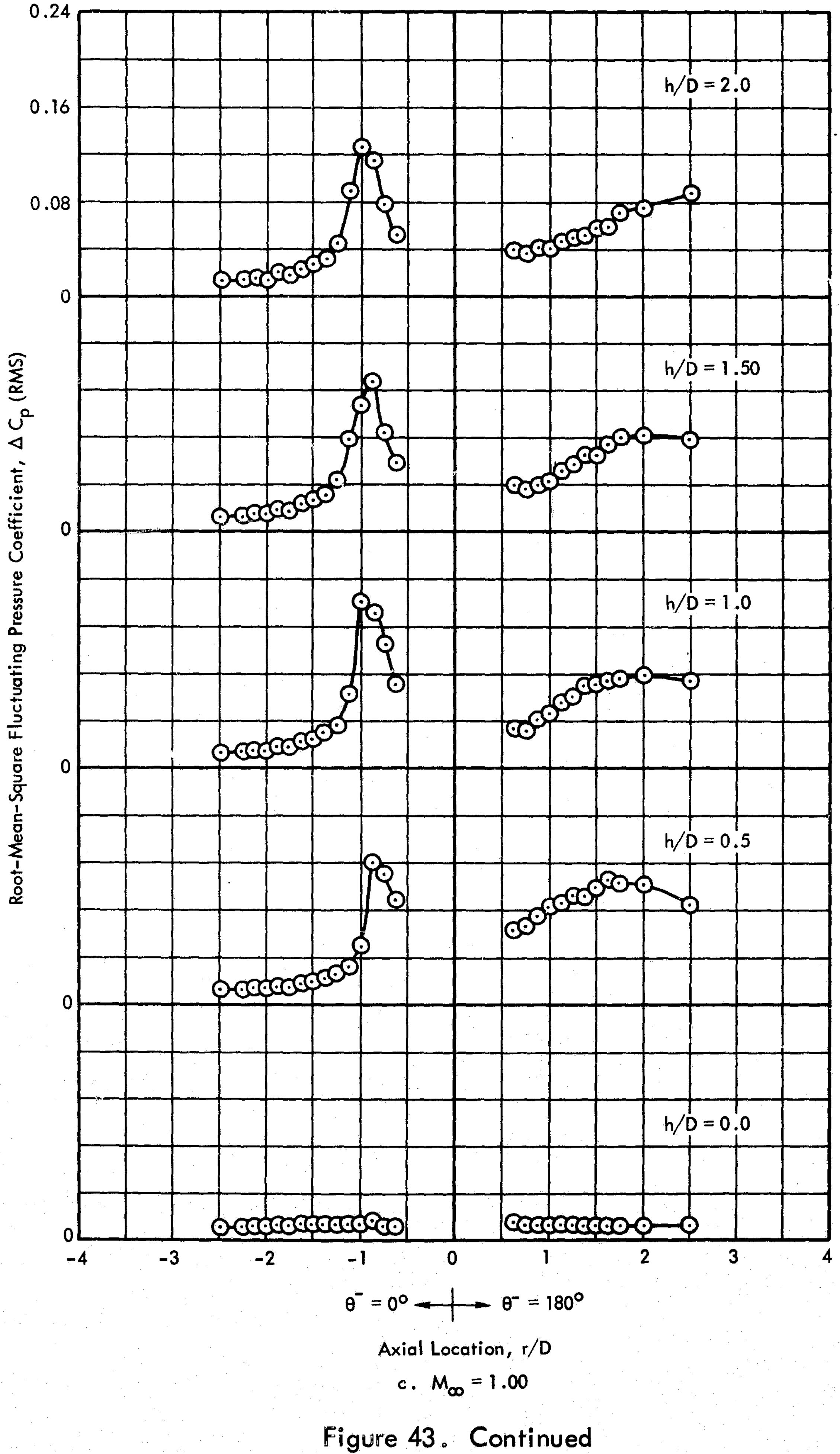

c. $M_\infty = 1.00$

Figure 43. Continued

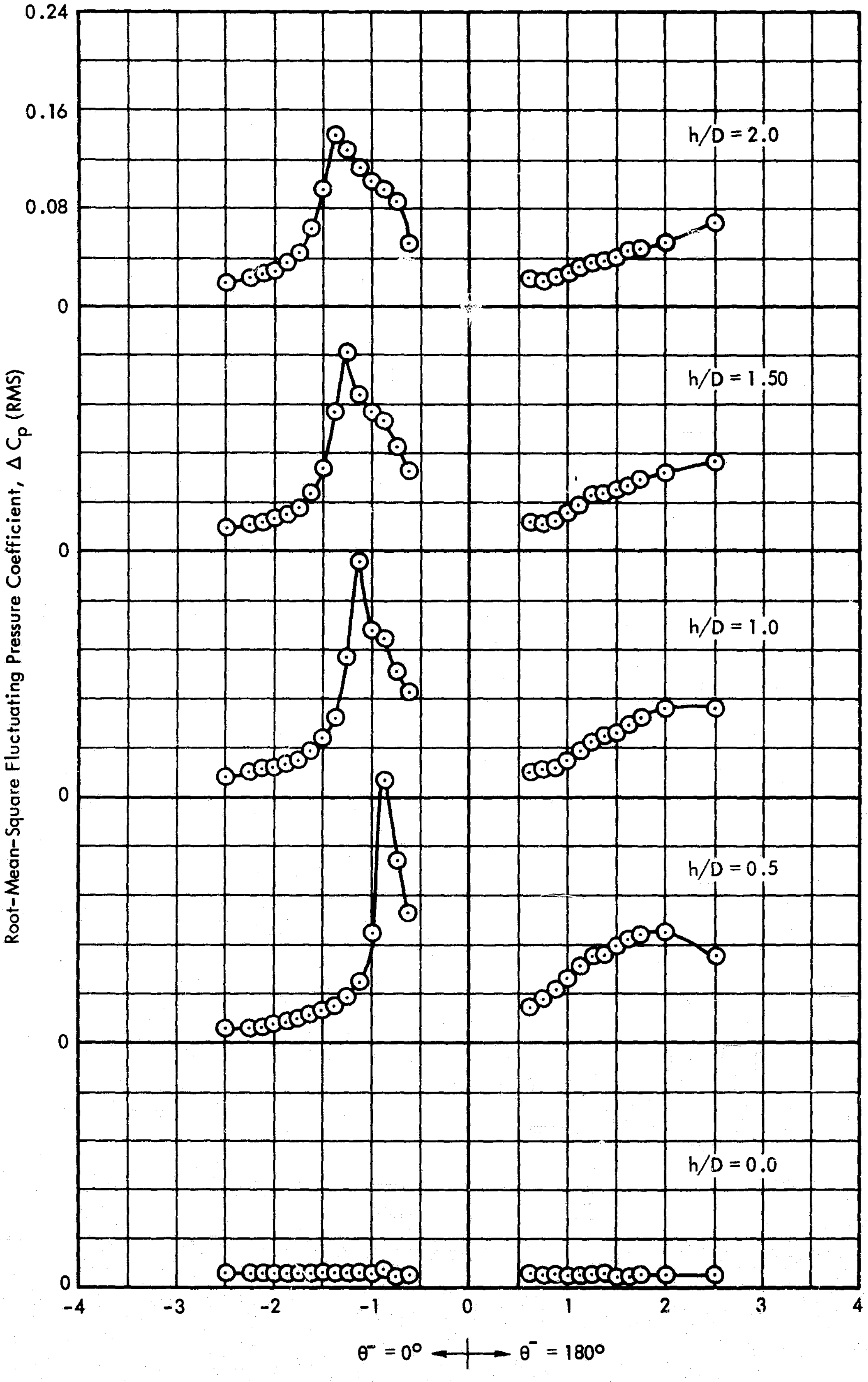

d. $M_\infty = 1.20$

Figure 43. Continued

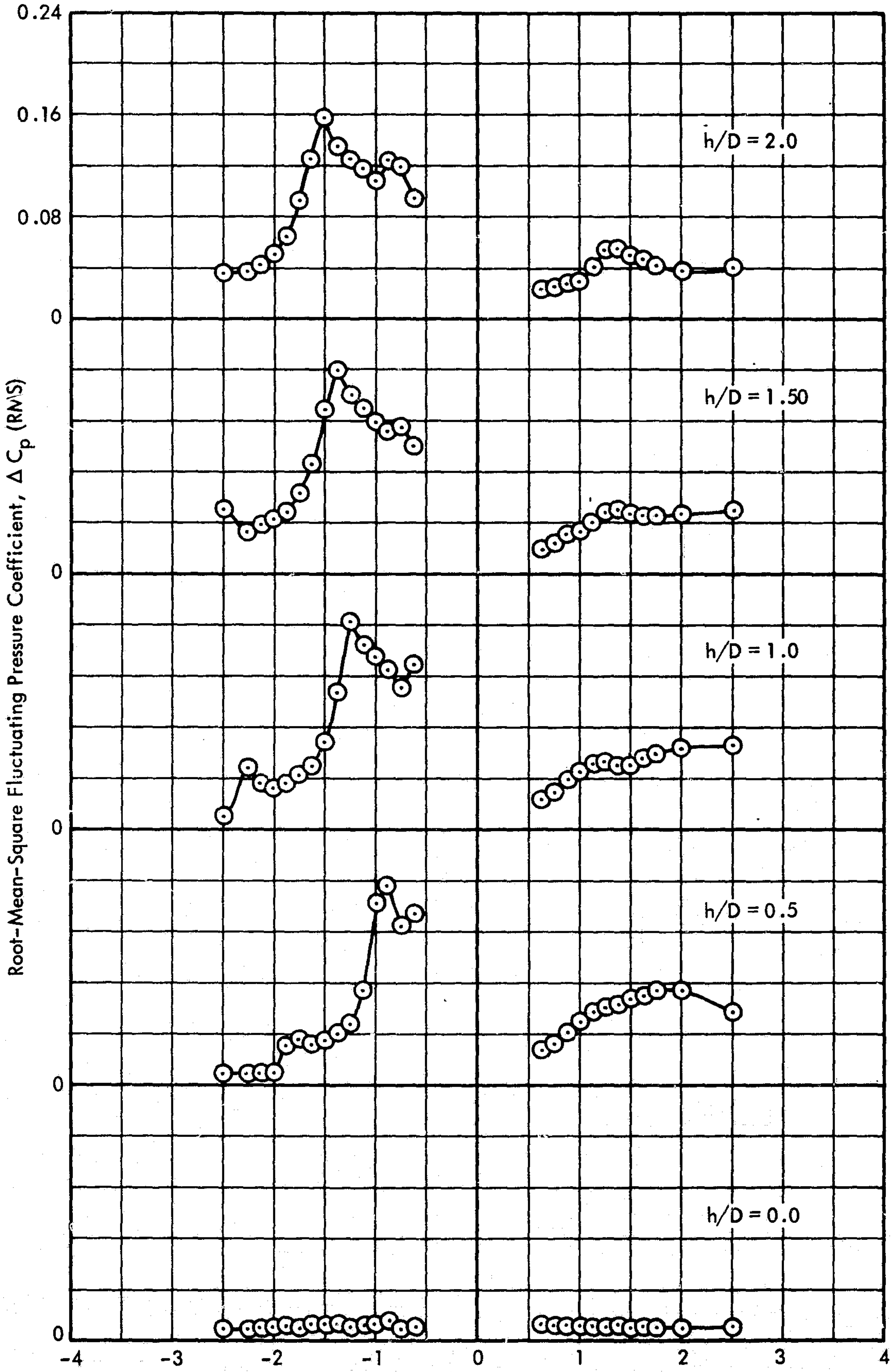

e. $M_\infty = 1.40$

Figure 43. Continued

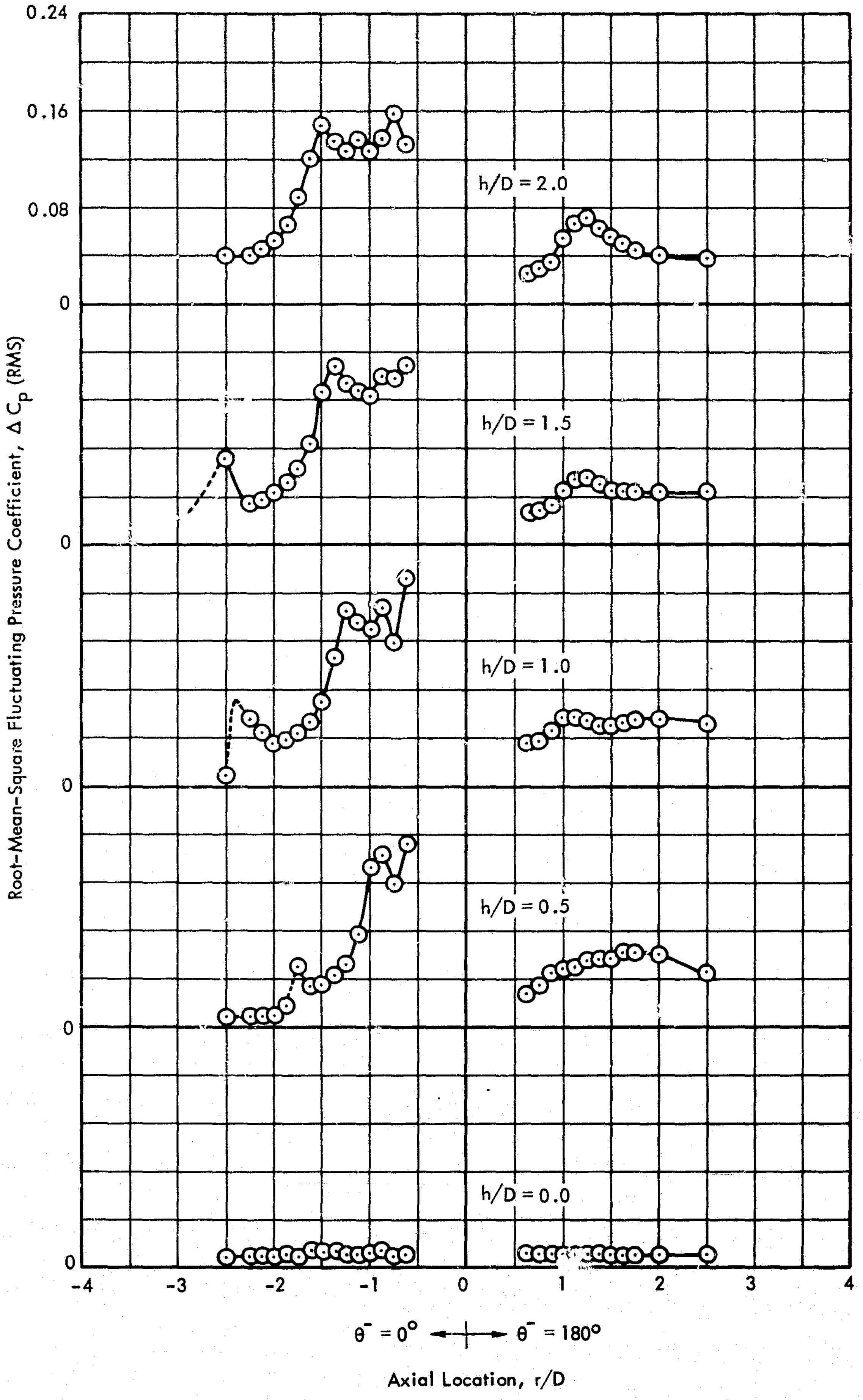

f. $M_\infty = 1.60$

Figure 43. Concluded

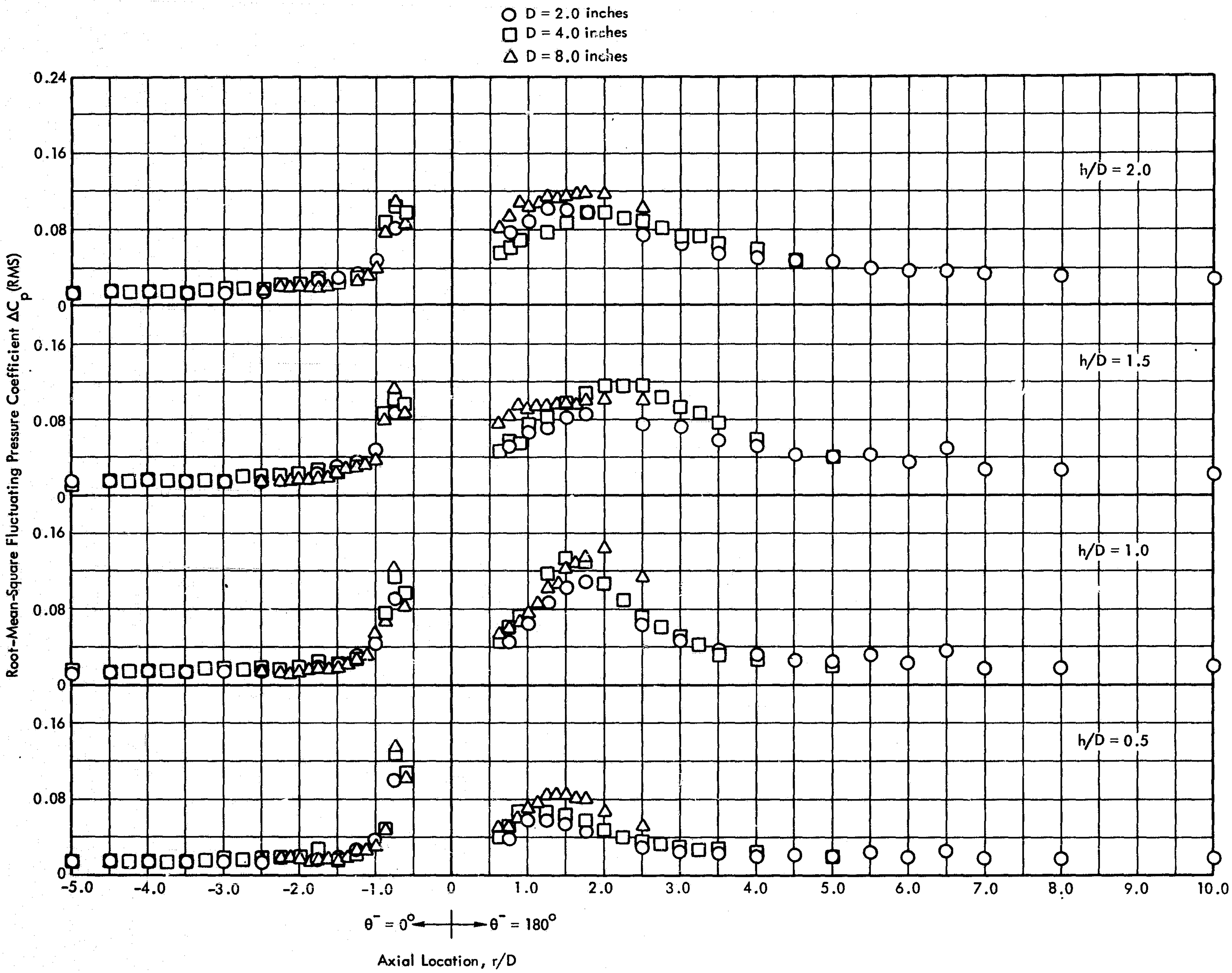

a. $M_\infty = 0.60$

Figure 44. Comparison of the Axial Distributions of RMS Fluctuating Pressure Coefficient For the Various Cylindrical Protuberances, Re/ft = 3 x 10^6

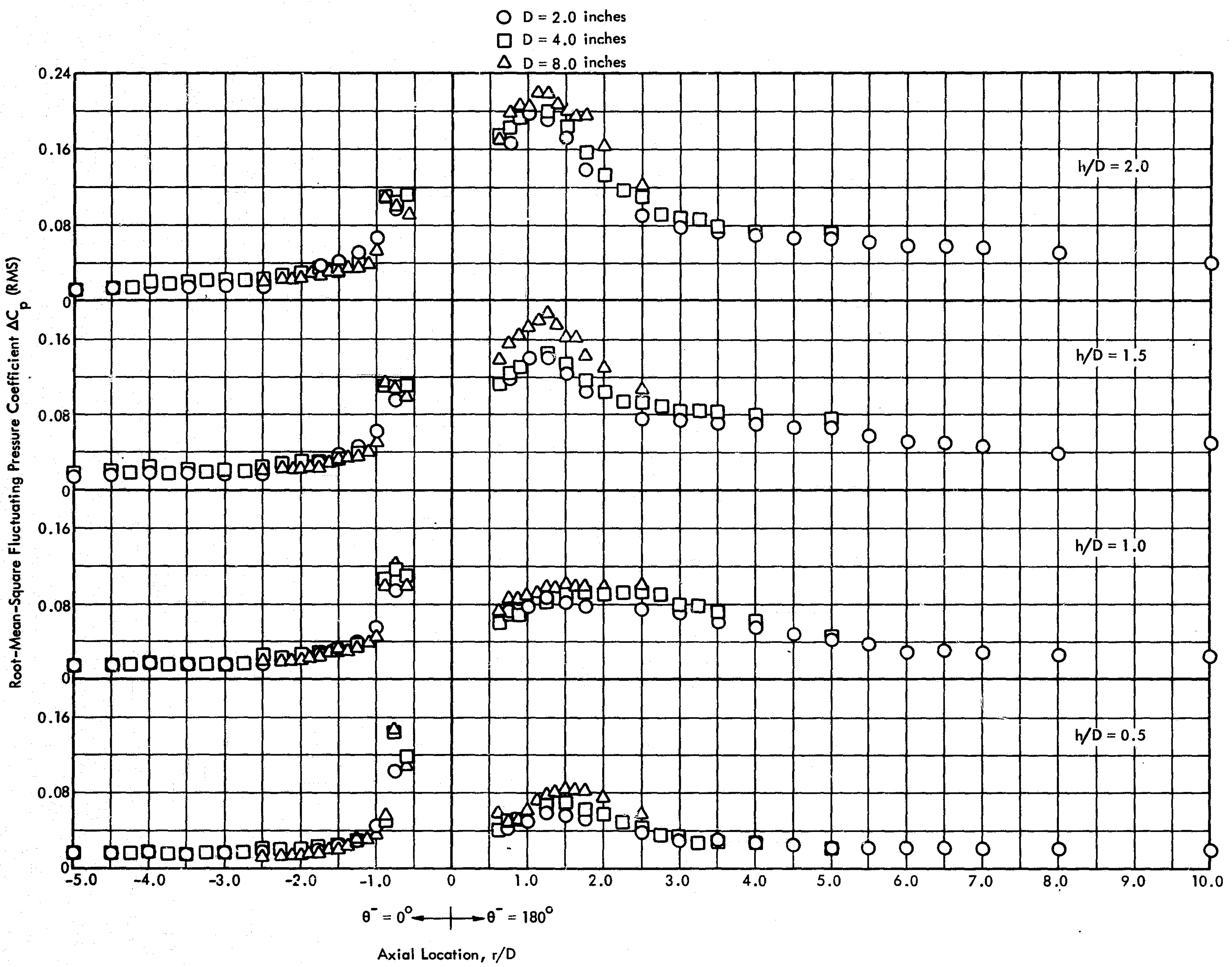

b. $M_\infty = 0.80$

Figure 44. Continued

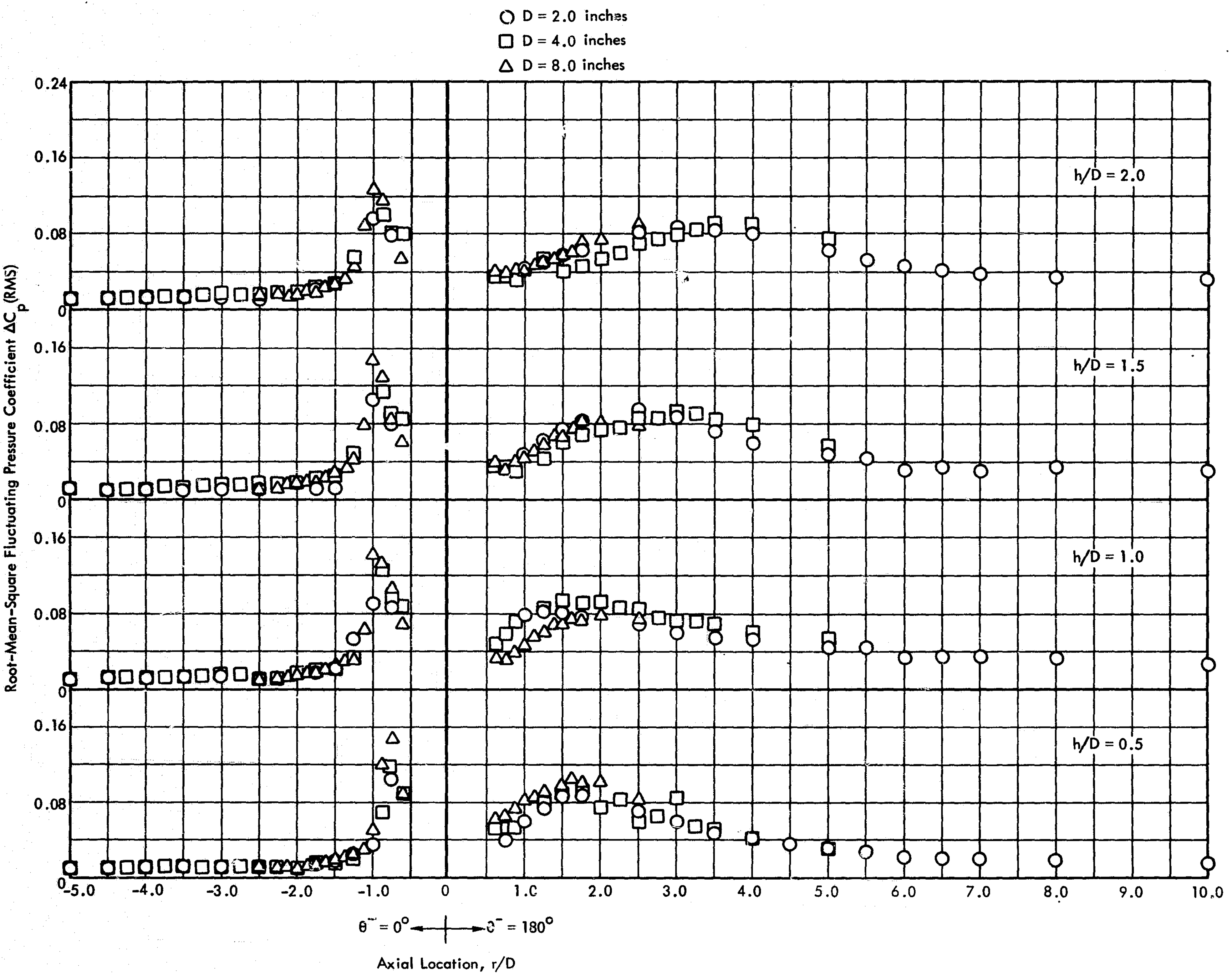

c. $M_\infty = 1.00$

Figure 44. Continued

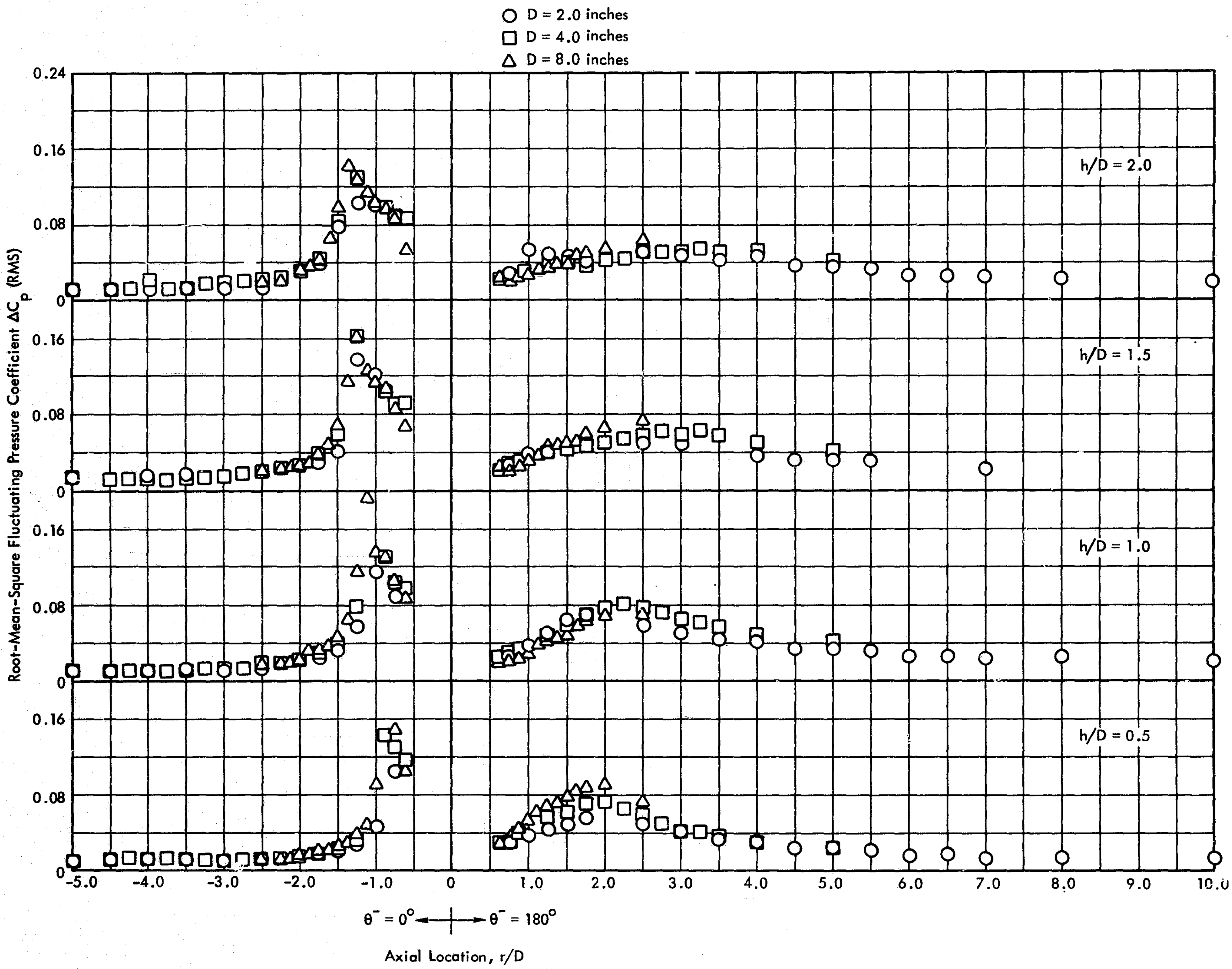

d. $M_\infty = 1.20$

Figure 44. Continued

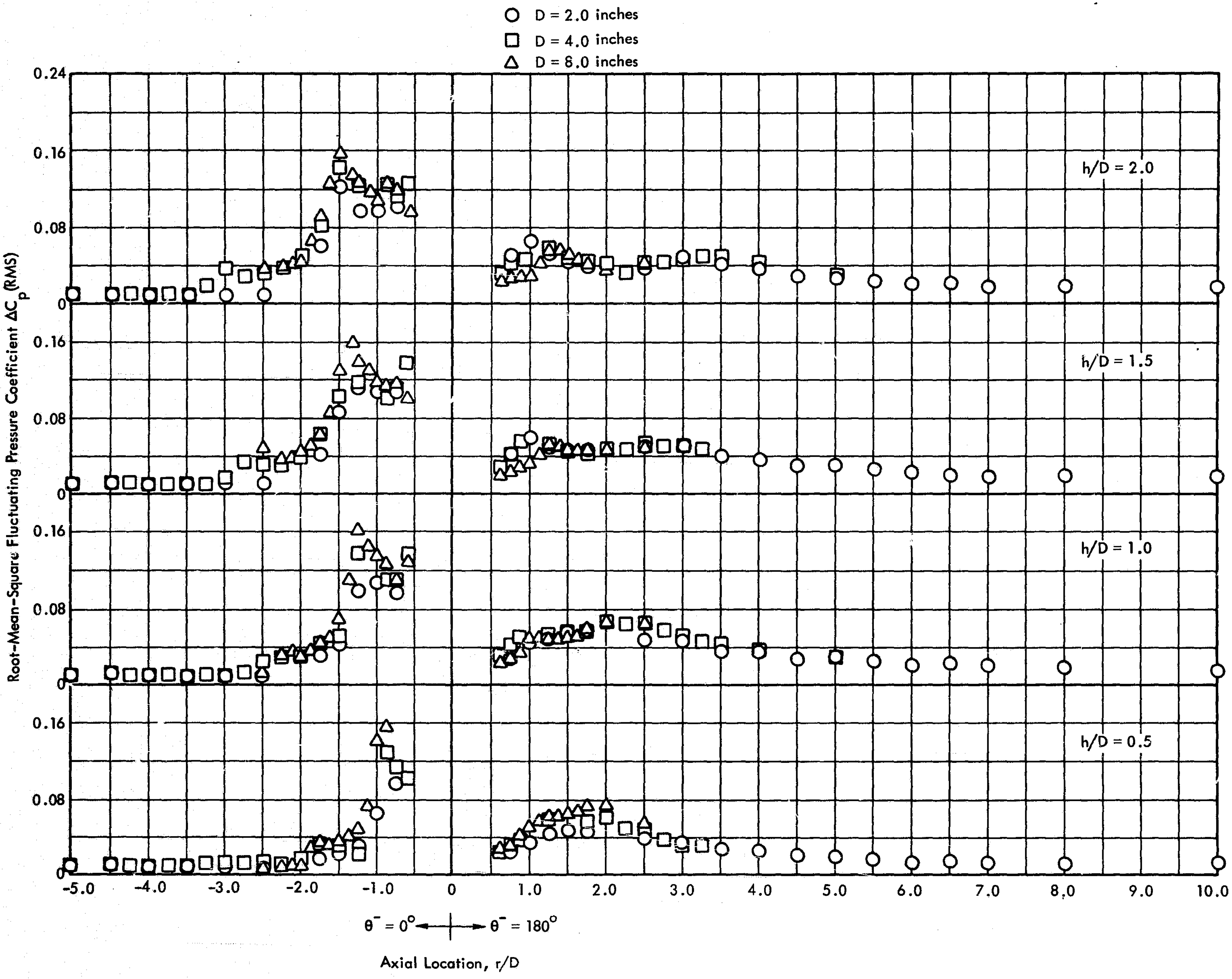

e. $M_\infty = 1.40$

Figure 44. Continued

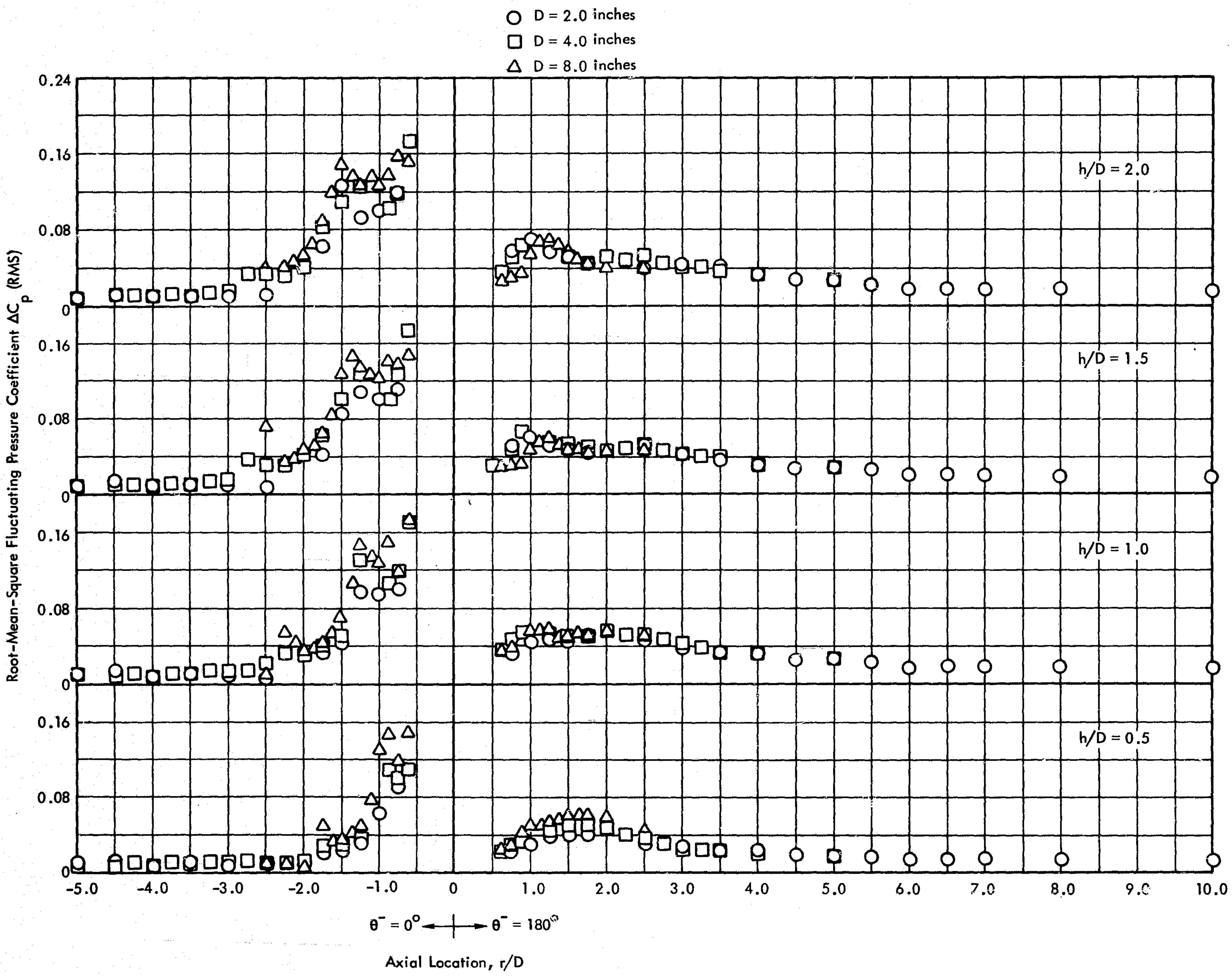

f. $M_\infty = 1.60$

Figure 44. Concluded

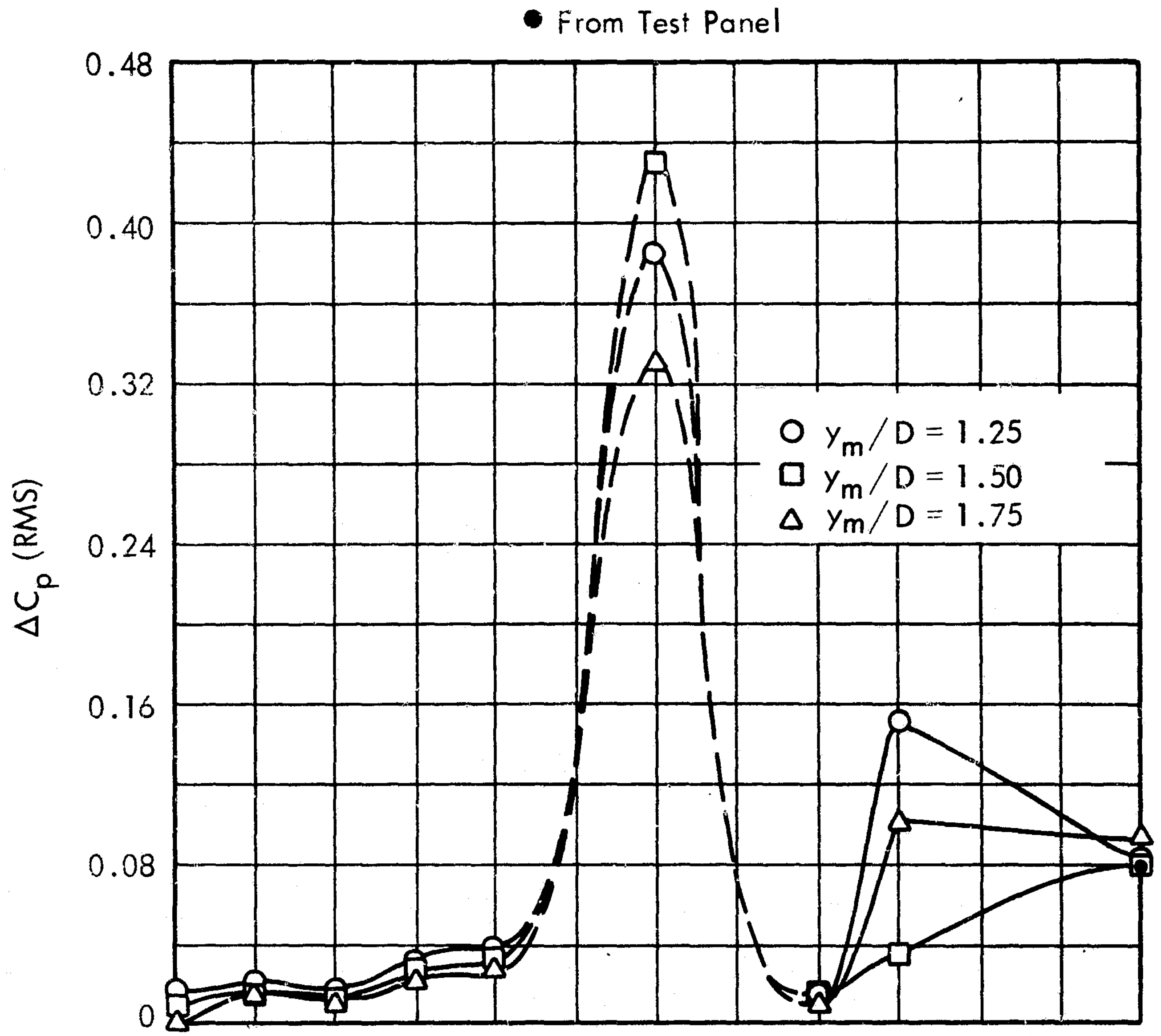

a. h/D = 2.0

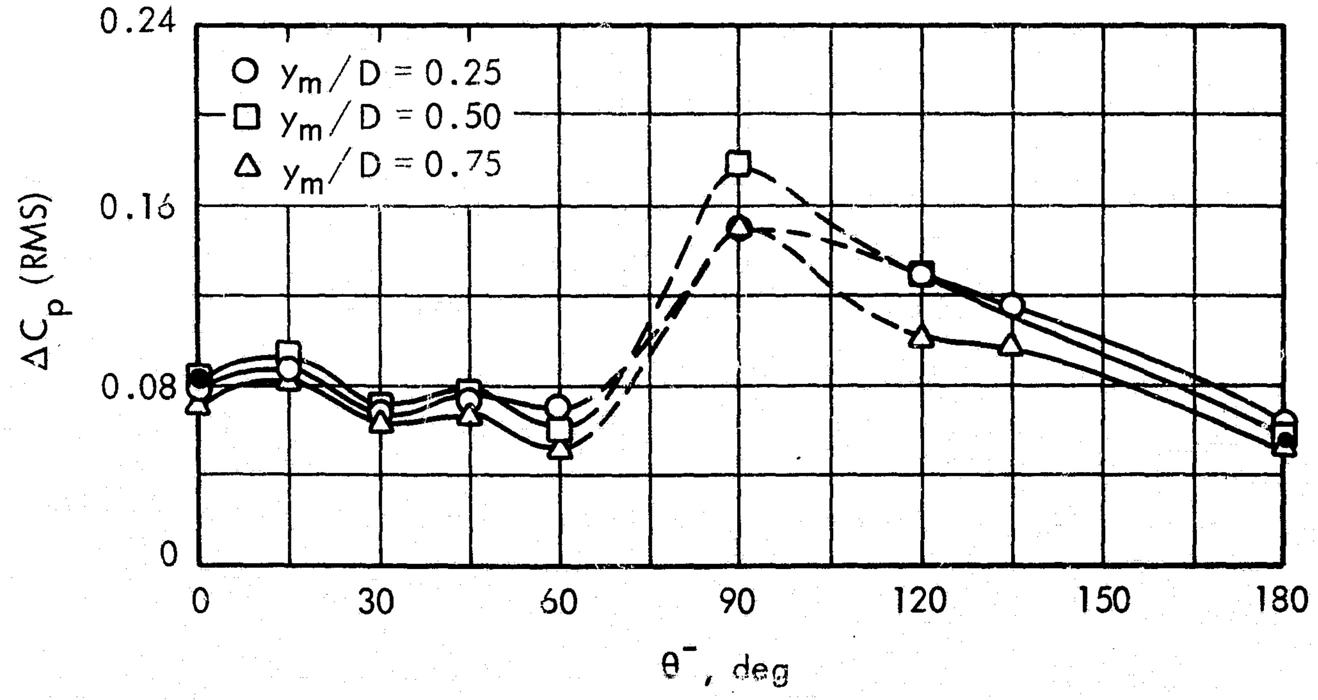

b. h/D = 1.0

Figure 45. Variation of RMS Fluctuating Pressure Coefficient Over the Wall of the 8-inch Diameter Protuberance, $M_\infty = 0.60$, $Re/ft = 3 \times 10^6$

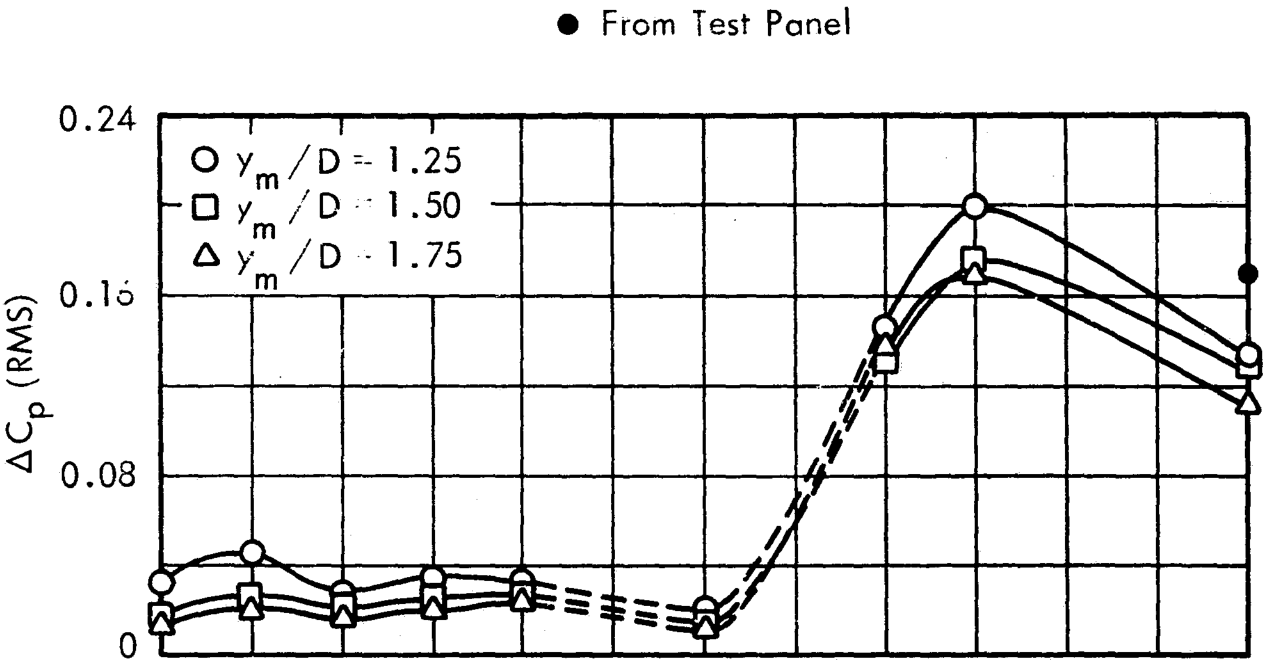

a. h/D = 2.0

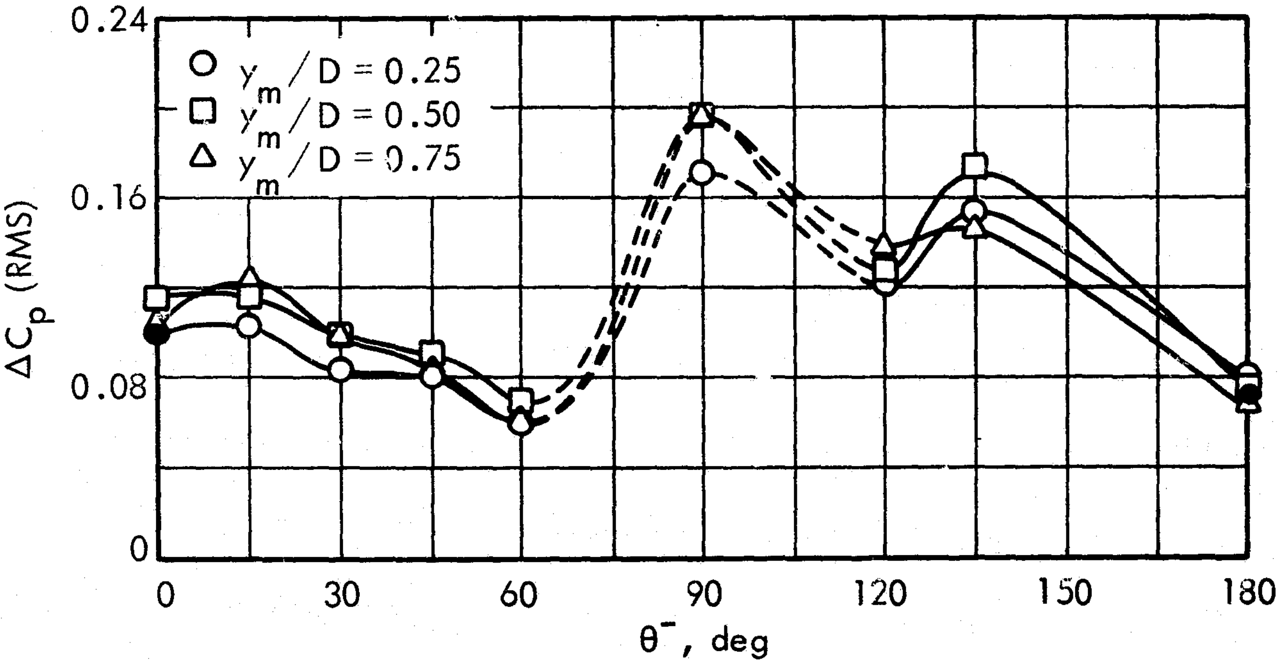

b. h/D = 1.0

Figure 46. Variation of RMS Fluctuating Pressure Coefficients Over the Wall of the 8-inch Diameter Protuberance, $M_\infty = 0.80$, Re/ft = 3 x 10^6

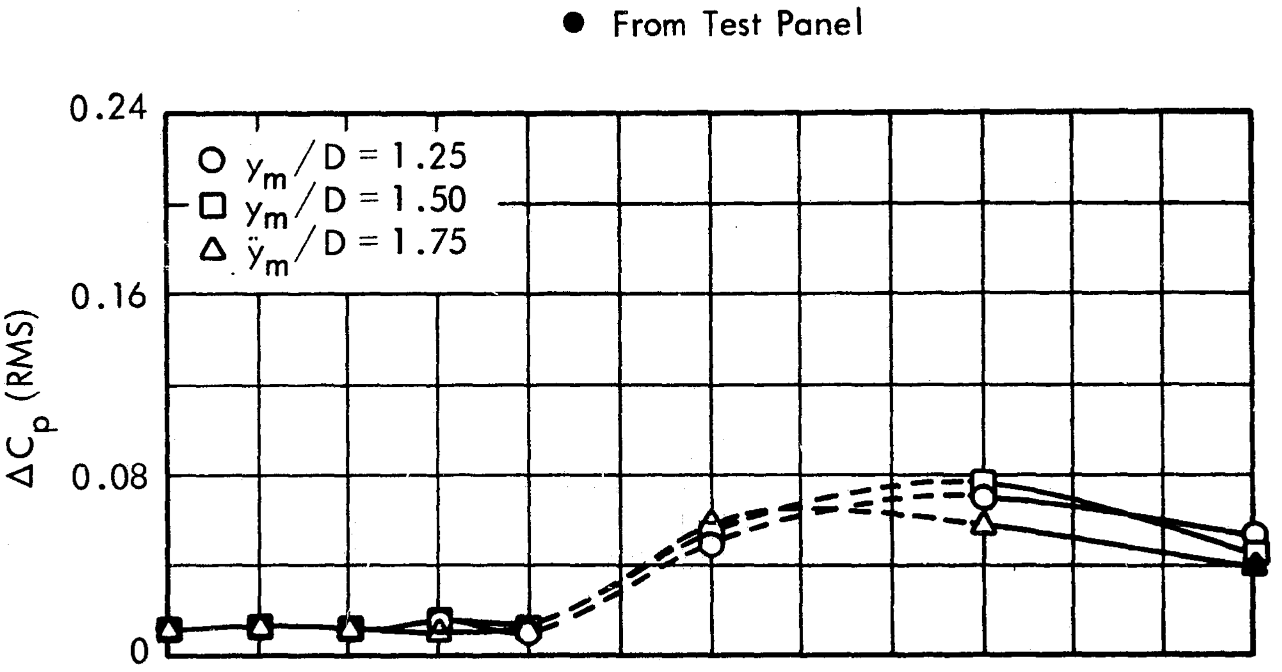

a. h/D = 2.0

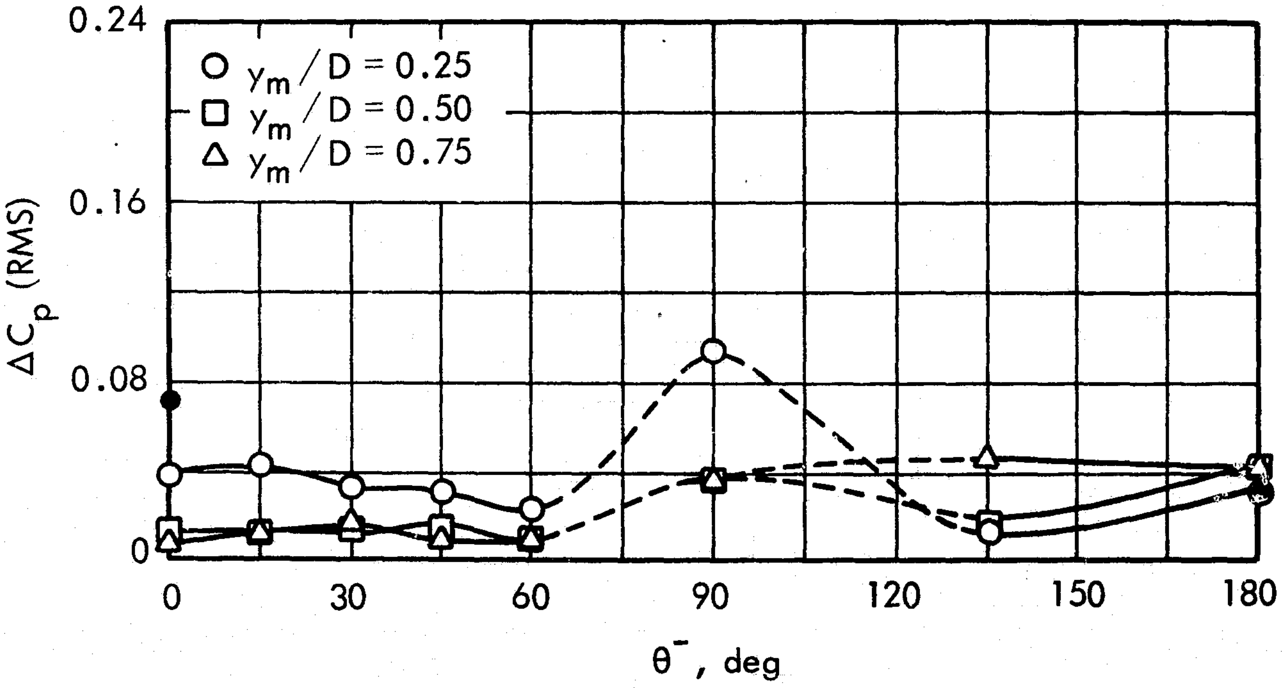

b. h/D = 1.0

Figure 47. Variation of RMS Fluctuating Pressure Coefficients Over the Wall of the 8-inch Diameter Protuberance, $M_\infty = 1.00$, $Re/ft = 3 \times 10^6$

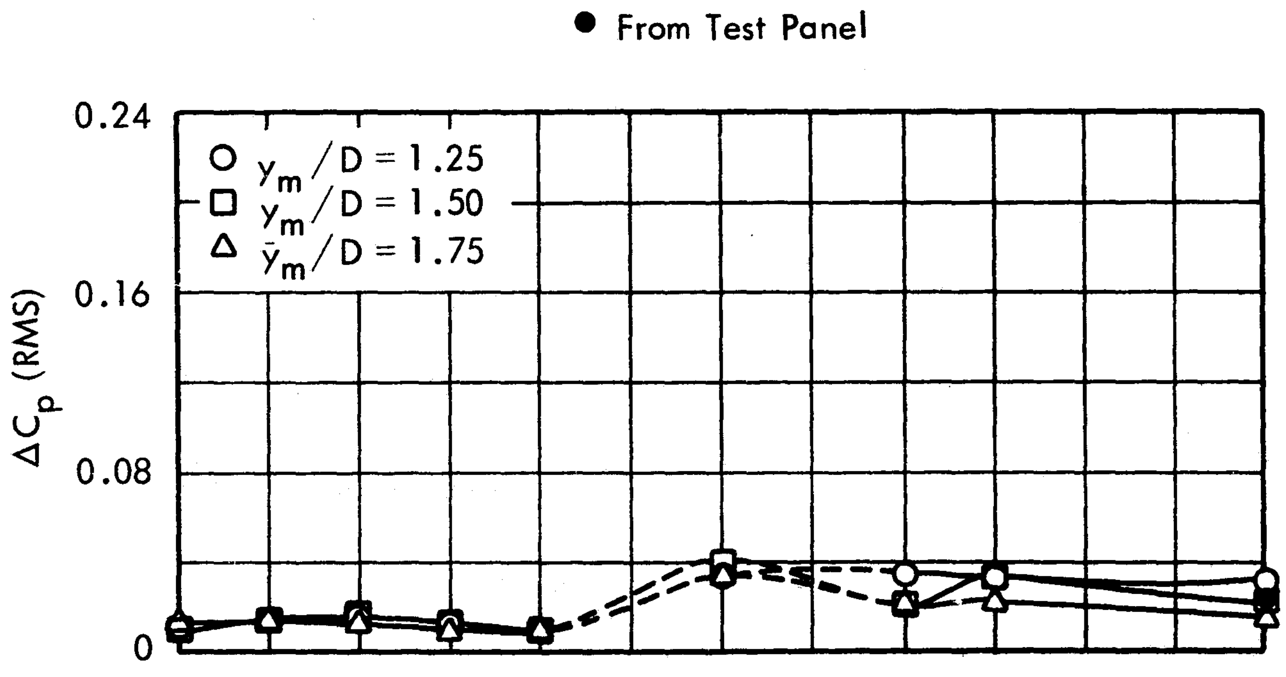

a. h/D = 2.0

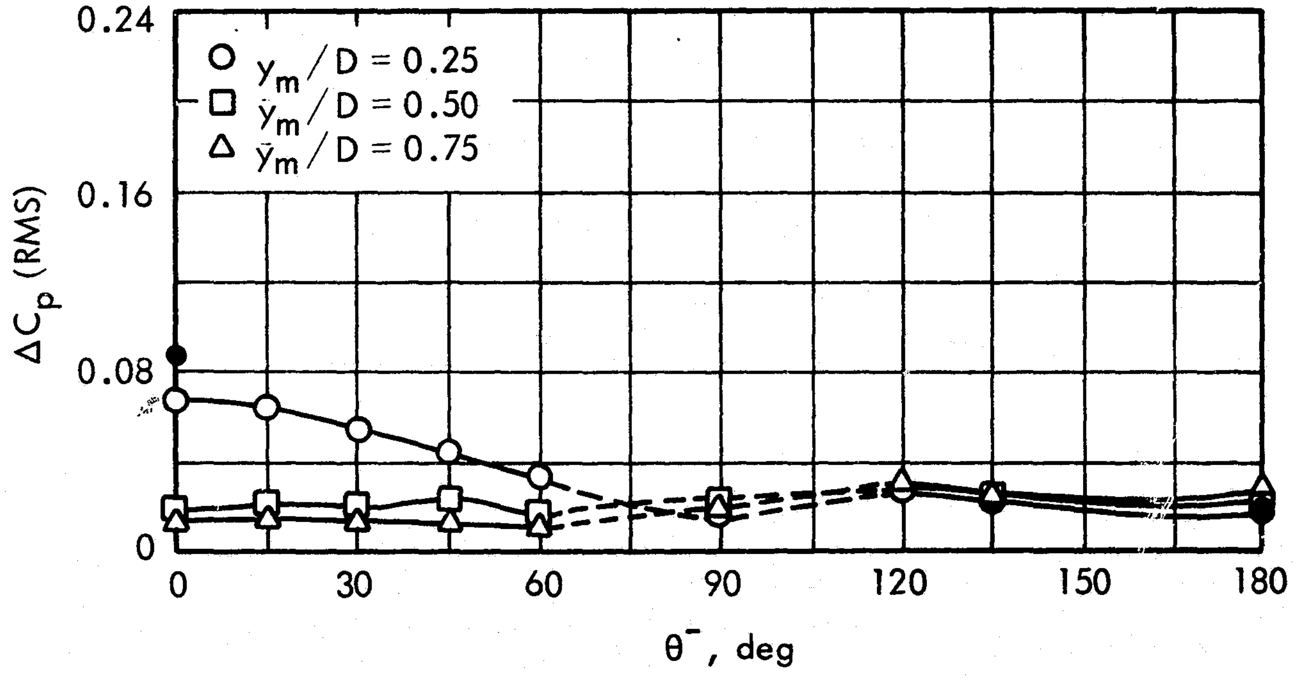

b. h/D = 1.0

Figure 48. Variation of RMS Fluctuating Pressure Coefficient Over the Wall of the 8-inch Diameter Protuberance, $M_\infty = 1.20$, $Re/ft = 3 \times 10^6$

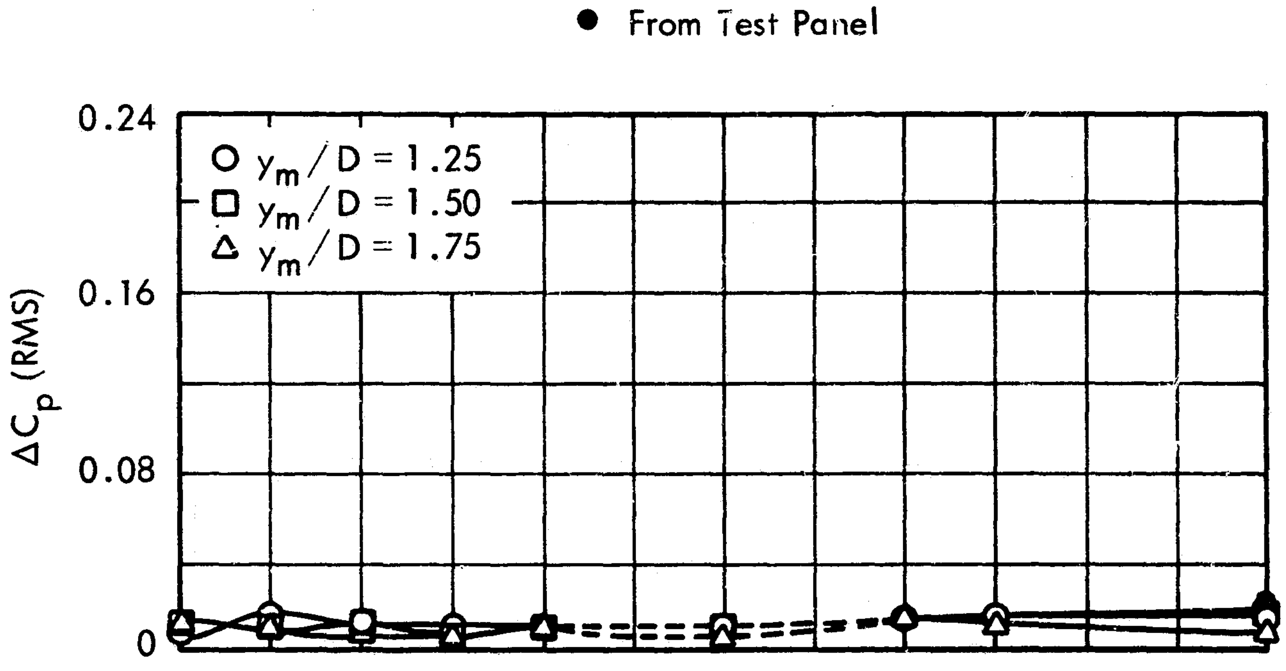

a. h/D = 2.0

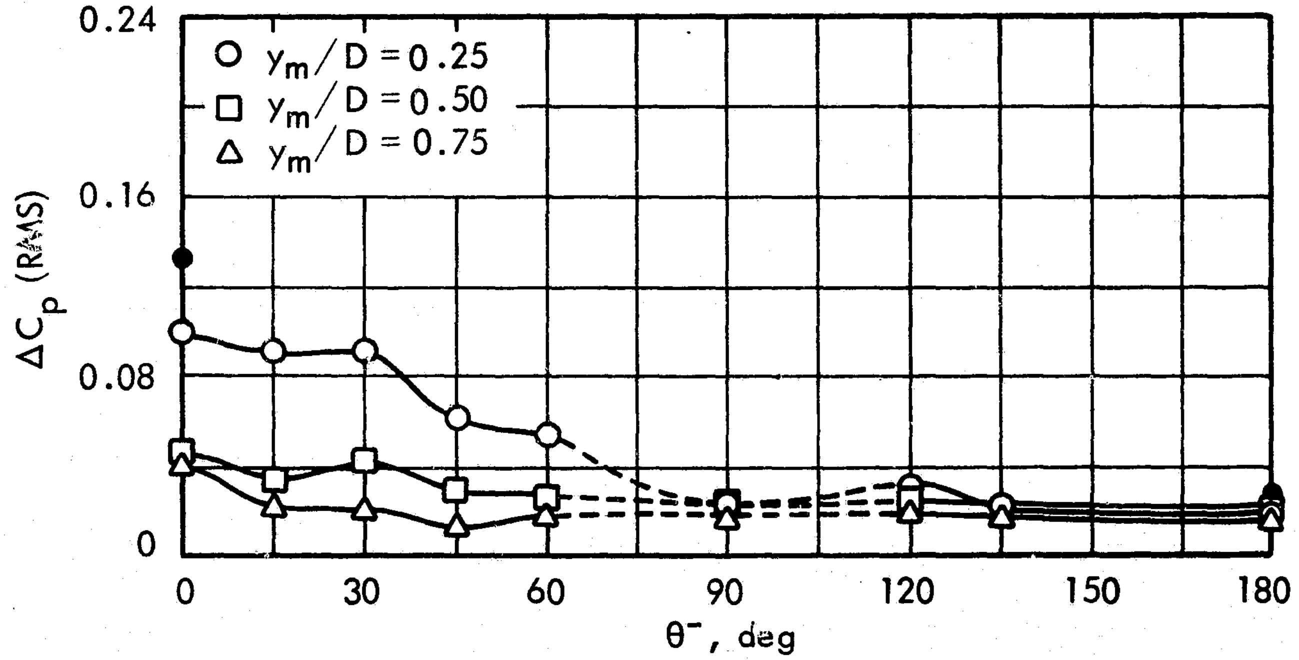

b. h/D = 1.0

Figure 49. Variation of RMS Fluctuating Pressure Coefficient Over the Wall of the 8-inch Diameter Protuberance, $M_\infty = 1.40$, Re/ft = 3×10^6

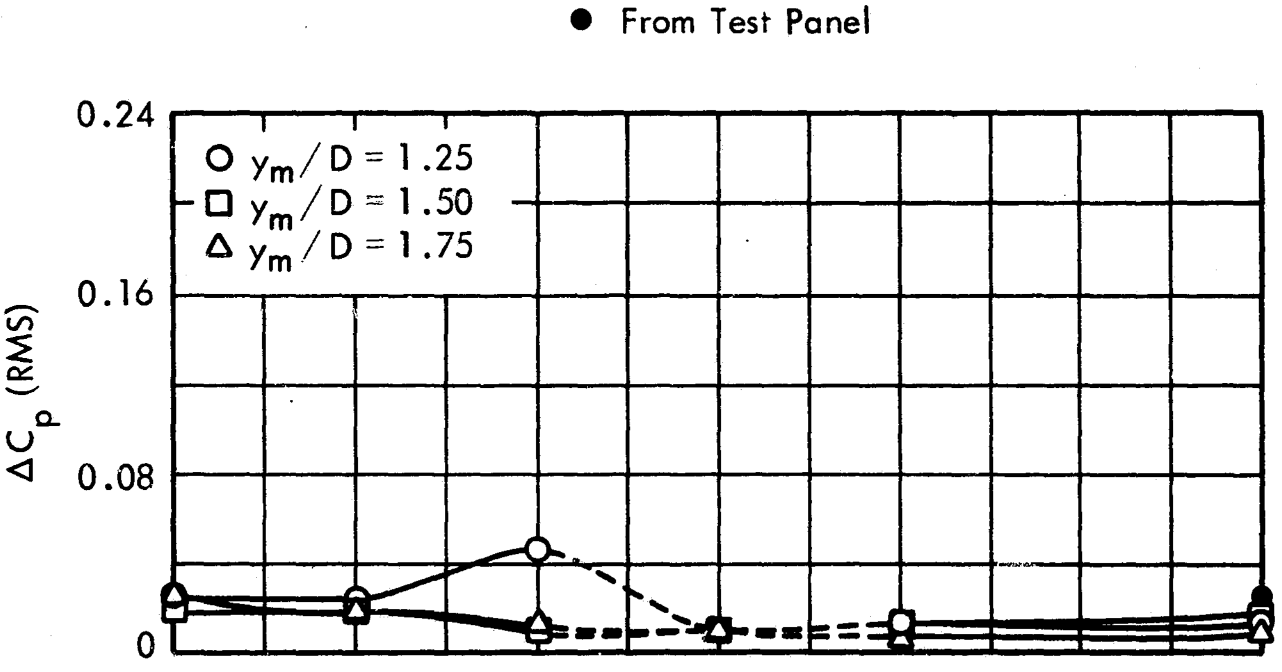

a. h/D = 2.0

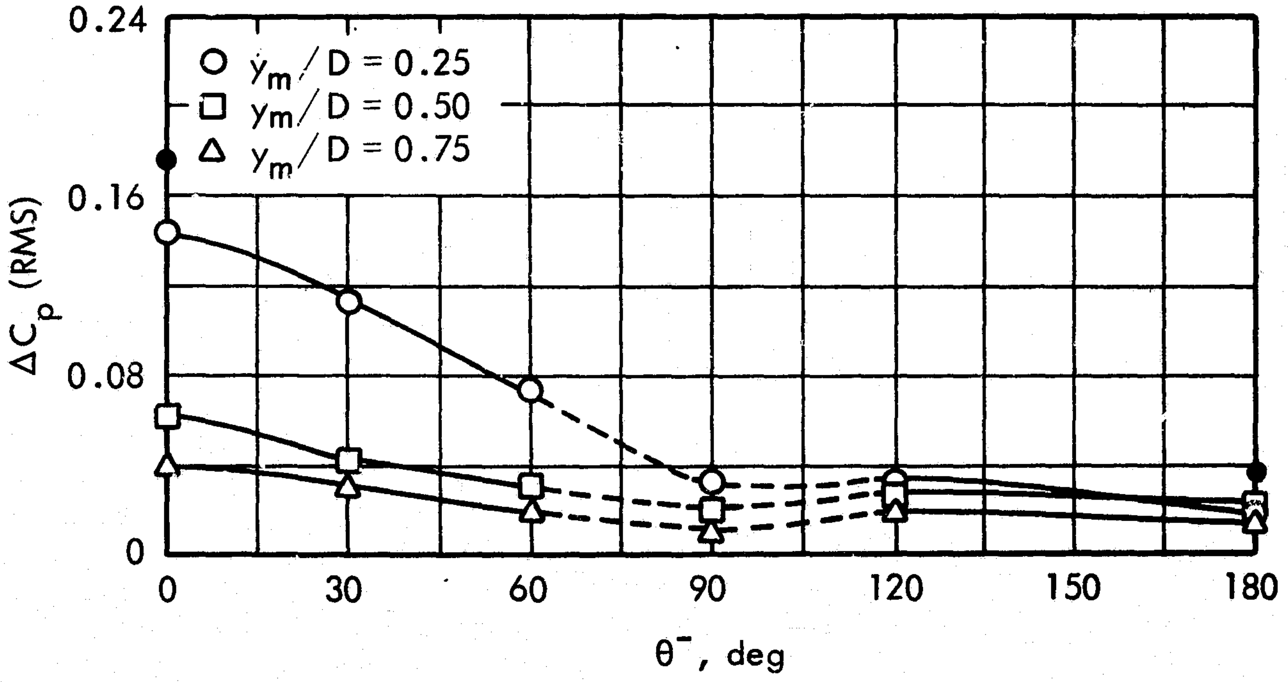

b. h/D = 1.0

Figure 50. Variation of RMS Fluctuating Pressure Coefficient Over the Wall of the 8-inch Diameter Protuberance, $M_\infty = 1.60$, Re/ft = 3×10^6

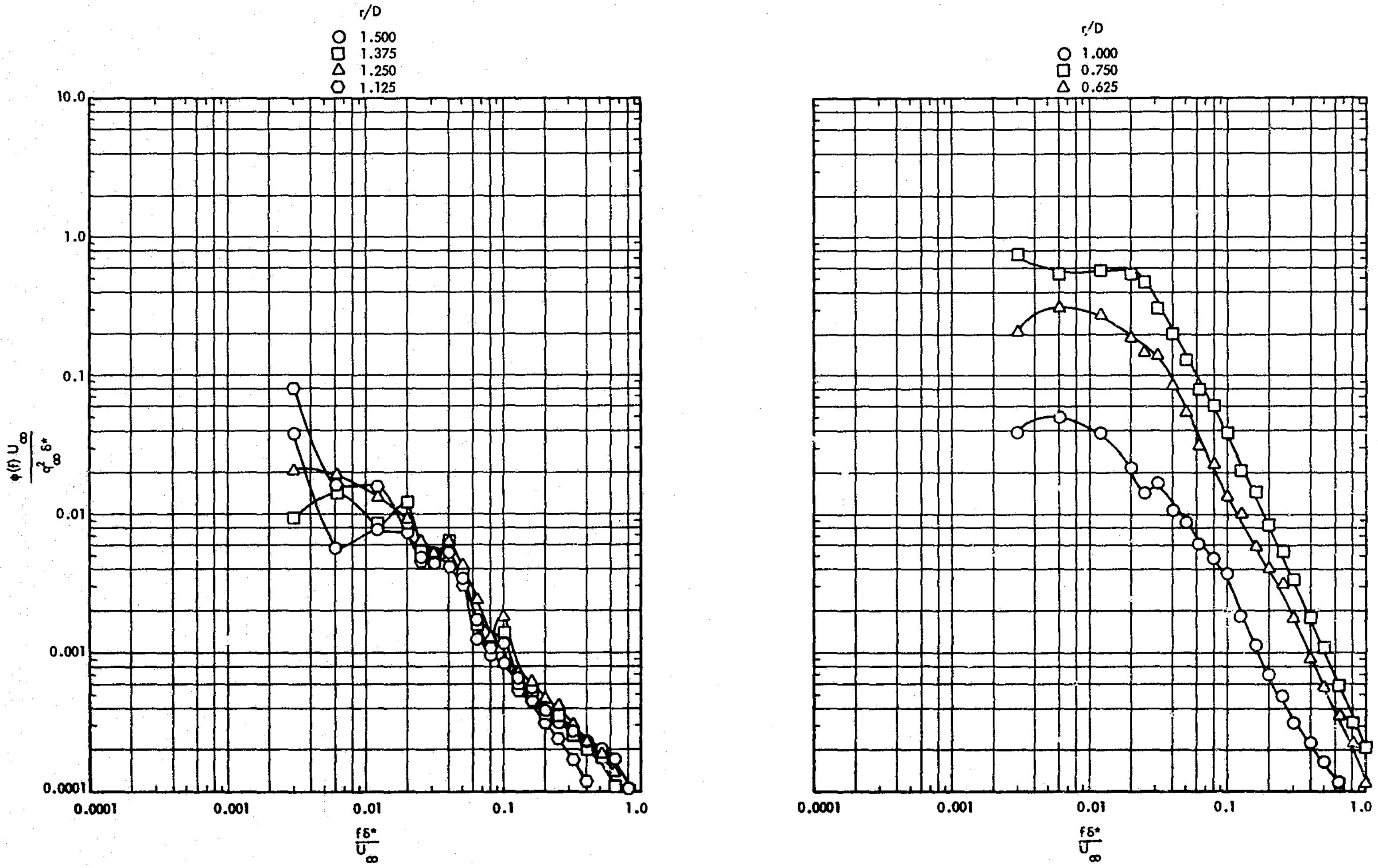

a. h/D = 1.0

Figure 51. Power Spectra of the Protuberance Induced Fluctuating Pressure Field, Upstream ($\theta^- = 0^\circ$), 8-inch Diameter Protuberance, $M_\infty = 0.60$, $Re/ft = 3 \times 10^6$

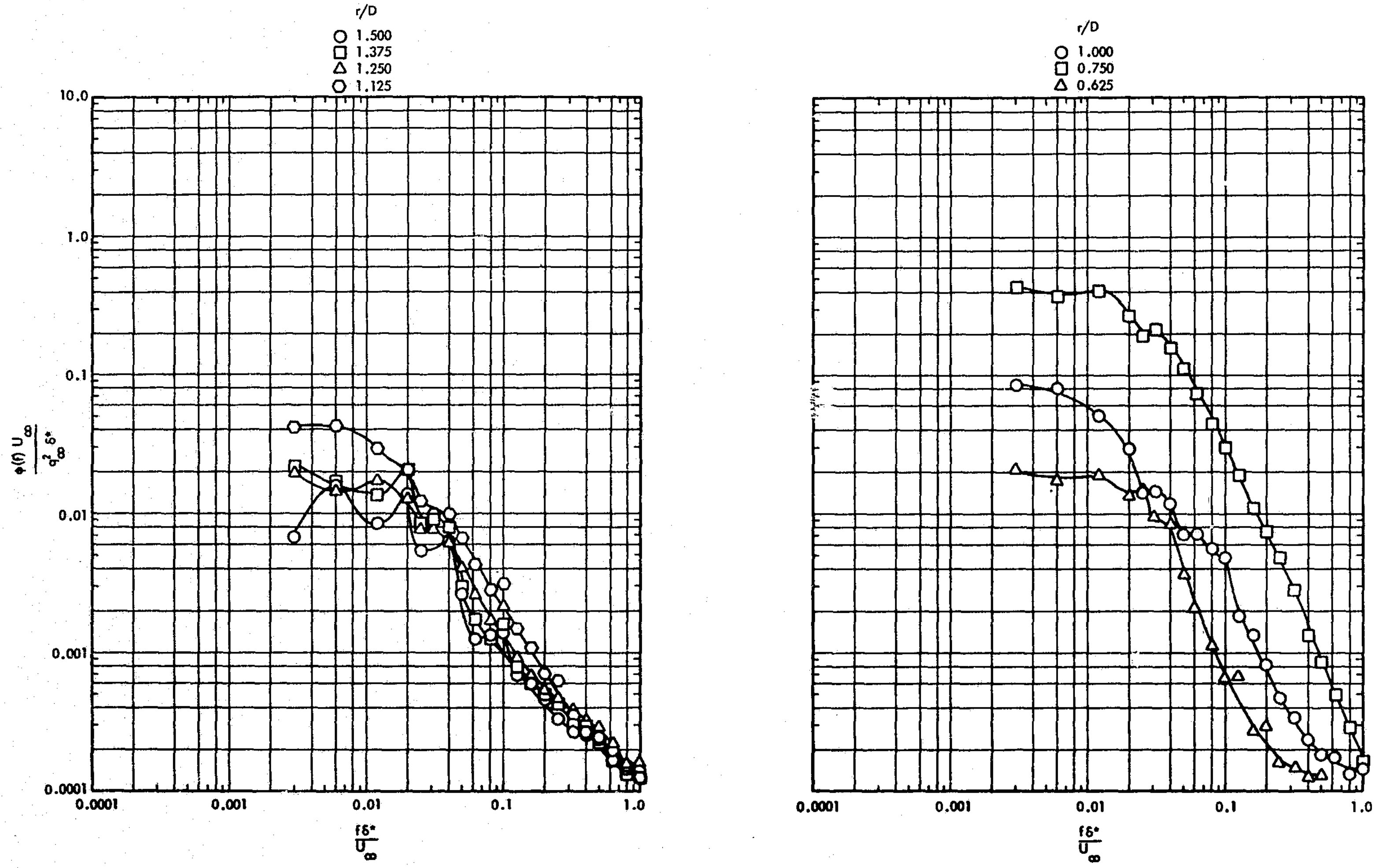

b. h/D = 2.0

Figure 51. Concluded

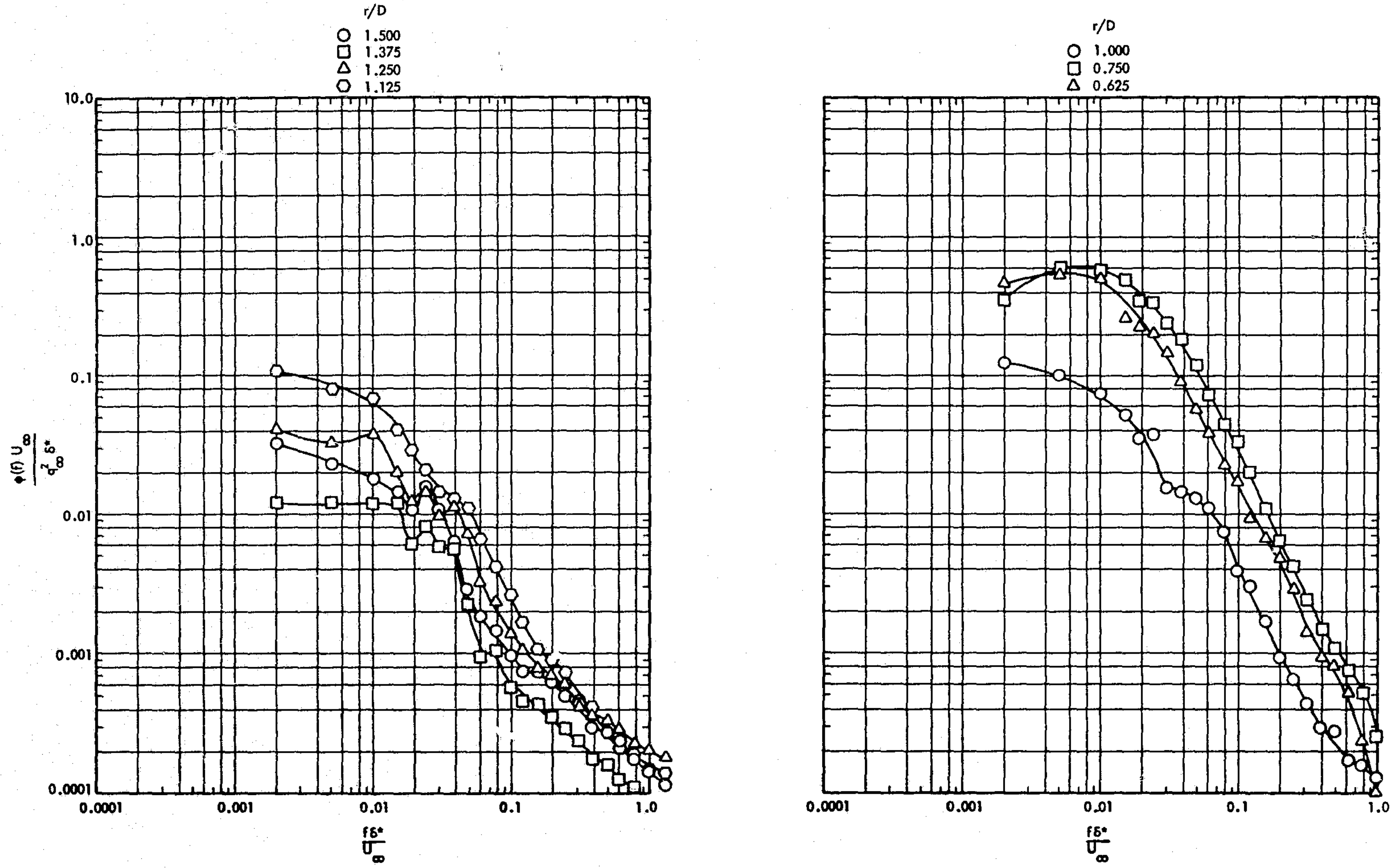

a. h/D = 1.0

Figure 52. Power Spectra of the Protuberance Induced Fluctuating Pressure Field, Upstream ($\theta^- = 0^\circ$), 8-inch Diameter Protuberance, $M_\infty = 0.80$, Re/ft = 3×10^6

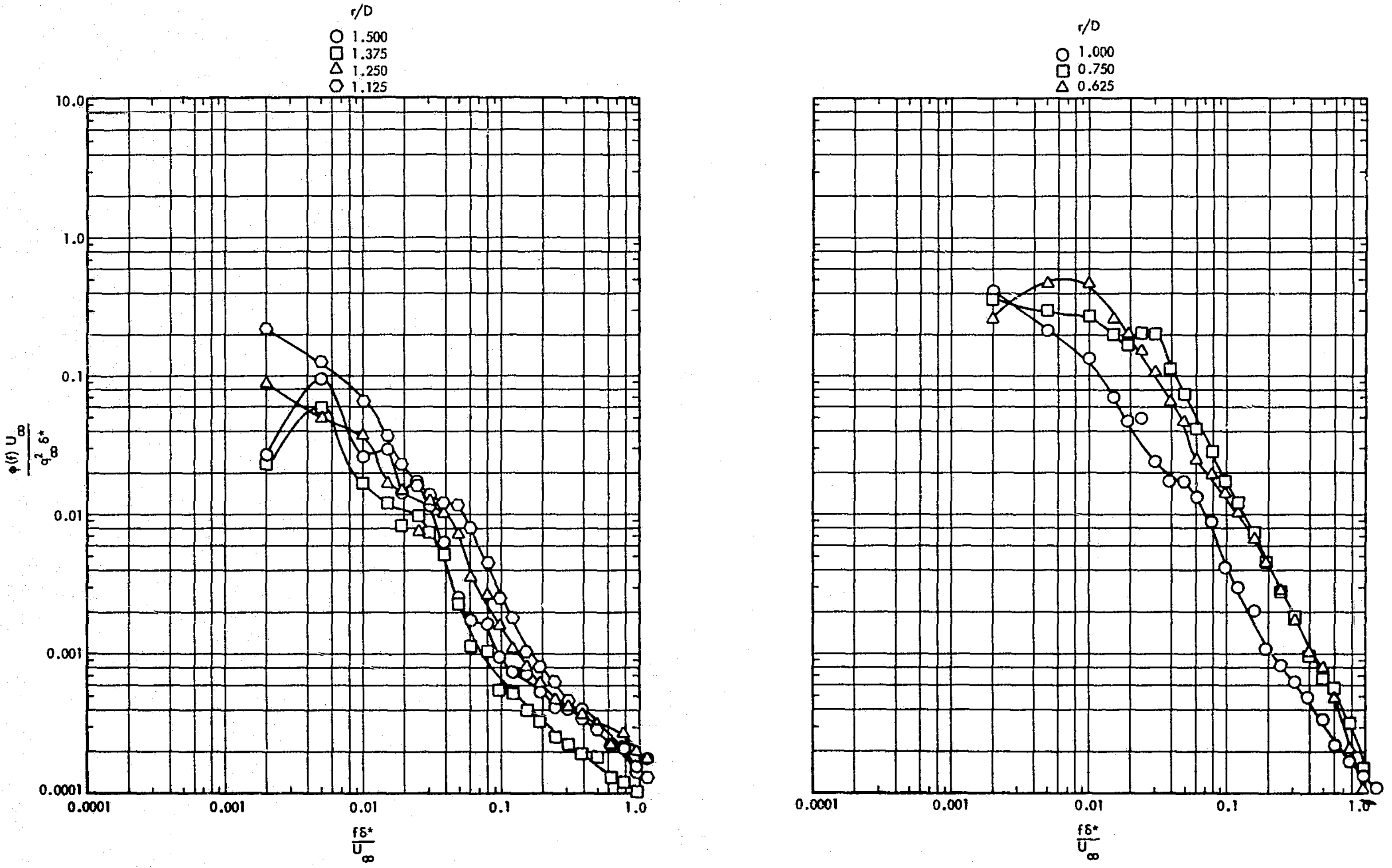

b. h/D = 2.0

Figure 52. Concluded

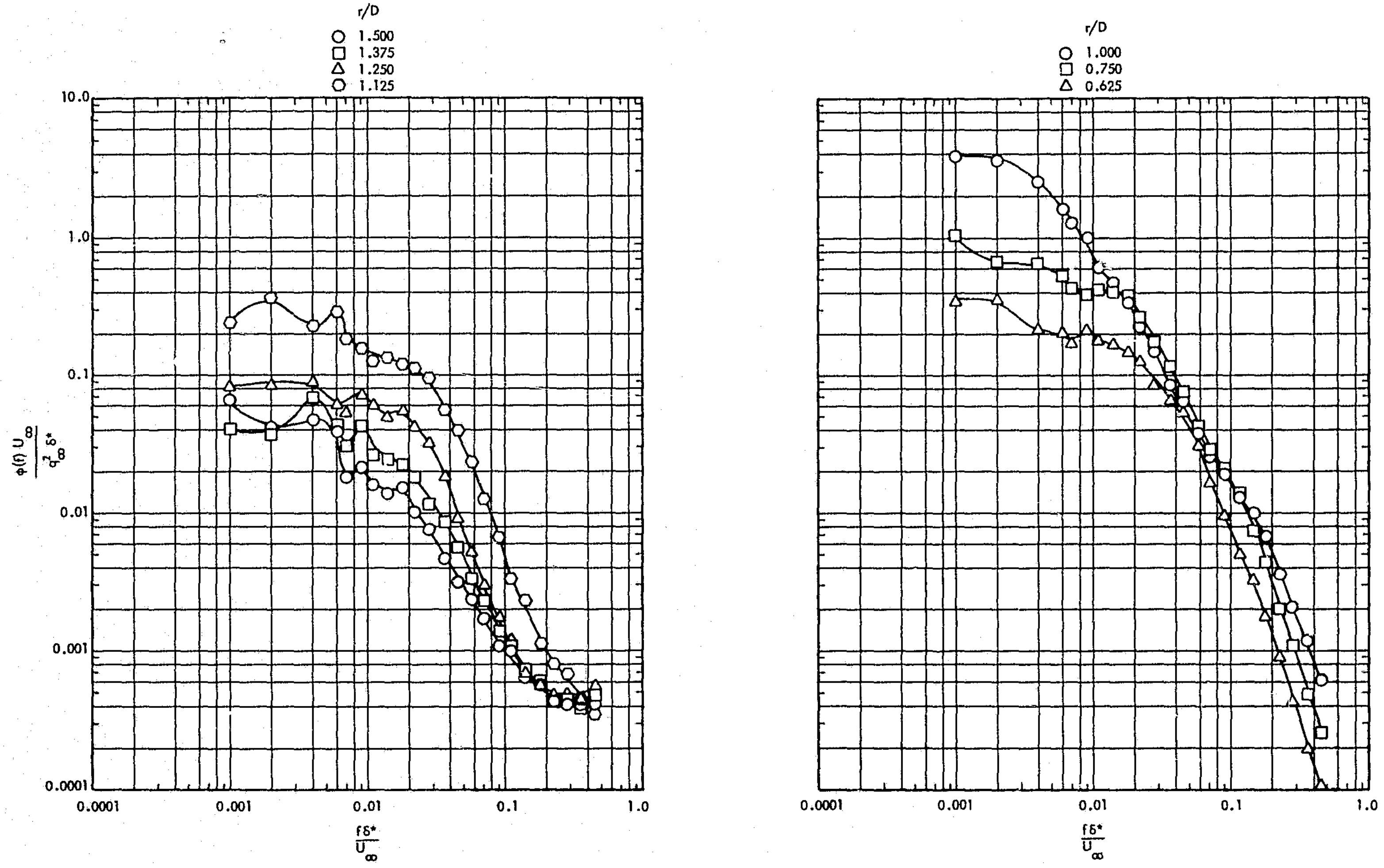

a. h/D = 1.0

Figure 53. Power Spectra of the Protuberance Induced Fluctuating Pressure Field, Upstream ($\theta^- = 0°$), 8-inch Diameter Protuberance, $M_\infty = 1.00$, $Re/ft = 3 \times 10^6$

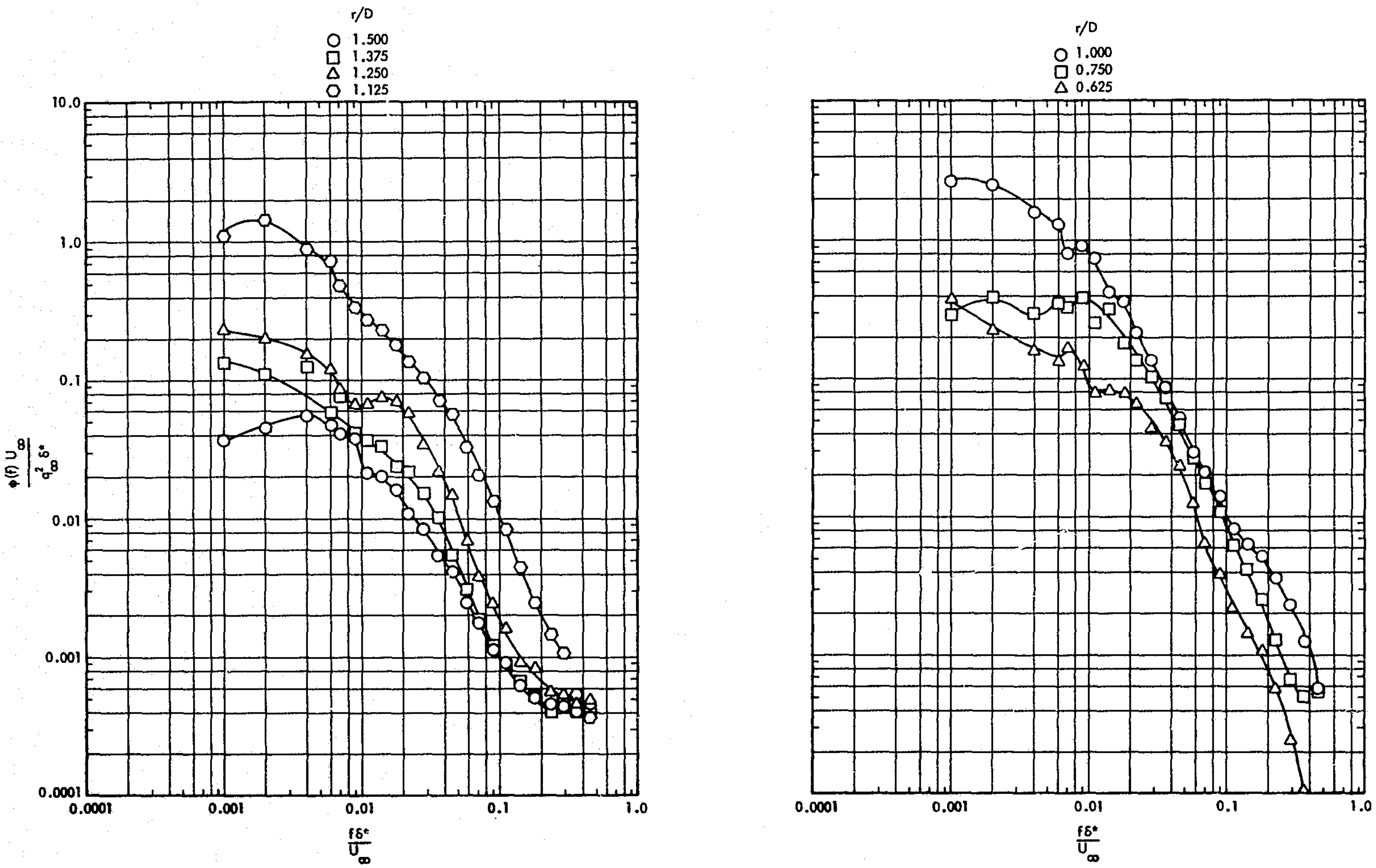

b. h/D = 2.0

Figure 53. Concluded

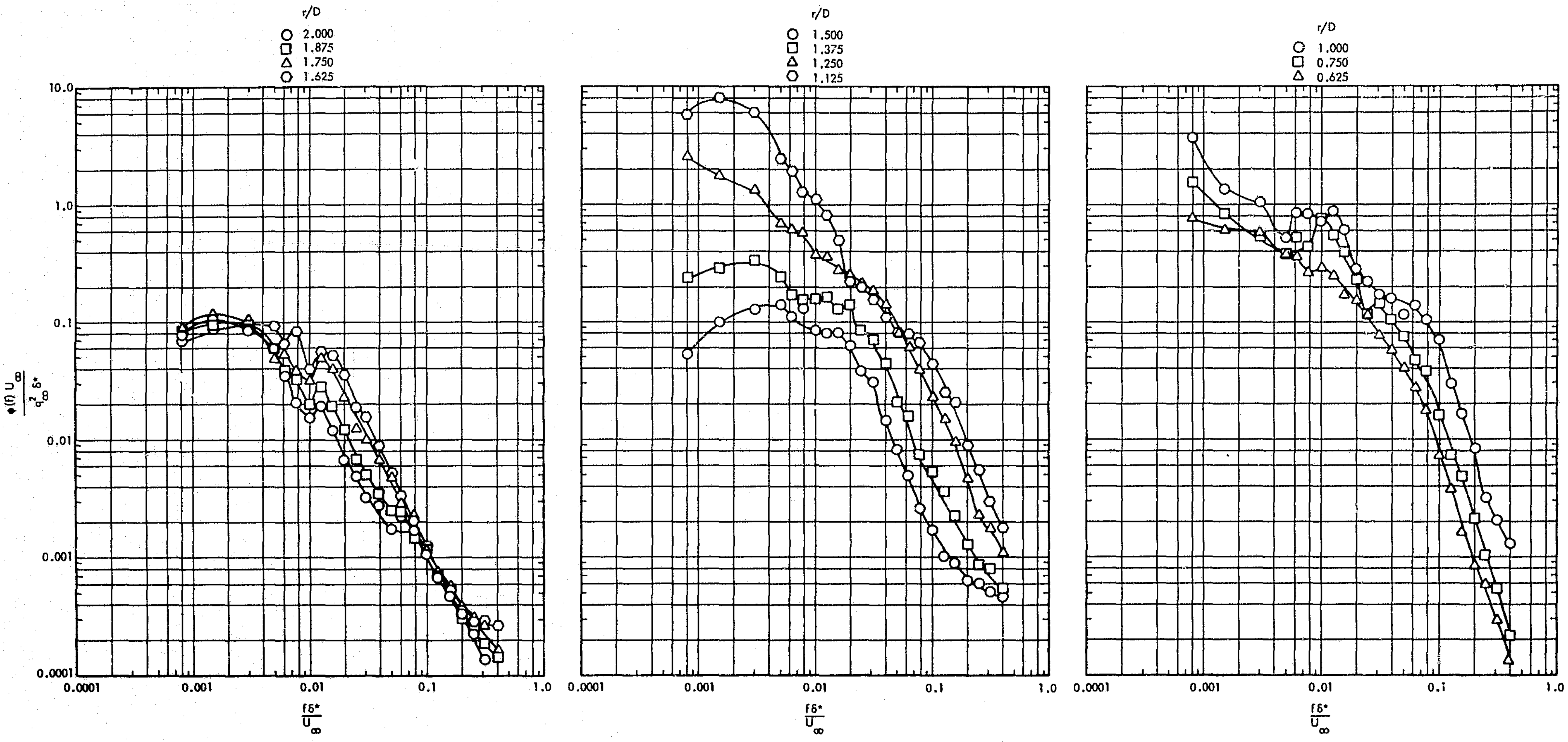

a. h/D = 1.0

Figure 54. Power Spectra of the Protuberance Induced Fluctuating Pressure Field, Upstream ($\theta^- = 0^\circ$), 8-inch Diameter Protuberance, $M_\infty = 1.20$, Re/ft = 3×10^6

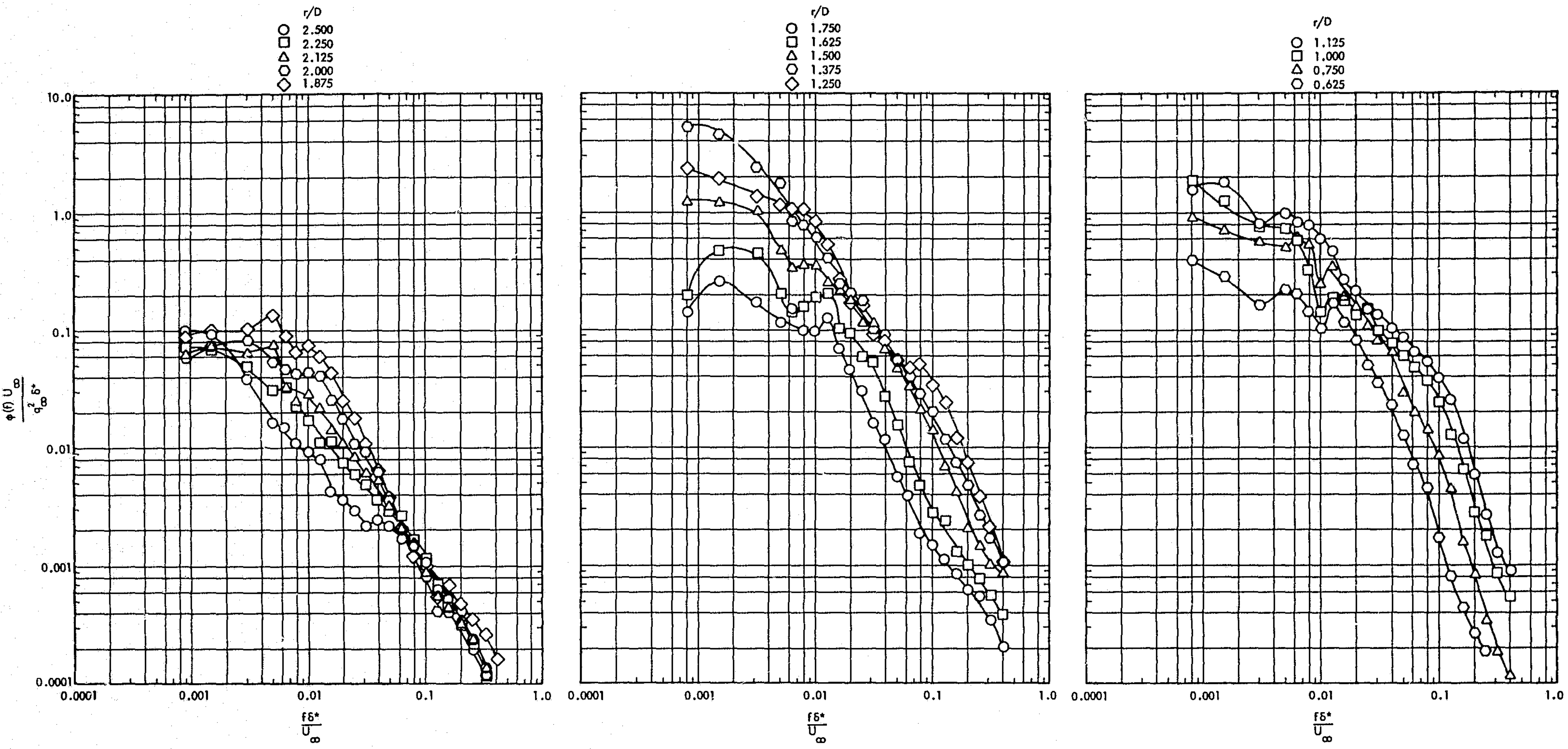

b. h/D = 2.0

Figure 54. Concluded

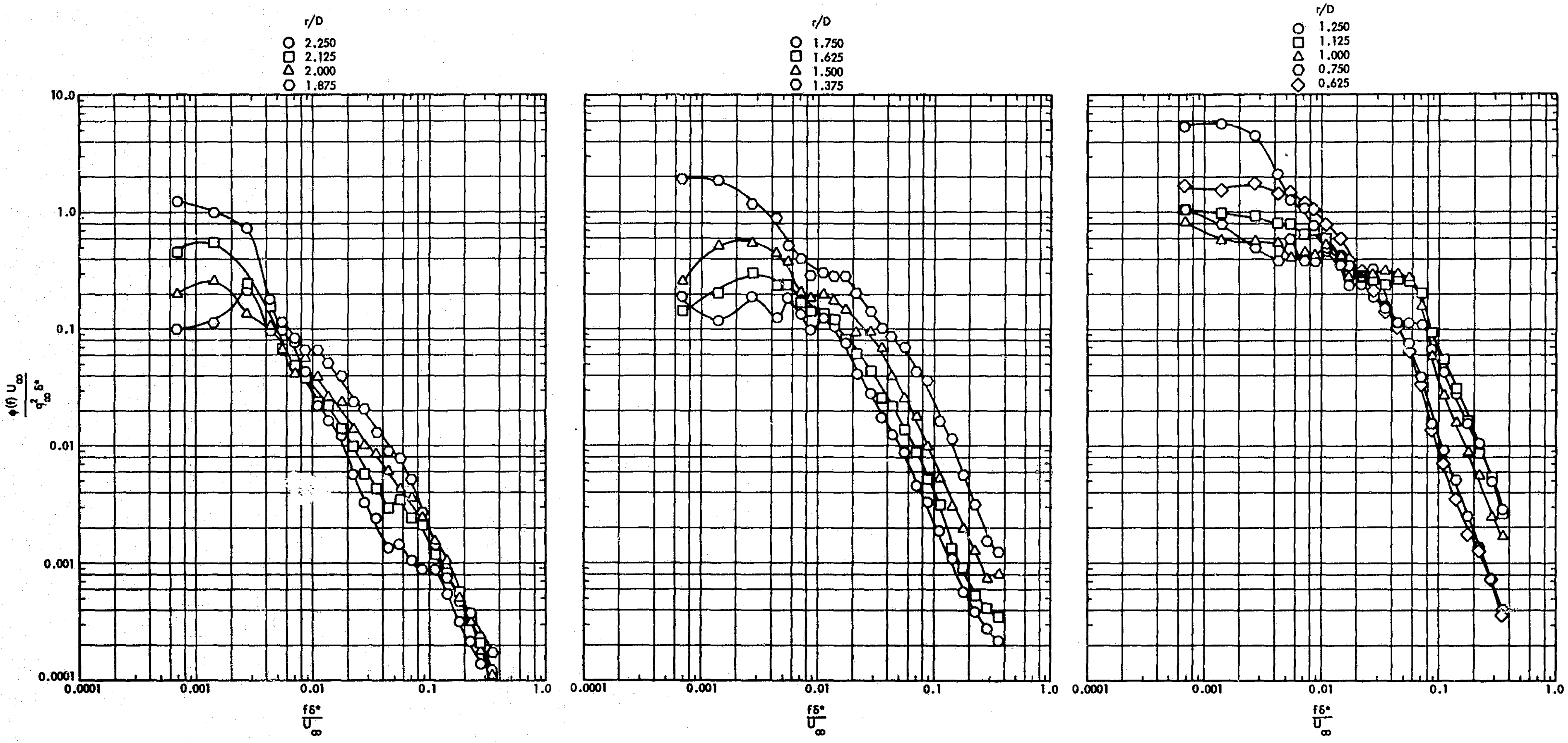

a. h/D = 1.0

Figure 55. Power Spectra of the Protuberance Induced Fluctuating Pressure Field, Upstream ($\theta^- = 0^\circ$), 8-inch Diameter Protuberance, $M_\infty = 1.40$, $Re/ft = 3 \times 10^6$

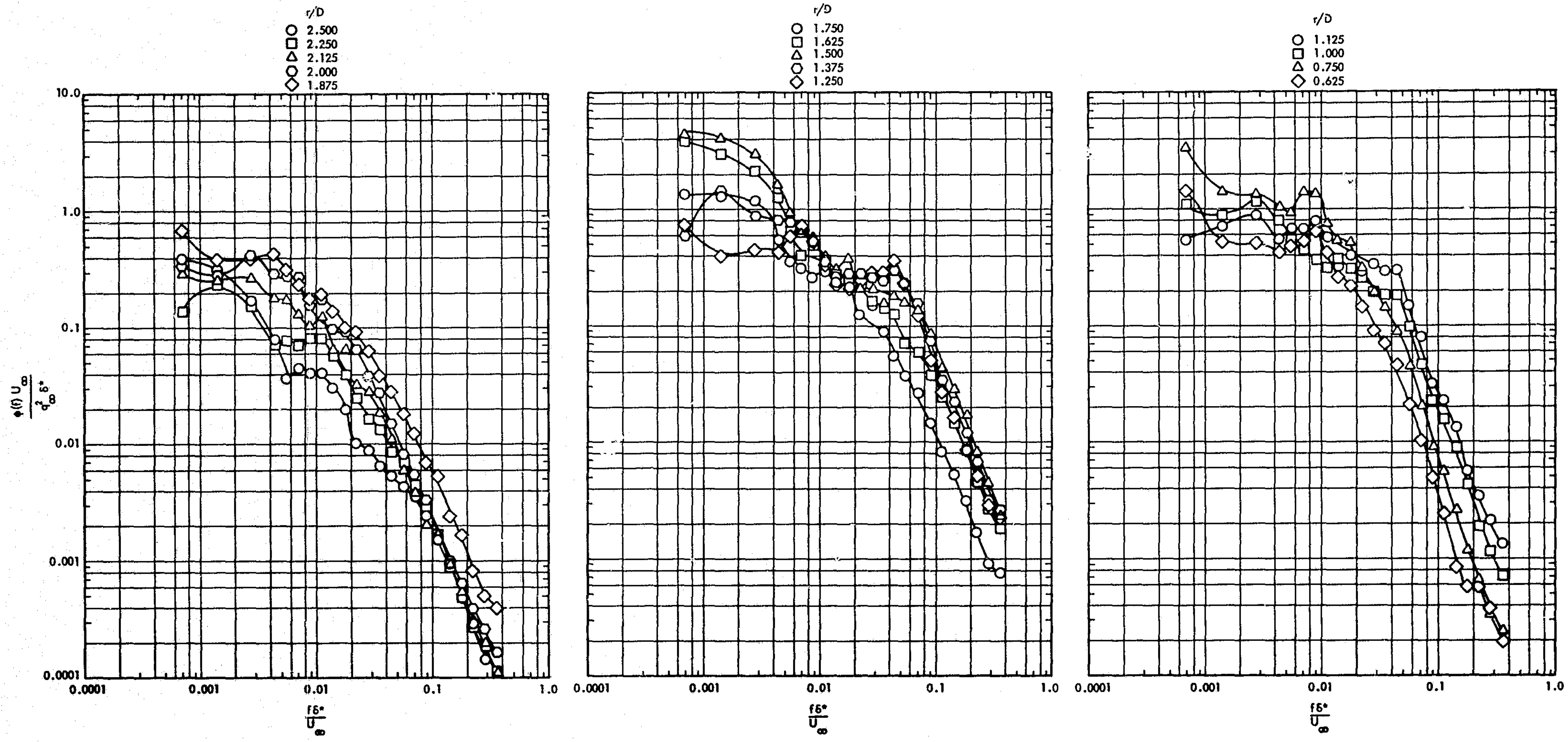

b. h/D = 2.0

Figure 55. Concluded

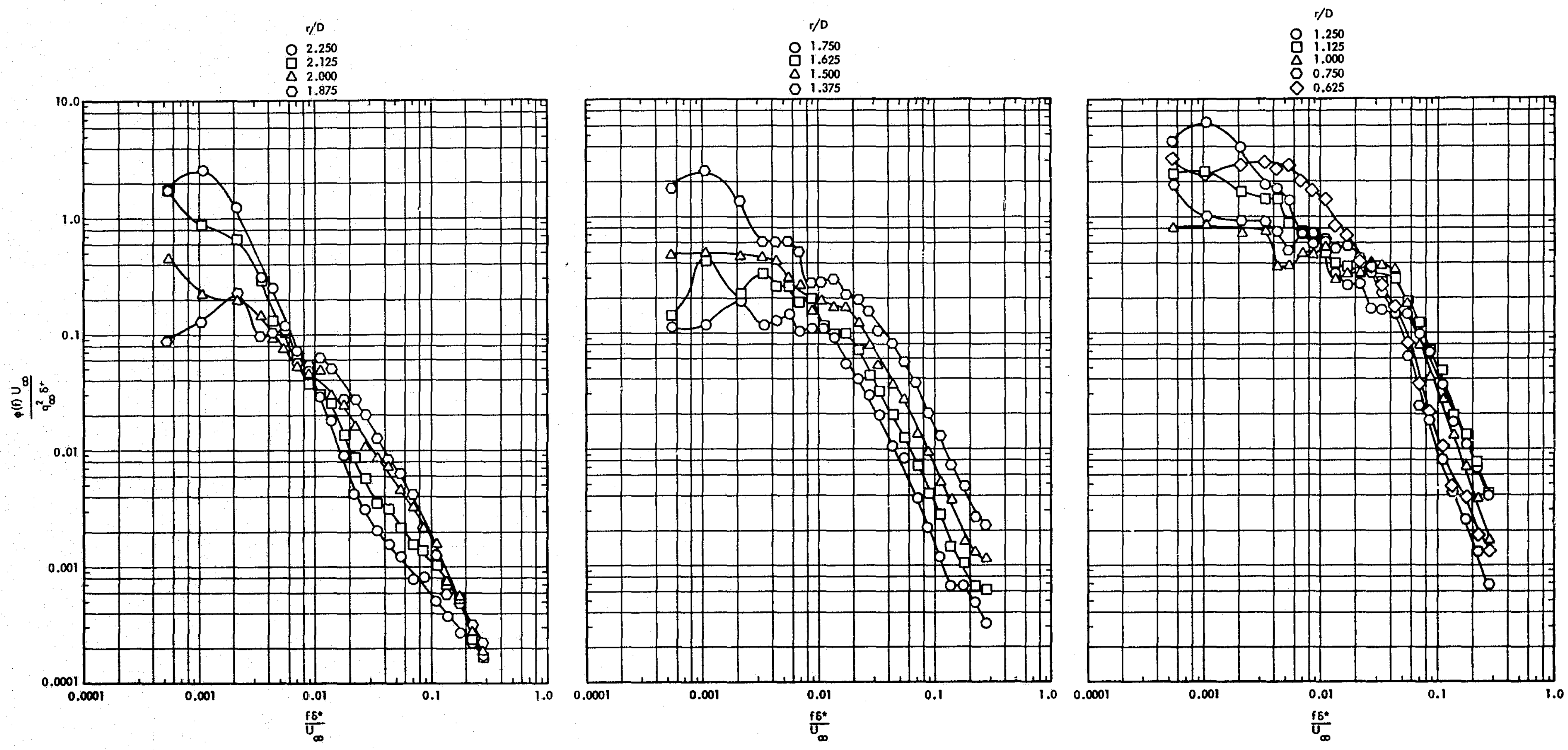

a. h/D = 1.0

Figure 56. Power Spectra of the Protuberance Induced Fluctuating Pressure Field, Upstream ($\theta^- = 0^\circ$), 8-inch Diameter Protuberance, $M_\infty = 1.60$, Re/ft = 3×10^6

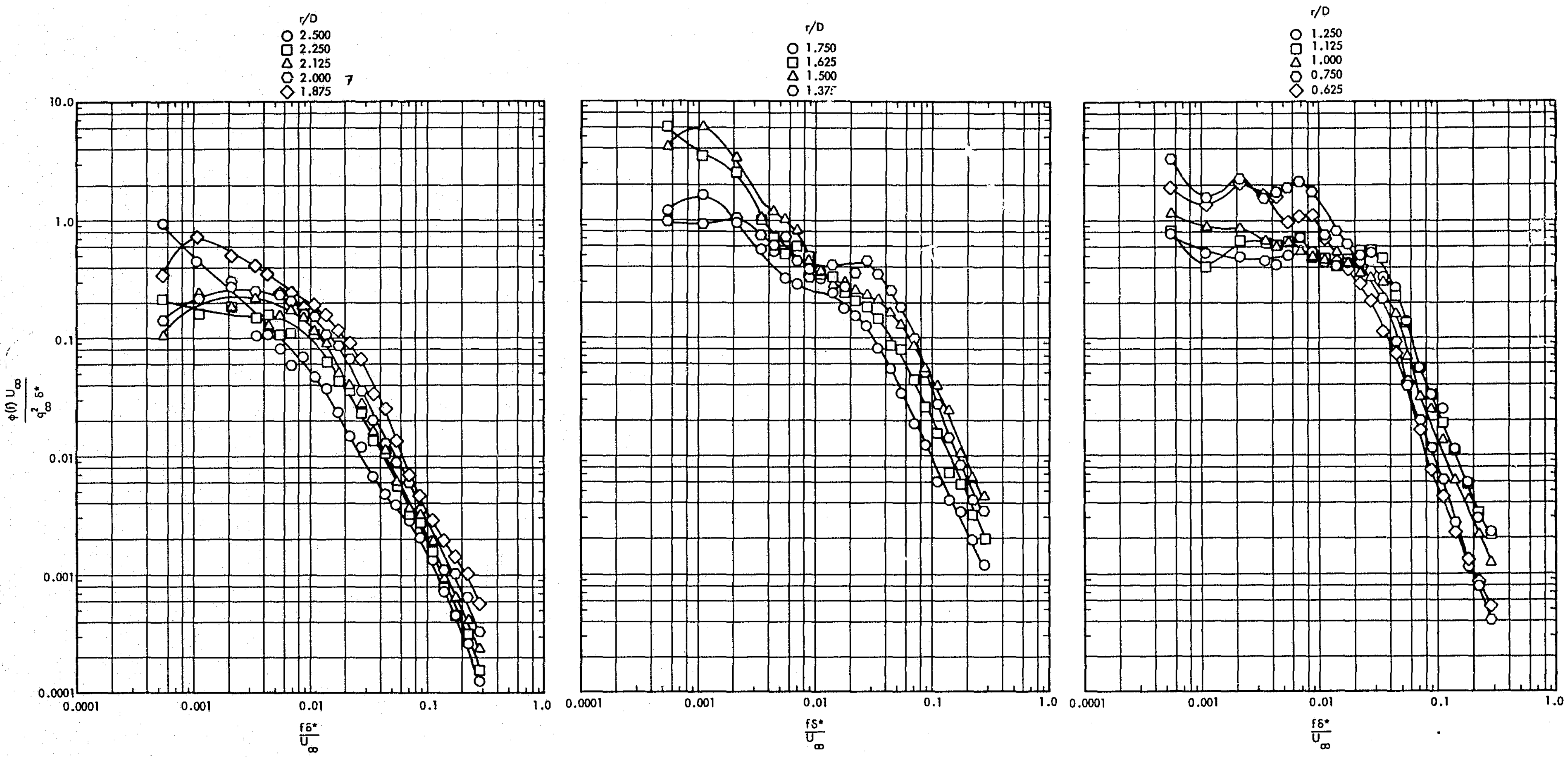

b. h/D = 2.0

Figure 56. Concluded

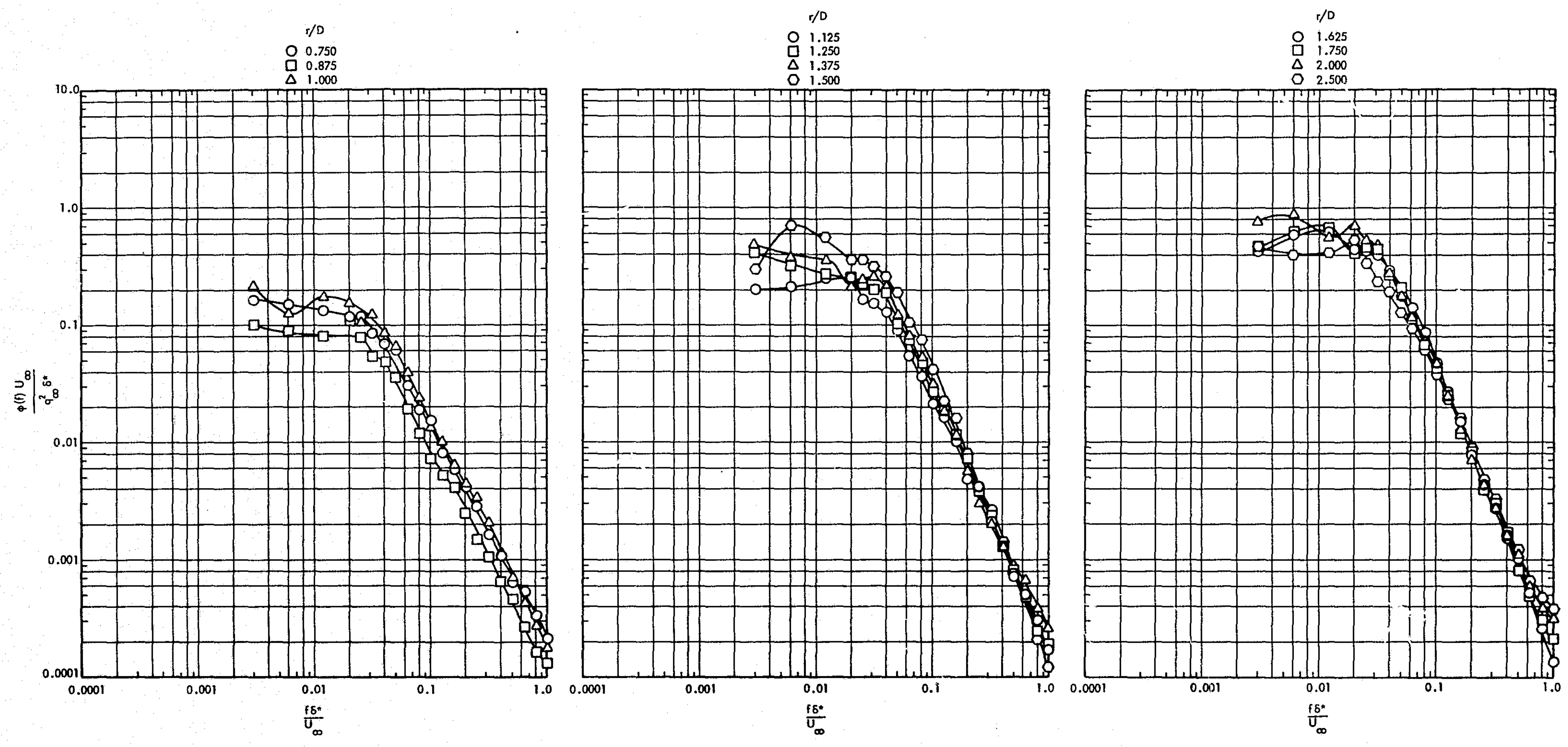

a. h/D = 1.0

Figure 57. Power Spectra of the Protuberance Induced Fluctuating Pressure Field, Downstream ($\theta^- = 180^\circ$), 8-inch Diameter Protuberance, $M_\infty = 0.60$, $Re/ft = 3 \times 10^6$

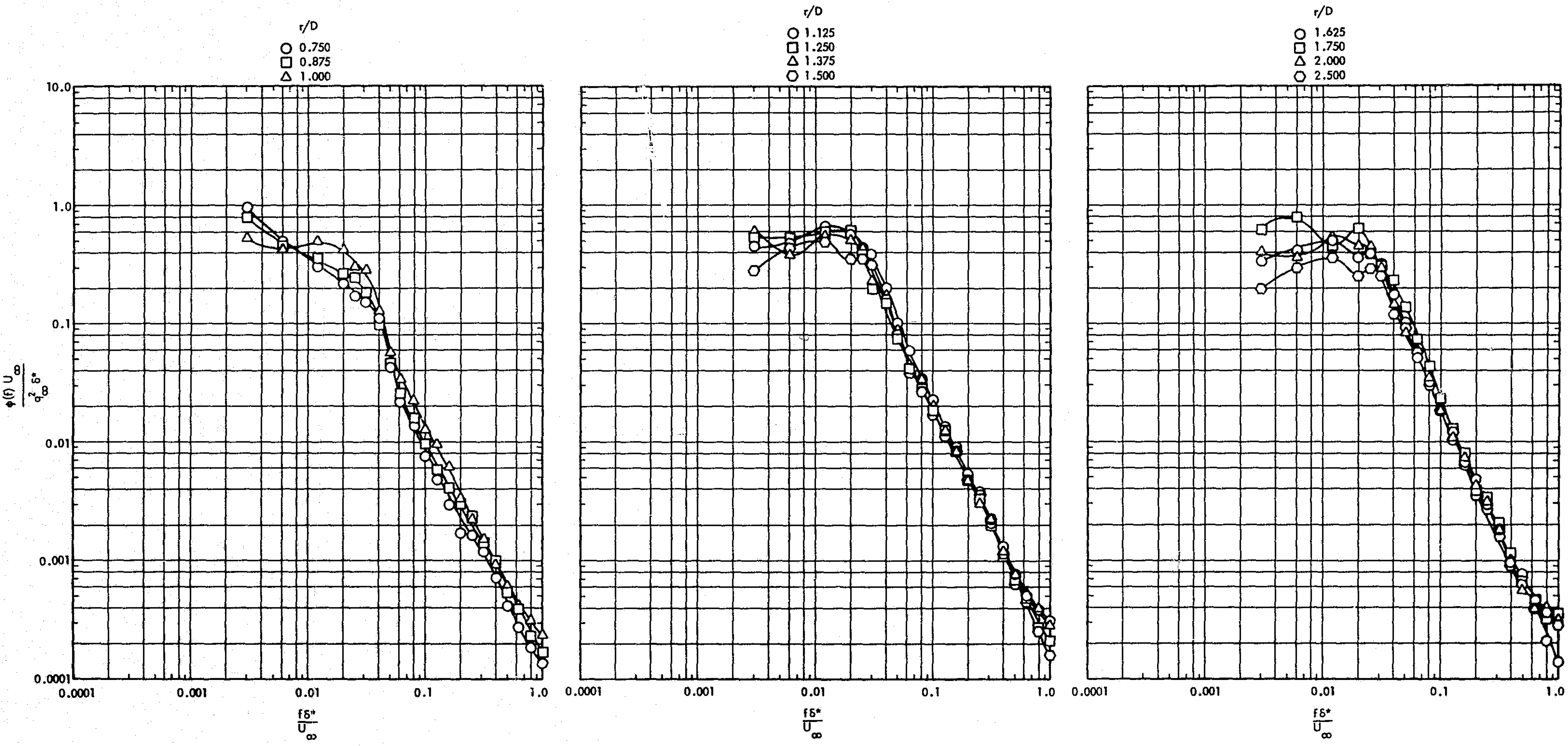

b. h/D = 2.0

Figure 57. Concluded

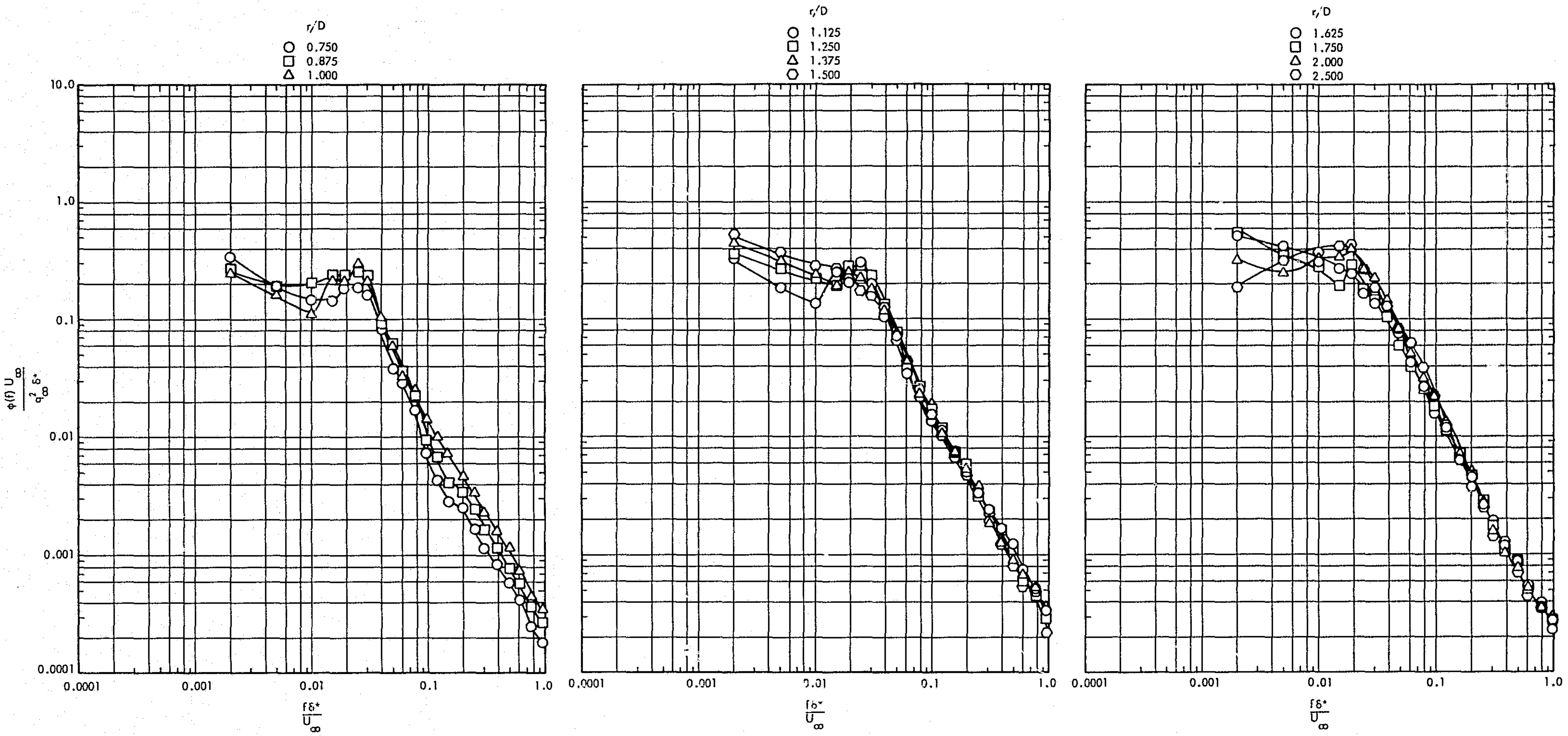

a. h/D = 1.0

Figure 58. Power Spectra of the Protuberance Induced Fluctuating Pressure Field, Downstream ($\theta^- = 180°$), 8-inch Diameter Protuberance, $M_\infty = 0.80$, $Re/ft = 3 \times 10^6$

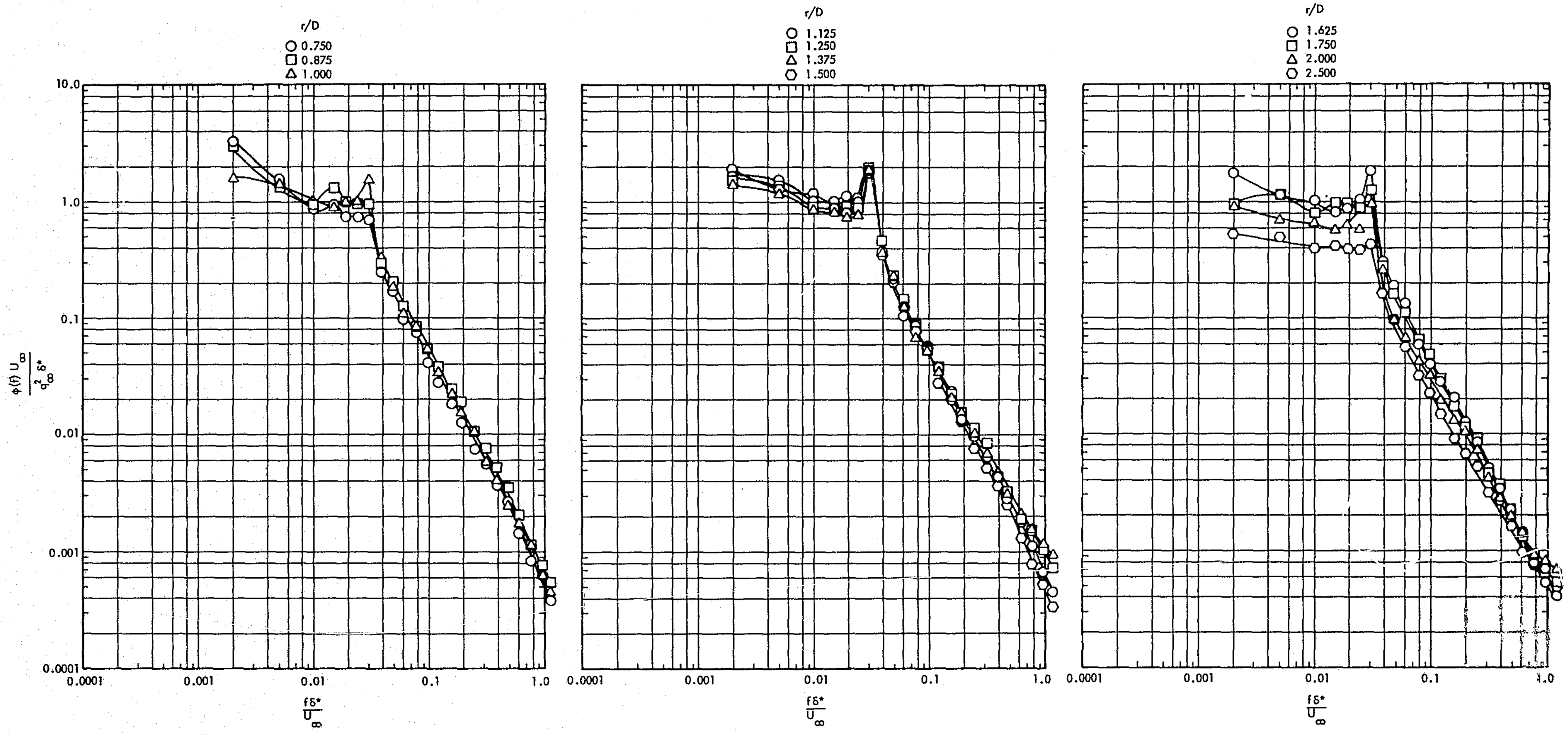

b. h/D = 2.0

Figure 58. Concluded

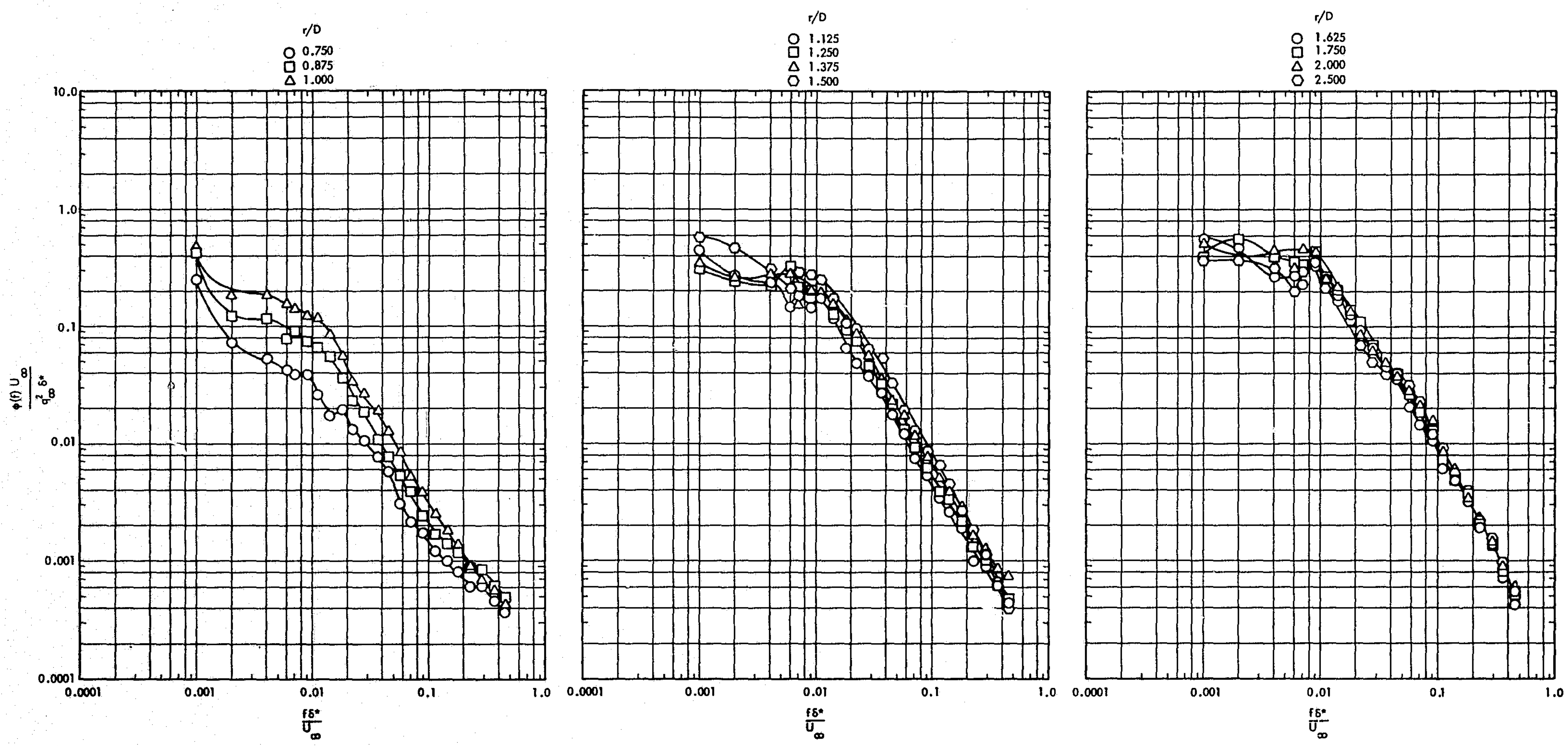

a. h/D = 1.0

Figure 59. Power Spectra of the Protuberance Induced Fluctuating Pressure Field, Downstream ($\theta^- = 180^\circ$), 8-inch Diameter Protuberance, $M_\infty = 1.00$, Re/ft = 3×10^6

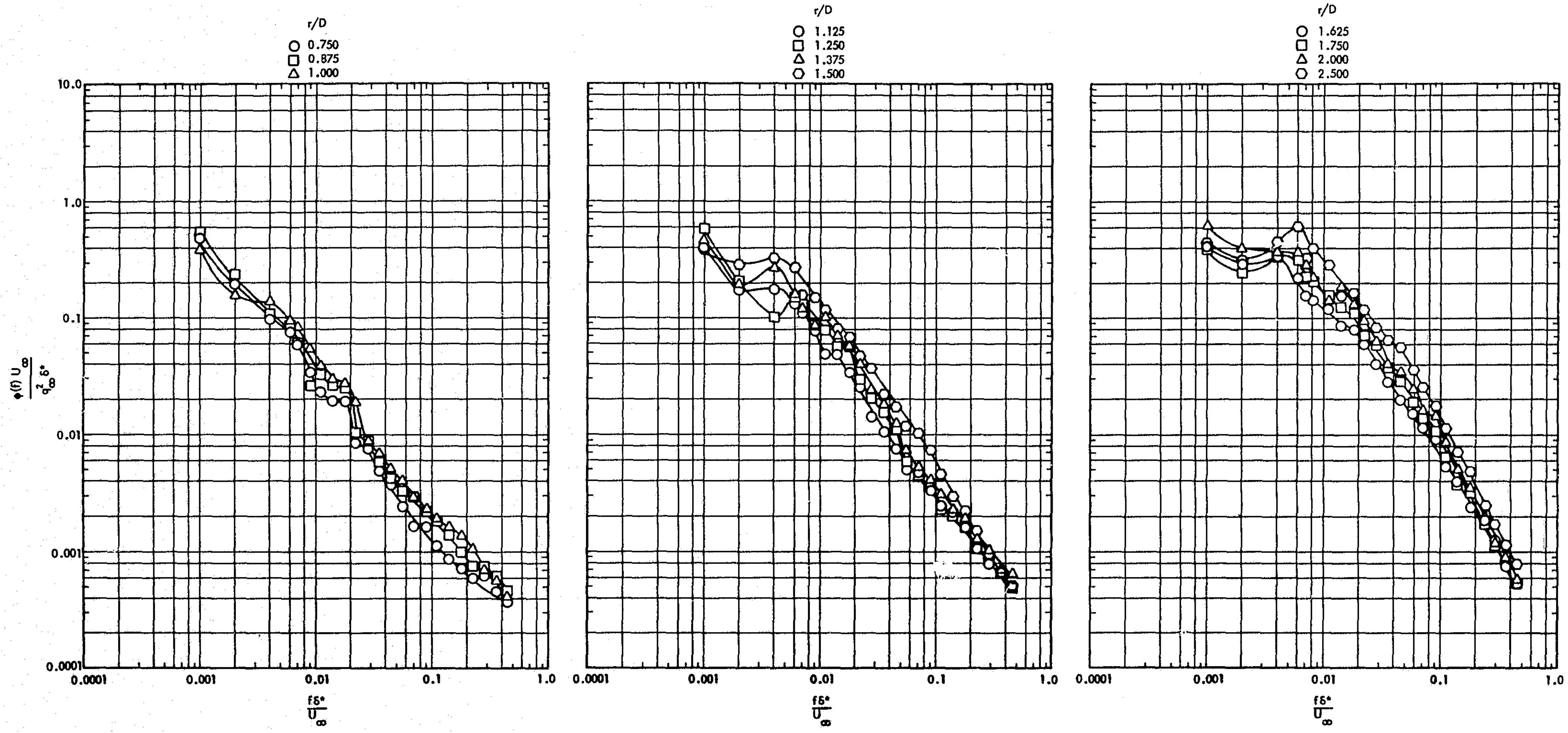

b- h/D = 2.0

Figure 59. Concluded

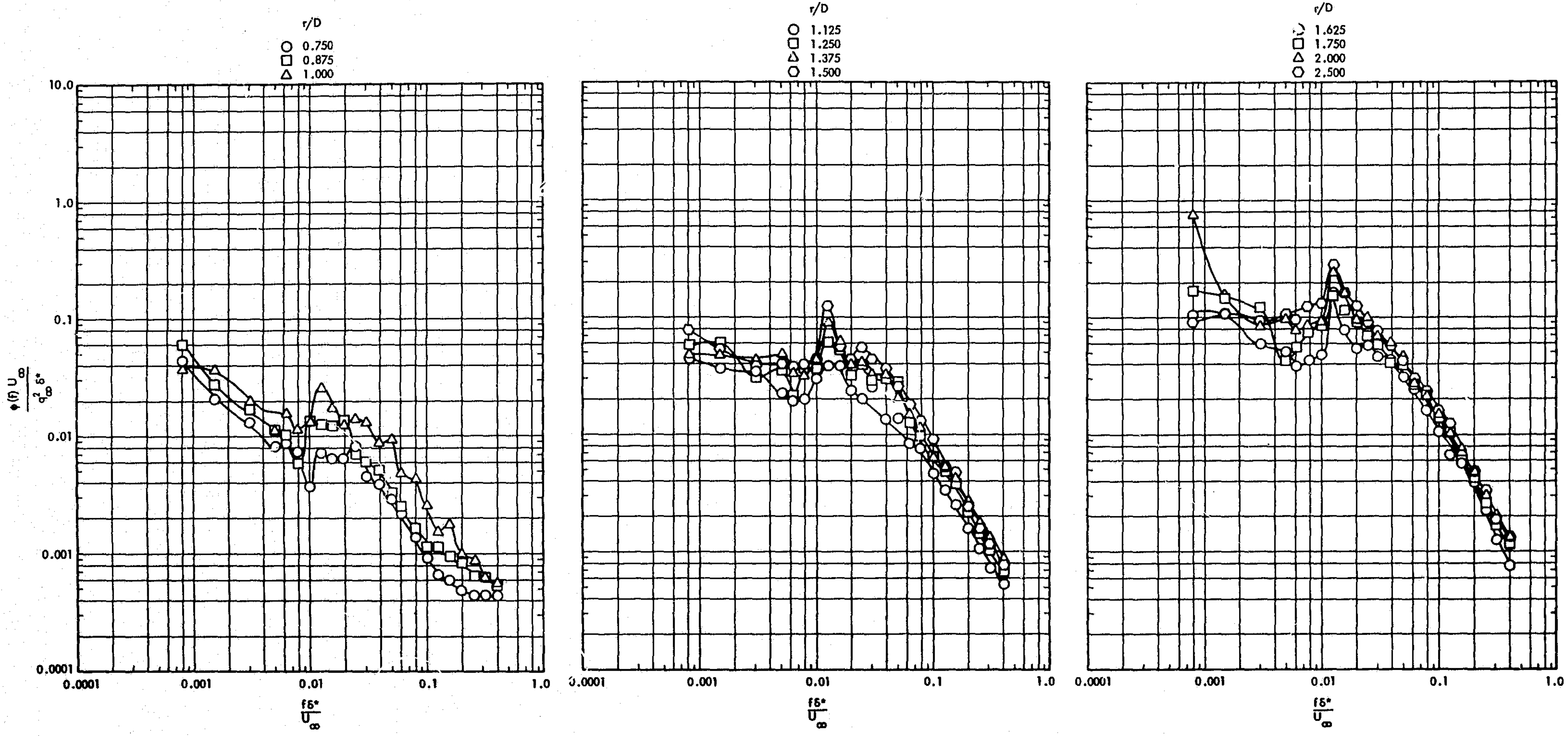

a. h/D = 1.0

Figure 60. Power Spectra of the Protuberance Induced Fluctuating Pressure Field, Downstream ($\theta^- = 180^\circ$), 8-inch Diameter Protuberance, $M_\infty = 1.20$, Re/ft = 3 x 10^6

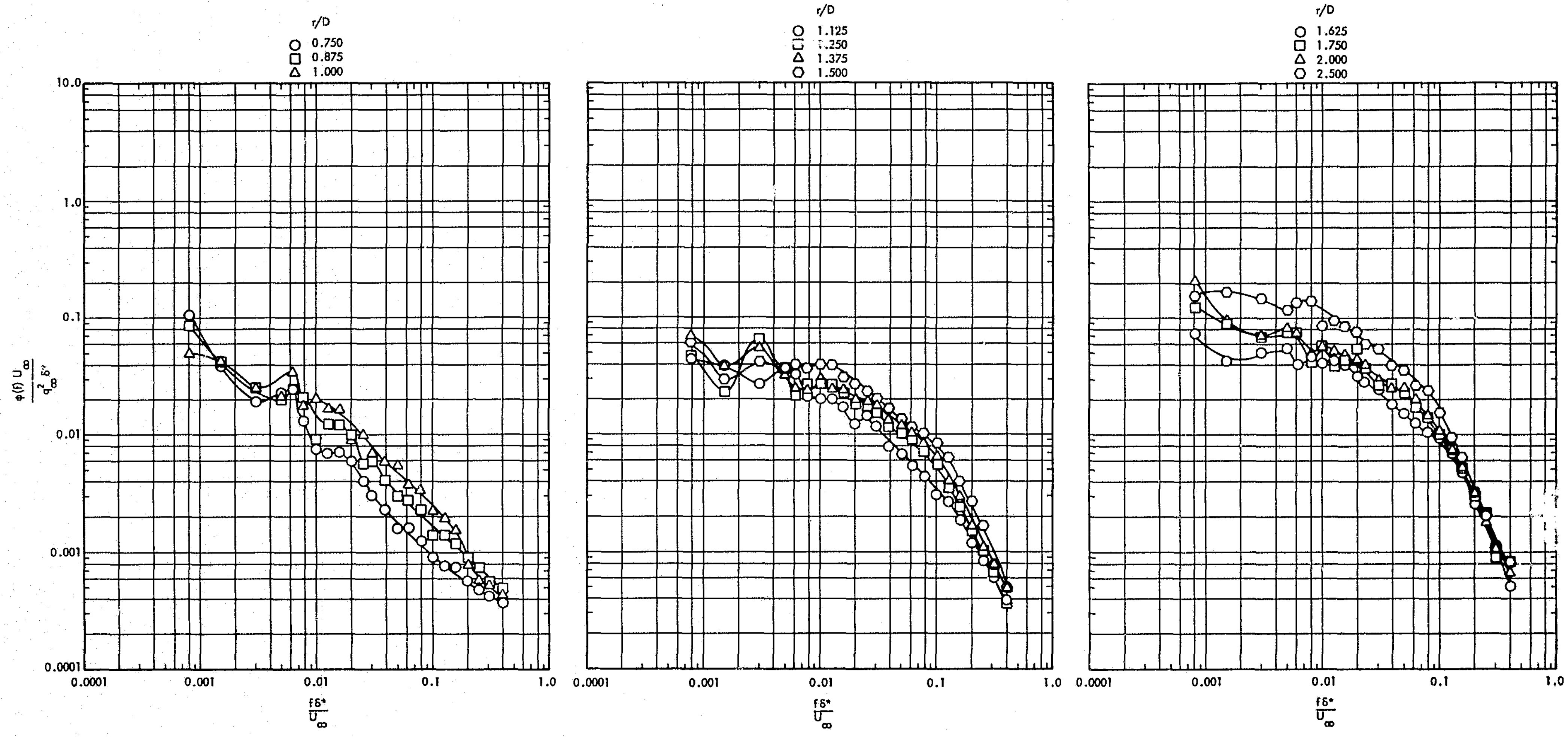

b. h/D = 2.0

Figure 60. Concluded

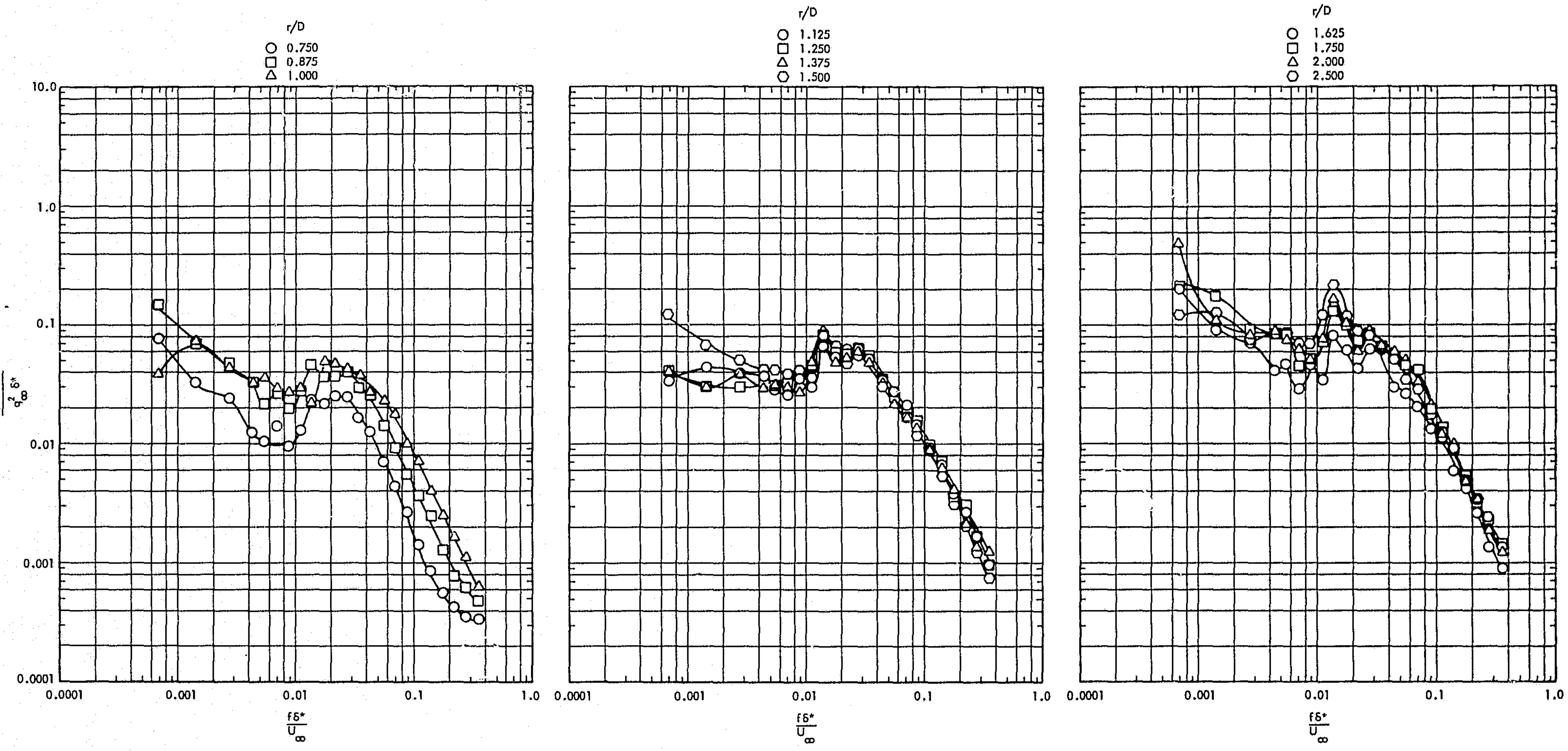

a. h/D = 1.0

Figure 61. Power Spectra of the Protuberance Induced Fluctuating Pressure Field, Downstream ($\theta^- = 180^\circ$), 8-inch Diameter Protuberance, $M_\infty = 1.40$, Re/ft = 3×10^6

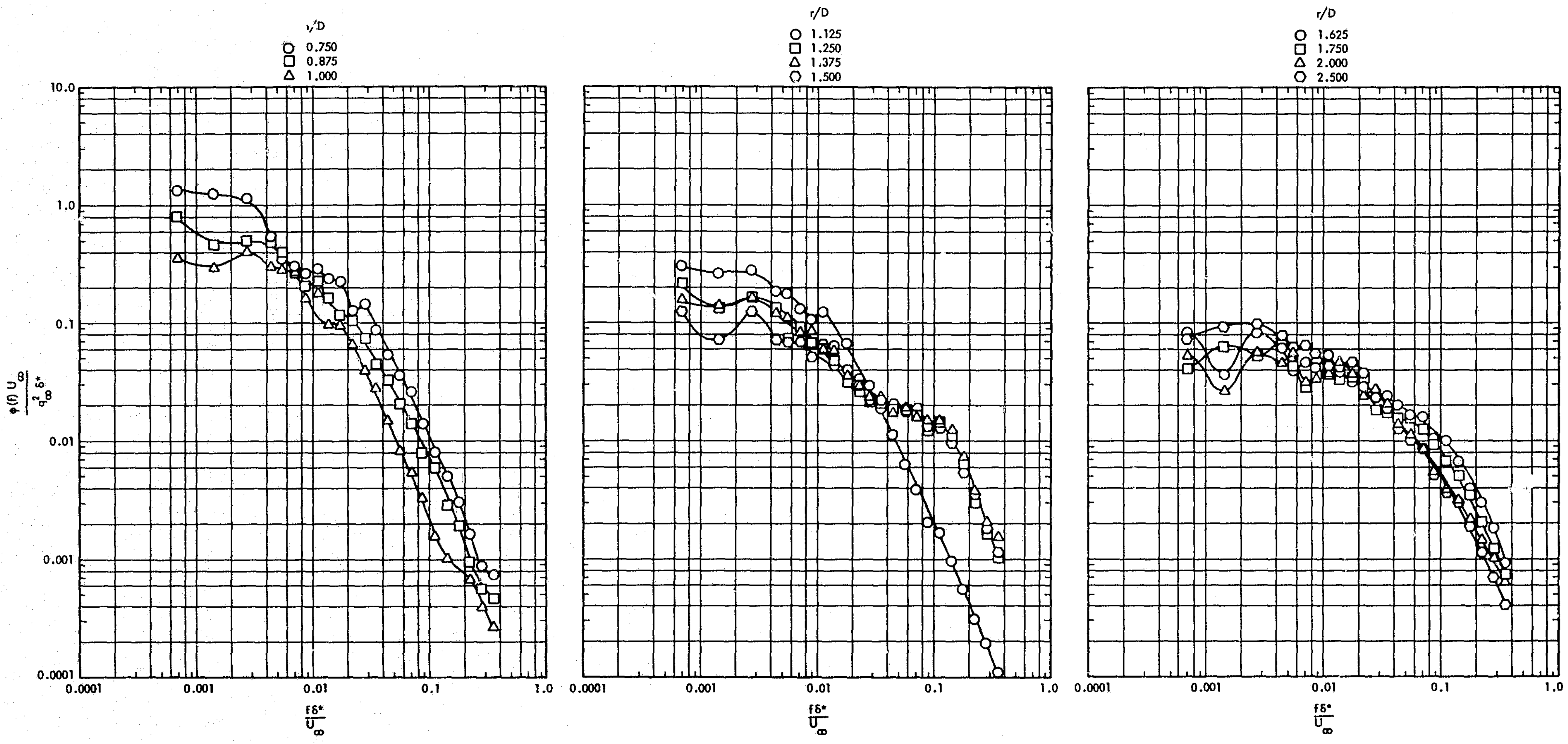

b. h/D = 2.0

Figure 61. Concluded

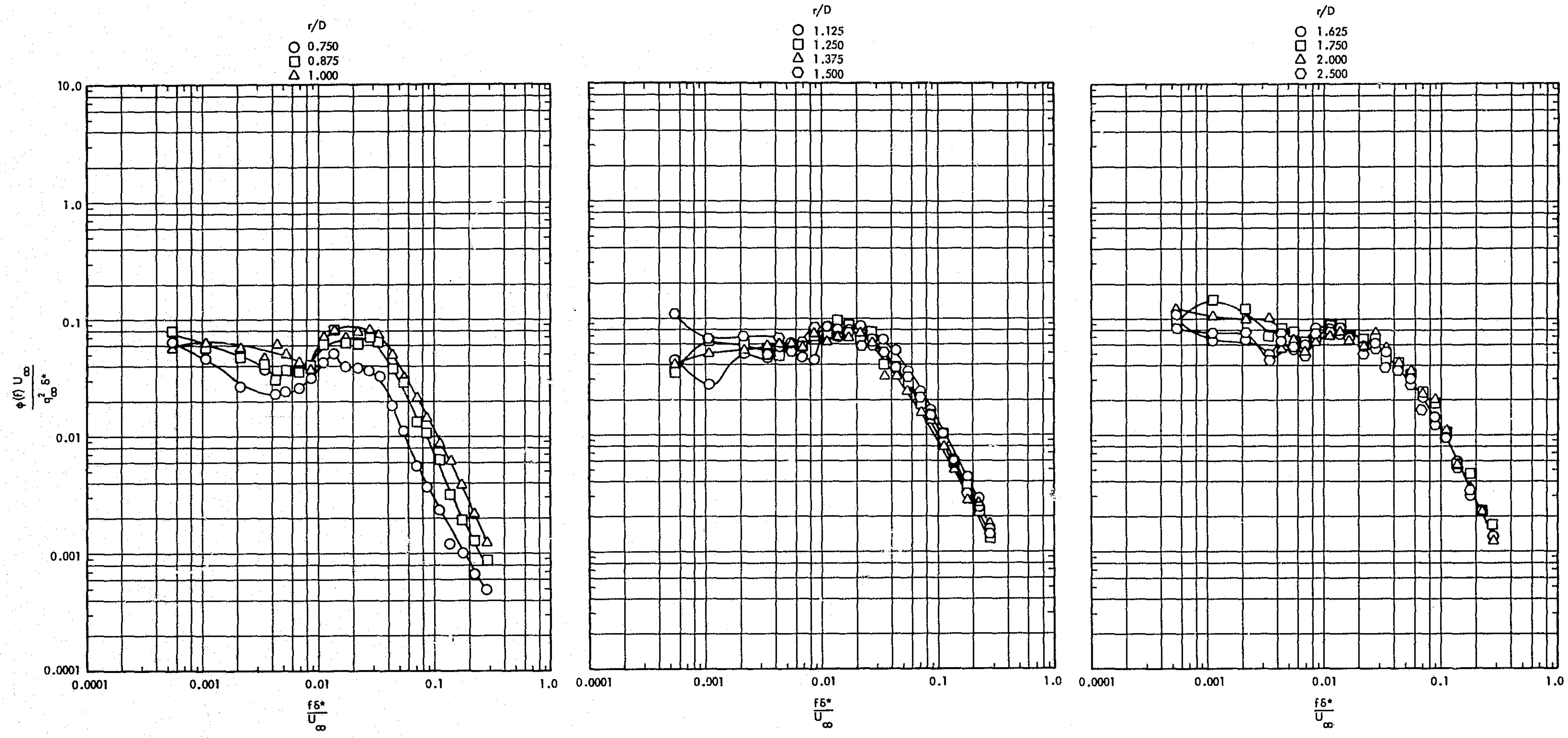

a. h/D = 1.0

Figure 62. Power Spectra of the Protuberance Induced Fluctuating Pressure Field, Downstream ($\theta^- = 180^\circ$), 8-inch Diameter Protuberance, $M_\infty = 1.60$, $Re/ft = 3 \times 10^6$

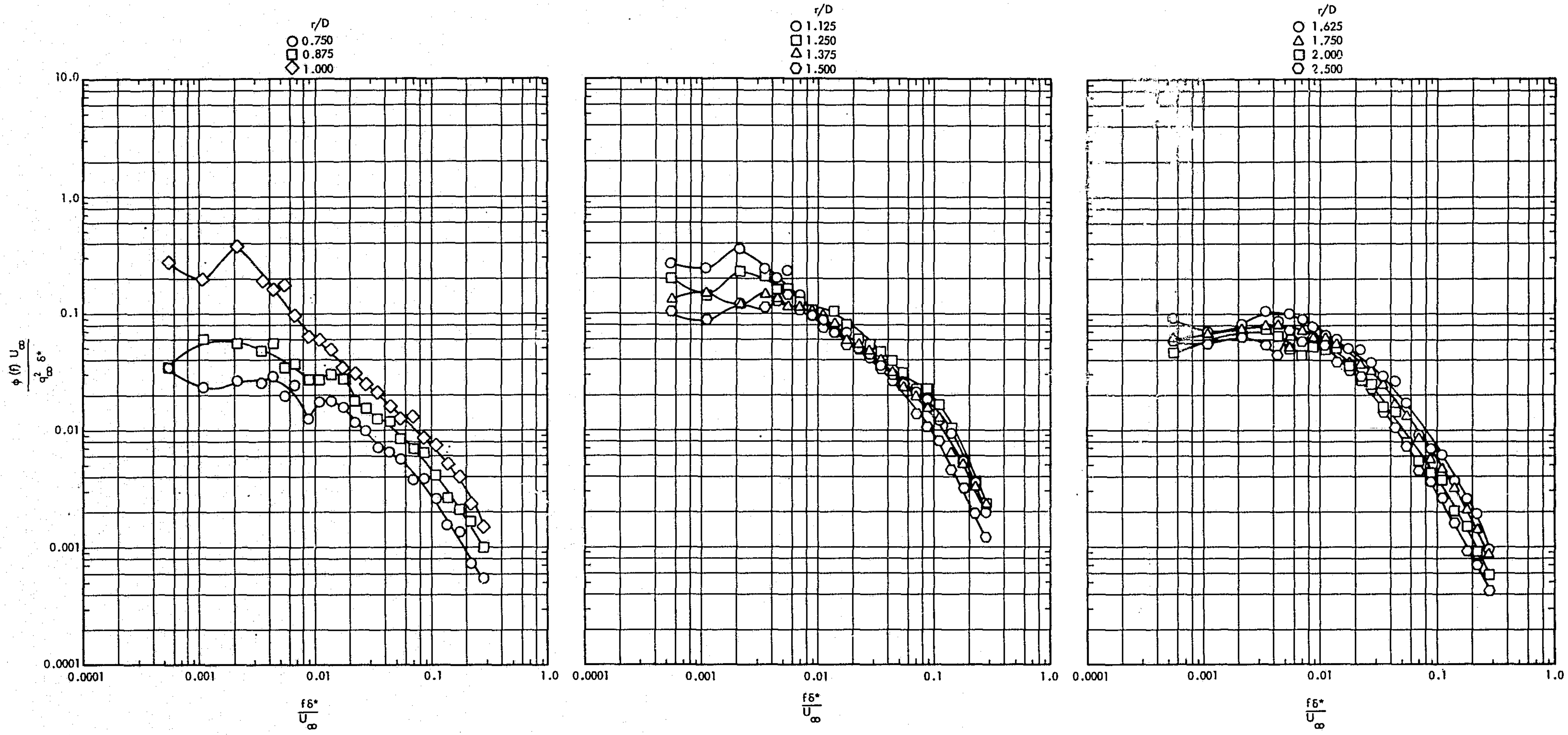

b. h/D = 2.0

Figure 62. Concluded

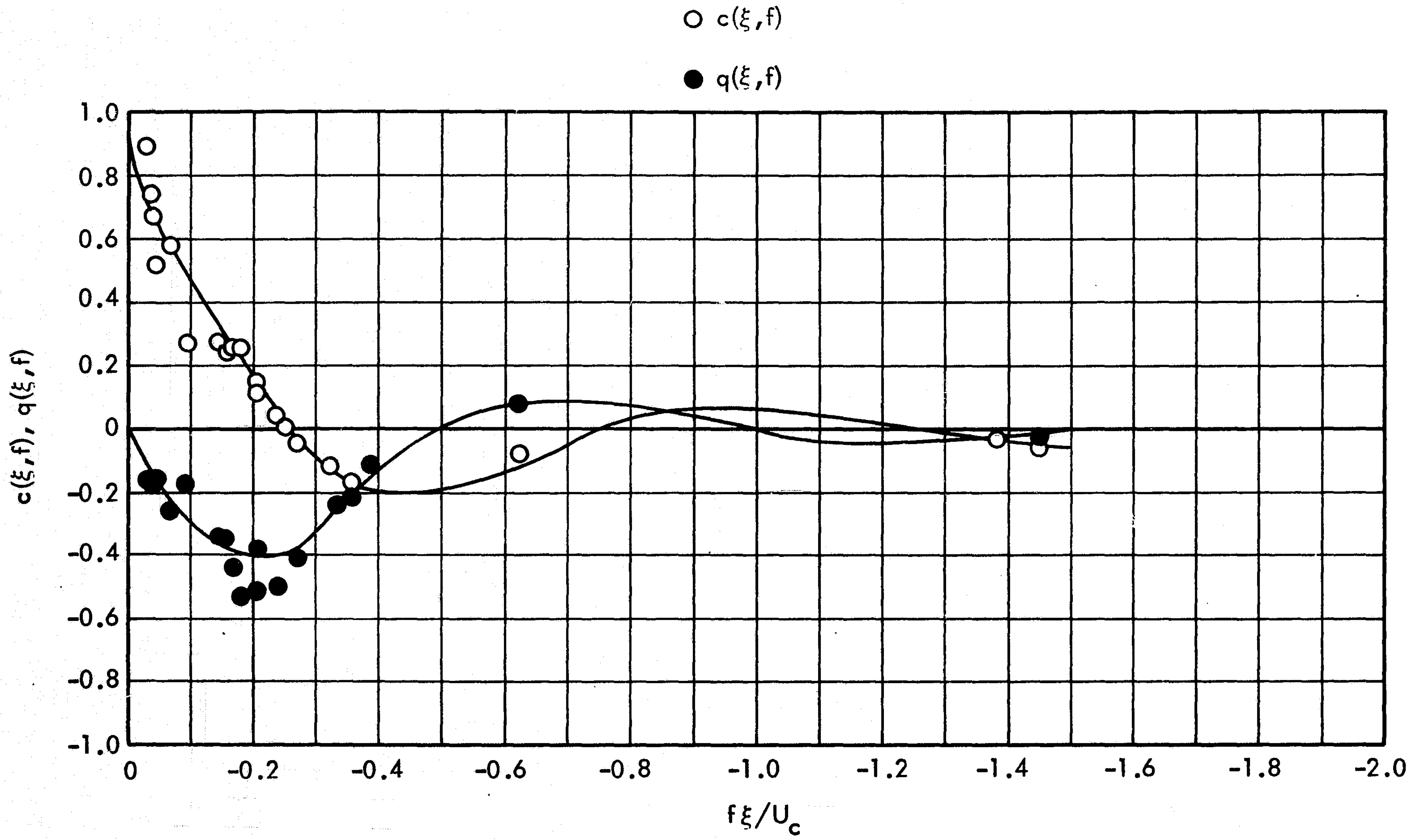

a. h/D = 1.0, r/D = -1.375 to -1.250

Figure 63. Longitudinal Cross-Spectra for the Protuberance Induced Fluctuating Pressure Field, Upstream ($\theta^- = 0^\circ$), 8-inch Diameter Protuberance, $M_\infty = 1.20$, $Re/ft = 3 \times 10^6$, $\xi/D = 0.125$

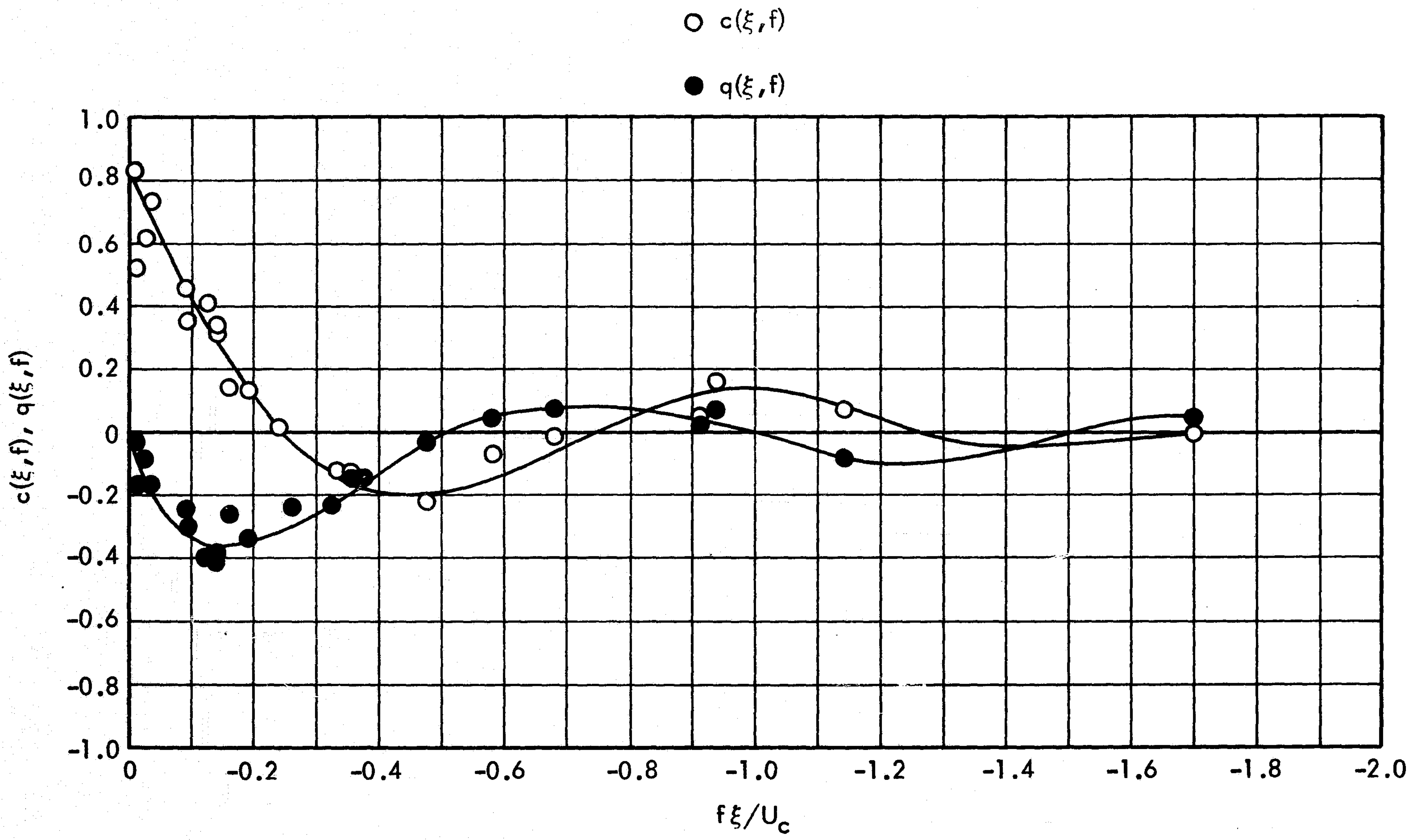

b. h/D = 2.0, r/D = -1.625 to -1.500

Figure 63. Concluded

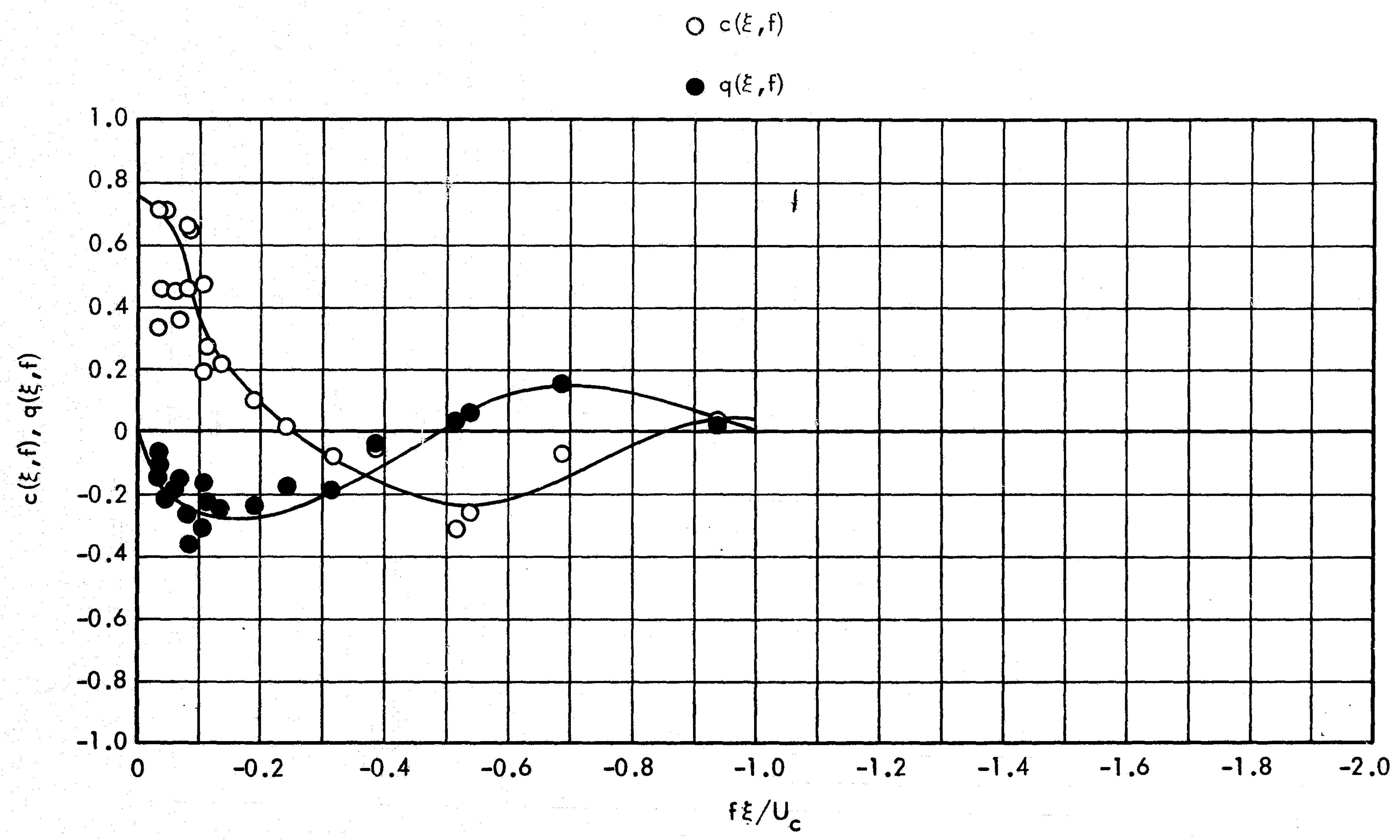

a. h/D = 1.0, r/D = -1.625 to -1.500

Figure 64. Longitudinal Cross-Spectra for the Protuberance Induced Fluctuating Pressure Field, Upstream ($\theta^{-} = 0^{\circ}$), 8-inch Diameter Protuberance, $M_{\infty} = 1.40$, Re/ft = 3×10^{6}, $\xi/D = 0.125$

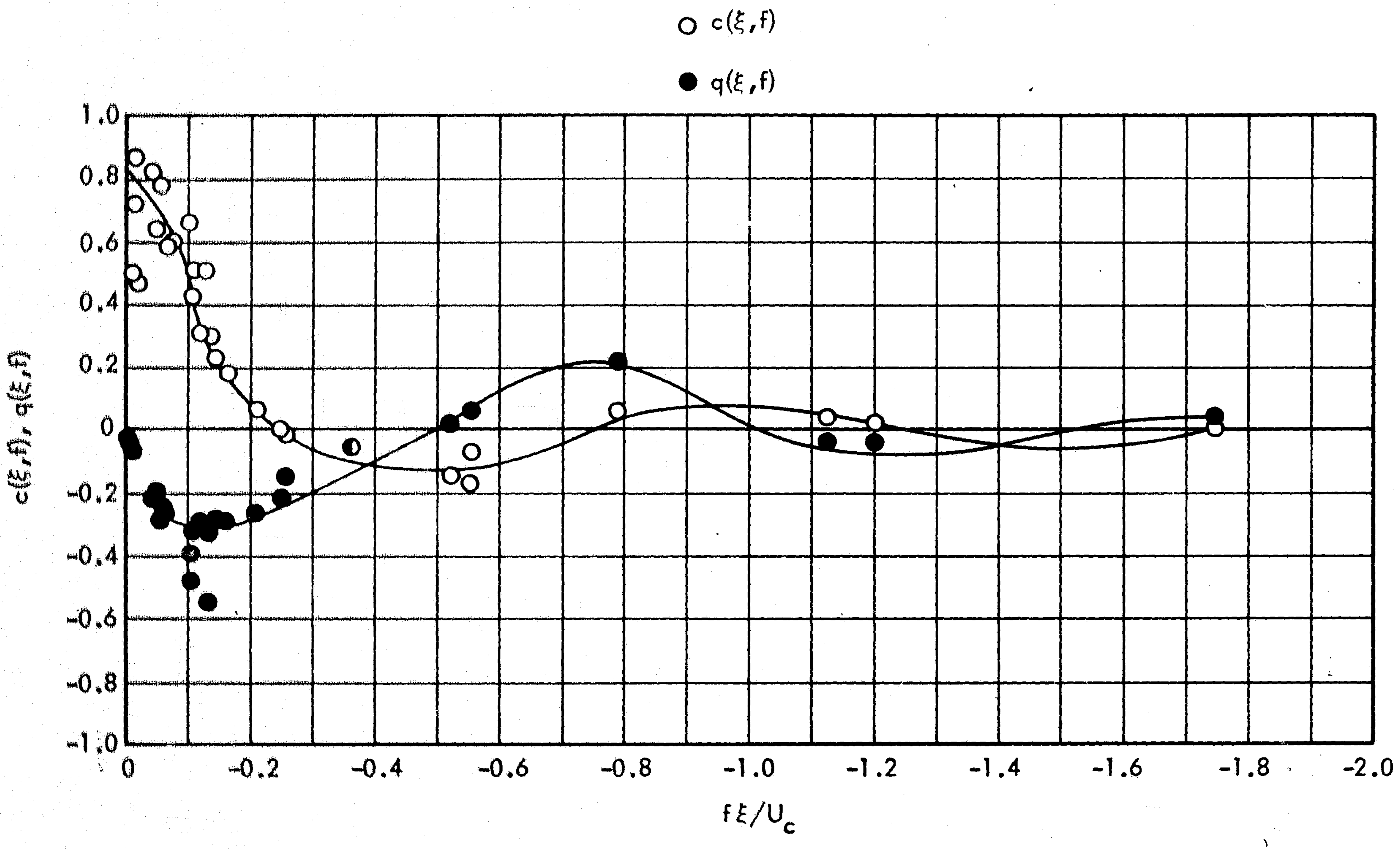

b. h/D = 2.0, r/D = -1.875 to -1.750

Figure 64. Concluded

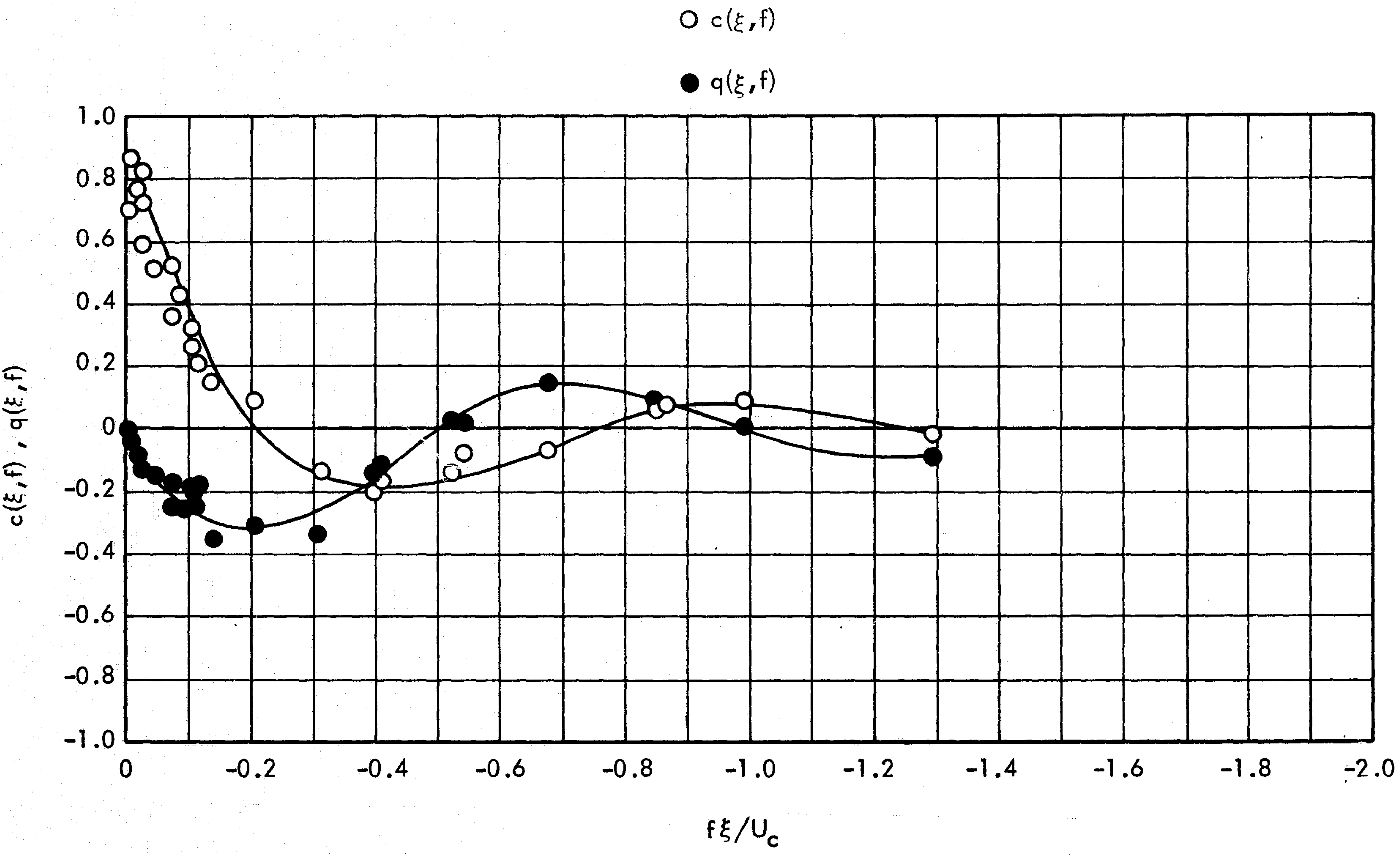

a. h/D = 1.0, r/D = -1.375 to -1.250

Figure 65. Longitudinal Cross-Spectra for the Protuberance Induced Fluctuating Pressure Field, Upstream ($\theta^{-} = 0^{\circ}$), 8-inch Diameter Protuberance, $M_{\infty} = 1.60$, Re/ft = 3×10^{6}, $\xi/D = 0.125$

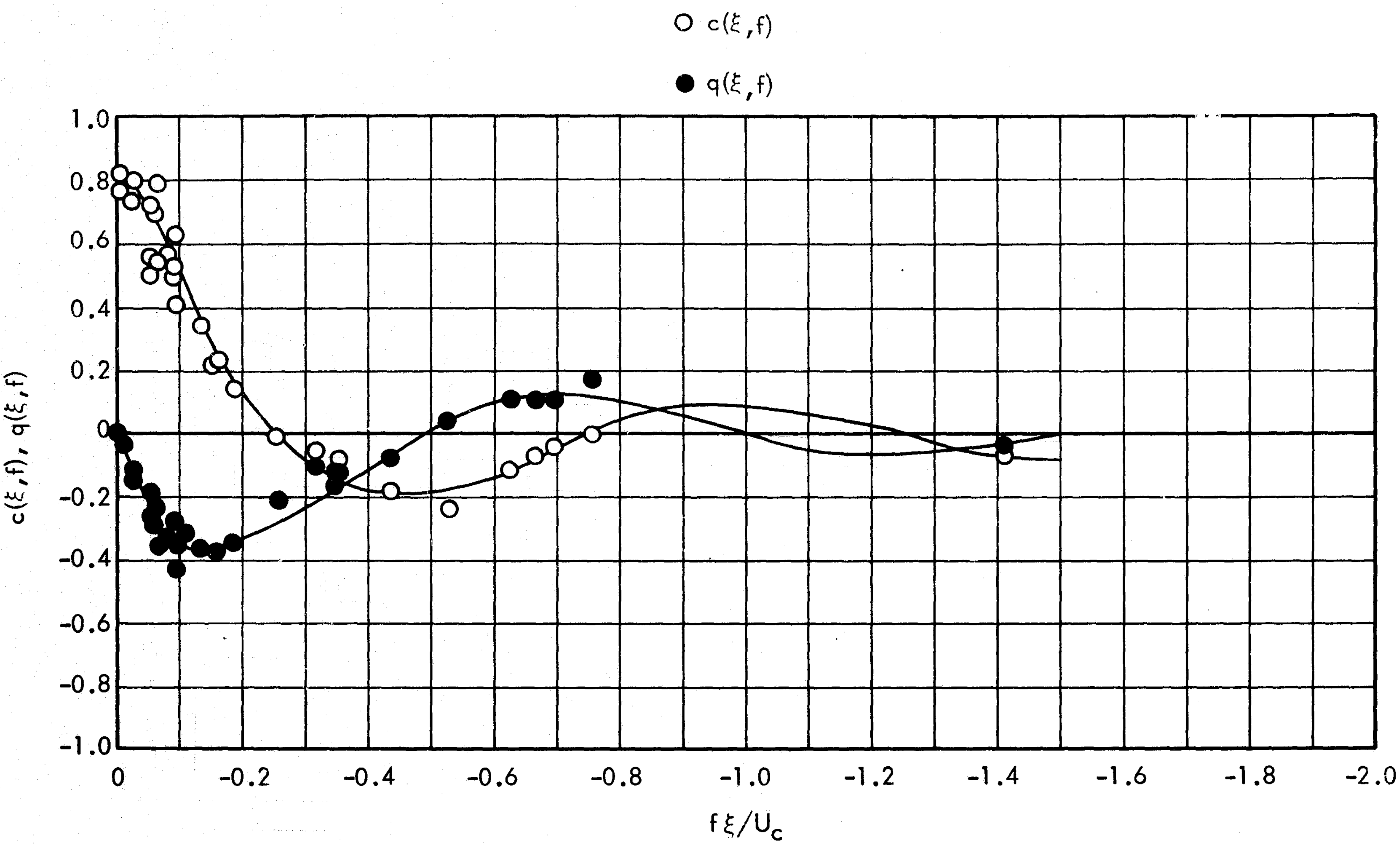

b. h/D = 2.0, r/D = -1.875 to -1.750

Figure 65. Concluded

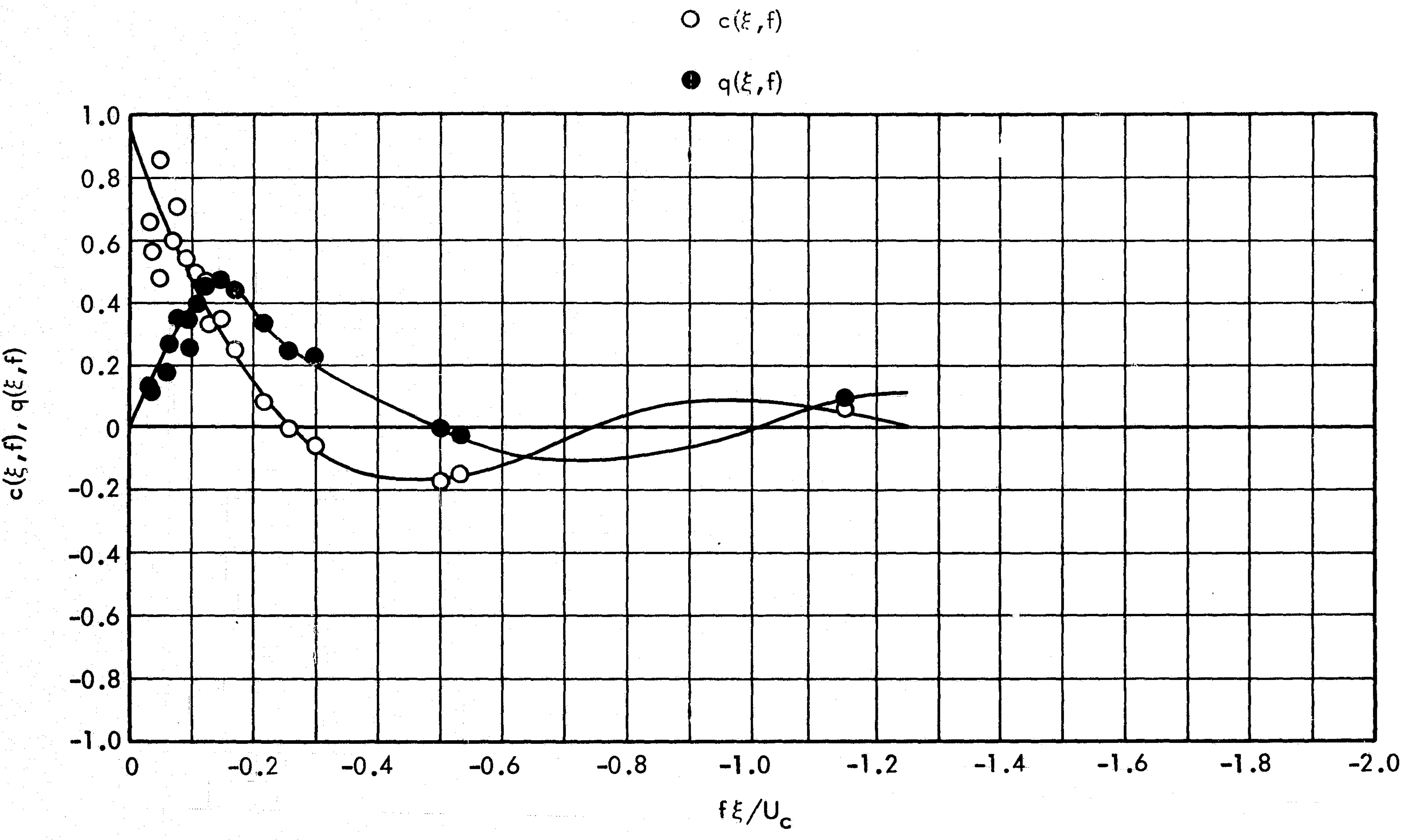

a. h/D = 1.0, r/D = 1.500 to 1.625

Figure 66. Longitudinal Cross-Spectra for the Protuberance Induced Fluctuating Pressure Field, Downstream ($\theta^- = 180°$), 8-inch Diameter Protuberance, $M_\infty = 1.20$, Re/ft = 3×10^6, $\xi/D = 0.125$

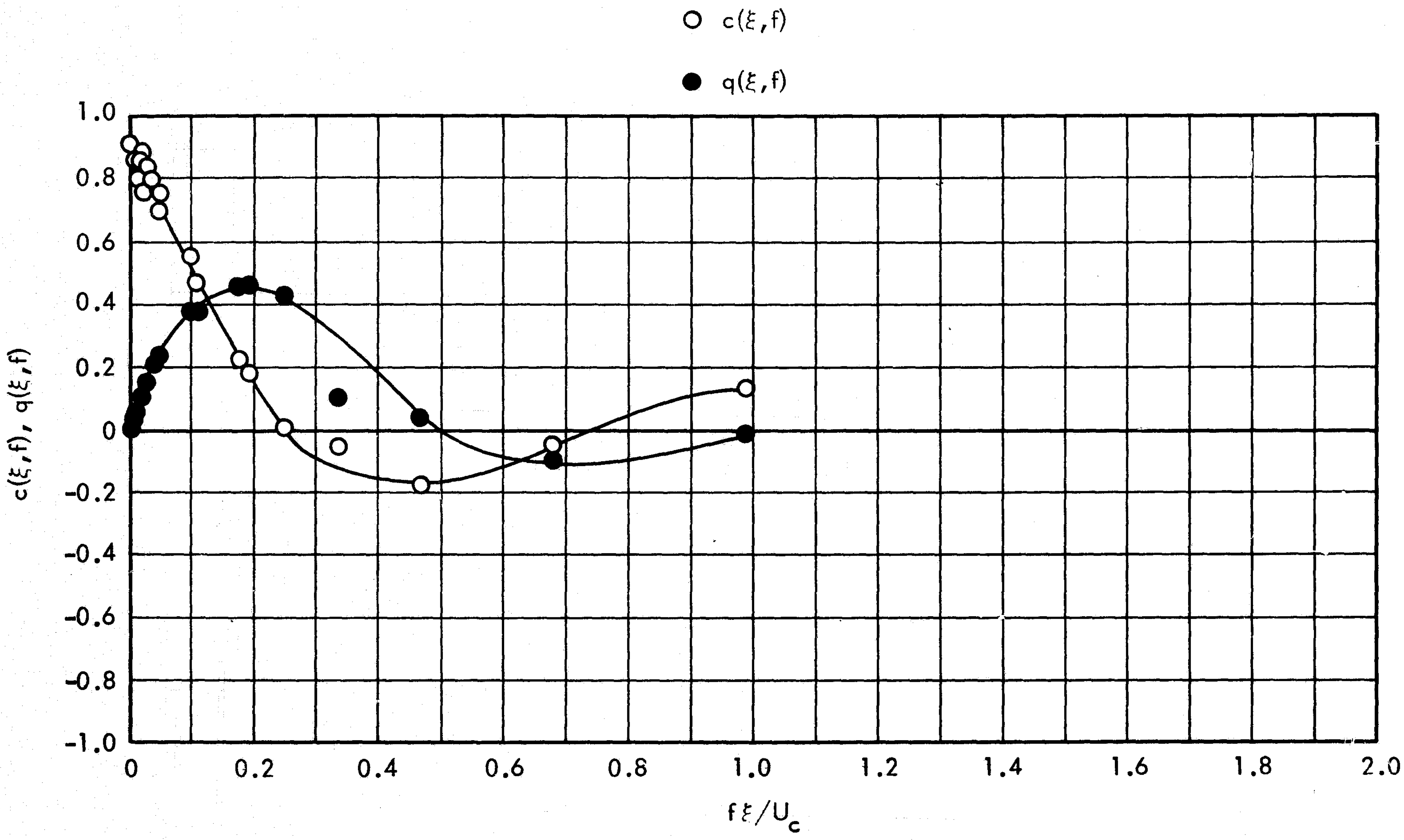

b. h/D = 2.0, r/D = 1.500 to 1.625

Figure 66. Concluded

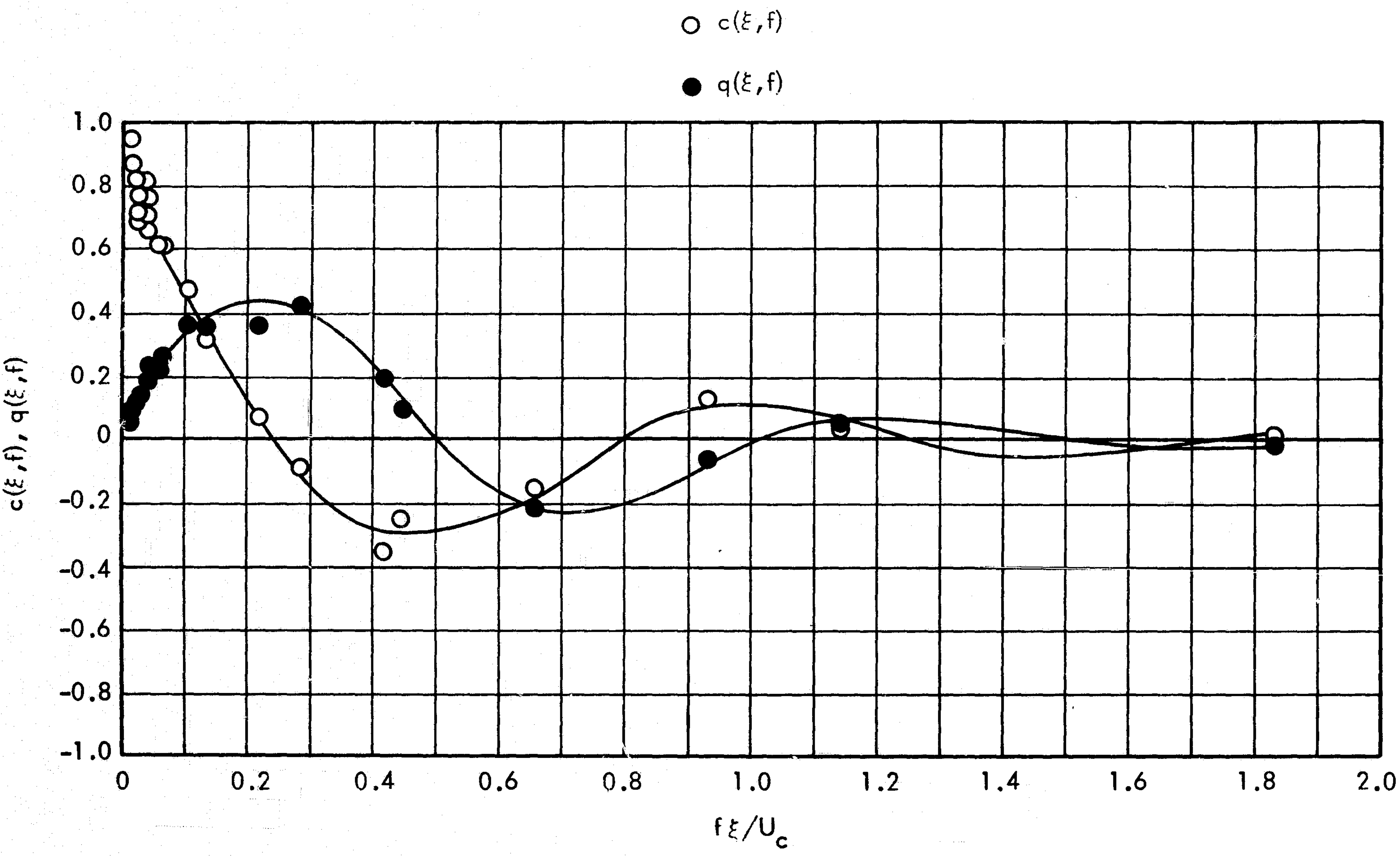

a. h/D = 1.0, r/D = 1.500 to 1.625

Figure 67. Longitudinal Cross-Spectra for the Protuberance Induced Fluctuating Pressure Field, Downstream ($\theta = 180^\circ$) 8-inch Diameter Protuberance, $M_\infty = 1.40$, Re/ft = 3×10^6, $\xi/D = 0.125$

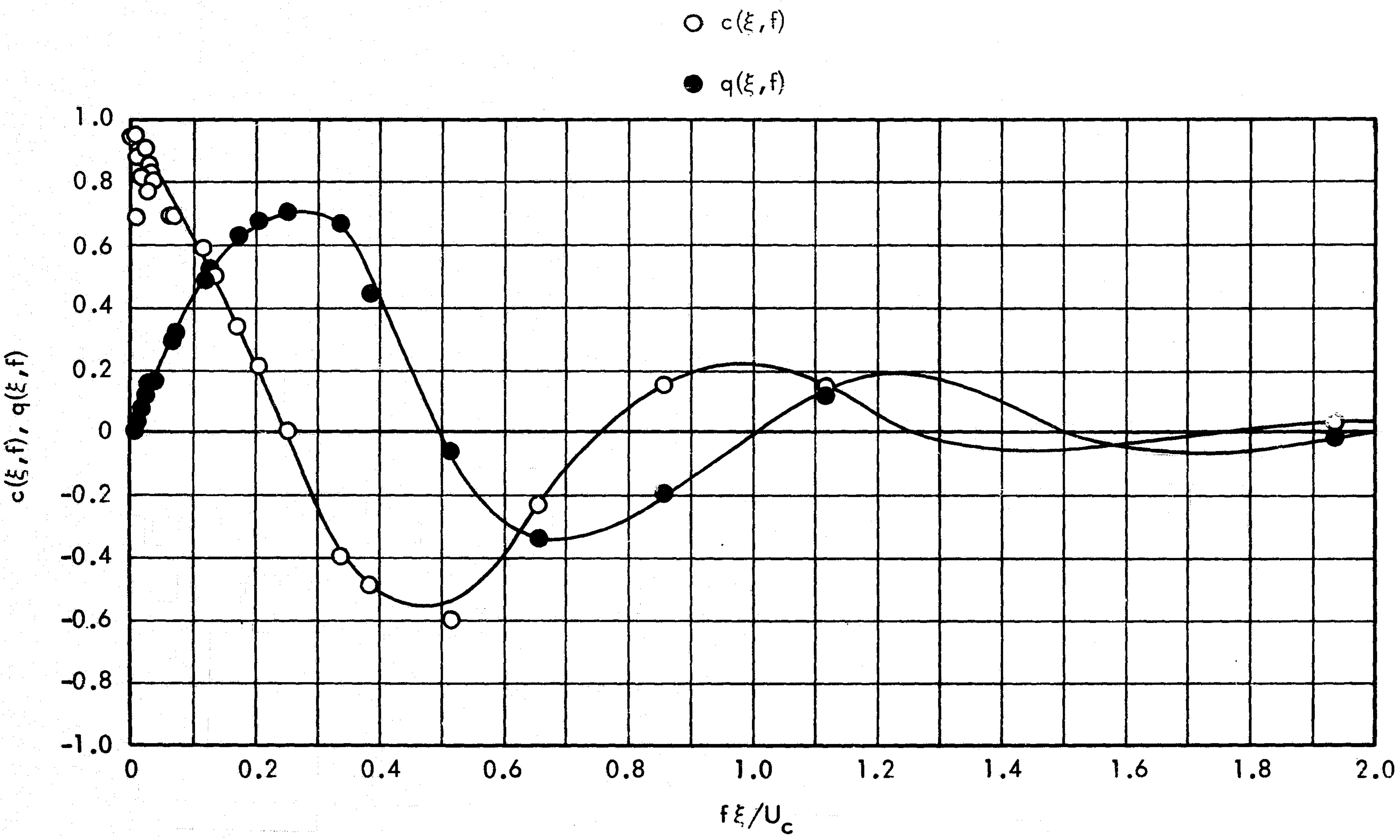

b. h/D = 2.0, r/D = 1.500 to 1.625

Figure 67. Concluded

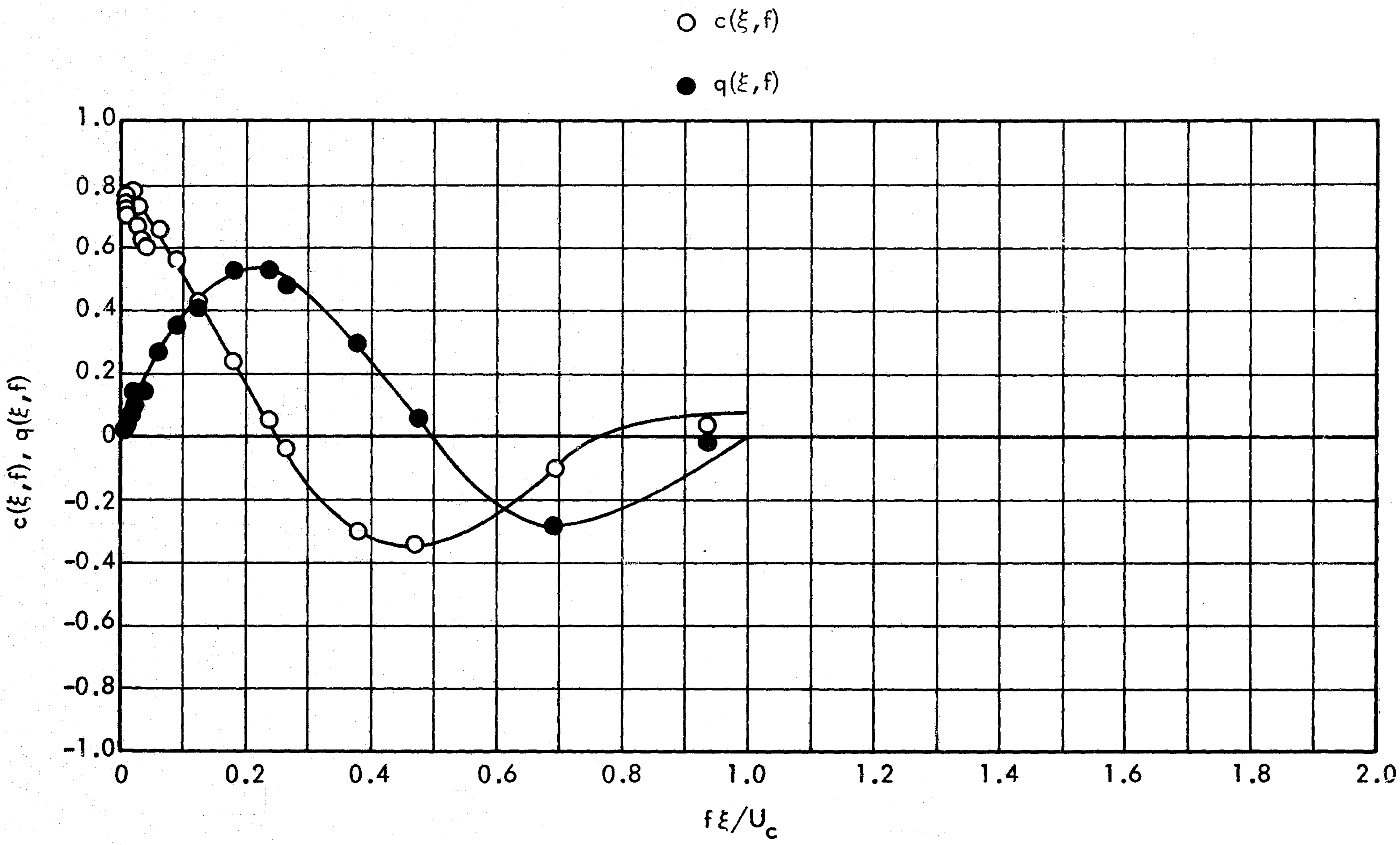

a. h/D = 1.0, r/D = 1.500 to 1.625

Figure 68. Longitudinal Cross-Spectra for the Protuberance Induced Fluctuating Pressure Field, Downstream ($\theta^- = 180^\circ$), 8-inch Diameter Protuberance, $M_\infty = 1.60$, $Re/ft = 3 \times 10^6$, $\xi/D = 0.125$

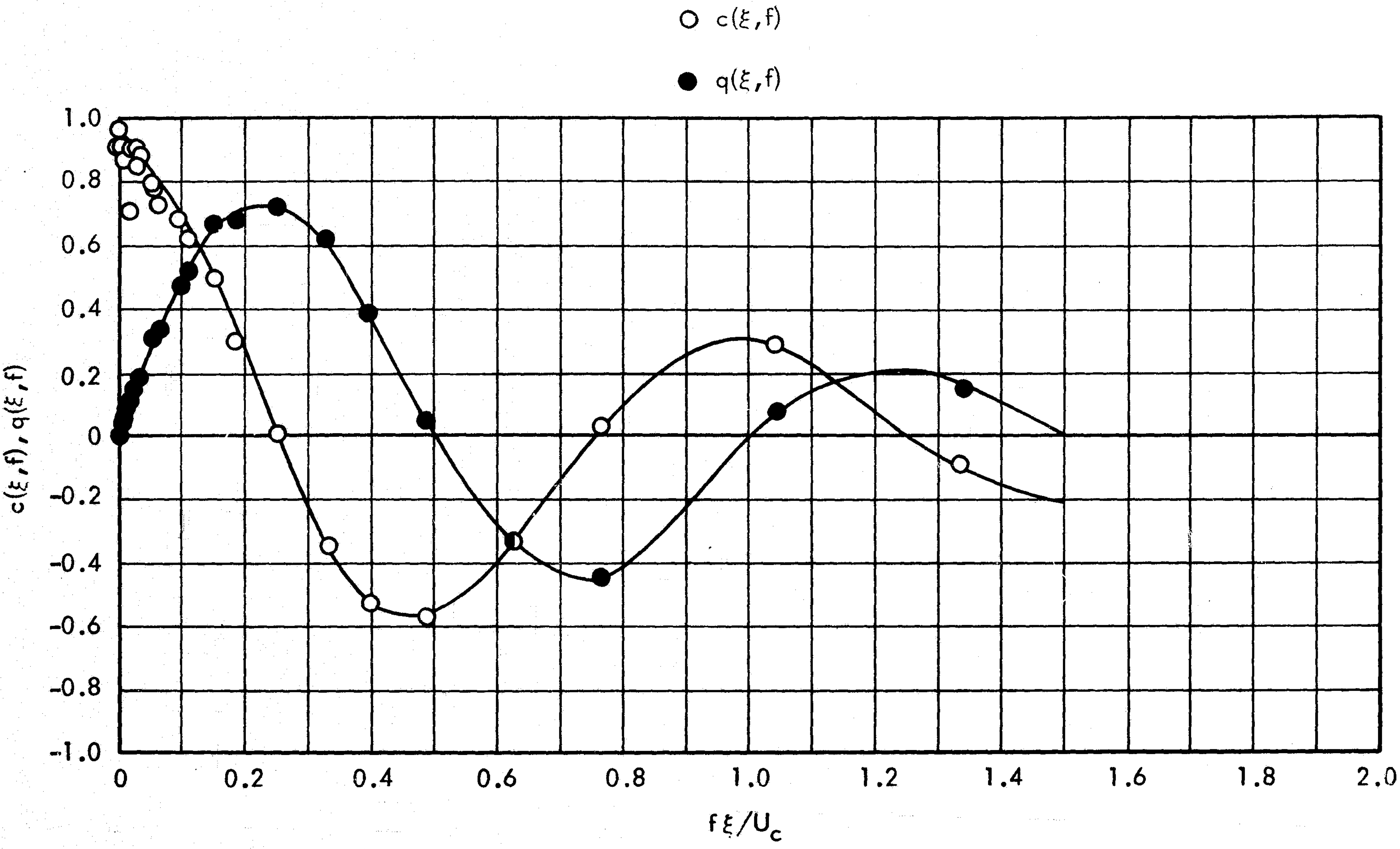

b. $h/D = 2.0$, $r/D = 1.500$ to 1.625

Figure 68. Concluded

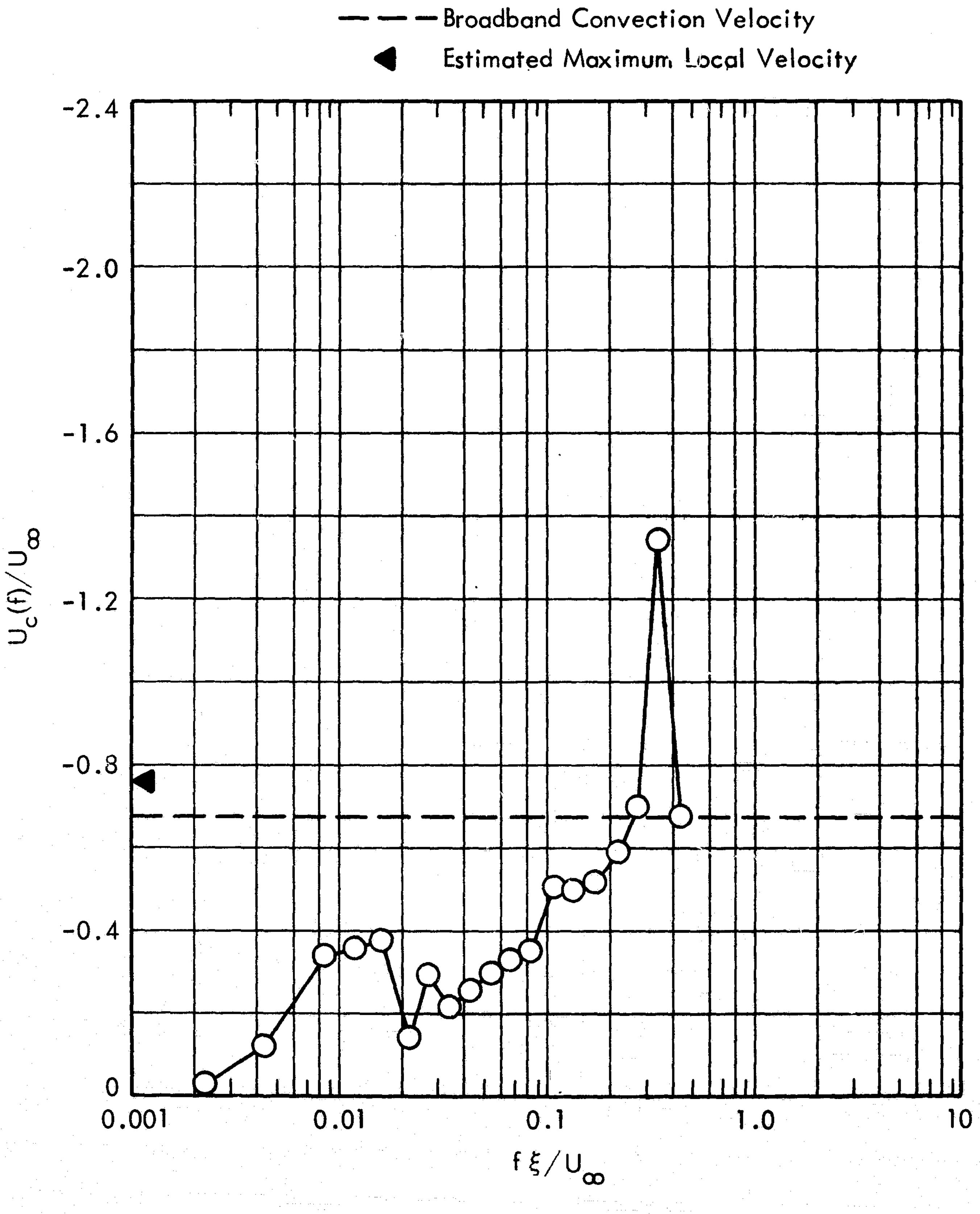

a. h/D = 1.0, r/D = -1.375 to -1.250

Figure 69. Longitudinal Narrow Band Convection Velocity for Protuberance Induced Fluctuating Pressure Field, Upstream ($\theta^- = 0°$), 8-Inch Diameter Protuberance, $M_\infty = 1.20$, $Re/ft = 3 \times 10^6$, $\xi/D = 0.125$

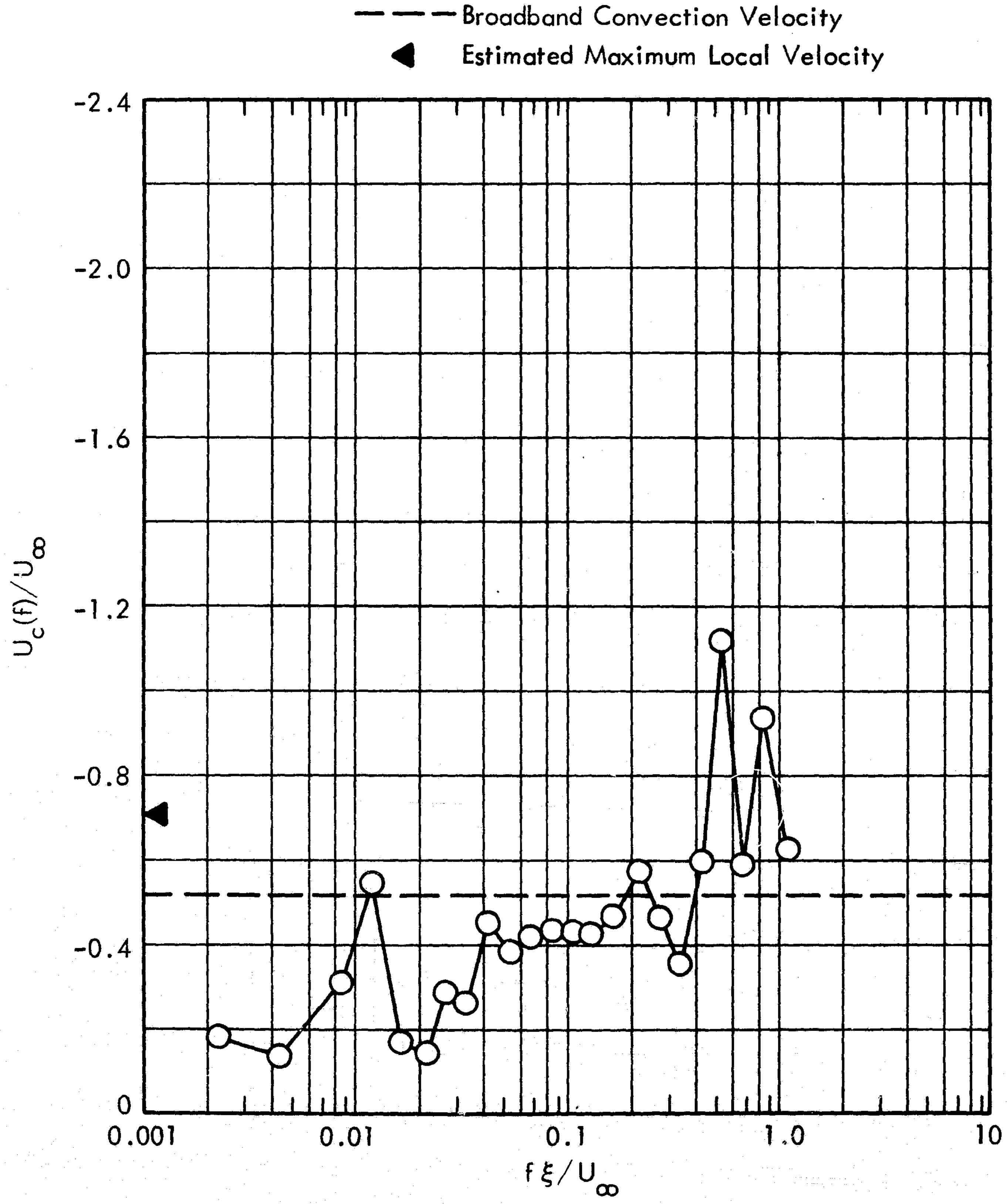

b. h/D = 2.0, r/D = -1.625 to -1.500

Figure 69. Concluded

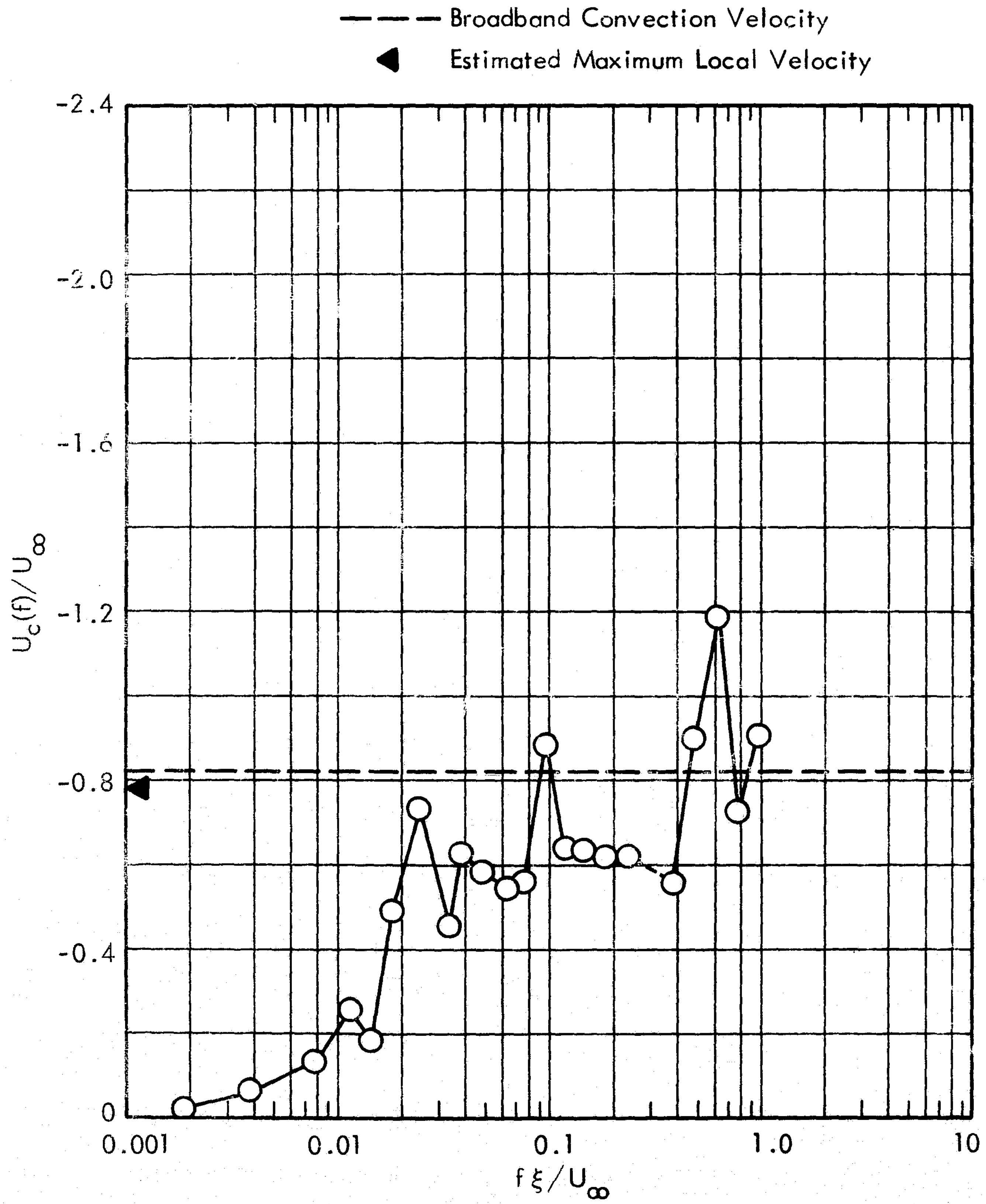

a. h/D = 1.0, r/D = -1.625 to -1.500

Figure 70. Longitudinal Narrow Band Convection Velocity for Protuberance Induced Fluctuating Pressure Field, Upstream ($\theta^- = 0^\circ$), 8-Inch Diameter Protuberance, $M_\infty = 1.40$, Re/ft = 3×10^6, $\xi/D = 0.125$

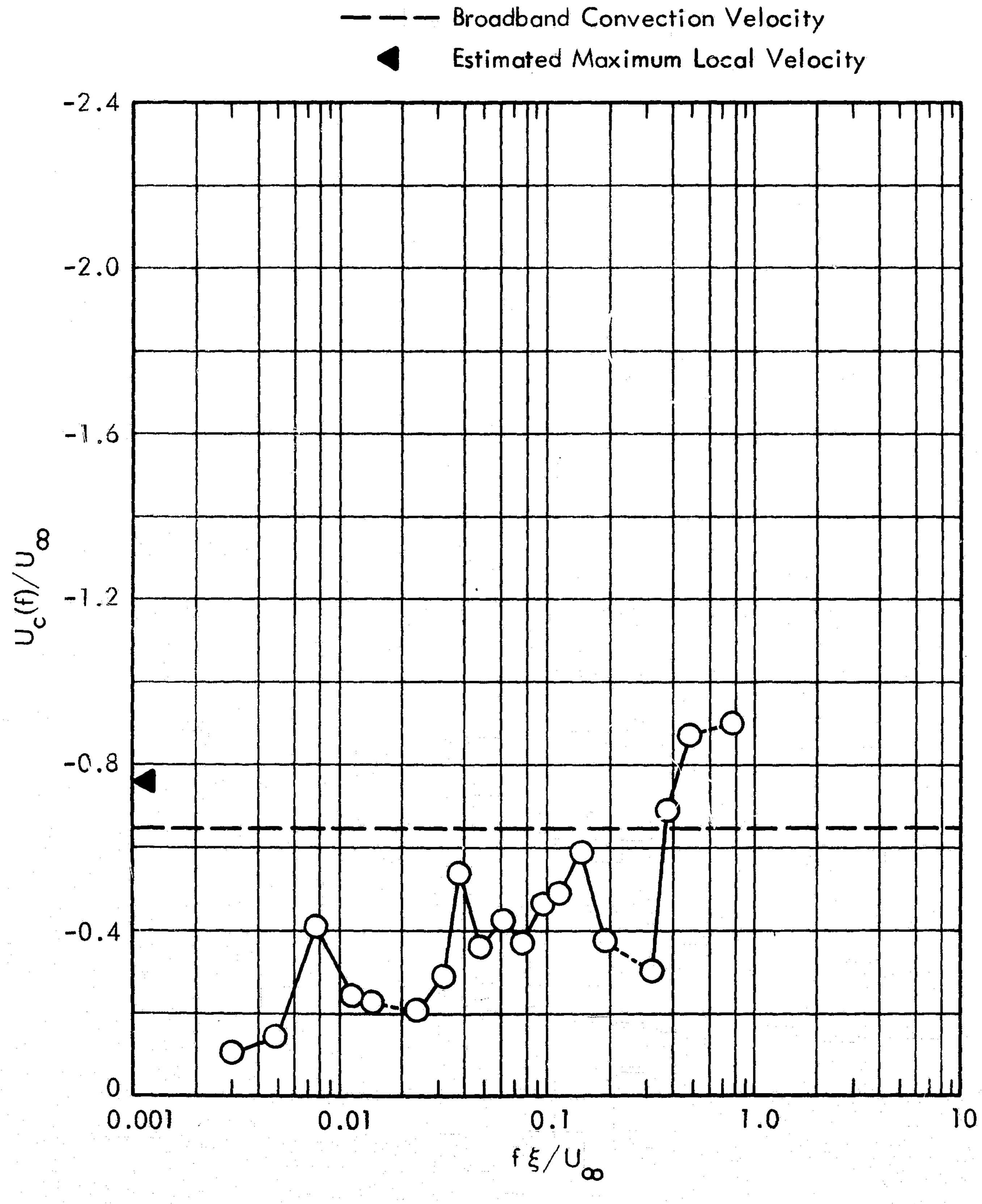

b. h/D = 2.0, r/D = -1.875 to -1.750

Figure 70. Concluded

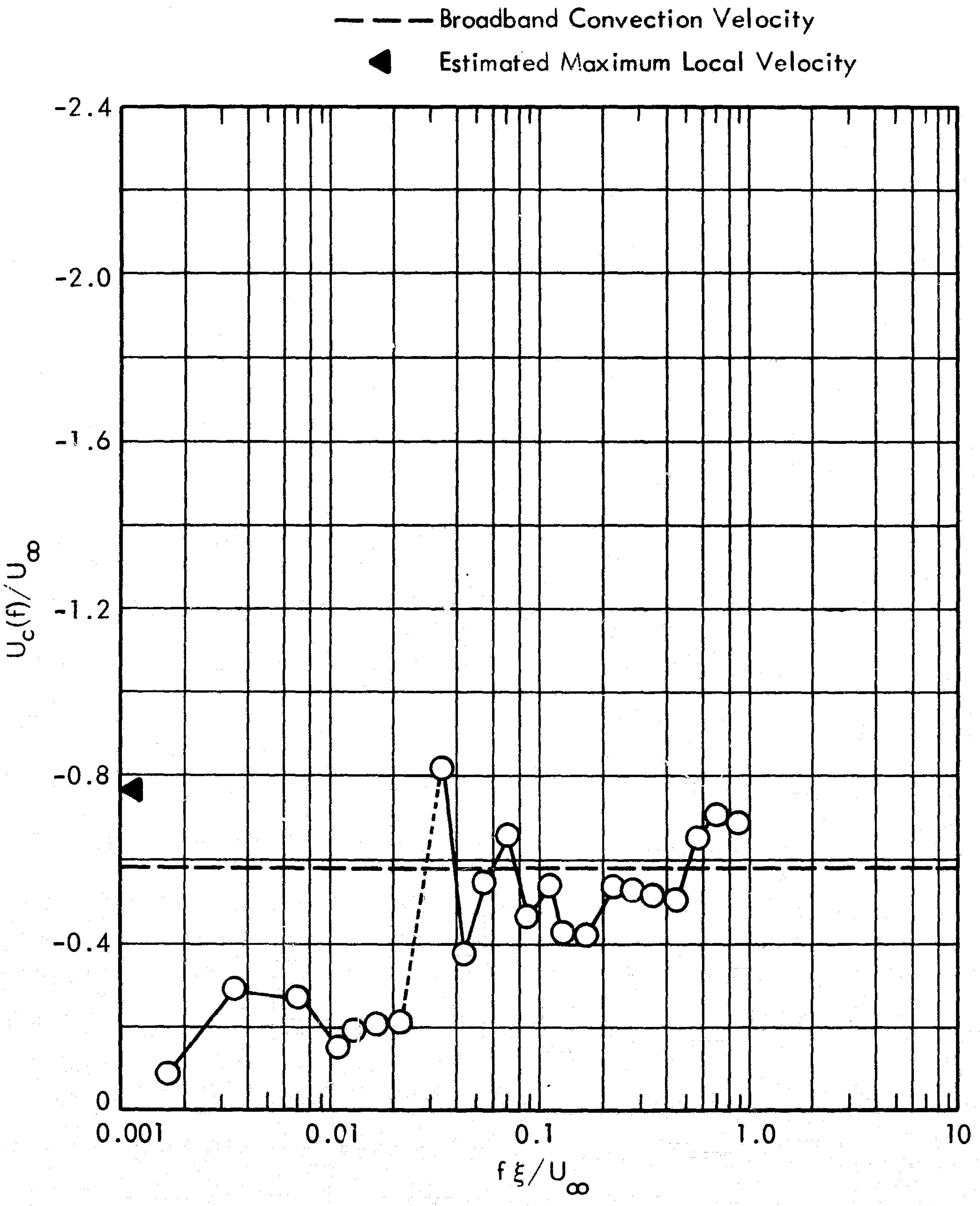

a. h/D = 1.0, r/D = -1.375 to -1.250

Figure 71. Longitudinal Narrow Band Convection Velocity for Protuberance Induced Fluctuating Pressure Field, Upstream ($\theta^- = 0^\circ$), 8-Inch Diameter Protuberance, $M_\infty = 1.60$, Re/ft = 3×10^6, $\xi/D = 0.125$

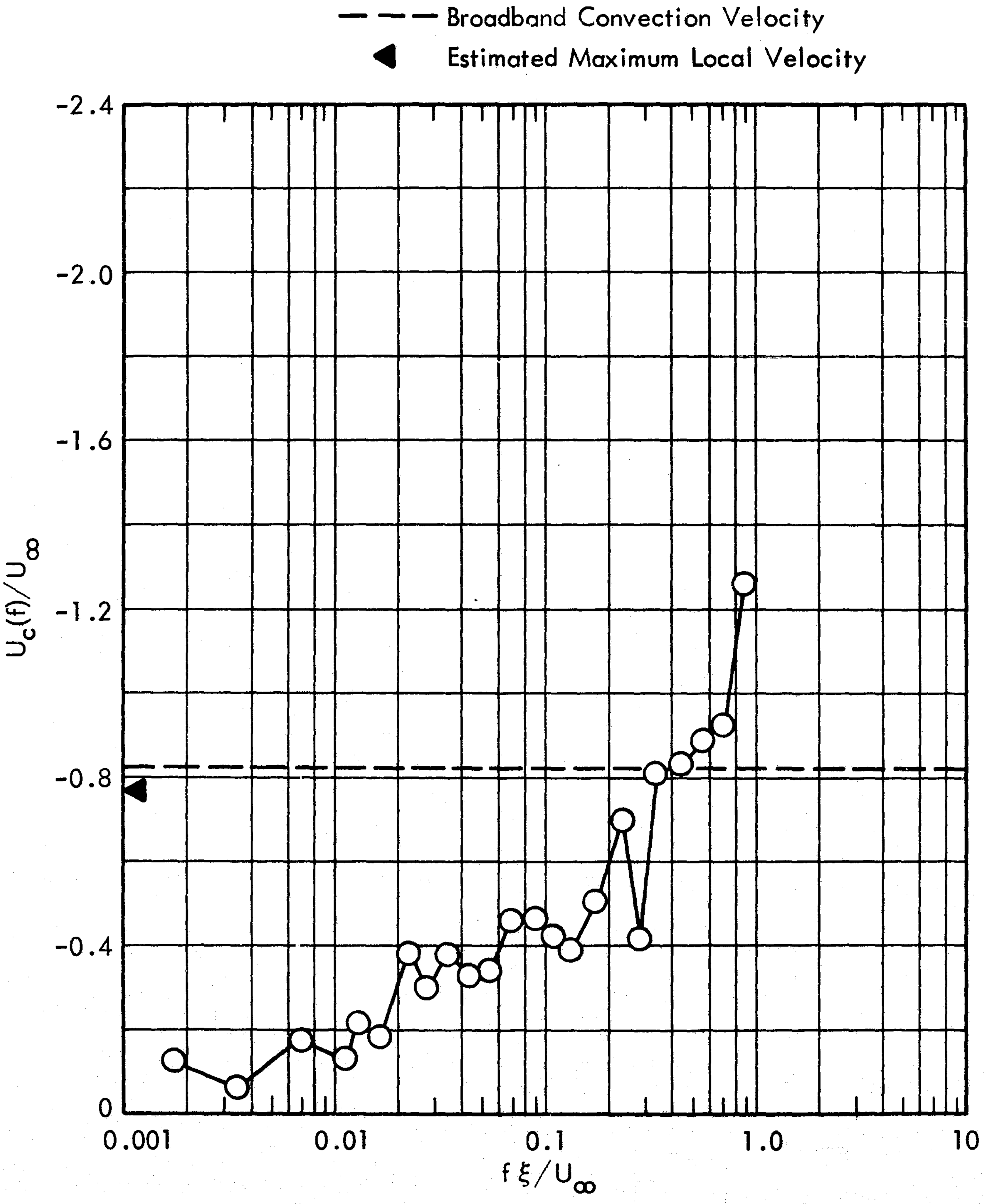

b. h/D = 2.0, r/D = -1.875 to -1.750

Figure 71. Concluded

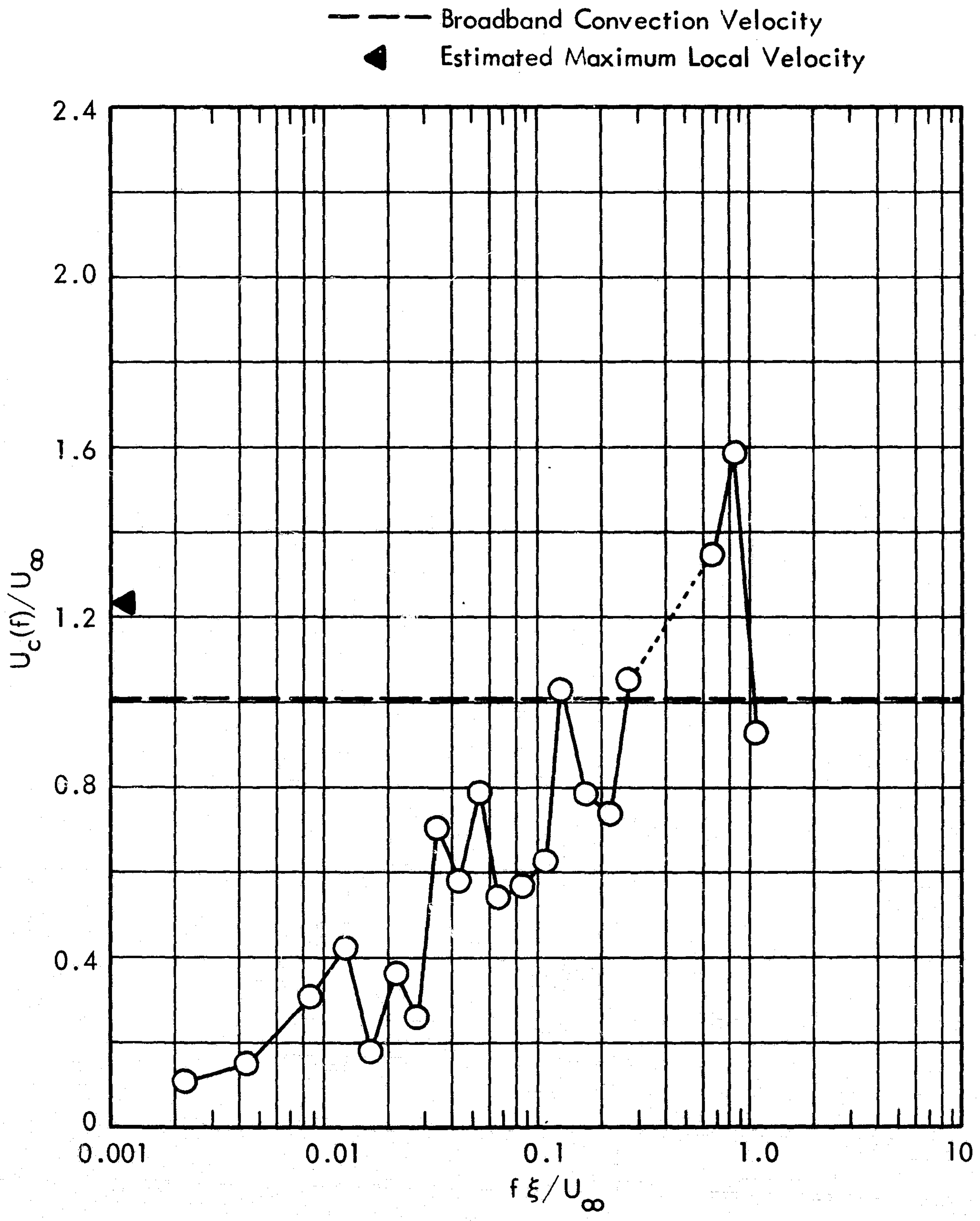

a. h/D = 1.0, r/D = 1.500 to 1.625

Figure 72. Longitudinal Narrow Band Convection Velocity for Protuberance Induced Fluctuating Pressure Field, Downstream ($\theta^- = 180^\circ$), 8-Inch Diameter Protuberance, $M_\infty = 1.20$, Re/ft = 3×10^6, $\xi/D = 0.125$

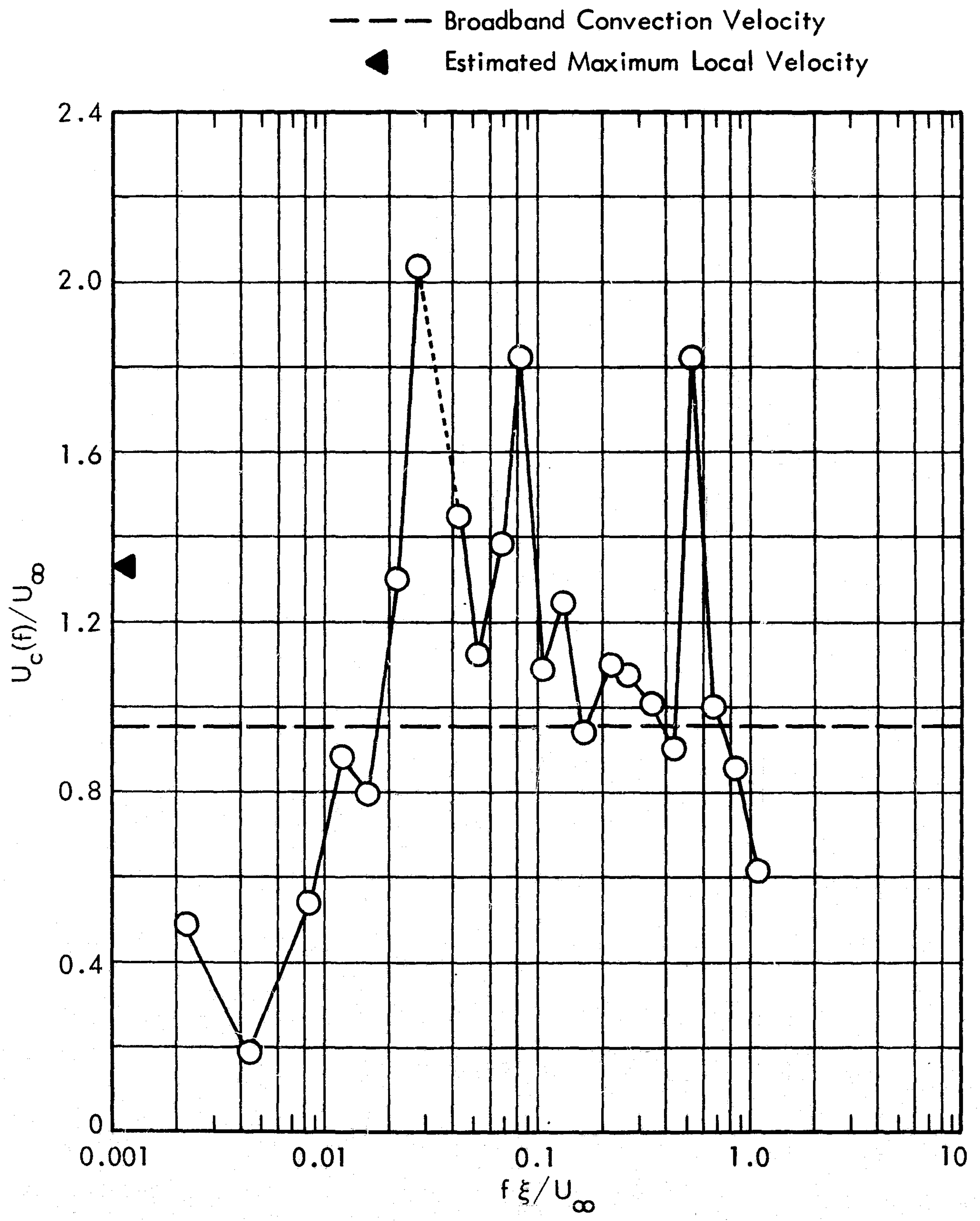

b. h/D = 2.0, r/D = 1.500 to 1.625

Figure 72. Concluded

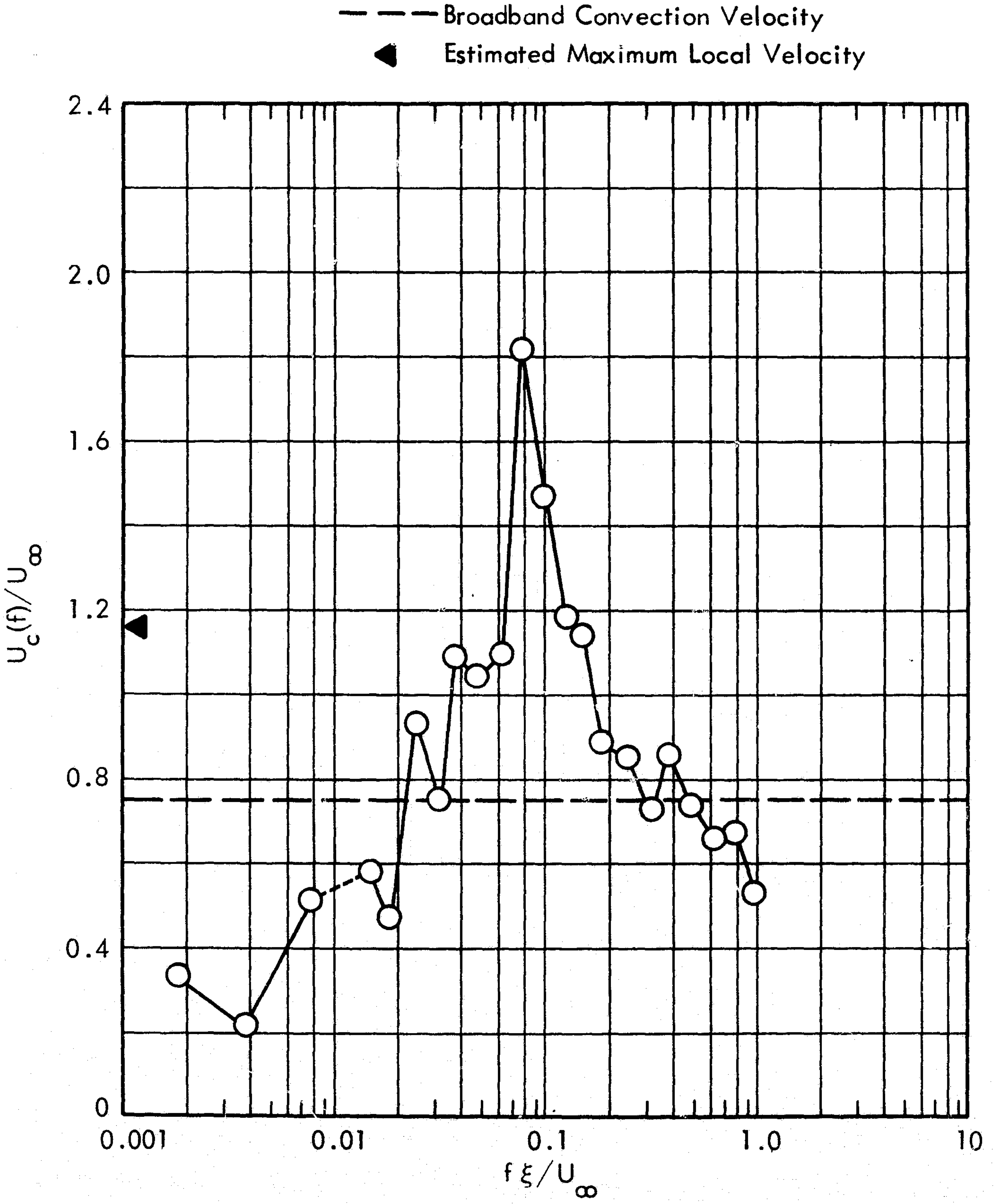

a. h/D = 1.0, r/D = 1.500 to 1.625

Figure 73. Longitudinal Narrow Band Convection Velocity for Protuberance Induced Fluctuating Pressure Field, Downstream ($\theta^- = 180^\circ$), 8-Inch Diameter Protuberance, $M_\infty = 1.40$, $Re/ft = 3 \times 10^6$, $\xi/D = 0.125$

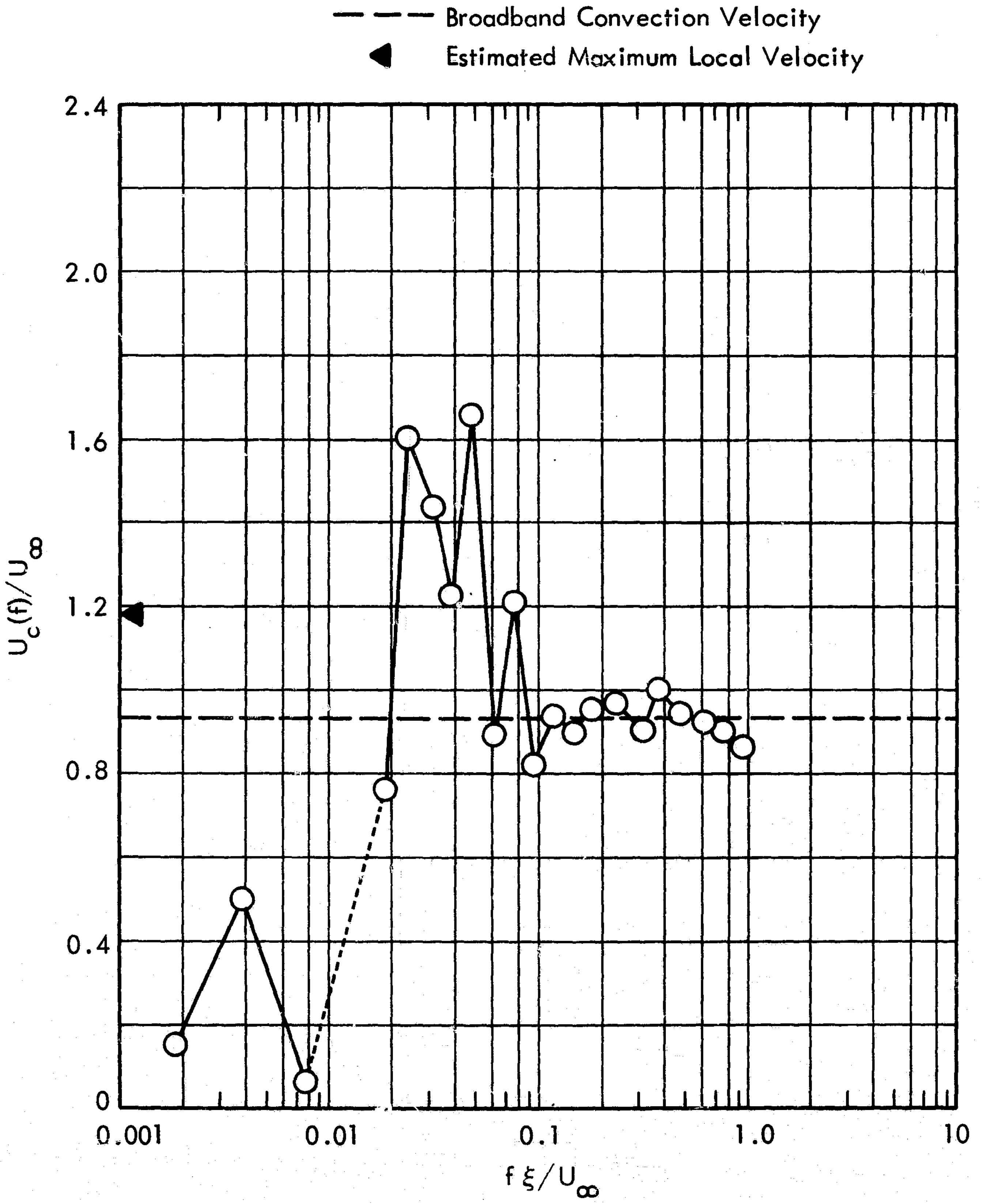

b. h/D = 2.0, r/D = 1.500 to 1.625

Figure 73. Concluded

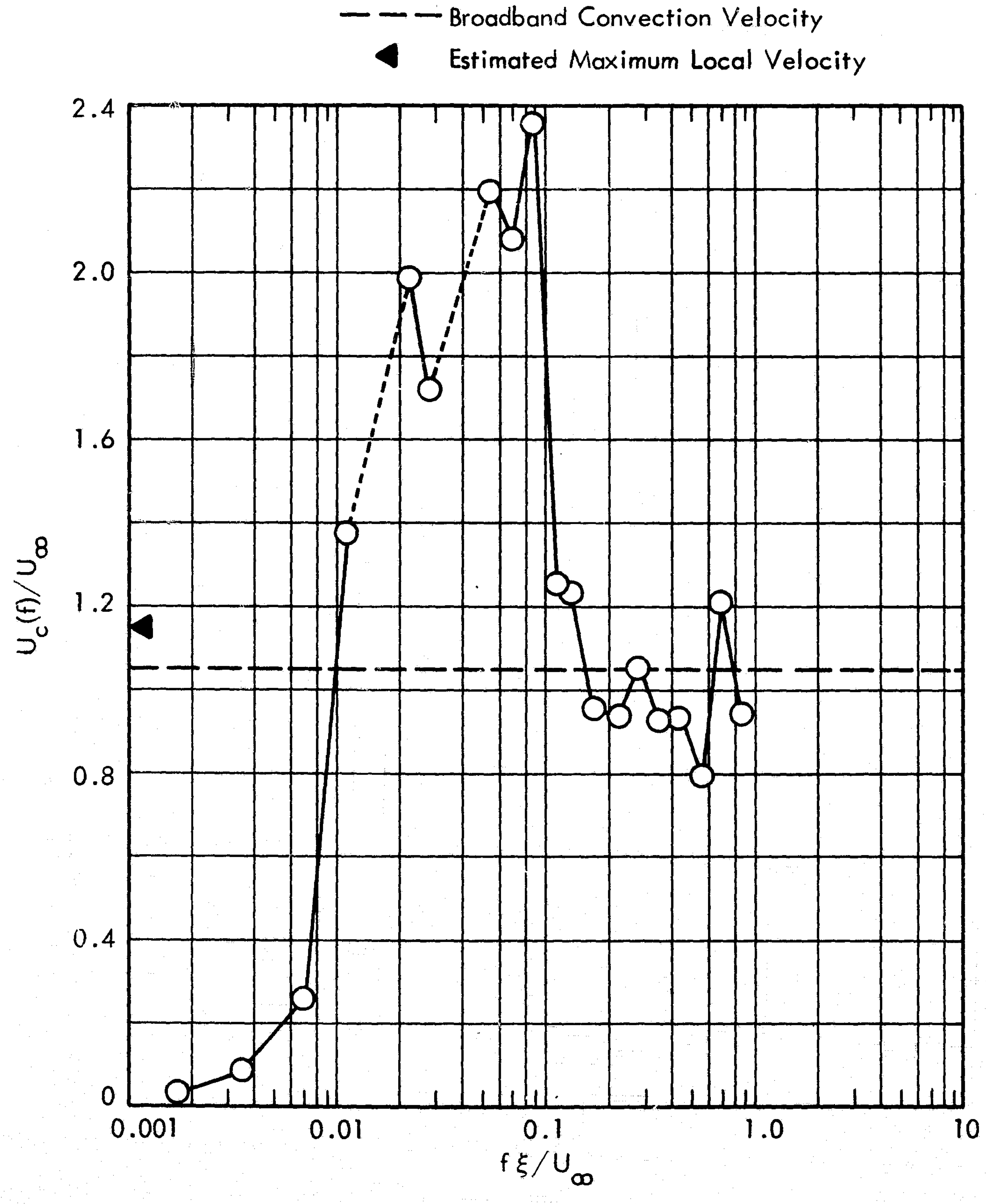

a. h/D = 1.0, r/D = 1.500 to 1.625

Figure 74. Longitudinal Narrow Band Convection Velocity for Protuberance Induced Fluctuating Pressure Field, Downstream ($\theta^- = 180^\circ$), 8-Inch Diameter Protuberance, $Re/ft = 3 \times 10^6$, $\xi/D = 0.125$

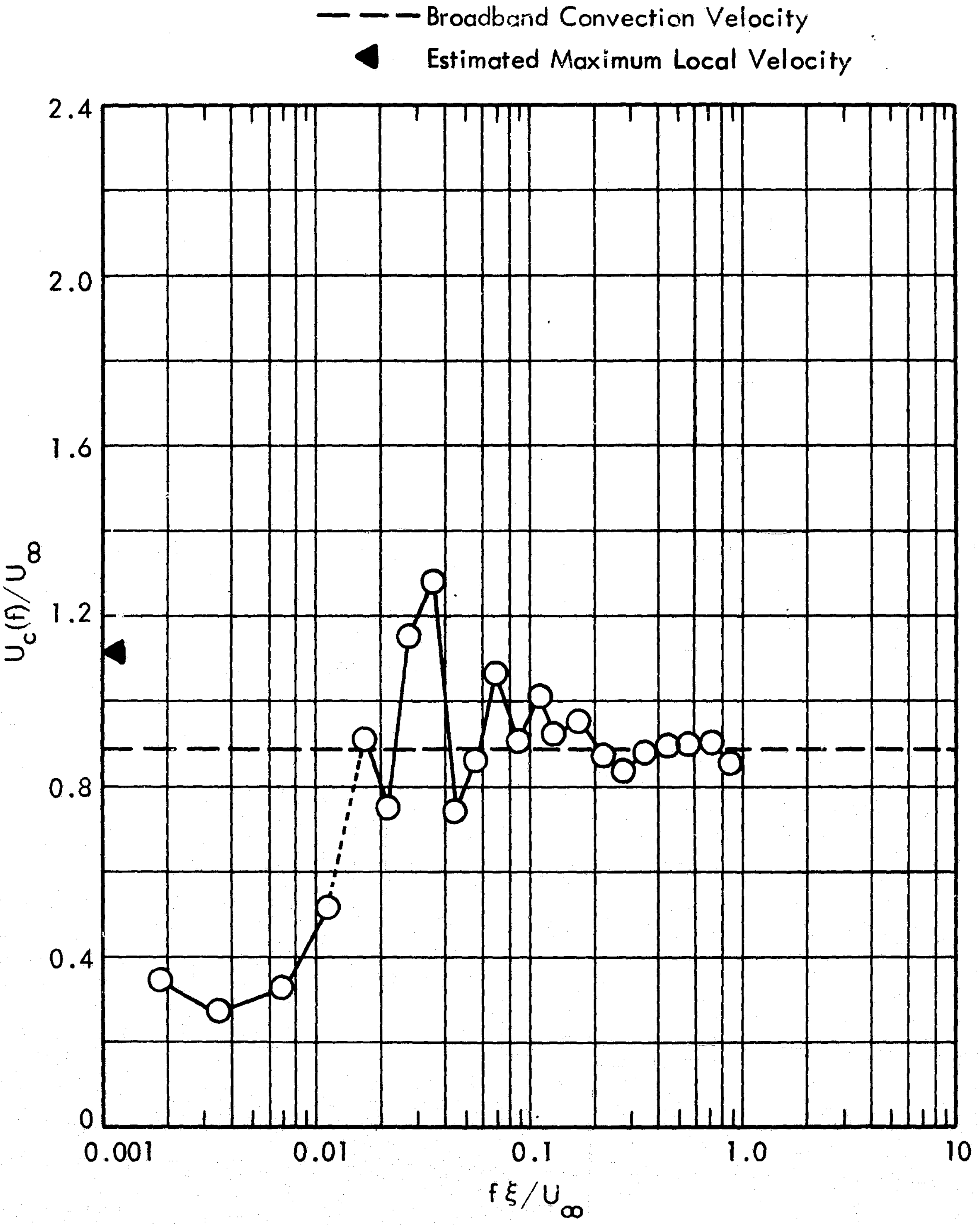

b. h/D = 2.0, r/D = 1.500 to 1.625

Figure 74. Concluded

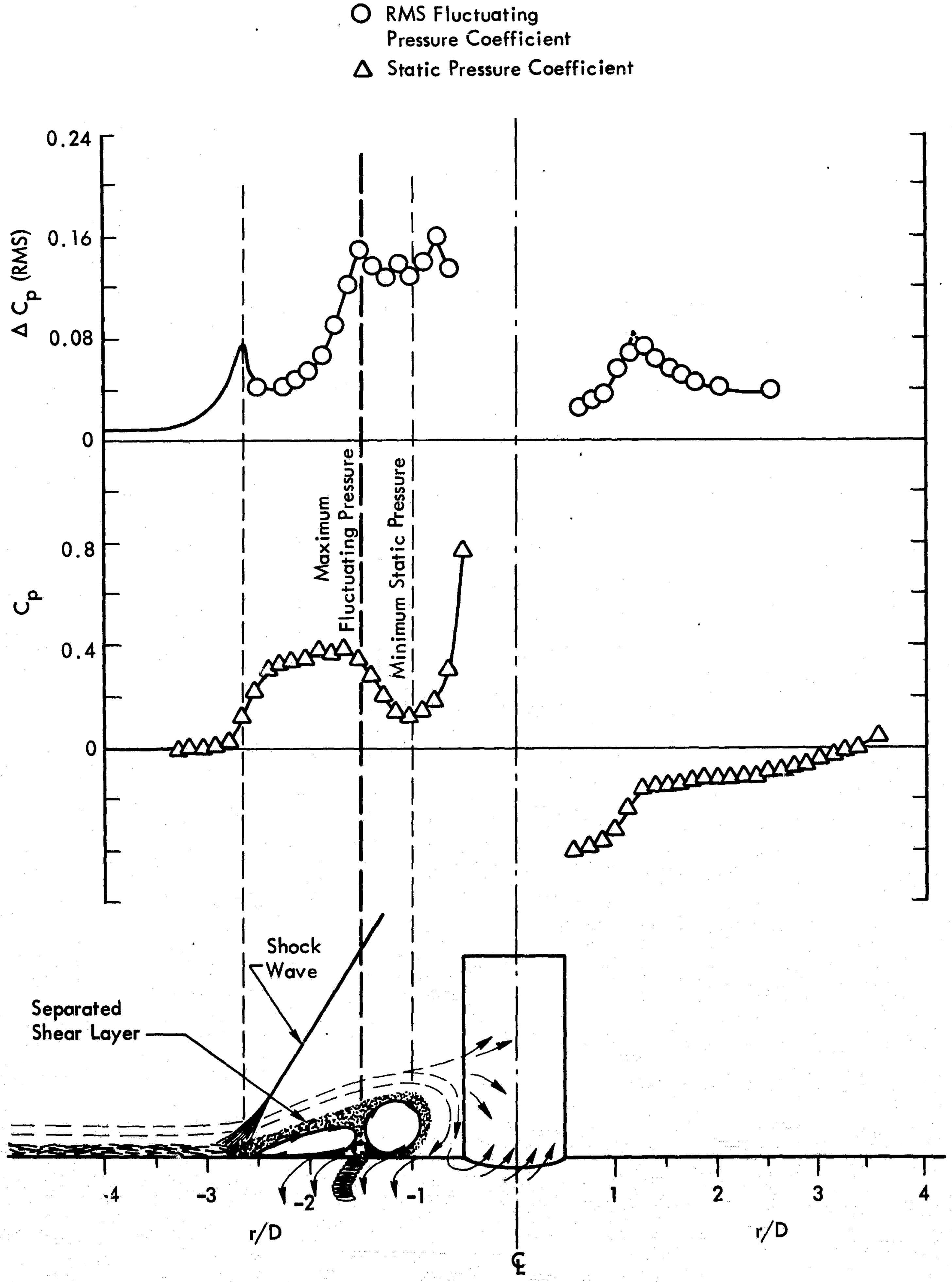

Figure 75. Composite Schematic of Protuberance Flow Field Characteristics, $M_\infty = 1.60$, h/D = 2.0

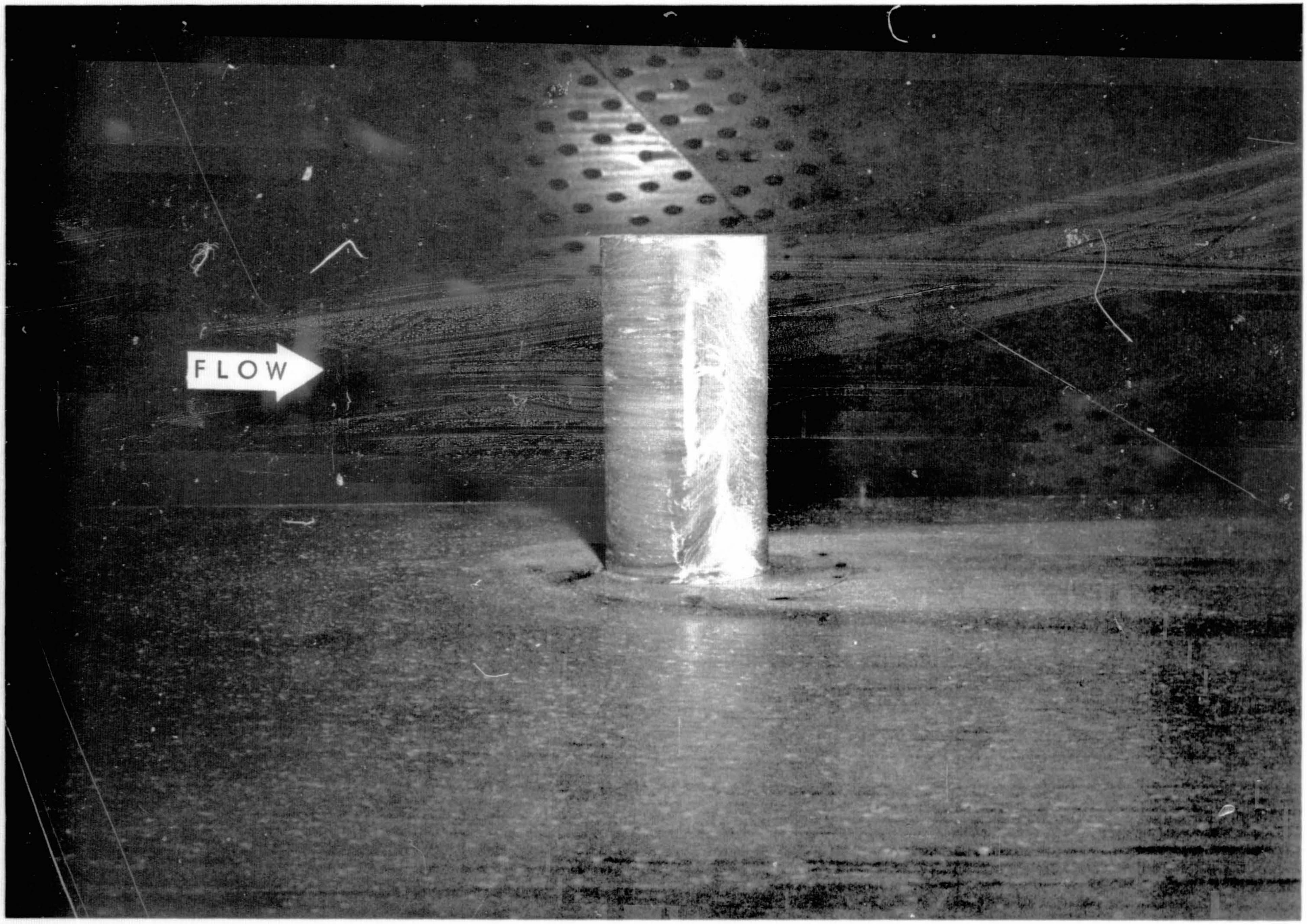

a. Side View

Figure 76. Titanium Dioxide Flow Patterns Over the Wall of Cylindrical Protuberance

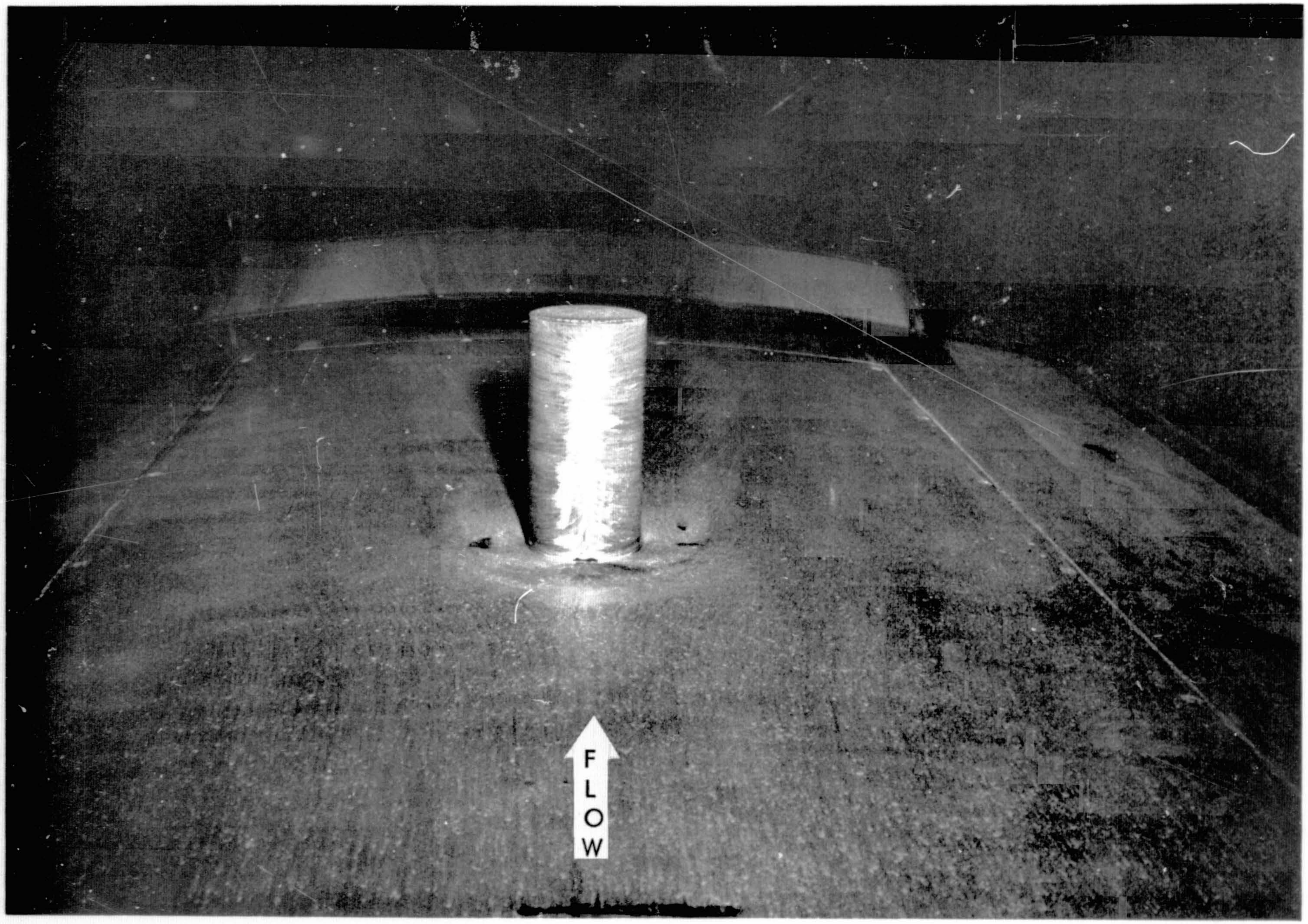

b. Front View

Figure 76. Concluded

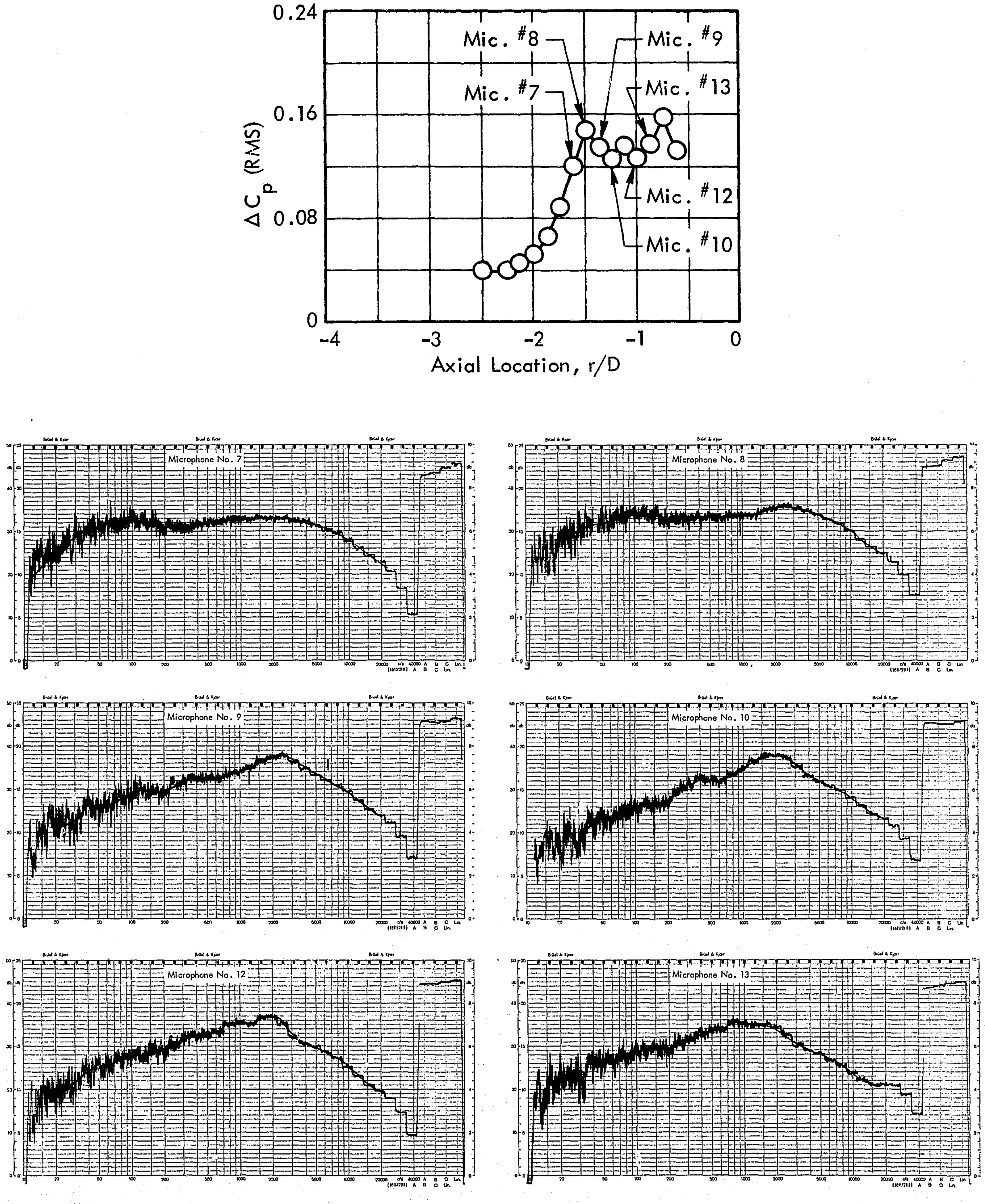

Figure 77. One-Third Octave Spectra for Typical Microphone Locations Upstream of the Protuberance, Zero Level = 120 dB, M_∞ = 1.60, h/D = 2.0

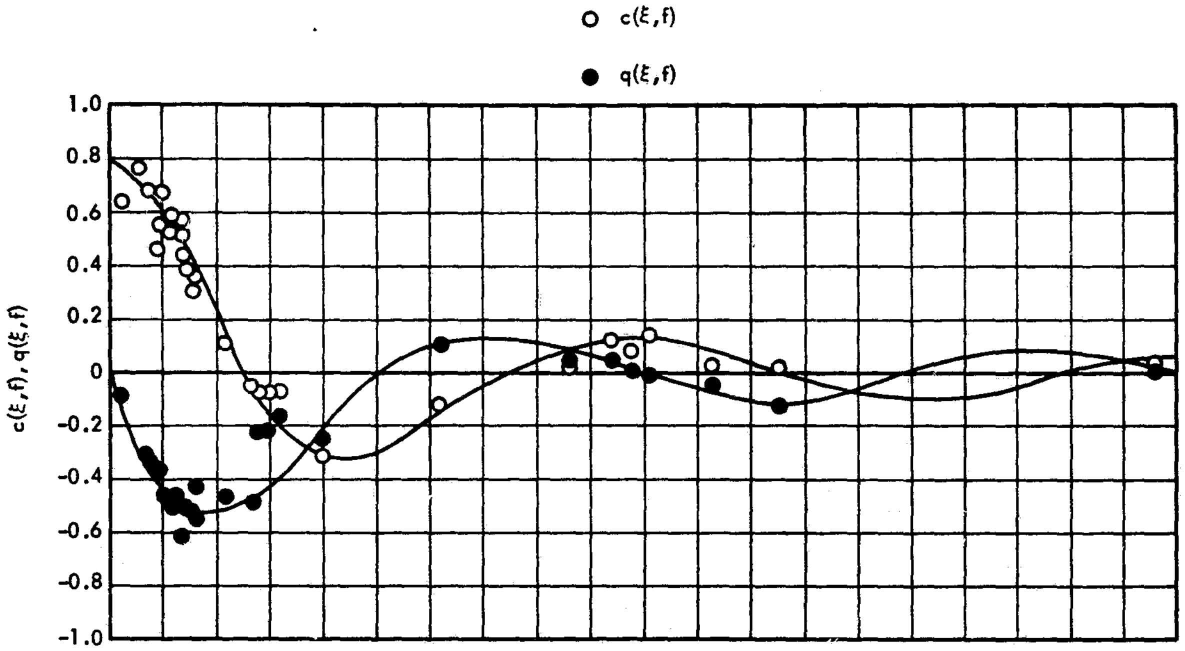

a. r/D = -2.500 to -2.250, ξ/D = 0.250

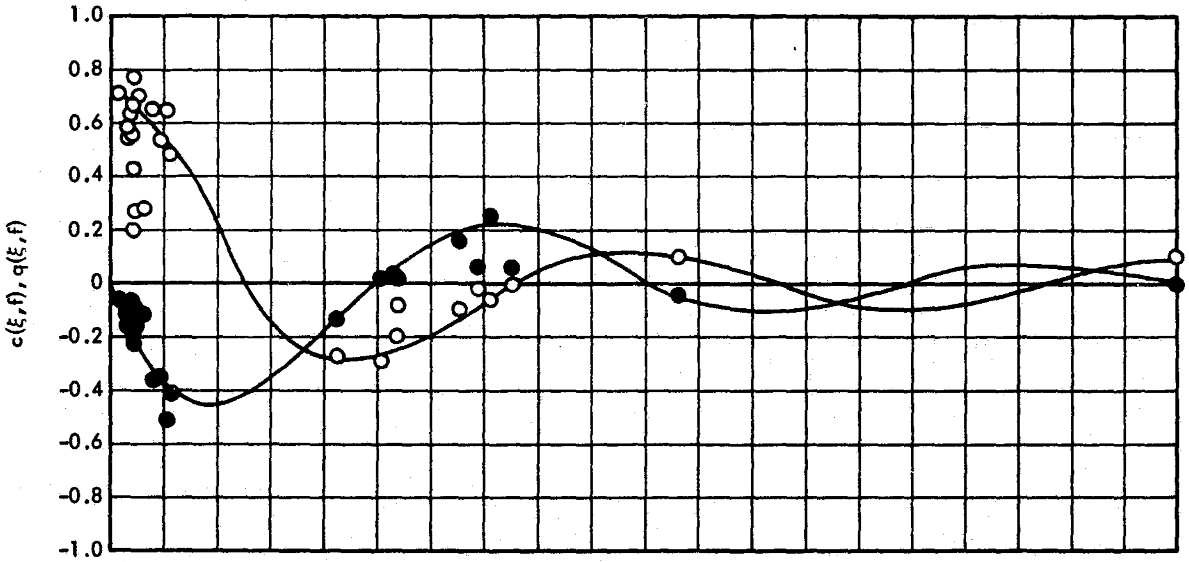

b. r/D = -2.125 to -2.000, ξ/D = 0.125

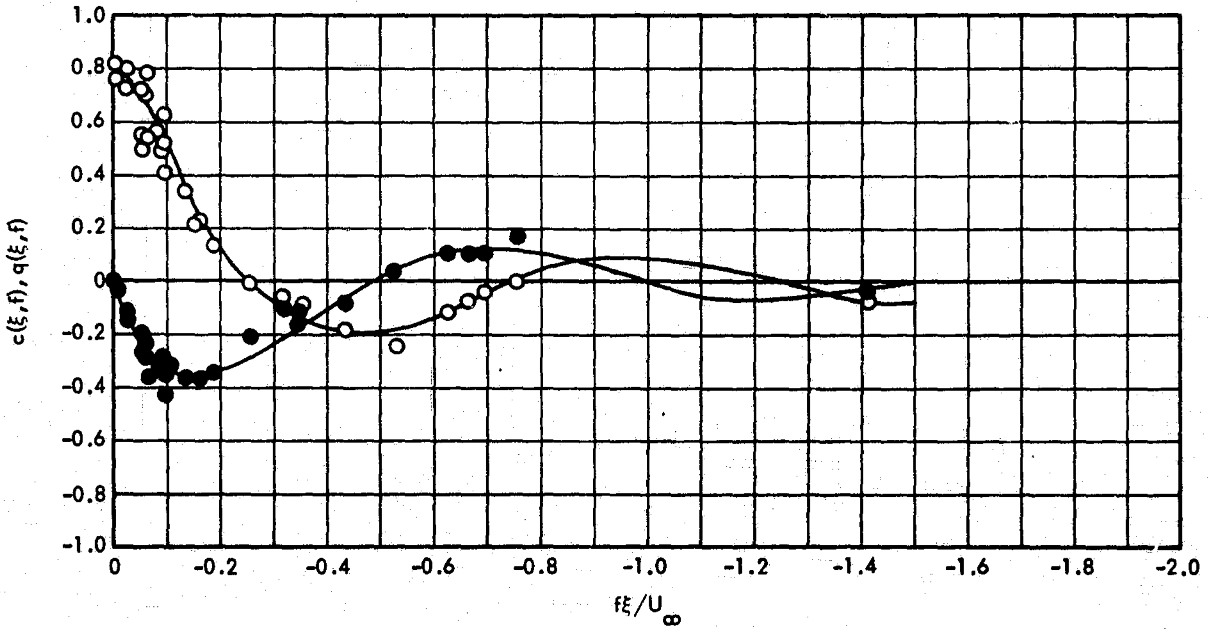

c. r/D = -1.875 to -1.750, ξ/D = 0.125

Figure 78. Variation of Longitudinal Cross-Spectra Within the Upstream Separated Flow Field, $M_\infty = 1.60$, h/D = 2.0

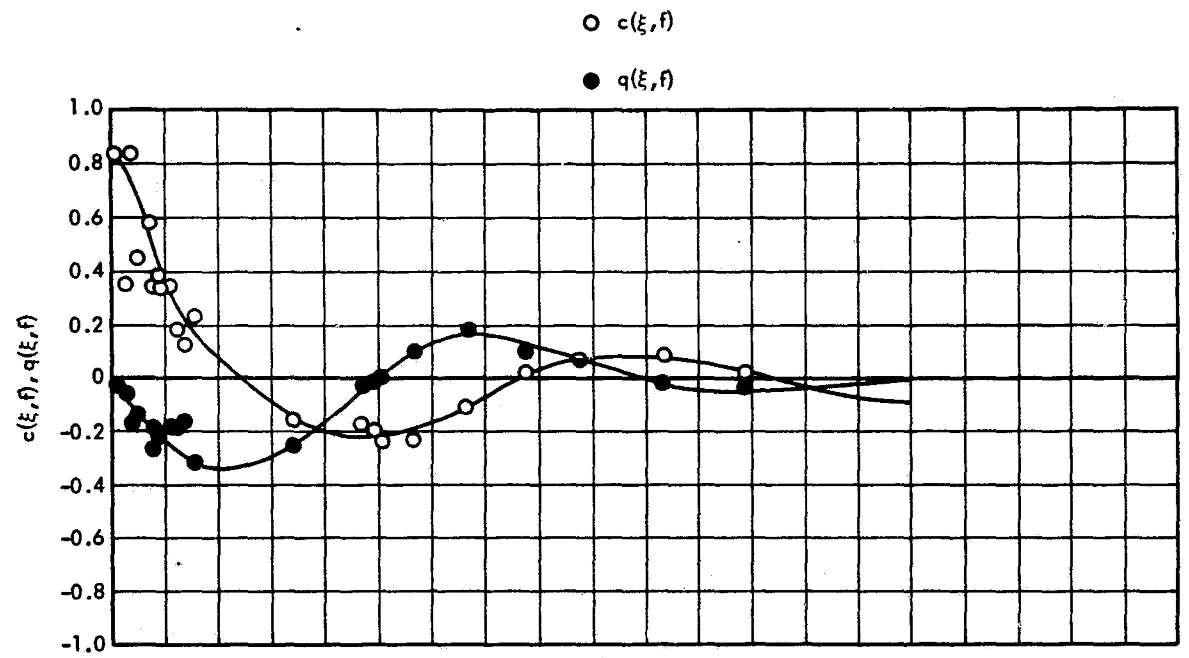

d. r/D = -1.625 to -1.500, ξ/D = 0.125

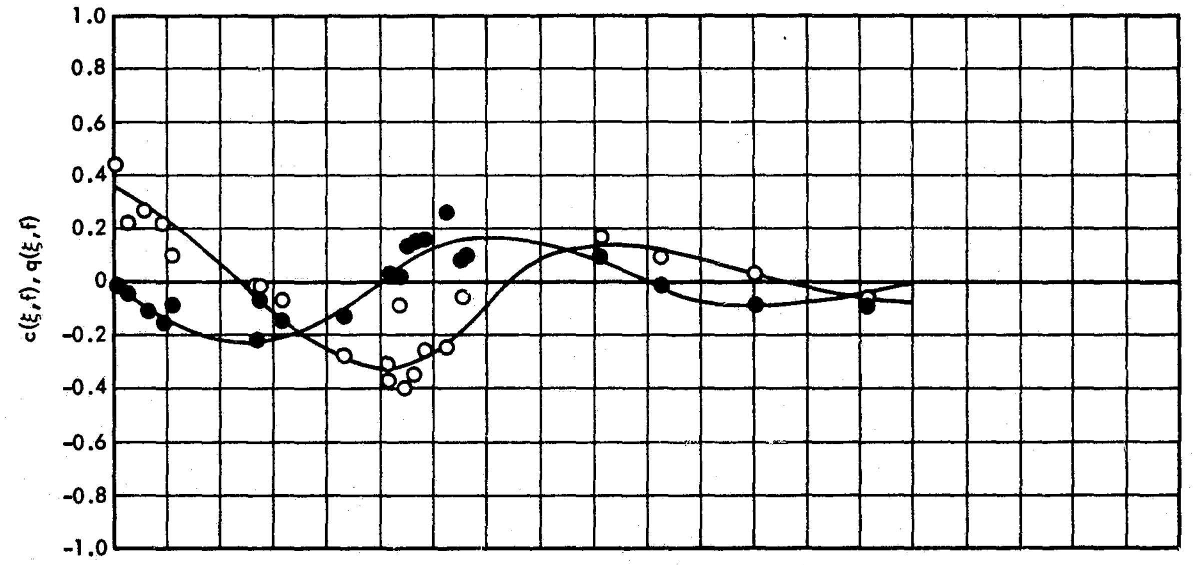

e. r/D = -1.375 to -1.500, ξ/D = 0.125

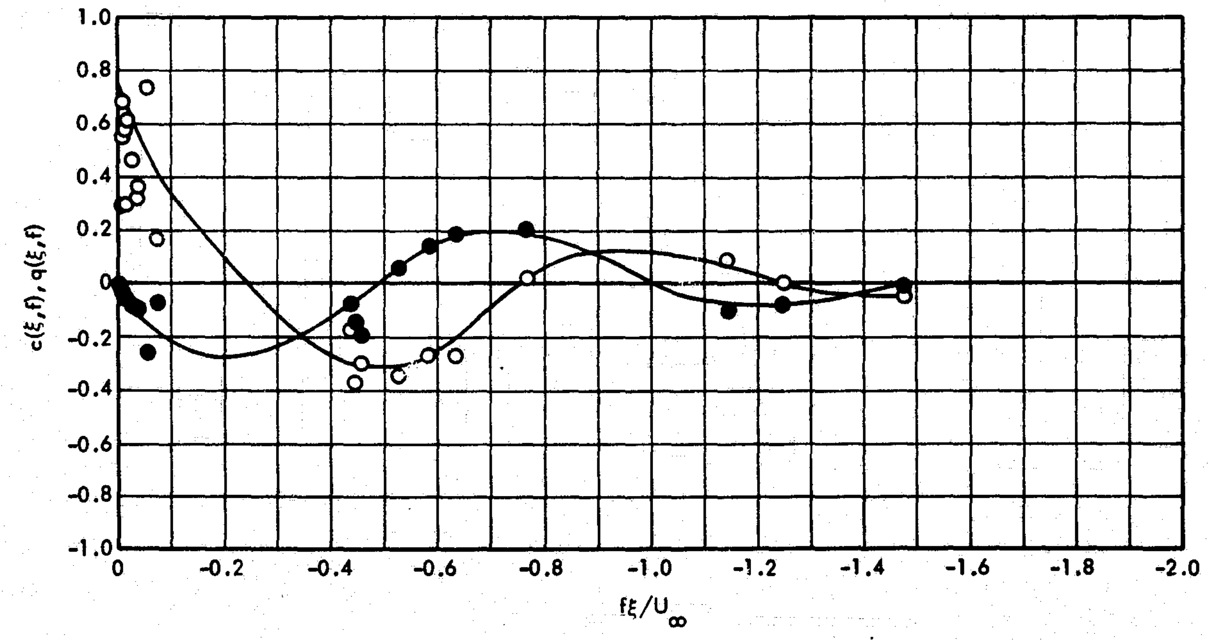

f. r/D = -1.125 to -1.000, ξ/D = 0.125

Figure 78. Concluded

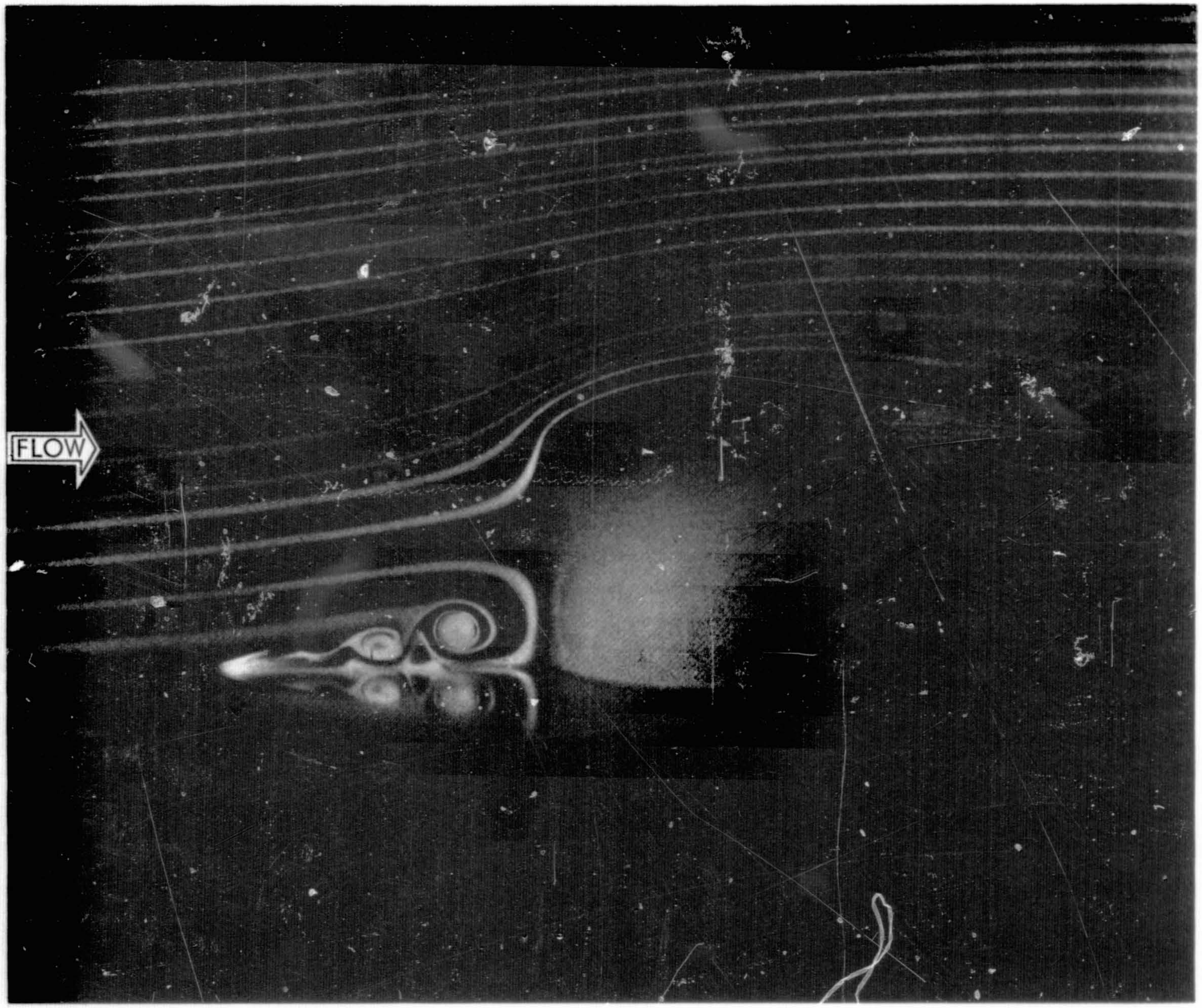

Figure 79. Smoke Filament Flow Pattern Upstream of a Cylindrical Protuberance at Low Speed (Reference 39)

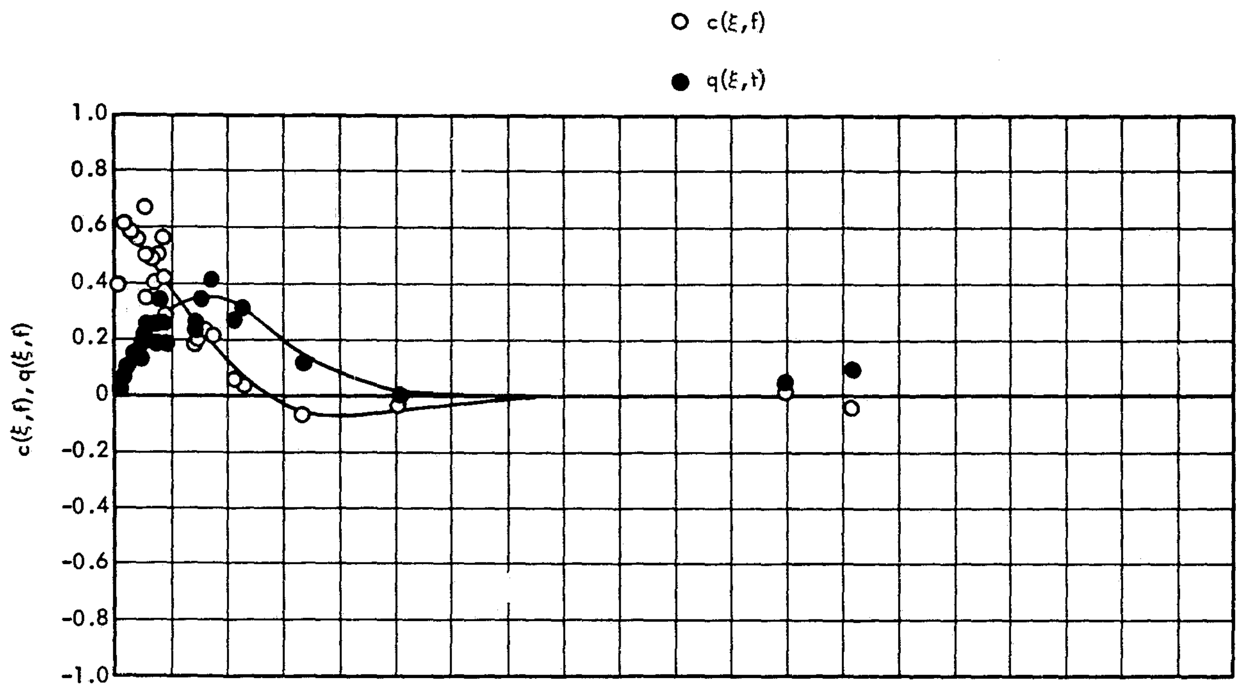

a. r/D = 0.750 to 0.875, ξ/D = 0.125

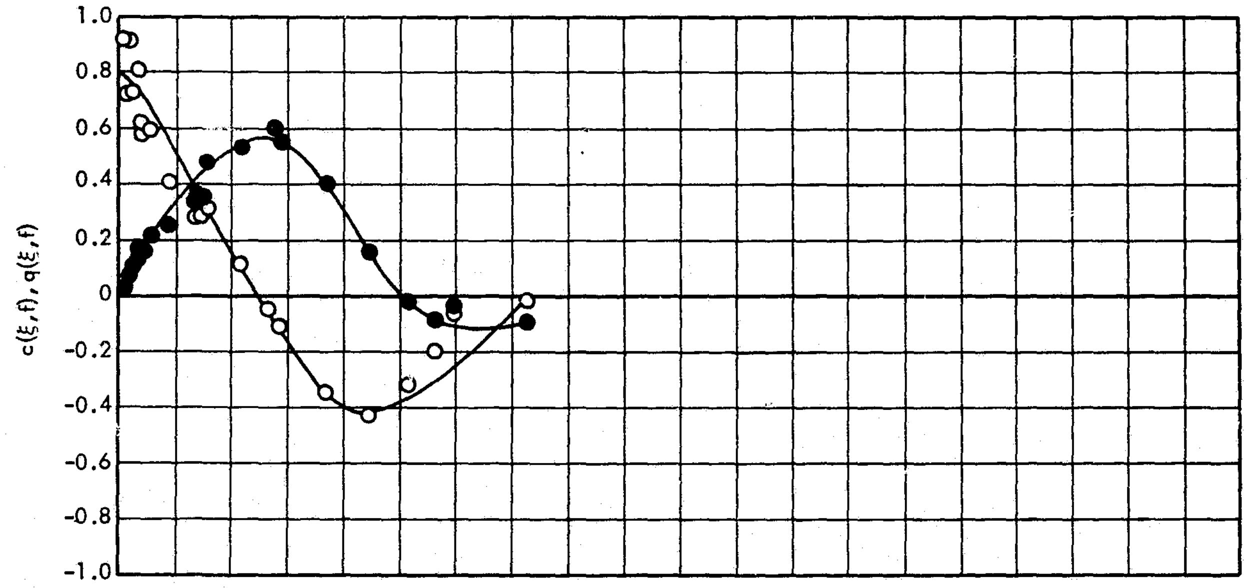

b. r/D = 1.000 to 1.125, ξ/D = 0.125

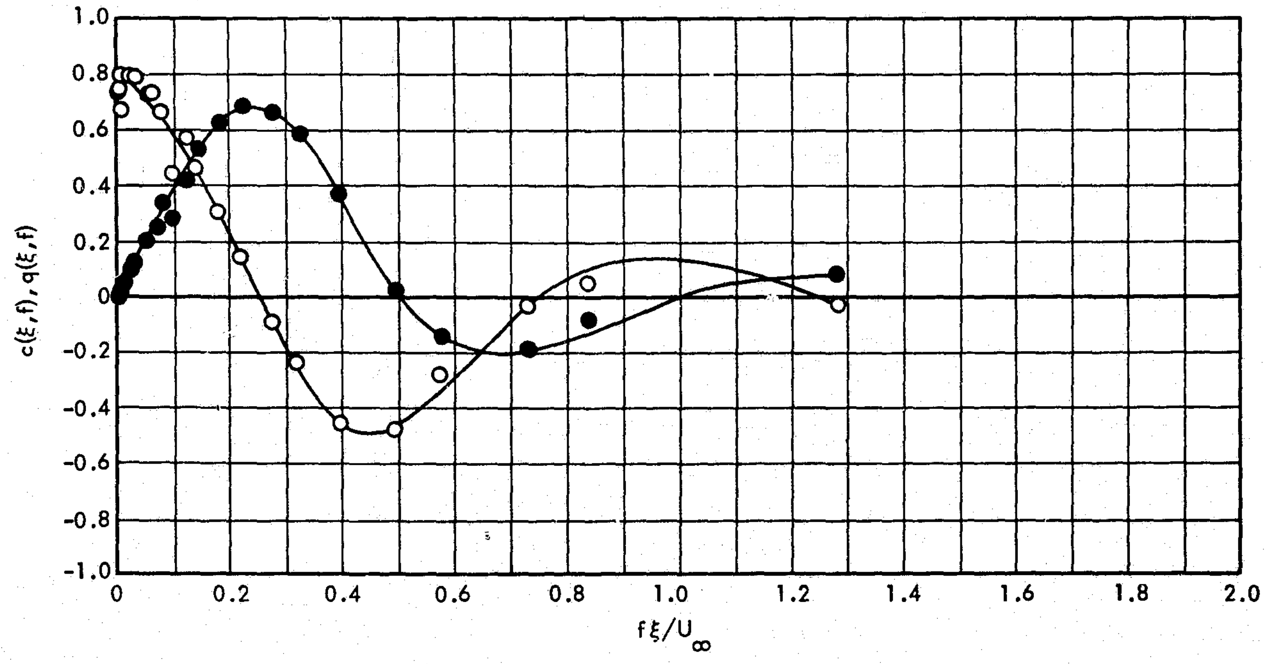

c. r/D = 1.250 to 1.375, ξ/D = 0.125

Figure 80. Variation of Longitudinal Cross-Spectra Within the Downstream Wake Flow Field, $M_\infty = 1.60$, $h/D = 2.0$

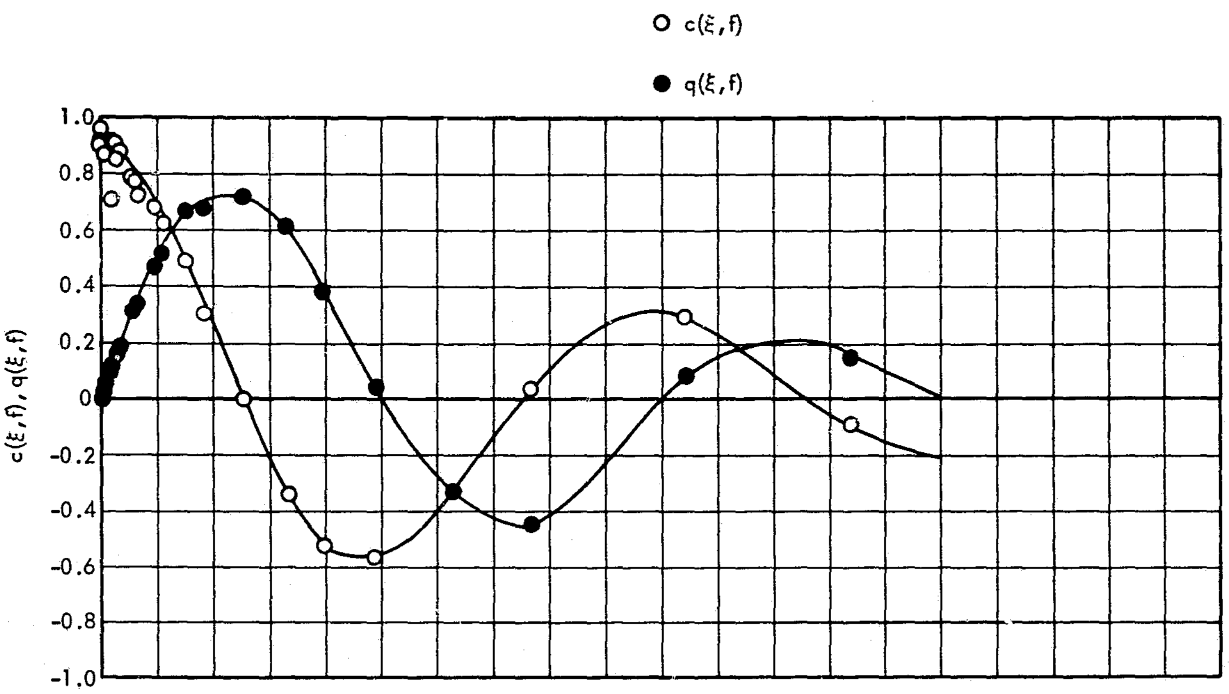

d. r/D = 1.500 to 1.625, ξ/D = 0.125

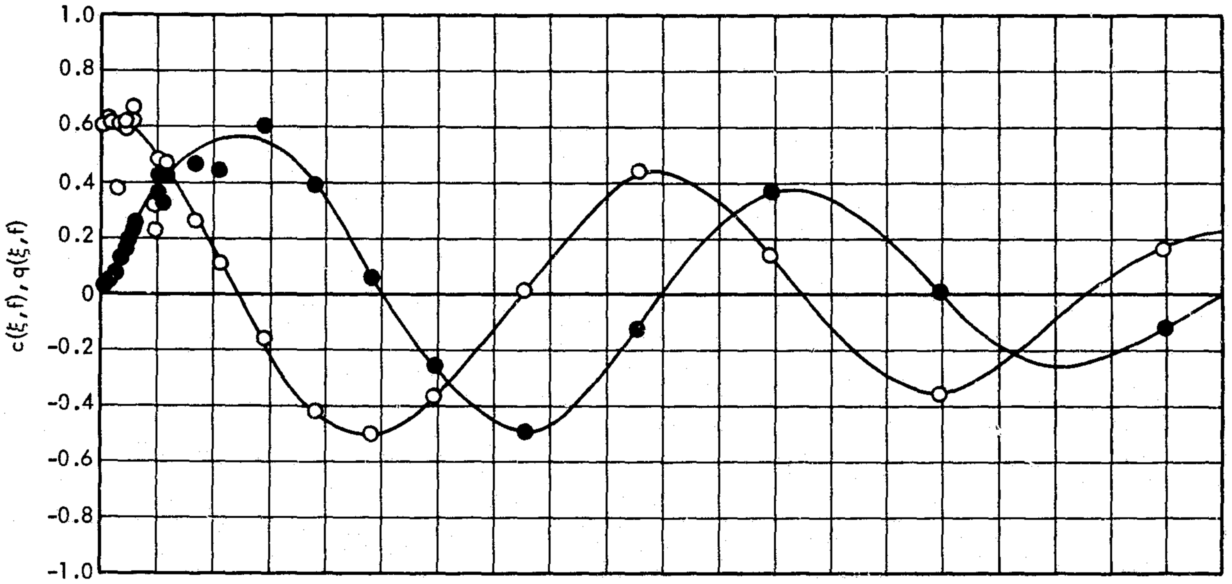

e. r/D = 1.750 to 2.000, ξ/D = 0.125

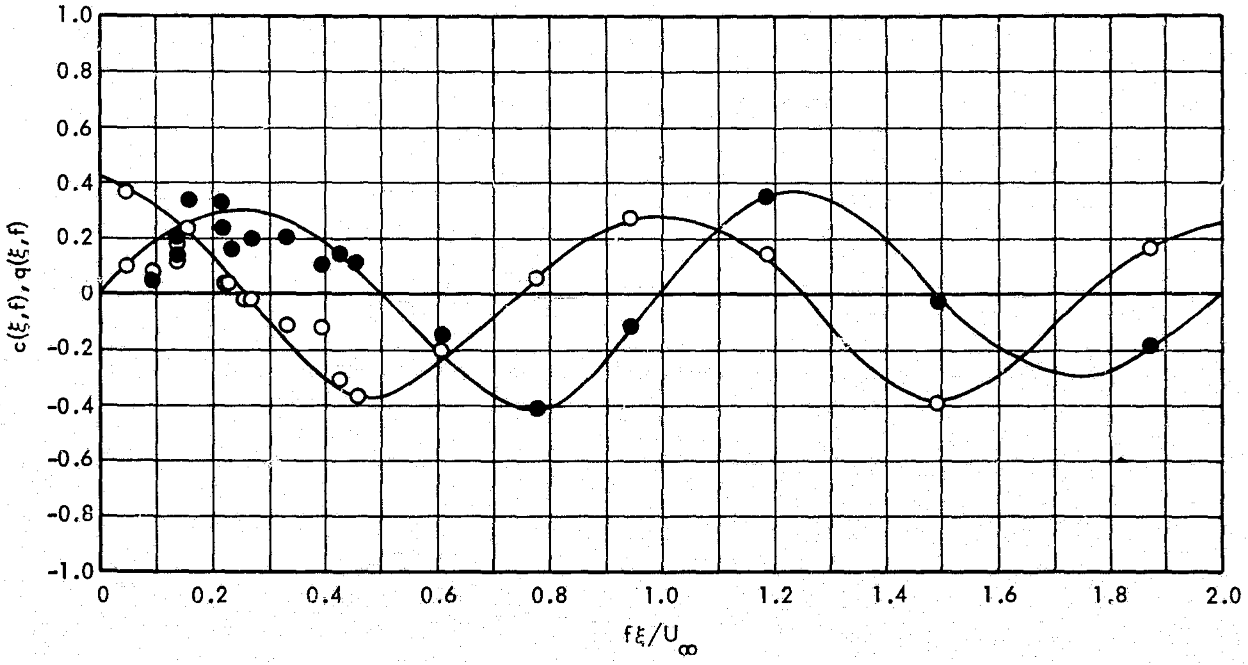

f. r/D = 2.000 to 2.500, ξ/D = 0.500

Figure 80. Concluded